



**HAL**  
open science

# Constraining p-Process nucleosynthesis through crucial cross-section measurements

Yasmine Demane

► **To cite this version:**

Yasmine Demane. Constraining p-Process nucleosynthesis through crucial cross-section measurements. Other [cond-mat.other]. Université Claude Bernard - Lyon I, 2023. English. NNT : 2023LYO10182 . tel-04702458

**HAL Id: tel-04702458**

**<https://theses.hal.science/tel-04702458v1>**

Submitted on 19 Sep 2024

**HAL** is a multi-disciplinary open access archive for the deposit and dissemination of scientific research documents, whether they are published or not. The documents may come from teaching and research institutions in France or abroad, or from public or private research centers.

L'archive ouverte pluridisciplinaire **HAL**, est destinée au dépôt et à la diffusion de documents scientifiques de niveau recherche, publiés ou non, émanant des établissements d'enseignement et de recherche français ou étrangers, des laboratoires publics ou privés.

**THESE DE DOCTORAT DE  
L'UNIVERSITE CLAUDE BERNARD LYON 1**

**Ecole Doctorale N°52  
PHYSIQUE ET ASTROPHYSIQUE**

**Discipline : Astrophysique Nucléaire**

Soutenue publiquement le 05/10/2023 par :

**Yasmine DEMANE**

---

**CONSTRAINING P-PROCESS  
NUCLEOSYNTHESIS THROUGH CRUCIAL  
CROSS-SECTION MEASUREMENTS**

---

Devant le jury composé de :

Dr. DE OLIVEIRA SANTOS François	GANIL-Caen	Président,examineur
Dr. STEZOSWKI Olivier	IP2I Lyon	Directeur de thèse
Dr. DUCOIN Camille	IP2I Lyon SUBATECH	Co-directrice de thèse
Prof. FALLOT Muriel	Nantes	Rapporteur
Prof. DORVAUX Olivier	IPHC-Strasbourg	Rapporteur
Dr. MILLARD-PINARD Nathalie	IP2I Lyon	Examinatrice



"Jamais trop, toujours plus" Y. *et al.*





## REMERCIEMENTS

Après trois années d'efforts, ces quelques lignes viennent enfin apporter réconfort marquant la conclusion d'un cycle d'études et l'amorce d'une nouvelle phase dans ma vie scientifique. Mais avant de refermer ce chapitre, je souhaiterais exprimer ma gratitude envers ma famille, mes amis, mes mentors et tous ceux m'ayant soutenu tout au long de cette merveilleuse aventure. Ce manuscrit est le fruit d'un effort collectif, et bien que lors de l'oral, l'émotion m'ait empêché de présenter mes remerciements de manière exhaustive, je souhaite ici pouvoir les exprimer pleinement.

Je souhaite tout d'abord exprimer mes plus sincères remerciements aux membres de mon jury, Muriel Fallot, Olivier Dorvaux et François De Oliveira Santos pour leur précieuse contribution à l'achèvement de ma thèse de doctorat. Le souvenir de notre collaboration restera dans ma mémoire, tout comme celui de l'oral où votre bienveillance a profondément marqué mon esprit.

Je tiens à exprimer ma profonde gratitude à Olivier Stezowski pour son rôle essentiel en tant que directeur de thèse. Sa guidance experte, son savoir étendu, sa patience et sa grande gentillesse ont été des piliers fondamentaux de notre collaboration. Je regretterai nos échanges, à la fois courts et tellement intéressants, de fin de journée.

Mais soulignons que ce travail n'aurait jamais pu voir le jour sans ma codirectrice de thèse, Camille Ducoin, à l'initiative de ce projet de recherche. Je lui suis reconnaissante pour tout le savoir transmis et particulièrement en astrophysique nucléaire théorique et fondamentale. Son appui et nos différentes discussions m'ont fourni un apprentissage précieux qui n'aurait pas été possible sans sa brillante perspicacité et son ouverture d'esprit.

Et pour tout cela, Camille et Olivier, je vous suis reconnaissante. J'ai eu la chance, et il est essentiel de le souligner, d'avoir pu travailler avec des personnes à la fois talentueuses et admirables d'un point de vue humain.

J'aimerais également remercier les membres du groupe "Matière Nucléaire" de l'IP2I avec qui j'ai pu échanger et qui m'ont également beaucoup apporté. Je pense notamment à Nathalie Millard Pinard pour qui je me suis attachée. Sa bonne humeur permanente égayait mes journées de travail, son état physique

olympique m'inspirait de l'admiration, et ses conseils m'ont permis de comprendre bien des notions sur de multiples domaines du monde de la recherche.

Je n'oublierai pas non plus la superbe rencontre avec Bernadette Rebeiro. Cette dernière m'a beaucoup appuyée dans mes débuts et j'ai eu de nombreuses reprises été inspirée par la manière redoutable qu'elle avait de travailler. Mais c'est sa personnalité unique et son amour des plantes qui resteront ancrés dans mes souvenirs.

Je souhaite également exprimer mes chaleureux remerciements aux personnes avec qui j'ai collaboré lors de la préparation d'expériences, et en particulier Nicolas De Sereville de l'IJCLab et Lionel Capoani de l'IP2I. Leurs soutiens constants et leurs aides précieuses m'ont permis de surmonter bien des obstacles au cours de cette thèse.

Ce doctorat a été financé par l'institut des origines de Lyon, le LABEX LIO, que je remercie sincèrement pour son soutien à la recherche et à la diffusion du savoir. Dans un monde scientifique confronté à des restrictions budgétaires constantes, ce laboratoire d'excellence représente une véritable bouffée d'air frais que j'espère voir perdurer. Je tiens également à exprimer ma gratitude envers Souad Lafehad et Aurélie Bougard pour leur accompagnement professionnel tout au long de ces trois dernières années.

À présent, place aux remerciements de la génération des thésards, en commençant par mes coups de coeur, Mojahed et Mohammed. Pour toutes ces balades autour du campus, nos longues et riches discussions, pour votre soutien au quotidien, pour tous ces restaurants, ces cafés, ces bowlings, ces spectacles, ces fous rires, un grand merci ! Je serai présente pour vos soutenances, l'histoire ne fait que commencer pour nous !

Et à tous les autres, Sarah, Tomasso, Valentin, Chang Woo, Paul, Jean-François, et à ceux que j'aurais pu oublier, merci pour tout !

Je ne saurais rédiger des remerciements sans penser à toi, Mylène. Ma plus tendre amie depuis toujours, la seule vraiment capable de me remonter le moral un jour d'hiver orageux, pluvieux, venteux... Merci pour tout, pour cette thèse, pour ton support inébranlable, pour tes conseils, pour avoir tenté de comprendre de quoi elle parlait... Et reste dans les parages, j'aurais encore besoin de toi à l'avenir ! Solène, Léa, Samira, Laura, Violette, Lisa, Ammashi, Christie

merci à vous toutes également pour votre soutien constant.

Tout cela n'aurait pas été possible sans la présence de mes quatre parents, qui ont toujours cru en moi et m'ont constamment apporté leur soutien, quel qu'il soit. Je dédie cette petite réussite à mon père, scientifique dans l'âme, qui m'offrait quand j'étais enfant les livres dont j'avais besoin pour satisfaire ma curiosité scientifique.

Je ne saurais dissocier mes parents de mes frères et soeurs qui ont tous fait l'effort de traverser la France pour me voir soutenir le jour J, et je ne saurais écrire des remerciements sans vous citer et sans vous dire à quel point vous comptez pour moi.

Mes presque dernières lignes sont pour toi, Arthur, et pour ces dernières années de vie commune. Pour la relecture de ma thèse, tes conseils scientifiques, ta gentillesse, ton soutien inconditionnel et tes encouragements durant les moments de doute et de difficulté. Être entouré c'est bien, mais être entouré par toi c'est mieux. Du master à la thèse, je te remercie du fond du coeur, et pour tout. Je suis convaincu que tu deviendras un brillant scientifique, et j'espère que nous continuerons sans relâche nos discussions passionnantes et passionnées.

J'en profite également pour exprimer mes sincères pensées à Evelyne, qui m'a toujours gratifié de son soutien et sa bienveillance lors de nos discussions. Je suis convaincue que la chaleur de nos nombreux dîners partagés a contribué, d'une manière ou d'une autre, à ma réussite.

Et enfin, je dédis ces quelques lignes à ma grand-mère, Hénia, et à mon chat, Swaggy, partis durant cette thèse, mais qui resteront à jamais auprès de moi.

Bien que cette étape de ma vie se termine, je ressens une profonde gratitude envers chacun d'entre vous pour avoir fait partie intégrante de ce parcours académique. Ce sont les personnes que l'on côtoie qui contribuent à nous façonner et à nous influencer, c'est donc avec un peu de vous tous que je continuerai à avancer.

## RESUMÉ

Ce manuscrit a pour objectif l'étude du processus p, essentiel à la formation des noyaux stables et riches en protons produits lors d'événements stellaires explosifs. La modélisation de ce processus repose sur des calculs théoriques de taux de réactions nucléaires, impliquant des sections efficaces de réactions. L'objectif de cette thèse est de mesurer plusieurs sections efficaces d'intérêt. Ces dernières seront cruciales à la compréhension des disparités existantes entre les calculs théoriques des abondances des noyaux-p et les observations expérimentales associées.

Cinq mesures de sections efficaces (p, $\gamma$ ) et (p,n) ont été réalisées en utilisant la méthode par activation sur des isotopes du germanium,  $^{70,72,73,76}\text{Ge}$ , dans le but d'étudier l'abondance du plus léger des noyaux-p, le  $^{74}\text{Se}$ . L'expérience a été menée à 2.5 MeV en utilisant le tandétron de l'Institut National Horia Hulubei. Deux sections efficaces de réactions ont été mesurées pour la première fois dans ce travail :  $^{73}\text{Ge}(p, \gamma)^{74}\text{As}$  et  $^{73}\text{Ge}(p, n)^{73}\text{As}$ . La section efficace de réaction  $^{72}\text{Ge}(p, \gamma)^{73}\text{As}$  a pu être comparée à une première mesure existante et réalisée via la technique du  $\gamma$ -summing [1]. Un écart d'environ 38% est observable entre ces deux études.

En parallèle, ce manuscrit détaille les préparatifs d'une expérience de diffusion élastique qui aura lieu à l'IJCLab Orsay par utilisation du spectromètre magnétique SplitPole et d'un faisceau d'alphas. L'objectif principal sera d'approfondir la compréhension des interactions fondamentales  $\alpha$ -noyau régissant les modèles d'abondances. Cette expérience se concentrera sur les mécanismes à l'origine de la formation des noyaux-p dont la masse est supérieure à  $A > 140$ .

Enfin, des concepts d'apprentissage automatique sont rapidement explorés. Ils font appel à des approches bayésiennes et fréquentistes et visent à démêler des corrélations complexes existantes entre différents paramètres influant sur les sections efficaces de réaction des noyaux-p.

## ABSTRACT

This thesis navigates the complexities of the p-process, crucial in understanding the formation of stable, proton-rich nuclei beyond iron, commonly created in explosive stellar events. The modeling of this intricate process relies on theoretical calculations of nuclear reaction rates, involving reaction cross-sections. The primary focus of this thesis will be on measuring relevant reaction cross-sections, aiming to facilitate the reconciliation of existing disparities between theoretical calculations and experimental observations.

Five cross-section measurements of  $(p,\gamma)$  and  $(p,n)$  reactions have been conducted using the activation method on germanium isotopes, specifically  $^{70,72,73,76}\text{Ge}$ , at 2.5 MeV using the tandetron of the Horia Hulubei National Institute. The main objective was to address discrepancies noticed in the abundance of  $^{74}\text{Se}$ , the lightest p-nucleus. The analysis provided the first experimental data for two reaction cross sections :  $^{73}\text{Ge}(p,\gamma)^{74}\text{As}$  and  $^{73}\text{Ge}(p,n)^{73}\text{As}$ . Furthermore, a new measurement of the  $^{72}\text{Ge}(p,\gamma)^{73}\text{As}$  reaction cross section revealed a notable discrepancy of approximately 38% when compared to another study that employed the in-beam  $\gamma$ -summing technique [1].

Additionally, the dissertation articulates plans for an upcoming  $\alpha$ -elastic scattering experiment at IJCLab Orsay using the SplitPole magnetic spectrometer. The primary objective is to refine our comprehension of the poorly known  $\alpha$ -nucleus interactions, fundamental in governing the reactions dictating the abundance patterns. This experiment will focus on elucidating the mechanisms behind the formation of high-mass p-nuclei beyond the mass range of  $A > 140$ .

Finally, Machine Learning concepts are introduced in order to bridge the gap between experimental data and the refinement of nuclear models. Bayesian and Frequentist approaches are explored to disentangle the existing correlations among various inputs affecting reaction cross-section simulations.

# Contents

---

<b>I</b>	<b>INTRODUCTION</b>	<b>15</b>
<b>II</b>	<b>BACKGROUND THEORY</b>	<b>18</b>
<b>1</b>	<b>ORIGIN OF THE CHEMICAL ELEMENTS</b>	<b>19</b>
1.1	Context . . . . .	19
1.2	Introduction . . . . .	20
1.3	Primordial Nucleosynthesis . . . . .	23
1.4	Quiescent Stellar Nucleosynthesis . . . . .	23
1.4.1	s-process . . . . .	25
1.5	Explosive Nucleosynthesis beyond iron . . . . .	26
1.5.1	r-process . . . . .	27
1.5.2	p-process . . . . .	27
<b>2</b>	<b>ASTROPHYSICAL CONCEPTS</b>	<b>32</b>
2.1	Nuclear Reaction Cross Sections . . . . .	32
2.2	Reciprocity Theorem . . . . .	33
2.3	S-factor . . . . .	35
2.4	Stellar Reaction Rates . . . . .	37
2.5	Gamow Windows . . . . .	38
2.6	Hauser Feshback formalism . . . . .	39
2.6.1	Level density . . . . .	41
2.6.2	Optical potential . . . . .	41
2.6.3	$\gamma$ -strength . . . . .	42
<b>3</b>	<b>EXPERIMENTAL TOOLS</b>	<b>43</b>
3.1	The Interaction of Radiation with Matter . . . . .	43
3.1.1	Gamma rays interaction . . . . .	43
3.1.2	Charged particles interaction . . . . .	47
3.2	Detection . . . . .	51
3.2.1	HPGe . . . . .	51
3.2.2	PIPS . . . . .	53
3.3	Target characterization techniques . . . . .	54
3.3.1	ICP-MS . . . . .	54

3.3.2	RBS . . . . .	56
3.4	Software . . . . .	58
3.4.1	SIMNRA . . . . .	58
3.4.2	TALYS 1.96 . . . . .	59
3.4.3	PENELOPE-2018 . . . . .	60
3.4.4	STOGS-GEANT4 . . . . .	60

**III P-PROCESS LIGHTER REGION : Activation measurement of p-induced reaction on several germanium isotopes 62**

**4 EXPERIMENTAL CONTEXT 63**

4.1	Overview . . . . .	63
4.2	Principle of the activation method . . . . .	66
4.3	Cross section calculation . . . . .	68
4.4	Experimental setup . . . . .	69
4.4.1	Germanium targets . . . . .	69
4.4.2	Proton beam and fluence . . . . .	74
4.4.3	Detection setup . . . . .	76

**5 DATA ANALYSIS 79**

5.1	The coaxial germanium detector . . . . .	79
5.1.1	Calibration . . . . .	79
5.1.2	Energy Resolution . . . . .	83
5.2	Spectroscopic study . . . . .	83
5.2.1	Target analysis : T[Ge <sub>nat</sub> ] . . . . .	84
5.2.2	Target analysis : T[ <sup>72</sup> Ge] . . . . .	85
5.2.3	Target analysis : T[ <sup>73</sup> Ge] . . . . .	86
5.2.4	Conclusion . . . . .	87
5.3	Detector efficiency . . . . .	88
5.3.1	Geometry simulation via PENELOPE(2018) and GEANT4 . . . . .	90
5.3.2	Results of simulations . . . . .	93
5.3.3	Efficiency curve . . . . .	96
5.4	Activity measurements . . . . .	97

**6 RESULTS AND DISCUSSION 101**

6.1	Determination of Cross Sections and S-Factors . . . . .	101
6.2	Discussion . . . . .	103



6.2.1	Cross section sensitivity to particle widths . . . . .	103
6.2.2	Theoretical models implemented in TALYS . . . . .	107
6.2.3	Comparison between models and experimental data . . .	111
6.3	Conclusion . . . . .	118

**IV P-PROCESS HEAVIER REGION : Alpha elastic scattering** **120**

<b>7</b>	<b>EXPERIMENTAL CONTEXT</b>	<b>121</b>
7.1	Overview . . . . .	121
7.2	Principle of the angular distribution . . . . .	124
7.3	Target . . . . .	127
7.3.1	List of targets to characterize . . . . .	127
7.3.2	RBS Characterization . . . . .	128
7.3.3	Global conclusions on target characterization . . . . .	134
7.4	Detection set-up . . . . .	135
7.4.1	Alpha beam . . . . .	135
7.4.2	SPLITPOLE spectrometer . . . . .	136
7.4.3	Particle identification . . . . .	137
7.5	Silicon detector . . . . .	139
7.5.1	Energy loss . . . . .	141
7.5.2	PIPS characterisation . . . . .	142
7.5.3	Current list of available detectors . . . . .	146
7.5.4	Electronic test . . . . .	147
7.5.5	Counting rate . . . . .	148
7.6	Piece manufacturing . . . . .	151
7.6.1	PIPS support . . . . .	151
7.6.2	Target support . . . . .	153
7.7	Summary and Outlook . . . . .	155

**V MACHINE LEARNING TECHNIQUES FOR P-PROCESS ADVANCEMENT** **157**

<b>8</b>	<b>TOOL EXPLORATION</b>	<b>158</b>
8.1	Introduction . . . . .	158
8.2	Cross section determination : Direct approach . . . . .	159

8.2.1	Bayesian Inference : The Gaussian process . . . . .	159
8.2.2	Boosted Decision Tree . . . . .	162
8.3	Cross section determination : Indirect approach . . . . .	166
8.3.1	Bayesian Optimization : The MCMC method . . . . .	166
8.4	Discussion . . . . .	168

## VI THESIS GLOBAL CONCLUSION AND PERSPECTIVES 170

## VII ANNEXES 173

### A EURISOTOP : Targets isotopic percentages 174

A.1	Analysis certificate of the target T[ <sup>70</sup> Ge] . . . . .	174
A.2	Analysis certificate of the target T[ <sup>72</sup> Ge] . . . . .	175
A.3	Analysis certificate of the target T[ <sup>73</sup> Ge] . . . . .	176

### B Results of ICP-MS analysis 177

B.1	Preliminary step to isotopic measurements . . . . .	177
B.2	ICP-MS measurements : target T[ <sup>70</sup> Ge] . . . . .	178
B.3	ICP-MS measurements : target T[ <sup>73</sup> Ge] . . . . .	179

### C Instrumentation : Germanium detector 180

### D Arsenic decay schemes 182

D.1	Decay schemes of the <sup>71</sup> As . . . . .	182
D.2	Decay schemes of the <sup>76</sup> As . . . . .	183
D.3	Decay schemes of the <sup>73</sup> As . . . . .	184
D.4	Decay schemes of the <sup>74</sup> As . . . . .	185

### E Monte Carlo simulations for Ge efficiency determination 187

E.1	Comparison of experimental vs. simulated data . . . . .	187
E.2	Effect of source shape modification . . . . .	190
E.3	Impact of source displacement in x and y directions . . . . .	191

### F Activity curves 192

### G Cross Section Sensitivity 194

H	Alphas energy loss in silicon	196
I	Boosted decision tree prediction on $(p,\gamma)$ reaction	197

Part I

# INTRODUCTION

On the proton-rich side of the valley of stability, lies a captivating puzzle involving 35 stable proton-rich nuclei beyond iron. These nuclei are believed to be produced in supernova events, where temperatures range from 1.5 to 3.5 GK. Their formation involves networks of thousands of reactions, starting from seed heavy nuclei previously created through neutron capture. This intriguing process is known as the p-process. The creation of these nuclei under specific conditions results in remarkably low abundances, and researchers have been striving to replicate and understand these phenomena through theoretical calculations for many years. The main scenario for the production of these p-nuclei involves essentially photodisintegrations  $(\gamma, n)$ ,  $(\gamma, p)$  and  $(\gamma, \alpha)$ , and is therefore called  $\gamma$ -process; but the contribution of alternative scenarios is necessary. Despite considerable efforts, notable discrepancies still remain between nucleosynthesis calculations and observed abundances, stemming from the scarcity of data necessary to constrain both nuclear and astrophysical models. Therefore this work will primarily focus on a pivotal factor that profoundly influences reaction rates : the reaction cross-sections.

Five cross-section measurements of  $(p, \gamma)$  and  $(p, n)$  reaction cross sections have been conducted on several germanium isotopes, namely  $^{70,72,73,76}\text{Ge}$ , at an energy of 2.5 MeV, targeting the Gamow window of the reactions. The experiments were carried out using the activation technique with the tandetron at the Horia Hulubei National Institute. The primary objective of these measurements was to determine the abundance of the lightest p-nucleus,  $^{74}\text{Se}$ , which currently exhibits discrepancies with the most widely accepted astrophysical scenario for p-nuclei creation. The cross sections and S-factors have been carefully extracted and compared to both available experimental data and theoretical predictions that use the Hauser-Feshbach theory. This detailed analysis provide the first experimental data for two cross sections,  $^{73}\text{Ge}(p, \gamma)^{74}\text{As}$  and  $^{73}\text{Ge}(p, n)^{73}\text{As}$ , which are currently poorly estimated by theoretical calculations. Furthermore, others measurements are compared with some already existing and in perfect agreement with the currently calculated reaction rate.

This dissertation also delves into the preparation of a planned  $\alpha$ -elastic scattering experiment at IJCLab Orsay, utilizing a SplitPole magnetic spectrometer. The research focus is now on the formation of heavy-mass p-nuclei, with particular emphasis on the mass region  $A > 140$ . The  $\alpha$ -nucleus optical potential in this region is badly known and crucial to determine the rates of  $(\gamma, \alpha)$  reactions

to which the heavy p-nuclei abundances are very sensitive. It has then been proposed to measure  $\alpha$ -elastic scattering differential cross sections on  $^{144}\text{Sm}$ ,  $^{162}\text{Er}$ , and  $^{177}\text{Hf}$ . Several crucial aspects are discussed, ranging from detailed simulations to enhancing the experimental setup, ensuring a robust and well-structured program. The ultimate goal is to gain a comprehensive understanding and help the development of a global  $\alpha$ -nucleus optical model potential, that can be reliably applied in the p-process region within the energy window of interest.

Finally, in the quest to tackle the complexity of nuclear systems, this work introduces and explores various machine learning concepts which could be useful for the study of the p-process. Bayesian and frequentist approaches are employed to disentangle correlations among the inputs affecting reaction cross section simulations. The initial findings suggest that these approaches are not in competition but rather complementary in addressing the challenges at hand.

Within the pages of this dissertation, the reader will embark on the captivating journey of a pioneering thesis, officially inaugurating the realm of nuclear astrophysics research at IP2I. Divided into four main sections on theory II, experimental studies III & IV plus a prospective part about machine learning V, this work will explore a myriad of subjects, encompassing the data analysis of past experiments, the anticipation of forthcoming experimental endeavors, and the initial strides towards using rising computing tools to refine the links between experimental data and improvement of nuclear models.

Part II

# BACKGROUND THEORY

# 1 ORIGIN OF THE CHEMICAL ELEMENTS

---

## 1.1 Context

---

Could the Universe have been born out of nothing? Some theories do not rule this out, but it remains a complicated question to answer. Throughout centuries, various traditional myths have attempted to describe and date the origin of the world, but the question encounters an inherent difficulty. How can something emerge from nothing, and how can we describe nothingness if it is truly devoid of anything? Fortunately for me, this will not be the subject of this thesis, although I wouldn't have minded additional thousand years of research. Let us instead start at the beginning of the observable, the Big Bang.

Approximately 13.8 billion years ago, the Universe started from an infinitely hot and dense singularity. At this stage, the laws of physics, with our current understanding, do not apply and our models cannot accurately describe what happened. During the first fractions of seconds, the Universe underwent an extremely fast expansion known as cosmic inflation. During this period, space-time experienced exponential growth, leading to a significant increase in the size of the Universe and a subsequent cooling effect. The term "Big Bang" is often used to refer to the beginning of the Universe, but it is important to clarify that the Big Bang theory is not just about a singular event or location : as emphasized by Professor James Peebles during the presentation of his 2019 Nobel Prize in Physics, the concepts of an event and a place are currently not applicable.

After 380 000 years of cooling and expansion, the temperature was low enough to allow the combination of electrons with nuclei to form the first atoms. At this stage, the light began to propagate, giving rise to what is now known as the cosmic microwave background (CMB). This light is today detected as microwave radiation coming from all directions in space. Over time, matter started to clump together, forming increasingly larger structures, leading to the formation of the first stars and galaxies. Stars, essential for life, are not only sources of light and heat but also play a crucial role in the creation of all the chemical elements in our world. They produce energy by nuclear fusions, forming chemical elements up to the mass of iron, a process known as stellar burning.

The heavier elements of the Universe are produced in a different manner, either



during the helium burning stage, or by different kinds of processes during the end stages of massive stars (beyond 8-10 solar masses), a phenomenon commonly referred as "supernova episodes". These explosive nucleosynthesis are the driving force and primary motivation behind this work. The origins of these heavy nuclei are explained through various processes, but some complex aspects still remain to be elucidated. For this reason, we will endeavor, through the lines of this thesis, to make a modest contribution to the body of knowledge and deepen our collective understanding of the explosive nucleosynthesis in the Universe.

## 1.2 Introduction

---

The Universe can be described in terms of the elements that make it up, and the same applies to cosmic objects. On Earth, matter is composed of atoms, and each atomic nucleus can be intrinsically identified by its composition of neutrons and protons which are non-elemental particles bound together by the strong nuclear force. The different possible arrangements of these particles in an atom give rise to various characteristics of matter, which have been classified according to what is known as chemical elements. Although people have been able to tell the difference between several elements since ancient times, such as iron reputed for its hardness, or gold reputed for its beauty, the knowledge of the atomic model came later. The atomic nucleus and the proton have been discovered by Rutherford and collaborators in 1909 and 1919 respectively. In 1932, the physicist James Chadwick discovered the neutron particle, thus completing the description of the atom as developed by his predecessors.

Nowadays, the classification of chemical elements is based solely on atomic numbers, as in Mendeleev's periodic table, and completed by the chart of nuclei based on the number of neutrons and protons. This allows for the inclusion of multiple isotopes within the same element family, as depicted in Fig.1. In this figure, stable nuclei are displayed in black in what is known as the valley of stability, while unstable radioactive nuclei are depicted in color according to their decay mode. It should be noted that the most exotic nuclei are not included in this chart. The short common convention describes nuclei using the symbols  ${}^A\text{X}$ , where A represents the total number of neutrons and protons, and X represents the chemical symbol of the element. This notation will be used throughout this essay.

It is widely accepted that the solar system formed from the collapse of a gaseous nebula that had a relatively uniform distribution of elemental and isotopic abundances. These solar abundances can be estimated through several sources of information, starting with different kinds of materials found on Earth. However, the formation of the solar system and planetary bodies that occurred approximately 4.5 billion years ago was accompanied by several differentiation processes that separated different types of chemical elements. As a result, some of the abundances determined from terrestrial material were inaccurately estimated. Elemental abundances can also be partially determined from spectral rays observed in the Sun, but the information is limited by the low Sun surface temperature and the impossibility to distinguish rays from different isotopes for most elements. The situation improved around the 1930s when several studies analyzed the composition of chondrite meteorites, the most primitive remnants of the known solar system to date. These objects were submitted to little differentiation and are recognized as giving a more reliable average of the solar system composition. Compilations and evaluations of solar ray, terrestrial and meteorite data were performed for instance by Suess and Urey in 1956 [2] and later by Anders and Grevesse in 1989 [3], producing abundance curves that represent quite reliable estimations of the solar system elemental and isotopic composition.

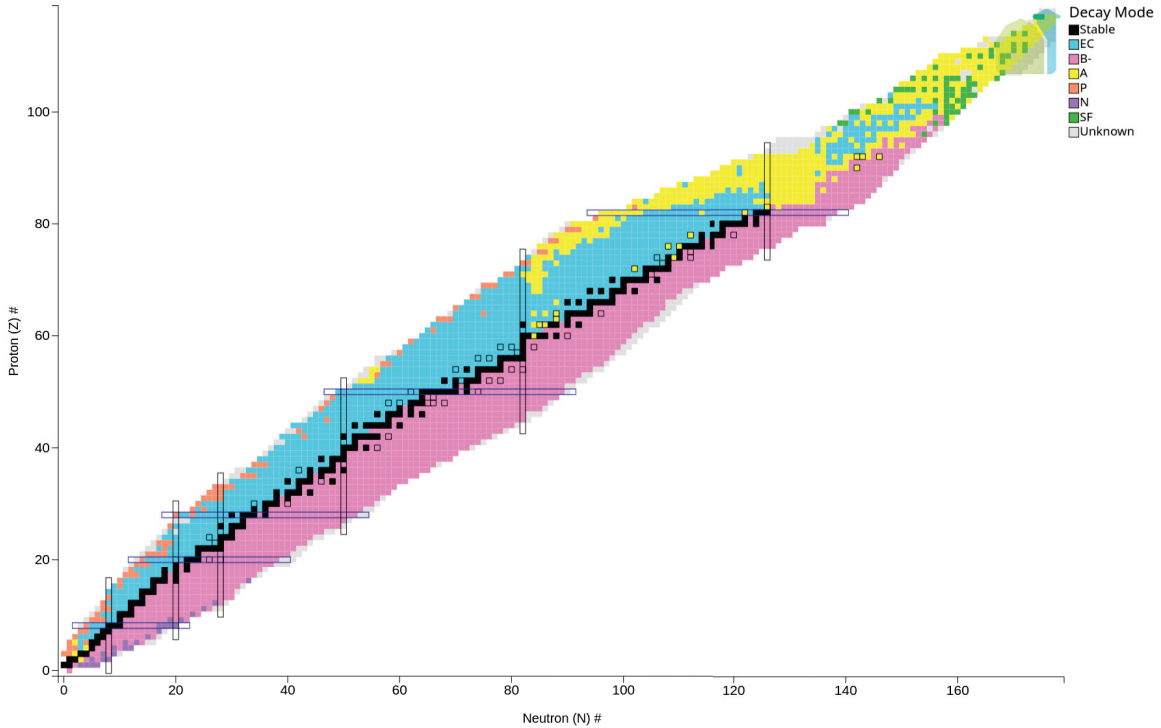


Figure 1: Chart of all nuclides referenced so far on NUDAT [4] with the decay mode indicated in colour.

During the study of the measured abundances, certain regularities and systematic patterns were observed, suggesting that some groups of nuclei could be attributed to common nucleosynthesis processes. The role of nuclear properties and the implication of different types of nuclear reactions were recognized (see [2] and references therein). A first global view of the different nucleosynthesis processes giving rise to the observed abundances was given in 1957, independently by Burbidge *et al.*[5] and Cameron [6]. These processes involve different astrophysical sites and types of nuclear reactions, which are still the object of intensive researches to identify the origin of the nuclei across the chart. Furthermore, it is now known that the solar abundances are not universal, as it was thought due to their similarity with those deduced from the spectral lines observed in different kinds of stars, in our Galaxy and even some other galaxies of the Universe. Indeed, the discovery in primitive meteorites of presolar grains that exhibit significant variations in some elemental and isotopic ratios show that local compositions can be influenced by specific astrophysical events. Thus, a detailed knowledge of how nuclei are produced by major sites of nucleosynthesis represents a major challenge to accomplish further progress in our

understanding of the origin of elements.

### 1.3 Primordial Nucleosynthesis

---

During the initial stages of the cosmos, few seconds after the Big Bang, the Universe was extremely hot and dense, filled with a primordial soup of particles and energy. As the Universe expanded and cooled, significant events took place, including the process known as Big Bang nucleosynthesis (BBN). This term was introduced between 1940-1949 for the first time by Gamow, Alpher, Bethe, Herman and associates to explain how the heavy elements might have been produced [7, 8]. As the Universe expanded and cooled further, the energy dropped around  $10^9$  Kelvin enabling protons and neutrons to combine to form light atomic nuclei:  $^1\text{H}$ ,  $^2\text{H}$ ,  $^3\text{H}$ ,  $^4\text{H}$ ,  $^6\text{Li}$ ,  $^7\text{Li}$  [9].

Furthermore, within a few minutes, the expansion reduced the temperature and density still further. The formation of heavier nuclei was hindered by the higher Coulomb barrier (electrostatic repulsion between charged particles), and reactions froze out before elements heavier than carbon could be formed.

Calculation predictions of this primordial nucleosynthesis align remarkably well with the observed abundances, especially  $^4\text{He}/^1\text{H}$  ratio, providing strong evidence of the BBN theory. The observed primordial abundances serve therefore as indicators of the baryonic density conditions prevailing during this time.

However, certain questions still remain, especially regarding the abundance of lithium, which is a subject of ongoing debate : in this case, the primordial abundance is affected by important astrophysical uncertainties, due for instance to its destruction through nuclear reactions in stars [10].

### 1.4 Quiescent Stellar Nucleosynthesis

---

The life of a star begins with vast clouds of gas and dust that are drawn together by the force of gravity. These clouds are predominantly composed of hydrogen and helium (respective mass fractions  $\approx 75\%$  and  $\approx 25\%$ ) with small amounts of other elements. As gravity pulls the gas and dust closer, the atoms in the core of the star become compressed, resulting in an increase in temperature and pressure and the formation of a plasma. At a critical point, the conditions become so extreme that the kinetic energy and the density of the charged particles allow them to overcome the repulsive Coulomb forces. This enables the fusion of lighter nuclei into helium. The two main mechanisms underlying the

conversion of hydrogen into helium were discovered during the years 1936-1939 : the proton-proton (p-p) chains and the Carbon-Nitrogen-Oxygen (CNO) cycles releasing an amount of energy of approximately 26.731 MeV for each  $^4\text{He}$  produced [9]. This stage of stellar evolution is known as hydrogen burning, and it plays a crucial role in the formation of stars from the "main sequence" on the Hertzsprung-Russell temperature-luminosity diagram, as illustrated in Fig.2. This powerful tool for understanding stellar evolution contributed significantly to our knowledge of the life cycles and evolutionary stage of stars.

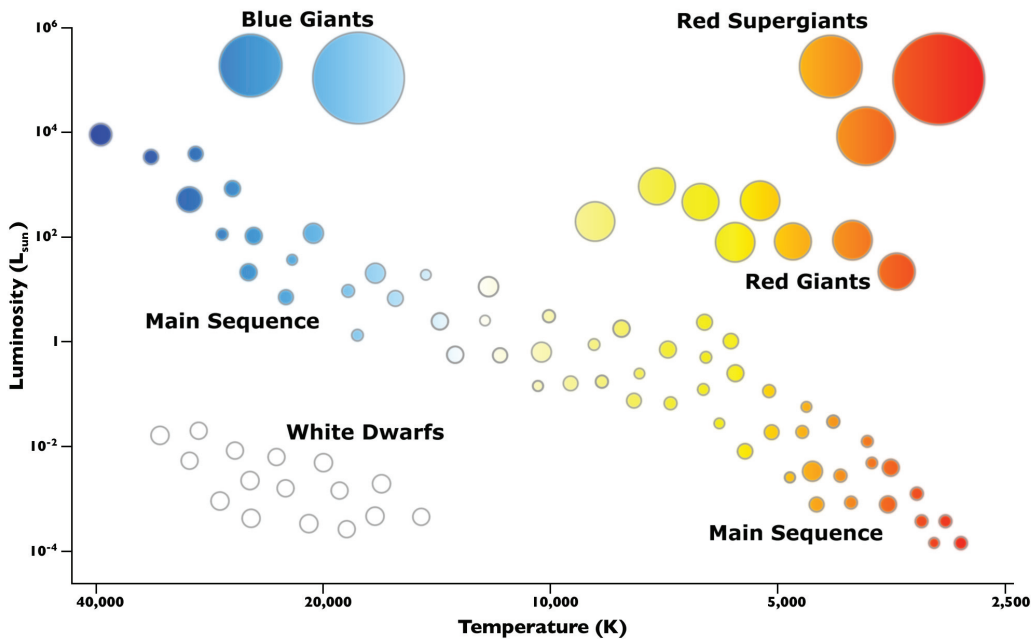


Figure 2: Hertzsprung-Russell simplified diagram showing the relationship between the star luminosities versus their effective temperatures. Extracted from [11].

The p-p chains are the main processes involved in low-mass stars, similar to the Sun, where the reaction chain starts mainly with the fusion of two protons. Currently, three p-p chains are distinguished leading to the transformation of four protons into  $^4\text{He}$ . On the other hand, the CNO cycles predominantly occur in massive stars. The four distinct CNO processes involve the participation of heavier nuclei which is favored by higher temperatures.

During the hydrogen burning phase, the energy released in the form of photons and neutrinos serves to counterbalance the gravitational forces, allowing the hydrostatic equilibrium of the star. After an extended duration of millions or billions of years, depending on the mass of the star under investigation, the

hydrogen fuel is consumed, resulting in the cessation of nuclear reactions. As the repulsive forces that maintain equilibrium with gravity decrease, the star undergoes a renewed phase of compression. Subsequently, a new rise in temperature and density occurs and a new cycle of nuclear fusion begins, this is the helium burning stage.

At the end of the helium burning phase, two categories of stars are distinguished. Those having a mass below  $8M_{\odot}$  are unable to initiate fusion reactions beyond helium. Since their contraction leads to hydrostatic equilibrium ensured by electron pressure, the core never reached a temperature sufficient to start new fusions. These stars will ultimately leave the main sequence to evolve into white dwarfs.

The massive stars exceeding  $8M_{\odot}$  will continue their fusion processes by successive burning phases through the fusion of the following elements : C, Ne, O, and Si respectively. The Si burning stage leads to a nuclear statistical equilibrium that favors the nuclei in the iron region, where the binding energy per nucleon is highest. For this reason, no exothermic fusion reaction can occur beyond this stage. At this point, the gravitational forces will regain the upper hand precipitating the collapse of the stellar core, and ultimately marking the end of the star life-cycle [9, 12, 13].

As a result, nuclei up to iron are produced through successive burning stages in stars. However, nuclei heavier than iron have to be created through other processes. Since neutrons are electrically neutral and do not experience repulsion from the atomic nucleus, the production of heavy nuclei predominantly occurs through neutron captures on existing nuclei within stellar environments (s- and r- process).

#### 1.4.1 s-process

---

One of the main mechanisms responsible for the creation of elements heavier than iron in the Universe is the s-process. This slow neutron capture process occurs during the helium burning stage of stellar evolution, due to the presence of  $(\alpha, n)$  reactions as source of neutrons. The s-process operates at neutron densities below or equal to  $10^{10} \text{ cm}^{-3}$  [14], which is relatively low and extends over thousands of years. Notably, these captures predominantly occur on stable or long-lived nuclei as the timescale for neutron capture exceeds the  $\beta$ -decay timescale for most unstable nuclei. This has been advantageous for measuring the reaction cross sections of the nuclei created by this process, as the stable

nuclei involved in these reactions are readily accessible due to their stability and high abundances.

These last are estimated based on two sub-processes of the s-process : the weak and the strong, involving respectively massive giant stars and asymptotic giant branch (AGB) stars undergoing thermal pulsations [15]. Without going into details, these two sub-mechanisms are responsible for the production of heavy nuclei ranging from the mass of iron up to  $^{209}\text{Bi}$  which represents the termination point of s-nuclei [9].

## 1.5 Explosive Nucleosynthesis beyond iron

---

During the late stages of massive star lives, nuclear fusion reactions and the associated radiation pressure wane concomitantly with the conversion of silicon into iron. Under these conditions, the gravitational pressure increase on the stellar core but is still counteracted by the electron pressure. However, as the density and temperature reach extreme levels, a phenomenon called electron capture ensues and reduces the support provided by electron degeneracy pressure. When the stellar core reaches the Chandrasekhar mass, it reaches a point where it can no longer maintain self-support and thus triggers a process of gravitational collapse. This stellar evolution leads to violent explosive event called core-collapse supernova, during which extreme temperature and density conditions trigger specific nucleosynthesis processes. [9, 12].

It soon became clear in the early days of supernovae observations that two types of supernovae exist : type-I and type-II. Observers have maintained this convention of classifying supernovae, although there are now many subcategories to both types of supernovae [16]. Type-I supernovae occur in binary systems where a compact star accretes matter from its companion until a nuclear runaway occurs while the core-collapse events described above correspond to Type-II supernovae, which mark the end of massive star lives.

More recently, the observation of gravitational waves evidenced neutron star coalescence events called kilonovae. These different types of events play a vital role in the cosmos by ejecting large amounts of material into space, including enriched stellar remnants and heavy elements synthesized during the star life. We will now address the main mechanisms involved in the formation of these heaviest nuclei.



### 1.5.1 r-process

---

The r-process for “rapid neutron-capture process”, is responsible for synthesizing approximately half of nuclei heavier than iron in the solar system, while the s-process is responsible for the other half. The r-process occurs in explosive astrophysical events characterized by high neutron densities ( $\geq 10^{19} \text{ cm}^{-3}$ ) and short timescales ( $\leq 1 \text{ ms}$ ), such as supernovae or neutron star mergers [12, 17] although the exact astrophysical sites are still not yet accurately established. The intense neutron flux in these environments leads to a rapid sequence of neutron capture reactions (around 10-20 excess neutrons compared to their stable isobaric neighbors [12]), which occur faster than  $\beta$ -decays. The series of neutron captures leads to a gradual reduction in neutron binding energy as the system approaches the "drip line," which marks the boundary of nuclear binding. The r-process then continues along the drip-line by alternative  $\beta$ -decays and neutron captures, until fission puts an end to the mass increase.

In neutron-rich environments, the rapid neutron capture process can theoretically create atomic nuclei up to a mass number of approximately 300 or greater, although the majority of them are typically unstable and undergo rapid decay. When the neutron flux stops,  $\beta$ -decay lead these exotic nuclei to the stability valley.

### 1.5.2 p-process

---

The p-process is historically acknowledged as the process responsible for the formation of about 35 stable nuclei that lie on the proton-rich side of the valley of stability, from  $^{74}\text{Se}$  to  $^{194}\text{Hg}$ . The abundances of these p-nuclei are typically  $10^{2-3}$  times lower than those produced by the s- and r-processes as it is well illustrated in Fig.3. It is generally accepted that the latter processes create the progenitors for most of the p-nuclei. This finding was initially reinforced by the striking similarity observed between the abundance curves associated with the different processes (black and blue curve in Fig.3).



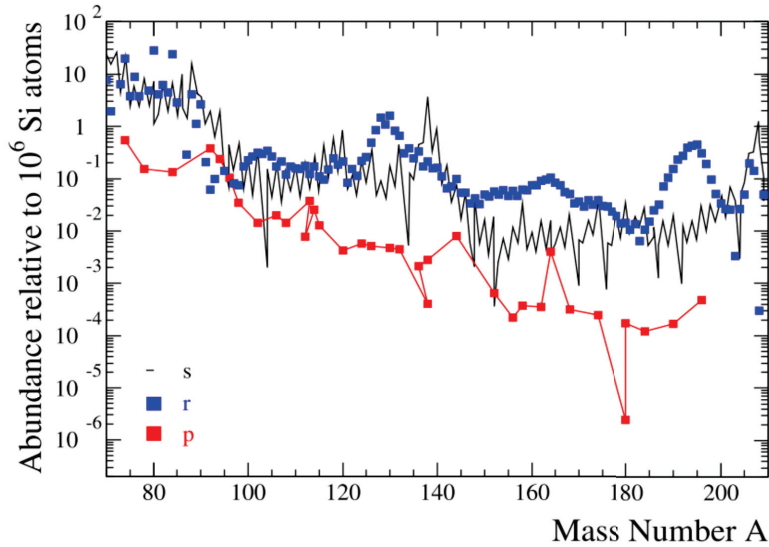


Figure 3: Contribution of s-nuclei, r-nuclei, and p-nuclei to solar system abundances relative to  $10^6$  Si atoms. These isotopic contributions are extracted from [3].

The term "p-process" was first introduced by Burbidge *et al.*[5] in 1957, highlighting the significant role supposedly played by protons in the formation of these nuclei. Since then, the term has been widely used to represent the broad category of mechanisms responsible for the production of all heavy neutron-deficient stable isotopes. Prior to that, they were referred to as "excluded even-even isobars" [2, 6] due to their inability to be formed through neutron capture and their characteristic of predominantly consisting of even-even nuclei, with a few exceptions. Fig.4 effectively illustrates how the stability valley acts as a shield against feeding by  $\beta$ -decay of nuclei formed by neutron capture, during either s- or r-process. The p-nuclei, represented by red squares, are displaced from the main stability line by typically two units of A. Consequently, these two neutron capture processes cannot account for the creation of p-nuclei.

In 1957, Cameron *et al.*[6] and Burbidge *et al.*[5] proposed that the formation of these nuclei occurs by  $(p,\gamma)$  or  $(\gamma,n)$  reactions. The proposed sites were the hydrogen-rich layers of type II supernovae [18], drawing inspiration from a previous study [19], or the outermost parts of the envelope of a Type I supernova where the r-process has taken place. It has been soon recognize that proton captures cannot explain the formation of p-nuclei, since the high temperature required to overcome the Coulomb barrier would lead to the destruction of the produced nuclei by photodisintegration.

Nowadays, the main mechanism for the formation of p-nuclei is referred as the  $\gamma$ -process, as proposed by Woosley *et al.*[18] in 1978, to better fit the formation of p-nuclei through a sequence of neutron, proton and  $\alpha$ -particle photodisintegration reactions [20, 15, 21, 22]. Indeed, it was observed early that the abundances of most p-nuclei exhibit an inverse correlation with their photodisintegration rates [18, 21, 5, 6]. These  $\gamma$ -induced reactions, with the particle capture rates, determine in-fine the balance of production and destruction channels for each nucleus. Hence, substantial attention has been dedicated to both theoretical predictions and experimental measurements of cross-sections for reactions that play a crucial role in determining the course of these astrophysical processes.

However, after 65 years of debate, the astrophysical circumstances under which these nuclei have been assembled is still under controversy. No definitive evidence has been presented to favor any specific astrophysical sites over others. In particular, type II and type Ia supernovae are two competing candidates as main sites for the  $\gamma$ -process. The shock front of type II supernovae traversing the O-Ne burning zone of massive stars remains however, one of the most extensively investigated locations [22, 21].

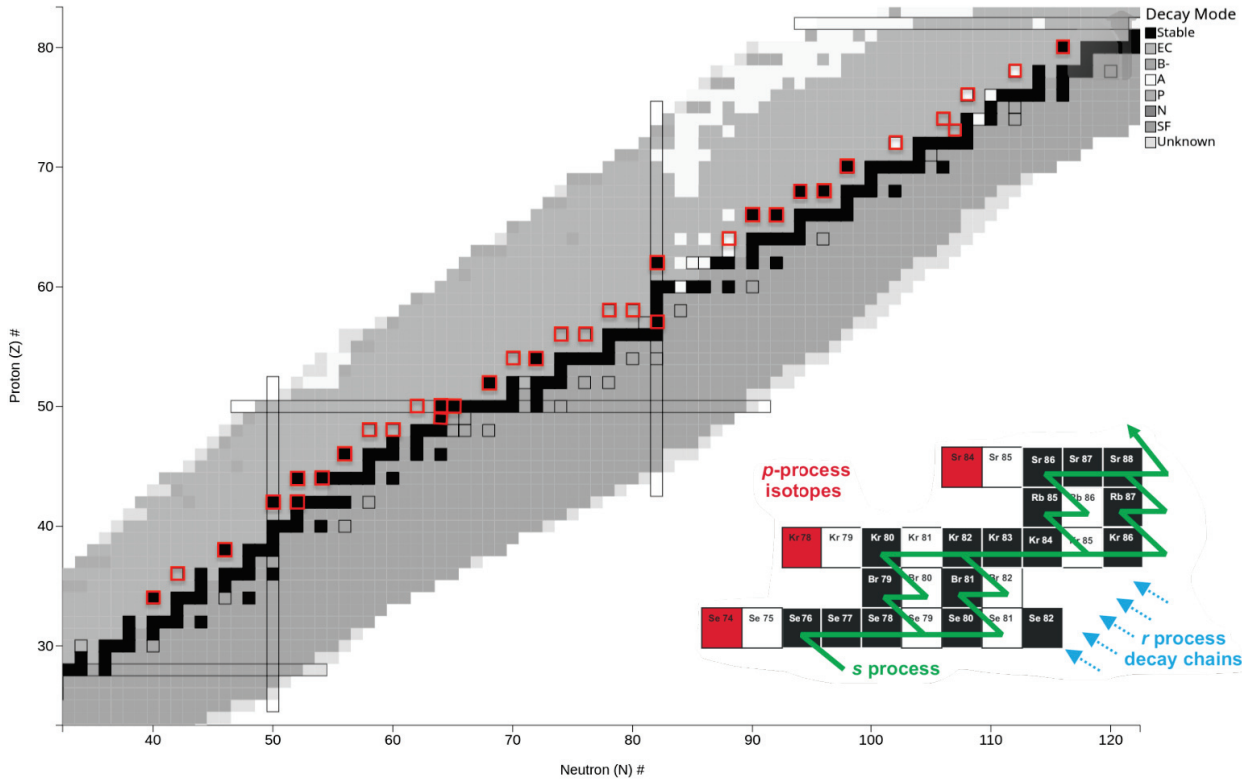


Figure 4: Zoomed-in chart of nuclides highlighting the region of p-nuclei where the red squares represent the stable neutron deficient isotopes. The flow of s- and r-process reactions demonstrates the impossibility of synthesizing p-nuclei solely through a series of neutron captures and  $\beta$ -decays. The chart is taken from [4] and the schematic process path from [21].

In this scenario, p-nuclei are believed to be produced within a temperature range of 1.5 to 3.5 GK and density range of 1 to  $8 \times 10^5 \text{ g.cm}^{-3}$ . Currently, nuclear reaction codes enable the estimation of p-nuclei abundances under these specific conditions by considering over 20,000 reactions that connect approximately 1800 nuclei ranging from hydrogen to bismuth [23].

Studies of sensitivity, such as those conducted by Rapp *et al.* [23] or predecessors [24, 25], demonstrate that we are able to explain the production of p-nuclei with an accuracy typically within a factor of 2. While this scenario effectively accounts for the majority of p-nuclei, there is a noted deficiency in its ability to produce the lightest ones. These limitations have been extensively discussed in papers, raising questions about various astrophysical and nuclear inputs. Significant improvements have been made since and alternative scenarios have emerged to address this discrepancy. We will outline in the next sections two of the most promising alternative processes responsible for the formation of these light p-nuclei, namely the  $\nu$ p-process and the rp-process.

### 1.5.2.1 $\nu$ p-process

The  $\nu$ p-process for “neutrino-proton process”, is known to occur during the ejection of the innermost layers of type II supernovae (and potentially in gamma-ray bursts). Throughout this process, the rapidly expanding proton-rich ejecta undergoes a series of proton captures, leading to the creation of elements up to a mass number of  $A = 64$  [26]. During this short time scale, the neutrino winds originating from the surface of the newly formed neutron star actively participate in the creation of heavier nuclei by being captured by protons, thereby transforming into neutrons. The creation of these new elements then allows to bypass waiting point nuclei which inhibit proton capture reactions, enabling the production of nuclei up to mass  $A = 152$  [27, 28].

This process was proposed in 2006 by Fröhlich *et al.*[26] as a potential explanation for the solar abundances of lighter p-isotopes such as  $^{92,94}\text{Mo}$  and  $^{96,98}\text{Ru}$ , which were challenging to account in other nucleosynthesis processes. By considering the impact of strong neutrino fluxes as well as their interactions with the surrounding matter, this  $\nu$ p-process offers a mechanism for the abundant formation of these nuclei in type II supernovae events. Nevertheless, further research and observational evidence are required to confirm and fully understand its role in the explosive nucleosynthesis.

### 1.5.2.2 rp-process

The rp-process, abbreviated for "rapid proton process", enables the creation of proton-rich nuclei through rapid proton captures and  $\beta$ -decays along the proton drip line [21]. This nucleosynthesis is believed to occur during X-ray bursts in explosive H- and He-burning. Such events occur in binary systems where a very compact stellar object accretes matter from its companion. The buildup of material would lead to instabilities at the surface of the compact object [29]. The sources of emission are still under debate, even if both a mass-accreting neutron star and the accretion disk of a low-mass black hole are considered to be strong candidates [21, 30]. The rp-process enables the production of p-nuclei with mass numbers ranging from  $A = 80-100$  [30]. However, its contribution to the observed abundance of p-nuclei is supposed to be low, due to the difficulty of ejecting material from the compact object.

## 2 ASTROPHYSICAL CONCEPTS

---

### 2.1 Nuclear Reaction Cross Sections

---

The cross section is a crucial parameter that quantifies the probability of a physical interaction between entities such as particles or nuclei. To define this important concept, consider a beam, consisting of  $N_b$  particles sent towards a target during a time  $t$ , resulting in a total of  $N_r$  interactions occurring. In the case of thin target, the probability of interaction can be determined by the reaction cross section, which is defined as follows :

$$\sigma = \frac{[N_r/t]}{[N_b/t][N_t/A]} \quad (1)$$

with  $N_t/A$  representing the areal density of the target. This can be better visualized by referring to the diagram shown in Fig.5, which helps to clarify the various parameters involved in this calculation.

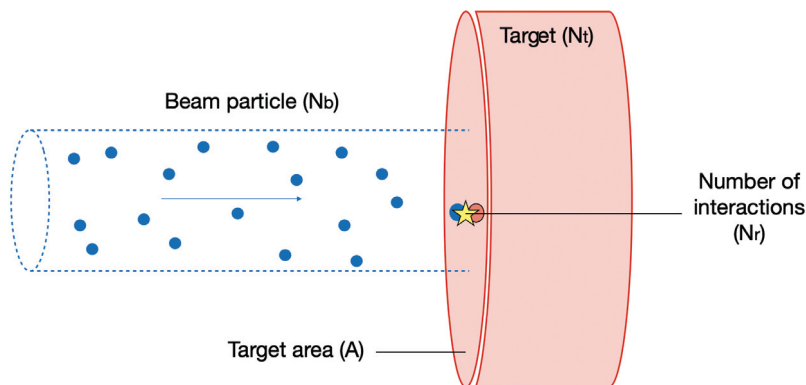


Figure 5: Illustration of the probability of interaction between beam particles and a target. The cross section reaction, from a classical point of view, represents the likelihood that a blue particle will encounter a red nucleus.

The barn, denoted by the symbol  $b$ , is a commonly used unit of measurement for nuclear reaction cross sections. It is defined as  $1b = 10^{-24} \text{ cm}^2$ . It is worth noting that we can similarly define differential cross sections, where the angle and/or energy of the ejectile is taken into account.

In a classical approach, and for a contact interaction, the cross section between a point-like projectile and a nucleus corresponds to the geometrical section of the nucleus ( $\pi R^2$  for a nucleus of radius  $R$ ).

If we now consider the quantum mechanical effects that arise at the small nuclear scale, this geometrical cross section will exhibit an energy dependence, which can be expressed as follows:

$$\sigma \propto \pi \lambda^2 = \pi \frac{\hbar^2}{2\mu E} \quad (2)$$

where  $\hbar$  is the reduced Planck constant,  $\mu$  the reduced mass,  $E$  the center of mass energy of the projectile and target system and  $\lambda$  the reduced De Broglie wavelength which reflects the wave-like nature of quantum mechanical processes. In addition to this expected energy dependence of the cross section, which follows a  $1/E$  relationship, there are several other contributory factors that can inhibit nuclear reactions. The Coulomb barrier, closely tied to the electric charge, and the centrifugal barrier, which is influenced by the angular momentum, are two such factors. Furthermore, the cross section must be defined within a specific set of conditions, starting with the nature of the force under consideration such as strong, weak, and electromagnetic forces. Consequently, the effective cross sections suitable for the cases studied in this thesis do not have analytic expressions. They have to be described by sophisticated models which have to be constrained by experimental measurements, as it will be expounded upon in the relevant sections [9][12].

## 2.2 Reciprocity Theorem

---

The reciprocity theorem states that the cross section of a reaction is fundamentally related to that of the reverse reaction since processes under consideration are invariant under time-reversal. If we approach this from the standpoint of a generic binary reaction, consider a forward reaction  $a + b \rightarrow c + d$ , where  $a$  and  $b$  represent the initial particles, and  $c$  and  $d$  represent the final particles, as depicted in Fig.6, each particle being in a specific single state.

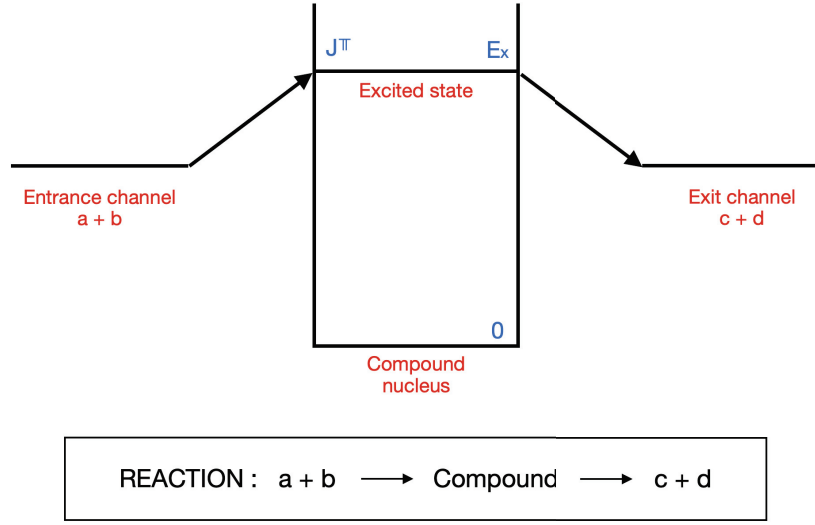


Figure 6: Diagram illustrating a nuclear reaction where particles  $a$  and  $b$  in the entrance channel result in the emission of particles  $c$  and  $d$  in the exit channel through an excited state in a compound nucleus. This state is characterized by its energy level, angular momentum, and parity. Drawing inspired from [12].

At a specific total energy, the cross sections for the reactions  $ab \rightarrow cd$  and  $cd \rightarrow ab$  are not equal. However, they are related by statistical spin factors and by the reduced De Broglie wavelength  $\lambda$  associated with the entrance channel of each reaction. As stated before, the geometric factor of the cross section is proportional to  $\lambda^2$ , hence :

$$\sigma_{ab \rightarrow cd} \propto \lambda_{ab}^2 \quad \text{and} \quad \sigma_{cd \rightarrow ab} \propto \lambda_{cd}^2 \quad (3)$$

Given that the wave number  $k$  and the De Broglie wavelength are related by the equation  $\lambda = 1/k$ , the ratio of the cross sections can be rewritten as follows:

$$\sigma_{ab \rightarrow cd} \propto \frac{1}{k_{ab}^2} \quad \text{and} \quad \sigma_{cd \rightarrow ab} \propto \frac{1}{k_{cd}^2} \quad (4)$$

Furthermore, the cross sections are proportional to the degeneracy of the exit channel considering that the reactions involve particles with spin. Each particle degeneracy factor is represented by  $(2j_i+1)$ , indicating the number of available states for a particle with spin  $j_i$ . In case of identical particles in the final state, the degeneracy of the exit channel has to be corrected for double counting changing the dependence of the cross section on the statistical factor as follows :

$$\sigma_{ab \rightarrow cd} \propto (2j_c + 1)(2j_d + 1)/(1 + \delta_{cd}) \quad \text{and} \quad \sigma_{cd \rightarrow ab} \propto (2j_a + 1)(2j_b + 1)/(1 + \delta_{ab}) \quad (5)$$

Taking both geometrical and statistical factors into account, we get :

$$\frac{\sigma_{ab \rightarrow cd}}{\sigma_{cd \rightarrow ab}} = \frac{k_{cd}^2 (2j_c + 1)(2j_d + 1)(1 + \delta_{ab})}{k_{ab}^2 (2j_a + 1)(2j_b + 1)(1 + \delta_{cd})} \quad (6)$$

This expression is commonly referred to as the reciprocity theorem, and it applies to both differential and total cross sections. Based on the above equations, it follows that if one of the cross sections is known either experimentally or theoretically, the other cross section can be deduced, using the existing symmetry between the direct and reverse reaction.

It is important to note that the symbols  $a$ ,  $b$ ,  $c$ , and  $d$  do not merely refer to specific nuclei, but more precisely to specific nuclear states. This highlights how the reciprocity theorem connects the same nuclear levels in both the forward and reverse reactions.

This principle holds significant implications in nuclear astrophysics, especially when investigating nuclear reactions in stellar environments. It enables scientists to estimate reaction rates for processes relevant to astrophysics by measuring experimentally accessible reactions in the laboratory and applying the principle of time reversal [9][12]. We will use this principle to justify the measure of reverse reaction of interest in the part.II of this thesis.

### 2.3 S-factor

---

In highly dense matter, nuclear reactions can occur at temperatures well below the Coulomb barrier, leading to extremely low reaction cross sections. Due to these specific conditions, laboratory measurements of the cross sections of interest are often made at energies larger than the astrophysical ones. Estimating stellar reaction rates solely through cross section extrapolation at low energies is therefore challenging. This difficulty arises primarily from the Coulomb barrier transmission coefficient in the cross section expression which implies a very strong energy dependence. On Earth, the cross section data available from laboratory experiments are primarily focused on the MeV energy range, with only



a few reactions reported in the keV range. While these energy ranges might be suitable for studying reactions in the early Universe, they are often largely beyond the energy range relevant to stellar nucleosynthesis [31]. In order to mitigate the challenges posed by the energy dependence of cross sections, a smoother quantity known as the astrophysical S-factor was introduced. This last serves, as well as the cross section, as a measure of the probability for two atomic nuclei to interact and undergo a nuclear reaction at energies relevant to astrophysical conditions, and also to isolate the factor that is sensitive to the nuclear interaction. It is expressed as follows [9]:

$$S(E) = \sigma(E)Ee^{2\pi\eta} \quad (7)$$

with  $\sigma(E)$  being the cross section,  $E$  the energy of the reaction and  $e^{-2\pi\eta}$  the Gamow factor which is an approximation of the transition probability at energies far below the Coulomb barrier. The Sommerfield factor  $\eta$  is expressed as follow :

$$\eta = \frac{Z_1 Z_2 e^2}{4\pi\epsilon_0 \hbar \nu} \quad (8)$$

where  $\nu$  corresponds to the relative speed between the reactants which can be expressed in the center of mass frame :

$$\nu = \sqrt{\frac{2E}{\mu}} \quad (9)$$

with  $\mu$  the reduced mass of the reactant nuclei.

The astrophysical S-factor definition eliminates the geometric  $1/E$  dependence of nuclear cross sections and Coulomb barrier transmission probability. This approach enables a more convenient extrapolation of the astrophysical S-factor to lower energies, thereby facilitating more accurate predictions of effective cross sections in cases where experimental measurements are impractical or burdened with significant uncertainties.

## 2.4 Stellar Reaction Rates

---

After taking into account the probability of nuclear reactions occurring, the concept of stellar reaction rates is introduced. These rates represent the frequency at which specific nuclear reactions occur between particles within a unit volume of stellar matter. For a fixed relative velocity  $\nu$ , the rate of a reaction between particles  $a$  and  $b$  can be expressed as :

$$r = \frac{N_a N_b \nu \sigma(\nu)}{1 + \delta_{ab}} \quad (10)$$

where  $N_a$  and  $N_b$  represent the number density of incident particles of type  $a$  and  $b$  per unit volume in a stellar gas. A Kronecker symbol is introduced in this expression for the reaction rate in order to avoid double-counting of the same pairs of particles. The nuclear cross section  $\sigma(\nu)$  is expressed depending on the relative velocity between the projectile and the target nucleus. However, in a stellar plasma at thermodynamic equilibrium, the relative velocity between particles of types  $a$  and  $b$  is not constant, but is instead described by a distribution function  $P(\nu)$  that expresses the probability to have a relative velocity between  $\nu$  and  $\nu+d\nu$ . Therefore, to obtain an accurate value for the reaction rate in this context, it is necessary to integrate the product  $\nu\sigma(\nu)$  with respect to this velocity distribution :

$$\langle \nu\sigma \rangle = \int_0^\infty P(\nu) \nu \sigma(\nu) d\nu \quad (11)$$

$$r = N_a N_b \frac{1}{1 + \delta_{ab}} \langle \nu\sigma \rangle \quad (12)$$

where  $\langle \nu\sigma \rangle$  is the average reaction rate per particle pair.

If we assume a normal stellar matter that is non-degenerate and non-relativistic, the relative velocity distribution function can be described by the following Maxwell-Boltzmann distribution :

$$P(\nu) = 4\pi\nu^2 \left( \frac{\mu}{2\pi kT} \right)^{\frac{3}{2}} \exp\left( -\frac{\mu\nu^2}{2kT} \right) \quad (13)$$

here  $T$  refers to the temperature of the gas,  $\mu$  to the reduced mass of the system, and  $\frac{1}{2}m\nu^2$  corresponds to the relative kinetic energy of the interacting nuclei in

their center of mass frame. By combining the Maxwell-Boltzmann distribution with equations (12) and (11), the total reaction rate can be expressed as follows [9][12]:

$$r = N_a N_b \frac{1}{1 + \delta_{ab}} \left( \frac{8}{\pi \mu} \right)^{\frac{1}{2}} \frac{1}{(kT)^{\frac{3}{2}}} \int_0^{\infty} \sigma(E) E \exp\left(-\frac{E}{kT}\right) dE \quad (14)$$

It should be noted that in order to obtain a reaction rate that accurately reflects the behavior of nuclear reactions in stellar environment, it is necessary to use the stellar cross sections, which involve entrance channels with nuclei in thermally excited states. The laboratory cross section  $\sigma^{lab}$ , obtained using a target in the ground state, cannot be directly used to calculate the stellar reaction rate. Instead, it must be adjusted by applying a stellar enhancement factor, denoted as  $f^*$ , which incorporates the thermal excitation of nuclei in the stellar environment [32] :

$$f^* = \frac{\sigma^*}{\sigma^{lab}} \quad (15)$$

with  $\sigma^*$  the cross section for a target in an excited state. It is crucial to account for any disparities between laboratory and stellar conditions to avoid substantial errors when calculating reaction rates. Such inaccuracies could indeed have a profound impact on our comprehension of astrophysical phenomena, including the synthesis of heavier elements within stellar environments.

## 2.5 Gamow Windows

---

The Gamow window associated with a specific nuclear reaction occurring in a stellar plasma at given temperature  $T$ , is the energy range where this reaction dominantly occurs within the corresponding stellar environment. Within this window, particle energies are below the Coulomb barrier, where classical mechanics would forbid the reaction. However, quantum mechanically, there is a finite probability for particles to tunnel through the barrier, known as the tunnelling probability, which is approximately given by the Gamow factor  $e^{-2\pi\eta}$ . On the other hand, the probability for the two particles to have the relative energy  $E$  is proportional to  $e^{-E/kT}$ . These two factors compete with each other, the tunnelling probability increases with energy, while the number of particles

decreases. Consequently, there exists a limited energy range where most reactions occur which is illustrated in Fig.7 in purple. The product of these two exponential terms results in the "Gamow peak" which determines the reaction rate [9][12].

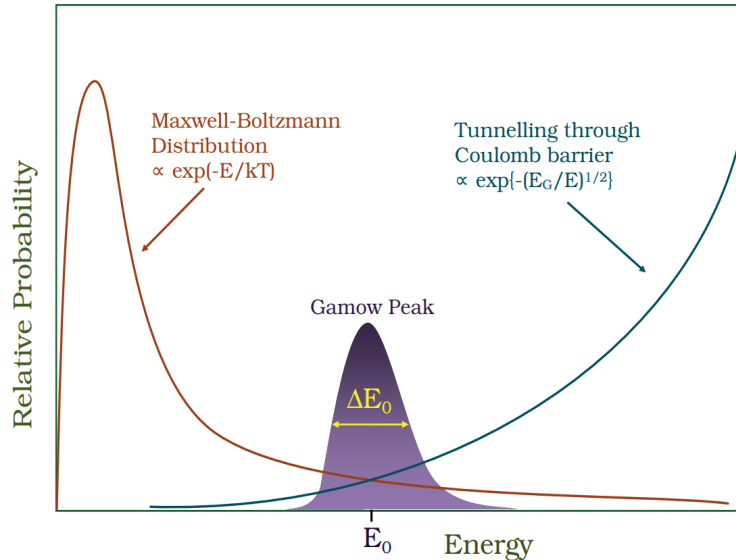


Figure 7: Gamow energy window, defining the astrophysical region of interest for nuclear reactions, as a function of the center-of-mass energy, where  $e^{-\sqrt{E_G/E}}$  corresponds to the Gamow factor  $e^{-2\pi\eta}$ . Extracted from [33].

## 2.6 Hauser Feshback formalism

---

The Hauser-Feshbach (HF) formalism, coined after the physicists Walter Hauser and Herman Feshbach, constitutes a theoretical framework employed for the estimation of cross sections pertaining to nuclear reactions involving excited states of nuclei. This formalism is grounded on the assumption that, throughout a nuclear reaction, an intermediary excited state referred to as a compound nucleus is engendered. This compound nucleus corresponds to a statistical equilibrium where the memory of the entrance channel is lost (except for the conservation of energy, spin and parity). It can subsequently undergo decay through various reaction channels, estimated statistically with decay probabilities specific to each channel, until it reaches a ground state or a long-lived isomer. These probabilities, also known as decay widths, depend on the properties of the interacting particles, such as their spins and energy levels, as well as the properties of the compound nucleus, such as its excitation energy and deformation [34][35]. An example of the process of creating a compound nucleus is illustrated in Fig.8,

where a binary reaction leads to the formation of a compound nucleus with an excitation energy  $E^*$ , characterized by its spin and parity  $J^\pi$ . It is assumed here that the compound nucleus is populated with sufficient excitation energy to be in the continuum part of its level scheme, where the levels are no more discrete but are described by a density distribution. The excitation energy of the compound nucleus is determined by the kinetic energy of the entrance channel and the reaction's Q-value.

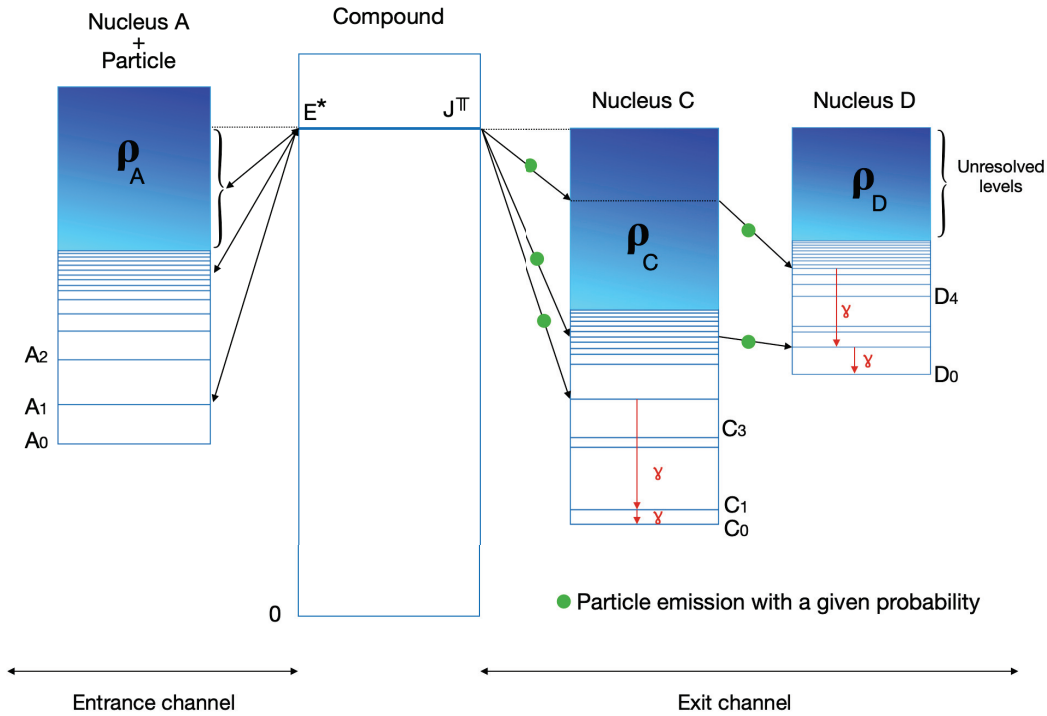


Figure 8: Energy scheme of a binary reaction leading to the creation of a compound nucleus in an excited state. The decay channels are characterized by several transitions of the compound nucleus from its excited state to lower energy states, possibly leading to the formation of another nucleus accompanied by the emission of particle (in green), and photons through energy level transitions.

The HF theory provides a reliable approach for estimating reaction cross-sections in scenarios involving multiple open emission channels at incident energies reaching several MeV, especially in medium mass and heavy nuclei where the level density is high. However, to achieve this, certain inputs for simulating the decay process must be well understood, such as the particle-nucleus optical potential, the level density within a nucleus, and the  $\gamma$ -ray strength involved in the relevant reactions.

### 2.6.1 Level density

---

In a nucleus, the energy levels correspond to quantized states associated with different configurations of nucleons (protons and neutrons). These energy levels are dictated by the nuclear potential, which is a result of the strong nuclear force responsible for binding the nucleons together. Similar to electron energy levels in an atom, the individual energy levels of nucleons in a nucleus follow a shell and sub-shell structure. In the nuclear shell model, nucleons occupy energy levels according to the Pauli exclusion principle. Each energy level can accommodate a specific number of nucleons with distinct quantum numbers, including spin and orbital angular momentum. The precise energy levels in a nucleus result from various coupling and occupation of these individual levels and must be determined experimentally. When experimental data are not available or incomplete, theoretical models of nuclear level densities are employed to predict reaction cross-sections. It is worth noting that the level density, denoted as  $\rho$ , represents the number of nuclear levels per MeV in the vicinity of an excitation energy  $E$ , for a specific spin  $J$  and parity  $\pi$ . These theoretical level density models are constructed based on various assumptions and considerations, such as the statistical properties of nuclear excitations and the underlying nuclear structure [34].

### 2.6.2 Optical potential

---

The name "optical model" is derived from the analogy between a light wave encountering an object and a nuclear projectile interacting with a target nucleus. The challenge of the optical model lies in determining, for a given target and projectile energy, the complex potential that accurately describes the scattering between these two objects [36].

The interaction between a projectile and the nucleons within the target nucleus can in principle be described microscopically by considering the target nucleus structure and the effective interaction between the projectile and the target nucleons. This effective interaction has to account for medium effects, such as Pauli blocking, and differs from the bare nucleon-nucleon interaction. The microscopic approach aims to provide a comprehensive and fundamental understanding of nuclear reactions based on the underlying nuclear forces, but is very complex to implement and does not lead yet to accurate cross section predictions.

When a sufficient amount of experimental data (such as differential elastic scat-

tering cross sections, total cross sections, reaction cross sections, etc...) is available, the preference is given to parameterize a phenomenological optical potential. The latter represents the nuclear interactions by a single nuclear potential well having a real part (responsible for elastic scattering) and an imaginary part (responsible for absorption through inelastic scattering and reactions). This type of potential is typically constructed using potential wells with shapes described by Woods-Saxon functions (or derivatives of these functions), and the depth, radius, and diffuseness parameters are adjusted based on experimental data [34]. Some modern descriptions use a double folding approach to determine the real part from microscopic density distributions.

### **2.6.3 $\gamma$ -strength**

---

The  $\gamma$ -strength, also known as the  $\gamma$ -strength function or photon strength function (PSF), quantifies the probability of gamma-ray emission from excited atomic nuclei. It represents the intensity or strength of the electromagnetic transition between nuclear energy levels and influences the competition between photon emission and other particle emissions within the Hauser-Feshbach model. The gamma strength function offers insights into the nuclear structure and electromagnetic properties of atomic nuclei. It provides a description of the probability of emitting a gamma ray per unit energy, dependent on the energy of the gamma ray itself. This function is often represented as a continuous distribution, reflecting the varying probabilities for different energy transitions. Experimental measurements, such as Giant Dipole Resonance or photo-absorption cross sections, and theoretical models are employed to determine this function for specific nuclei and energy ranges [34].

## 3 EXPERIMENTAL TOOLS

---

### 3.1 The Interaction of Radiation with Matter

---

The interaction of radiation with matter involves fundamental processes that determine how radiation interacts with the material it encounters. Energetic photons called gamma rays interact predominantly through photoelectric absorption, Compton scattering, and pair production. Charged particles, such as electrons, protons, or alphas, undergo frequent Coulomb interactions, including elastic and inelastic scattering, as well as nuclear reactions. The knowledge of these processes enables the development of advanced materials, devices, and techniques for harnessing or mitigating the effects of radiation in various applications : in the present case, for particle detection. We will elaborate here on the essential key processes to address this thesis effectively.

#### 3.1.1 Gamma rays interaction

---

While numerous interaction mechanisms have been identified for gamma rays interacting with matter, three primary types significantly impact radiation measurement as said before. All these processes lead to the partial or complete transfer of the photon energy to the absorbing material. The relative importance of the three processes for different absorber materials and gamma ray energies is conveniently illustrated in Fig.9 as a function of the atomic number.

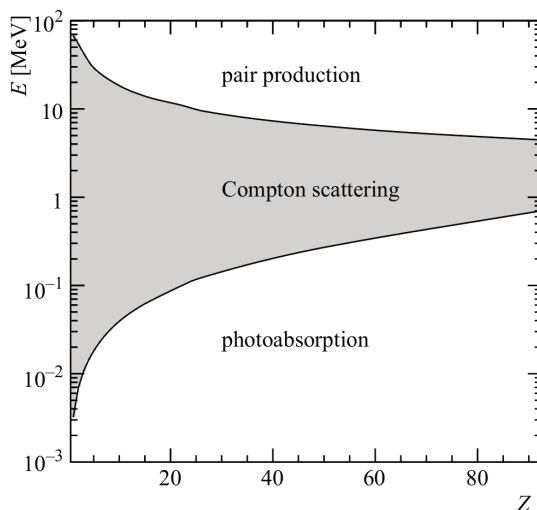


Figure 9: Most probable interaction mechanisms between radiation and matter at energies beyond the ultra-violet range. Extracted from [37].



The plot depicts two curves representing the critical photon energy thresholds for different interaction mechanisms with the target material. The lower curve represents the energy below which photoelectric absorption is the dominant process, while the upper curve represents the energy above which pair production becomes the most important. The shaded region between the two curves signifies the energy range where Compton scattering is the prevailing interaction mechanism [37].

### 3.1.1.1 Photoelectric absorption

The photoelectric absorption phenomenon occurs when a photon interacts with an atom, resulting in the complete annihilation of the incident photon. In its place, a photo-electron is ejected from one of the atom's bound electron shells as can be seen on the left of Fig.10. In the case of high-energy gamma rays, the most probable origin of the photoelectron is the tightly bound K shell of the atom.

For the photoelectric effect to occur, the energy of the incident photon must surpass the binding energy that confines the electron within the material. Consequently, there exists a critical frequency below which the photoelectric effect cannot occur. The difference between the photon's energy and the electron's binding energy corresponds to the kinetic energy carried by the outgoing photoelectron.

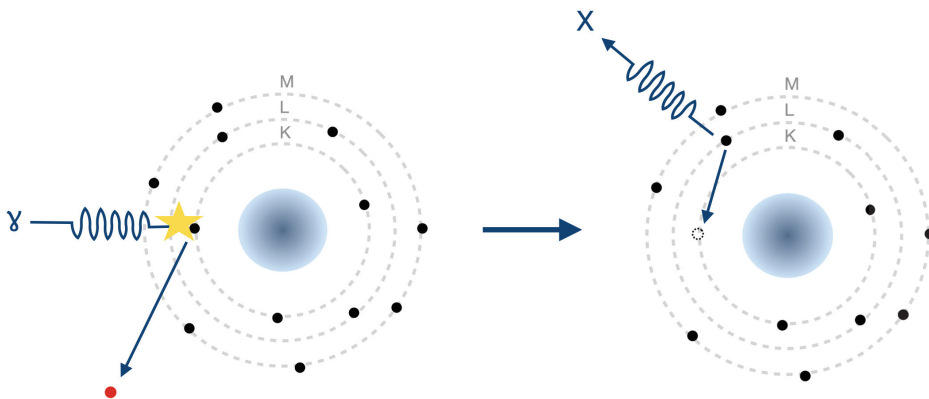


Figure 10: Diagram illustrating the process of the photoelectric absorption (left). The following rearrangement of the atom gives rise to X-ray emissions (right).

Furthermore, as a consequence of the interaction, the absorber atom undergoes ionization, resulting in the creation of a vacancy within one of its bound electron shells. This vacancy is promptly filled by either capturing a free electron

from the surrounding medium or rearranging electrons from other atomic shells. Consequently, the interaction can give rise to the emission of characteristic cascades of X-ray (see right of Fig.10), which may undergo re-absorption near the point of origin through photoelectric absorption involving electron shells of lower binding energies. The potential migration and escape of these X-rays from radiation detectors can impact the response of the detectors.

In certain instances, the excess energy from the atomic excitation can be released through the emission of an Auger electron, which takes the place of the characteristic X-ray emission as a carrier of the excitation energy [38][37].

### 3.1.1.2 Compton scattering

Compton scattering is a fundamental interaction between a gamma-ray and an electron within the absorbing material. It is the prevailing process for gamma-ray energies commonly emitted by radioisotope sources. During Compton scattering, the incident gamma-ray photon transfers a part of its energy to the electron and undergoes a change in direction, causing the electron to recoil, as shown in Fig.11. The extent of energy transfer varies depending on the scattering angle, ranging from negligible for small angles to a substantial fraction of the initial gamma-ray energy for larger angles. Even at the maximum scattering angle of 180 degrees, known as the Compton edge in the energy spectrum, the photon retains a portion of its original energy.

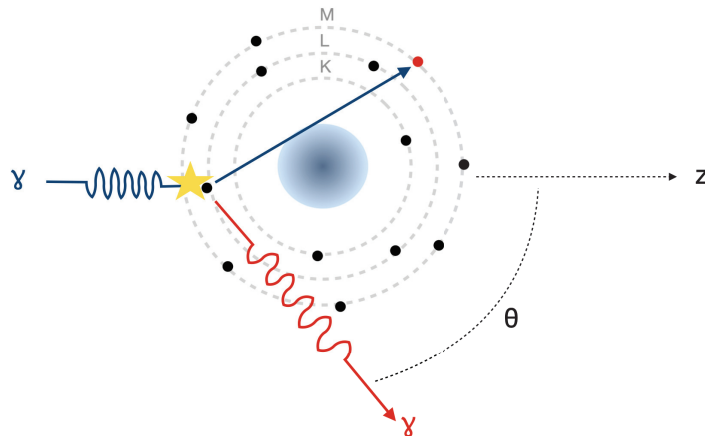


Figure 11: Diagram illustrating the process of Compton scattering in the particular case where the electron is accepted by an inner electron shell of the electronic configuration.

The probability of Compton scattering occurring per atom in the absorbing

material is directly proportional to the number of available electrons, which increases with the atomic number  $Z$  [38][37].

The expression that relates the energy transfer and the scattering angle for any given interaction can be derived by simultaneously considering the conservation of energy and momentum. The energy associated with a single photon is given by  $E = h\nu$ , where  $h$  is Planck's constant and  $\nu$  the frequency of the radiation. Thus, if an incident photon has an energy  $E_0$ , the energy of this photon after scattering on an electron with mass  $m_e$  will be given by the following expression [38]:

$$E = \frac{E_0}{1 + \frac{E_0}{m_e c^2} (1 - \cos\theta)} \quad (16)$$

with  $\theta$  the scattering angle of the reaction.

### 3.1.1.3 Pair production

Pair production becomes energetically possible when the gamma-ray photon energy  $E_\gamma$  surpasses twice the rest-mass energy of an electron, which corresponds to the photon energy threshold of 1.022 MeV. While the probability of pair production remains low for gamma-ray energies slightly above this threshold, it becomes the dominant interaction mechanism as the energy escalates into the multi-MeV range. This interaction occurs within the Coulomb field of a nucleus (whose recoil ensures momentum conservation), leading to the annihilation of the photon and the emergence of an electron-positron pair. The surplus energy carried by the photon, beyond the minimum threshold of 1.022 MeV required for pair creation, manifests as kinetic energy shared between the positron and the electron. Subsequently, as the positron decelerates within the absorbing medium, it typically undergoes annihilation with an electron, resulting in the emission in opposite directions of two annihilation photons as secondary products emitted as illustrated in Fig.12. In detector spectra, pair creation induces escape peaks at  $E_\gamma = 511$  keV and  $E_\gamma = 1022$  keV depending on the detection of these annihilation photons.

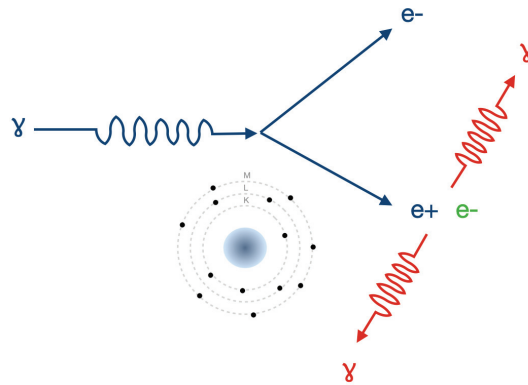


Figure 12: Diagram illustrating the process of pair production.

Although no straightforward expression exists for the probability of pair production per nucleus, it is considered approximately proportional to the square of the atomic number of the absorber material [38][37].

### 3.1.2 Charged particles interaction

---

#### 3.1.2.1 Elastic scattering

Elastic scattering concerns all kinds of particles (including photons, neutrons...) but in our case it will be studied for alpha particles incident on nuclei. This scattering describes the interaction between a particle and a nucleus where no alteration to internal structure occur. The total kinetic energy in the center of mass of the observed system before and after the collision are thus conserved. The elastic scattering predominantly occurs with low-energy particles and is characterized by the absence of particle excitation or ionization.

Ernest Rutherford's groundbreaking work on elastic scattering played a pivotal role in advancing our knowledge of atomic structure and the fundamental nature of matter. One of his most significant contributions was the famous gold foil experiment, in which he observed the elastic scattering of alpha particles as they passed through a thin sheet of gold foil. This experiment provided crucial insights into the inner workings of the atom.

His discovery brought to light the well-known formula for the differential cross-section of elastic scattering, known as the Rutherford formula, which is based on the purely Coulomb interaction between a particle and a nucleus both approximated as point-like charges [39] :

$$\frac{d\sigma}{d\Omega} = \left( \frac{Z_1 Z_2 e^2}{8\pi\epsilon_0 E_0} \right)^2 \frac{\left( \cos\theta + \sqrt{1 - \left(\frac{m_1}{M_2} \sin\theta\right)^2} \right)}{\left( \sin^4\theta + \sqrt{1 - \left(\frac{m_1}{M_2} \sin\theta\right)^2} \right)} \quad (17)$$

where  $Z_1, m_1$  and  $Z_2, m_2$  are the charge and the mass of the incident particle and the nucleus respectively. In the equation,  $E_0$  denotes the energy of the incident particle,  $\epsilon_0$  represents the dielectric constant,  $e$  is the electron charge and  $\theta$  is the scattering direction in the laboratory frame.

This formula found extensive utility in various applications, notably in the field of Rutherford Backscattering Spectrometry. We will delve into the details of this technique in the upcoming section.

### 3.1.2.2 Inelastic scattering

Inelastic scattering involves the exchange of energy between the projectile and the nucleus, causing modifications in its internal state. This type of scattering occurs when the incident particle interacts with the target particle or medium leads to processes of excitation or de-excitation. As a result, photons may be emitted or absorbed, secondary particles can be generated, and the nucleus may undergo rearrangement. The energy transferred in the process of inelastic scattering provides valuable insights into the properties of materials and particles. By studying the distribution of energy and angles of the scattered particles or emitted radiation, researchers can extract valuable information about the composition, structure, and dynamics of the target material.

Besides, inelastic scattering on electrons is the dominant energy loss mechanism when a charged particle traverses an absorbing medium. During this process, the charged particle undergoes simultaneous interactions with multiple electrons present in the medium, resulting in energy loss and potential excitation or ionization of the electrons. Depending on the proximity of these interactions, and on the available energy, the charged particle can either excite an electron to a higher energy level within the atom or completely remove the electron from it. Since some energy of the incident charged particle is transferred to the electron, this leads to a decrease in the particle velocity. The maximum energy that can be transferred from a charged particle of mass  $m$  with kinetic energy  $E$  to an electron of mass  $m_0$  in a single collision is approximately  $4Em_0/m$  [38]. The total energy transfer is determined by the differential distance traveled by the

charged particle through the medium. This energy loss can be quantified using the linear stopping power, also referred to as specific energy loss. The Bethe formula provides a mathematical expression to calculate this stopping power, taking into account the properties of the medium and the charged particle :

$$S = -\frac{dE}{dx} = \frac{4\pi e^4 Z_p^2 N}{m_0 \nu^2} B \quad (18)$$

with

$$B = Z_t \left[ \ln \frac{2m_0 \nu^2}{I} - \ln \left( 1 - \frac{\nu^2}{c^2} \right) - \frac{\nu^2}{c^2} \right] \quad (19)$$

where  $\nu$  and  $Z_p$  represent the velocity and charge of the primary particle,  $N$  and  $Z_t$  are the number density and atomic number of the absorber atoms,  $m_0$  the rest mass of the electron and  $e$  the elementary charge.  $I$  represents the average excitation and ionization potential of the absorber and is typically determined experimentally for each element.

The Bragg curve represents the stopping power as a function of the penetration depth into the material. The energy loss through materials of targets and detectors is an important property to take into account in the conception and analysis of an experiment.

When considering a mono-energetic beam of particles, it is important to acknowledge that the energy loss experienced by these particles follows a stochastic process, stemming from the inherent randomness of microscopic interactions. As a result, the energy loss of the particles exhibits a normal distribution, where the width of the distribution is commonly referred to as the energy straggling. This distribution becomes broader as the particles penetrate deeper into the absorber material. Consequently, when traversing a thick material, it may become imperative to account for this additional loss of energy resolution with precision and accuracy.

### 3.1.2.3 Nuclear reactions

While Coulomb scattering is the primary reaction that occurs when a charged particle interacts with the atoms of the medium, in some cases a nuclear reaction occurs. During this type of reaction, the interaction between the charged particle and the nucleus leads to its transformation and the generation of different elements or isotopes. This process can involve nuclear fusion, nuclear

fission, or nucleon emissions. The specific reaction that will take place depends on various factors such as the energy and charge of the particle, the type of particle involved, and the characteristics of the nucleus. In the context of this thesis, particular attention is given to capture reactions, which will be further elaborated upon in the following discussions.

The capture of a charged particle by the nucleus results in a rearrangement of its nucleons, leading to the formation of a new composite nucleus. For the mass and energy region of interest here, this kind of reaction is well described by the statistical mechanism involving the formation of a compound nucleus, which is an excited intermediate state formed by the combination of the incident particle and target nucleus. This assumes that the incident particle and the target nucleus become indistinguishable at a given stage of the reaction. The decay mechanism by which the compound nucleus disintegrates is then determined by its excitation energy, spin, parity, and by the allowed states available in the outgoing channel, following the laws of probability. This decay can involve the emission of particles such as neutrons, protons, alpha particles, beta particles, or in the case of radiative capture, only gamma rays. When the residual nucleus is radioactive, it undergoes decay with its characteristic half-life, and the daughter nucleus may undergo de-excitation through the emission of gamma rays, which enables it to reach its ground state. These de-excitations play a crucial role in spectroscopy, especially when studying the half-lives of specific nuclei or the nuclei formed during capture experiments. By studying these decay processes and the emitted radiation, valuable information can be obtained about the properties of the nucleus, such as its structure, stability, and reaction cross sections [38][37].

## 3.2 Detection

---

### 3.2.1 HPGe

---

High Purity Coaxial Germanium (HPGe) detectors have been extensively used for precise spectroscopic analysis of gamma rays and X-rays. These detectors play a crucial role in identifying radionuclides and quantifying their concentrations in various samples and applications. The HPGe detector is constructed using a cylindrical-shaped crystal made of high-purity germanium with a coaxial electrode configuration. Techniques for the production of such material were first developed in the mid-1970s for use in the semiconductor industry. The last are a specific type of material that exhibit electrical conductivity between that of conductors and insulators. They can be modified and controlled to achieve desired conductivity through methods such as the application of an electric field or the introduction of impurities. Silicon is the most commonly used semiconductor material, although other materials like germanium are also frequently used.

The central component of a coaxial detector is a cylindrical germanium crystal, which possesses a larger volume compared to planar detectors. Germanium is chosen as the sensitive material due to its high density, high atomic number, and excellent energy resolution. These properties make it well-suited for precise detection and measurement of gamma rays and X-rays. The coaxial electrode configuration consists (at least for the detector used in this thesis) of a central p-type electrode surrounded by an n-type coaxial contact where the p-type electrode is in direct contact with the germanium crystal (see Fig.13). The coaxial electrode configuration ensures a rather uniform electric field distribution throughout the germanium crystal, enabling efficient charge collection in an almost fully depleted detector. When a gamma ray or X-ray interacts with the crystal, the deposit energy allows the creation of electron-hole pairs. The applied electric field then accelerates these charge carriers towards the electrodes where they generate electrical pulses proportional to the energy deposited. These pulses can be amplified, processed, and analyzed to accurately determine the energy spectrum and intensity of the detected radiation.



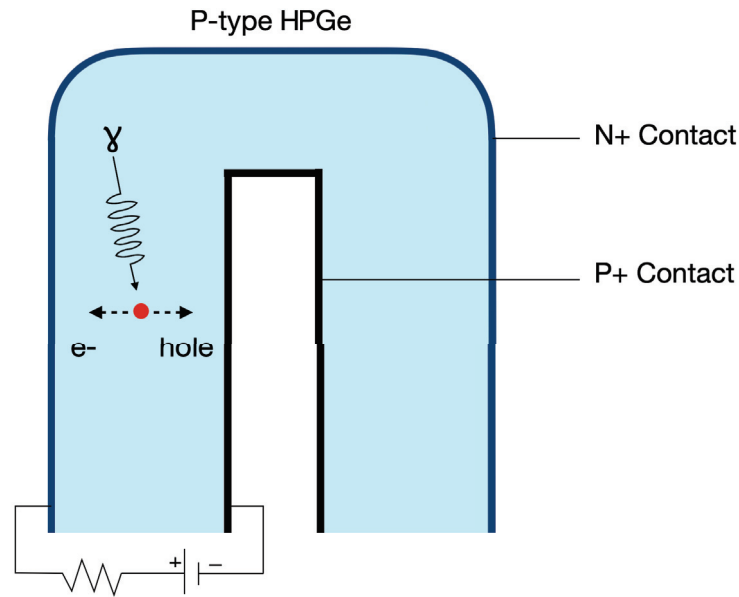


Figure 13: Transversal view of a coaxial germanium detector showing the operational dynamics of the electrodes in response to an interaction photon-crystal.

To optimize the performance of HPGe detectors, they are typically operated at cryogenic temperatures, usually around  $-200^{\circ}\text{C}$ . This is achieved by using a cooling system, such as liquid nitrogen or a cryocooler, which reduces thermal noise and improves the energy resolution of the detector. As a result, HPGe detectors offer excellent energy resolution, typically ranging from 1 keV to several hundred keV, enabling precise identification and quantification of radiation sources. Due to their convenience and high-performance capabilities, HPGe detectors find widespread use in various fields, such as nuclear physics, environmental monitoring, medical imaging, and nuclear safeguards. However, an important factor that affects the detector efficiency is the thickness of the dead layer. The last refers to a thin region near the outer surface of the detector that is not fully depleted, and it is typically doped with lithium atoms to create a semiconductor junction. The incident photons must pass through this region before entering the active volume of the crystal and being detected. Unfortunately, only the higher-energy photons, typically above 40 keV, are able to penetrate and be counted. The precise thickness of this region cannot be accurately determined through X-ray imaging, and the manufacturer's information may not reflect the actual thickness. This is due to the continuous diffusion of lithium atoms within the germanium crystal, leading to an increase in the thickness of the dead layer over time. Therefore, it is crucial to periodically determine the efficiency curve of the detector, ideally before each experiment,

to ensure accurate measurements [40][41][38].

### 3.2.2 PIPS

---

The Passivated Implanted Planar Silicon (PIPS) Detector is primarily composed of silicon, making it well-suited for the detection and measurement of light and ionizing radiation resulting from interactions with charged particles and photons. Silicon detectors, like germanium detectors, operate based on the principles of a p-n junction. However, there are some important differences that give them intrinsic characteristics. The lower atomic number of silicon ( $Z=14$ ) compared to germanium ( $Z=32$ ) results in a lower photoelectric cross section for typical gamma-ray energies, approximately 50 times lower. As a result, the gamma-ray full-energy peak efficiency of silicon detectors is very low, making them less suitable for general gamma-ray spectroscopy applications. On the other hand, silicon is more widely used due to its availability, lower cost, and more favorable electrical properties in certain applications. Additionally, they are generally not cooled as intensely as germanium detectors due to their intrinsic properties : higher electrical resistivity and lower thermal conductivity. This means that silicon detectors generate less thermal current and are less sensitive to thermal noise compared to germanium detectors. Therefore, they can provide adequate performance without requiring intense cryogenic cooling.



Figure 14: Picture of PIPS detectors sold by the MIRION company [41]. These compact devices present a small diameter, typically of the order of a few centimeters. The shiny layers visible on the top of detectors are the  $\text{SiO}_2$  passivated layers.

The PIPS detectors are products of modern semiconductor technology and the Fig.14 provides a visual representation of their appearance. They are known for their high sensitivity, fast response times, and good energy resolution. The key distinction between PIPS detectors and older silicon detectors, such as silicon surface barrier detectors and diffused junction detectors, lies in their structure and fabrication techniques. PIPS detectors have a planar structure with a passivated surface, which effectively reduces surface leakage currents and enhances the overall performance of the detector. The passivation process plays a crucial

role in PIPS detectors by applying a layer of insulating material, such as silicon dioxide, to the surface of the silicon. This helps to minimize unwanted electrical effects and improve the overall performance of the detector. Furthermore, PIPS detectors benefit from advanced technologies, such as precise implantation techniques and the use of high-purity silicon materials. These advancements result in improved energy resolution, reduced noise levels, and enhanced capabilities for detecting and measuring radiations. As a result, PIPS detectors are highly sensitive and reliable for a wide range of applications, including radiation detection, dosimetry, and particle physics experiments [41][38][37].

### **3.3 Target characterization techniques**

---

#### **3.3.1 ICP-MS**

---

The Inductively Coupled Plasma Mass Spectrometry (ICP-MS) is an elemental technique that allows the identification of the elements present in a sample at the atomic level. This method uses a high-temperature plasma generated by inductively coupled plasma (ICP) and measures the elemental composition of a sample using a mass spectrometer (MS). As a mass spectrometric technique, ICP-MS can separate and measure the individual isotopes of an element, making it suitable for applications where isotopic abundances or isotope ratios are of interest.

In the ICP-MS technique, the sample is prepared as a liquid by dissolving or acid digesting the studied piece of material. The liquid sample is then introduced into a high-temperature plasma of ionized argon, inside which the sample undergoes atomization and ionization processes. The schematic in Fig.15 provides a detailed representation that can help in the understanding of the various sample processing steps inside the plasma.

The extent of ionization for each element in the sample depends on its ionization potential (IP) and the temperature of the plasma. IP represents the energy required to remove an electron from a neutral atom, resulting in the formation of an ion. Argon is an ideal support gas for ICP-MS due to its unique ionization properties. It has a first IP that is higher than the first IP of most other elements but lower than their second IP. This characteristic allows for efficient ionization of most elements in the plasma, primarily producing singly charged positive ions, while minimizing the formation of doubly charged ions. In typical plasma conditions, a high percentage (at least 75%) of naturally occurring ele-

ments are ionized. This high level of ionization contributes to the exceptional sensitivity of ICP-MS and optimal plasma conditions are therefore crucial for achieving high sensitivity and low detection limits for measured elements.

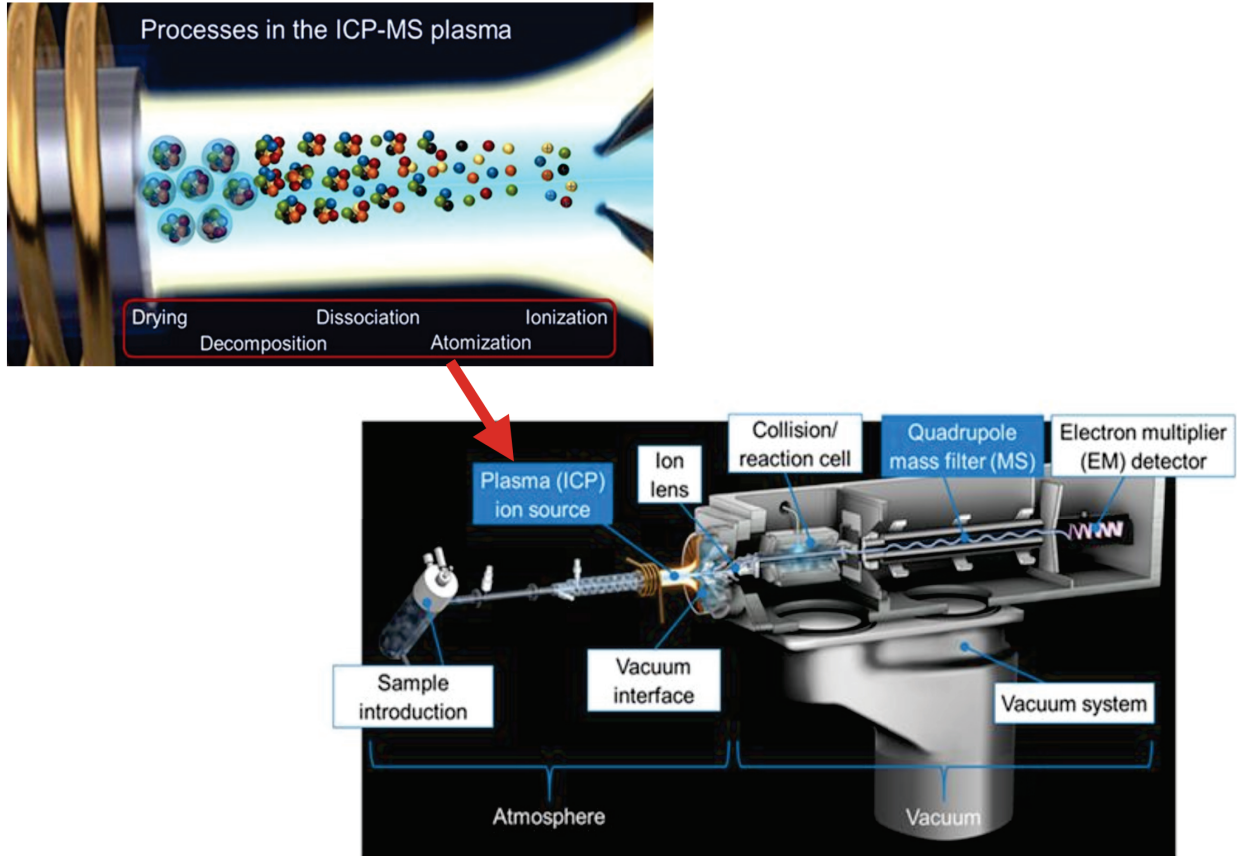


Figure 15: Layout of an ICP-MS system illustrating the different stages of element processing within the entire device, and specifically within the inductively coupled plasma. Extracted from [42].

The atoms and ions generated in the plasma are then extracted and introduced into the quadrupole mass spectrometer which filters the ions based on their mass-to-charge ratio ( $M/Z$ ) and measures their intensity. Since most ions produced by the ICP are singly charged, ICP-MS typically produces a mass spectrum. For each measured mass, the detector records the counts, which are then analyzed by the data analysis software. The concentration of each element is calculated in the unknown samples by comparing the measured counts to those obtained from known-concentration reference solutions. Multiple reference solutions named as "standards" [43] are usually measured to create a calibration plot of counts versus known concentration for each element.

While the ICP is done at atmospheric pressure, the mass spectrometer and

detector operate in a vacuum chamber, so an ICP-MS also requires a vacuum pump, a vacuum interface, and some electrostatic ion lenses to focus the ions through the system. The Fig.15 illustrates the different steps of the procedure, providing a visual representation of how the entire system operates.

The technique of ICP-MS can detect elements down to parts per million (ppm) levels, and in some cases, even to parts per billion (ppb) levels. This exceptional sensitivity, enabling the detection of trace elements at extremely low concentrations, makes it a valuable tool in various fields [42][44][45][46].

### 3.3.2 RBS

---

Rutherford backscattering spectrometry (RBS) is an experimental technique that consists in sending a mono-energetic beam of charged particles towards a target and detecting the particles that undergo backscattering upon atomic nuclei. The underlying principle of this phenomenon is based on elastic scattering and the energy loss experienced by the primary and back-scattered charged particles. As a result of the repulsive nature of the Coulomb force, the majority of particles traverse a material with minimal interaction. Nevertheless, in certain instances, a particle may approach a nucleus closely enough to experience a substantial repulsive force, leading to a significant scattering angle or even back-scattering. By quantifying the energy and angle of the backscattered particles, valuable insights into the composition and structure of the target material can be obtained.

This non-destructive technique enables the characterization of thin targets, ranging from nanometers to micrometers in thickness. It allows for the measurement of sample thickness and provides additional information about the atomic composition and distribution within the target. This technique can also be applied to thick samples (above the micrometer scale), but it does have its limitations. Charged particles such as protons or alphas can undergo multiple scattering events, which can hinder the accurate prediction of the detected energy of the backscattered particles. Additionally, these particles may be absorbed within the material, further affecting the measurement accuracy.

Let's examine the kinematics of the RBS technique in more detail. When a particle of mass  $M_1$  collides with an atom in the target material of mass  $M_2$ , the incident particle kinetic energy  $E_0$  is related to the energy  $E$  of the scattered particle through the following equation :

$$E = k^2.E_0 \quad (20)$$

with  $k^2$  being the kinematic factor of the reaction, which is expressed in terms of the projectile mass, the target atom mass, and the backscattering angle  $\theta$  in the laboratory system such that :

$$k = \frac{M_1.\cos\theta + (M_2^2 - M_1^2.\sin^2\theta)^{\frac{1}{2}}}{M_1 + M_2} \quad (21)$$

By obtaining knowledge of the energies  $E$  and  $E_0$  along with the fixed scattering angle during the experiment, it is feasible to deduce the kinematic factor and thus ascertain the mass  $M_2$  of the target atom. Furthermore, the energy dissipated by the incident particle as it penetrates the sample enables determination of the scattering depth and, consequently, the thickness of the target.

The mass resolution of the method depends of the sensitivity of the kinematic factor  $k$  to  $M_2$ , which depends on the choice of  $\theta$  and  $M_1$ . The Rutherford cross section is maximal at a scattering angle of  $0^\circ$ . However, at this angle, the differentiation between different values of the mass  $M_2$  is minimal since the kinematic factor is at an extreme value as illustrated in Fig.16. At  $180^\circ$ , mass selectivity appears to be maximal, but experimental conditions do not always permit the placement of a detector at this angle. In addition, the Rutherford elastic scattering formula in equation (17) reveals that the sensitivity, in terms of cross-section, is highest for elements near  $0^\circ$  scattering angle. Consequently, a trade-off needs to be made between different parameters, leading to RBS experiments being often performed at detection angles around  $160^\circ$ .



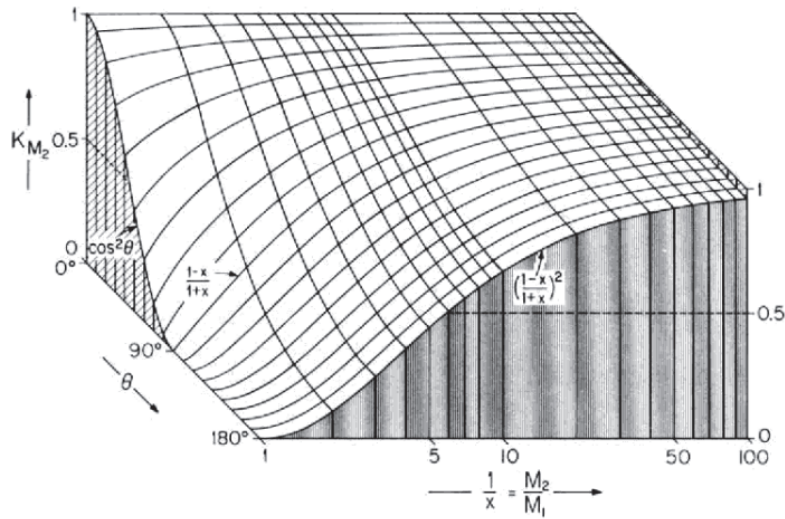


Figure 16: Evolution of the kinematic factor as a function of the  $M_2/M_1$  ratio and the scattering angle. Extracted from [39].

The mass of the incident particle also influences the detection process. When the projectile is much lighter than the target, the kinematic factor remains close to 1. The mass resolution is then better with heavier projectiles. However, using heavier projectiles degrades the energy resolution of the detector and causes more damage to the material. Therefore, the choice of alpha particles as incident particles often strikes a balance between these competing considerations. The utilization of alpha particles as incident particles implies that lighter atoms may remain undetected if they are present in the sample [39].

## 3.4 Software

### 3.4.1 SIMNRA

SIMNRA (Simulation Program for the Analysis of NRA, RBS and ERDA) [47] is a software program designed for the simulation and analysis of charged particle energy spectra and gamma-ray yields in ion beam analysis. It is specifically used for incident ions with energies ranging from about 100 keV to several MeV. The program allows for the determination of depth profiles of elemental composition based on backscattering spectra loaded into an interactive window. The software provides advanced analysis capabilities for experimental spectra by utilizing a comprehensive database of over 300 reaction cross-sections, including both Rutherford and non-Rutherford reactions, for incident particles such as protons, deuterons,  $^3\text{He}$ , and  $^4\text{He}$ .

The software is used for the identification of elements present in our target samples, as well as for the determination of their thicknesses. However, it should be noted that SIMNRA does not have the capability to distinguish between isobars elements, and does not allow to determine isotopic composition. Therefore, prior knowledge or additional experimental techniques may be necessary to fully characterize the target composition. Nonetheless, SIMNRA provides valuable insights and data for researchers to analyze and interpret the results obtained from experimental spectra, enhancing our understanding of the elemental composition and structure of studied materials.

### 3.4.2 TALYS 1.96

---

TALYS [34] is a computer program developed to analyze and predict nuclear reactions across a broad energy range (eV to 200 MeV). It is designed to simulate reactions involving various particles, including neutrons, photons, protons, deuterons, tritons,  $^3\text{He}$ , and alpha particles, and different reactions mechanism (direct, compound, pre-equilibrium and fission). The program aims to provide a comprehensive collection of nuclear reaction models within a single code system.

In general terms, the TALYS software serves two interrelated purposes. Firstly, it is utilized as a powerful tool for analyzing nuclear reaction experiments, facilitating a deeper understanding of the fundamental interaction between particles and nuclei. The interplay between experimental data and theoretical models allows for refinement and validation of nuclear reaction theories. Secondly, TALYS is employed to generate nuclear data for a wide range of reaction channels allowing users to specify the desired energy and angle grid. These nuclear data libraries play a crucial role in various applications such as nuclear power reactors, radioactive waste transmutation, fusion reactors, accelerator-based technologies, homeland security, medical isotope production, radiotherapy, and astrophysics. TALYS strives for both completeness and quality in its nuclear reaction models. It encompasses a wide range of reaction types and endeavors to improve the accuracy and reliability of its calculations. While some reaction channels may receive more focused attention and refinement, the overarching objective is to consistently enhance the overall quality of the program. The software offers a range of capabilities, such as the incorporation of multiple nuclear reaction models, integrating optical model and coupled-channels calculations, continuous descriptions of reaction mechanisms, and the generation of nuclear data for



diverse reaction channels. It also includes nuclear structure parameters, width fluctuation models, fission models, and various level density models. However, there are certain limitations to consider. TALYS is not designed for heavy-ion reactions and does not generate complete nuclear data libraries. It also does not explicitly model resonance reactions or light-nuclide physics. Additionally, it lacks a high-quality prediction for the average number of fission neutrons and prompt fission neutron spectra. For these specific aspects, other specialized codes and programs should be used in conjunction with TALYS.

### **3.4.3 PENELOPE-2018**

---

The PENELOPE code [48] is a Monte Carlo algorithm and computer code used for simulating the transport of electrons, positrons, and photons in matter. It is particularly relevant in studying radiation transport phenomena and is widely used in various fields such as surface spectroscopy, electron microscopy, radiation dosimetry, and radiotherapy. The code handles the interaction of high-energy particles with matter, which leads to the generation of showers or cascades of secondary particles. PENELOPE employs a mixed simulation approach, combining detailed simulation for hard interactions and multiple-scattering theories for soft interactions. It accurately describes the energy degradation and lateral displacements of particles, as well as the effects of interfaces and energy straggling. The code is well-suited for simulating photon transport, while simulation of electron and positron transport is more challenging due to their numerous interactions. PENELOPE incorporates multiple-scattering theories and allows for trade-offs between computational time and accuracy. It has evolved since its initial release in 1996 and includes updates such as revised photo-absorption cross sections, improved angular distributions, and expanded functionalities for different applications. The PENELOPE code is now distributed through the NEA Data Bank and RSICC, and provides reliable and flexible simulation capabilities for studying the transport of charged particles and photons in matter. Further details on how the code operates will be provided in Part II of this thesis.

### **3.4.4 STOGS-GEANT4**

---

The SToGS simulation package, based on GEANT4, aims to provide a versatile environment for designing and studying response functions of new detectors, preparing experiments with realistic simulations and analysis, and improving

physics generators. It builds upon the PARIS GEANT4 package and is compatible with GEANT4.10 and higher versions, using Multi-threading capabilities. The package allows users to configure the physics generator, physics list, geometry, and user-defined actions within GEANT4 through a general ASCII file. Various executables are provided for different purposes, such as converting geometries from other tools, building detector setups, running simulations with simple sources, and simulating experiments with beams and reactions. The package encourages the use of the General Particle Source (GPS) as the primary generator, offering options for modeling simple and complex sources. Additionally, it provides an external generator to read primaries from external files. Geometries in SToGS are based on the GDML format and can be imported/exported from/to different frameworks. The package includes action managers to extract physics information from GEANT4. The SToGS package has been developed by the IP2I of Lyon and can be downloaded from a gitlab server. It provides a collection of executables, which can be configured and compiled for different versions of GEANT4 [49]. Further details on how the package operates will be provided in Part II of this thesis.

Part III

## P-PROCESS LIGHTER REGION :

Activation measurement of p-induced reaction on several germanium isotopes

## 4 EXPERIMENTAL CONTEXT

---

### 4.1 Overview

---

The most favoured scenario for the astrophysical production sites of the p-nuclei is considered as the O-Ne layers of massive stars ( $25M_{\odot}$ ) during explosive or pre-explosive processes of type II supernovae. In 2006, a study from Rapp *et al.* [23] investigated the p-process nucleosynthesis using a full nuclear reaction network based on this scenario. The purpose was to determine the main reaction path and branching points responsible for the synthesis of these nuclei. Several crucial points were highlighted by the authors, and especially that the abundances of p-nuclei are strongly affected by some specific  $(\gamma, n)$ ,  $(\gamma, p)$ , and  $(\gamma, \alpha)$  reactions and their inverses. It has been found that  $(\gamma, p)$  reactions have a high impact on lighter p-nuclei whereas  $(\gamma, \alpha)$  have a major impact on heavy p-nuclei.

This part of the work is dedicated to the production of the light p-nuclei, especially the lightest  $^{74}\text{Se}$ . Fig.17 extracted from the sensitivity study of Rapp *et al.* shows the direct effect of the  $(\gamma, p)$  and  $(p, \gamma)$  reactions on the creation and the destruction of this nucleus. More precisely, the study indicates that the  $^{72}\text{Ge}(p, \gamma)^{73}\text{As}$  and  $^{74}\text{Ge}(p, \gamma)^{75}\text{As}$  reactions, as well as their inverse reactions, play a crucial role in the production of  $^{74}\text{Se}$  via the reaction chains  $^{72}\text{Ge}(p, \gamma)^{73}\text{As}(p, \gamma)^{74}\text{Se}$  and  $^{74}\text{Ge}(p, \gamma)^{75}\text{As}(p, n)^{75}\text{Se}(\gamma, n)^{74}\text{Se}$ . This motivated several cross section measurements of the  $^{74}\text{Ge}(p, \gamma)^{75}\text{As}$  reaction in the past few years [50, 51, 52].

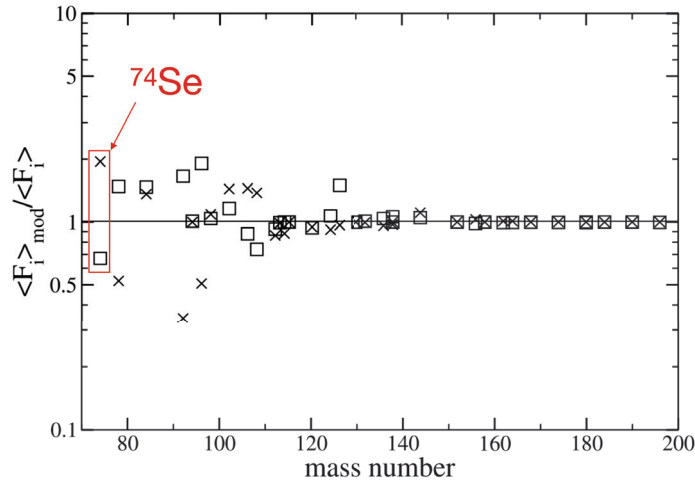


Figure 17: Ratio of simulated abundances calculated with modified  $(\gamma,p)$  rates, with respect to calculations using currently accepted rates. The squares and crosses represent the ratios for which the rates were multiplied and divided by three respectively. In these calculations, all the other relevant parameters which have an impact on the p-nuclei abundances were fixed. Extracted from [23].

The  ${}^{72}\text{Ge}(p, \gamma){}^{73}\text{As}$  cross section, however, had no measure known at the time of submission of the proposal. For this reason, our collaboration decided to measure this reaction cross section at 2.5 MeV, inside the Gamow window, using the activation technique on an enriched  ${}^{72}\text{Ge}$  target. Meanwhile it has been measured by Naqvi *et al.* [53] using an in-beam method; it is then interesting to compare results obtained with these two experimental techniques. The  ${}^{72}\text{Ge}(p, \gamma)$  is indeed crucial for the production of the  ${}^{74}\text{Se}$ , but it should be emphasized that the modeling of p-abundances involves a large reaction network comprising approximately 20.000 reactions involving more than a thousand nuclei. Many other reactions contribute hence, directly or indirectly, to the creation of  ${}^{74}\text{Se}$ . For instance, the lightest stable isotope of germanium,  ${}^{70}\text{Ge}$ , is involved in the understanding of the r-process through the reaction  ${}^{70}\text{Ge}(p, \gamma){}^{71}\text{As}$ . These seed nuclei play a significant role in the p-process by determining the nucleosynthesis path and the final distribution of p-isotopes produced. The  ${}^{70}\text{Ge}(p, \gamma){}^{71}\text{As}$  measurement has been conducted only once in 2007 by Kiss *et al.* [1], using an activation technique on a natural germanium target and it was planned to perform a new measurement of this cross section to have a point of comparison. In this kind of experiment, it is common practice to increase the concentration of the isotopes of interest in the target material. This helps to improve the statistical accuracy of counting the radionuclides that are produced during the irradiation process, especially when the cross section is low. Germanium, in par-

ticular, has five stable isotopes. According to data from the National Nuclear Data Center [4], these isotopes and their respective abundances are as follows :  $^{70}\text{Ge}$  (20.57%),  $^{72}\text{Ge}$  (27.45%),  $^{73}\text{Ge}$  (7.75%),  $^{74}\text{Ge}$  (36.50%),  $^{76}\text{Ge}$  (7.73%). The purpose of our experiment was to study proton-induced reactions on three enriched targets of germanium :

- $^{70}\text{Ge}$  enriched target denoted T[ $^{70}\text{Ge}$ ]
- $^{72}\text{Ge}$  enriched target denoted T[ $^{72}\text{Ge}$ ]
- $^{73}\text{Ge}$  enriched target denoted T[ $^{73}\text{Ge}$ ]

Although the T[ $^{72}\text{Ge}$ ] target used in our activation experiment was enriched to a level of 98%, the presence of  $^{73}\text{Ge}$  as a contaminant possibly up to 2% introduced a source of uncertainty in the calculated cross section value. At 2.5 MeV, the neutron channel is already open, and the  $^{73}\text{Ge}(p, n)^{73}\text{As}$  reaction can produce the same radionuclide as the  $^{72}\text{Ge}(p, \gamma)^{73}\text{As}$  reaction. This uncertainty is difficult to quantify as the cross sections for  $(p, n)$  reactions are generally much larger than the  $(p, \gamma)$  cross sections above the neutron threshold. Additionally, there are currently no existing cross section measurements of the  $^{73}\text{Ge}(p, n)^{73}\text{As}$  reaction in the Gamow window. For all of these reasons, the research group also decided to perform a proton activation experiment at 2.5 MeV on a T[ $^{73}\text{Ge}$ ] enriched target. The cross section for the  $^{73}\text{Ge}(p, \gamma)^{74}\text{As}$  and  $^{73}\text{Ge}(p, n)^{73}\text{As}$  reactions were consequently measured for the first time.

Overall, our main objective will be to study proton-induced reaction data inside the Gamow window for all the stable germanium isotopes in order to better understand the production of the  $^{74}\text{Se}$ . This study will include our new data points, some of which will be compared to previous data by Kiss *et al.* [1] and Naqvi *et al.* [53].

## 4.2 Principle of the activation method

---

Among the experimental techniques allowing the measurement of capture cross section reactions, the activation method is probably one of the most widely used in nuclear astrophysics [53]. The complete process involves two experimental phases illustrated in Fig.18. The first phase is called "irradiation" and consists of bombarding a target material with a particle beam (protons or alphas particles) for a certain time in order to obtain the reaction product of interest. If this product is radioactive, the target is activated. In favorable cases where the lifetime of the reaction product is of order of hours or days, the number of produced nuclei can be determined by activity measurement of the target after irradiation : this is the principle of the activation method. The second phase, called "counting", consists of activity measurements by offline detection of the  $\gamma$  and X rays emitted during the decay of the reaction products [54].

One of the major advantages of the activation technique is that the detection occurs outside of the irradiation region. This eliminates the need to consider the background coming from the beam, and all  $\gamma$  and X-rays resulting from the deexcitation of the stable nuclei are removed from the detection part. Another benefit of the technique is the ability to measure several cross sections during a single experiment, as a single target can contain multiple nuclei of interest. This obviously depends on the quantity of available elements and their respective cross-sections for a given reaction. From a practical standpoint, it is also worth noting that the obtained cross sections are total angle-integrated production cross sections. The angular distribution is not considered in this type of experiment, which makes the data processing faster.

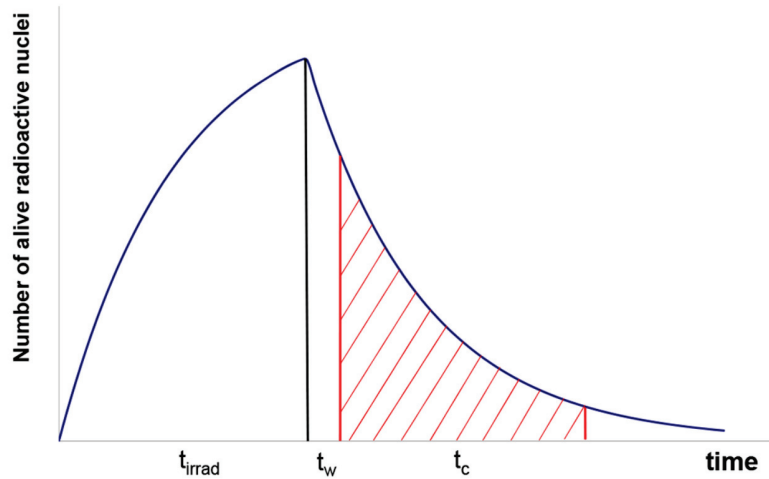


Figure 18: Illustration of a complete activation process extracted from [54]. ( $t_{irrad}$ ) is the irradiation time, ( $t_w$ ) the waiting time required to transport the sample to the detection setup and ( $t_c$ ) the counting time.

Although activation techniques are practical and very useful, they are limited in their application by a number of requirements. Generally, it is necessary to use stable or long-lived target nuclei for an experiment. The half-lives of the produced radionuclides should not be too short (typical time : minutes), to avoid losing them during the waiting time (see Fig.18). It should not be too long as well (years), to measure the decay curve in a reasonable time. Depending on the studied nuclei, the time required for an activation measurement can vary significantly. In addition, the decay radiation scheme of all the nuclei in the target must be known precisely to allow a correct interpretation of the detected  $\gamma$  and X-rays spectrum. When the application of activation techniques is not feasible, alternative methods can sometimes be applied, such as Accelerator Mass Spectrometry or the so-called in-beam technique when the reaction product is stable or has a too long half life (from the order of years) [54, 21]. However, some difficulties remain for these different techniques, especially concerning target requirements. In some cases, it may be necessary to measure reactions cross section on nuclei with very low natural abundances. When such a situation occurs, enriched isotopic powders must be purchased, which can be extremely expensive. Finally, another constraint is the creation of thin targets with thicknesses of the order of  $\mu\text{g}/\text{cm}^2$ . When an incident particle passes through a target, the latter loses energy. If the thickness of the target is too large, the incident particle-nucleus interactions will no longer be at the same energy all across the target, which will increase the uncertainties on the energy at which is measured the reaction cross section. This effect is even more



pronounced when the incident particle energy is low.

### 4.3 Cross section calculation

---

In a typical activation measurement, the effective reaction cross section can be describe by [54]:

$$\sigma_{reac} = \frac{N_{prod}}{N_{inc}N_{target}} \quad (22)$$

where  $N_{prod}$  is the number of radionuclides produced during the irradiation phase [atoms],  $N_{inc}$  the total number of incident particles sent on the target during the irradiation [atoms] and  $N_{target}$  the number of nuclei of interest in the target estimated before the experiment [atoms/cm<sup>2</sup>].

During the irradiation, radioactive nuclei will be produced and will decay according to a specific decay constant  $\lambda$  related to the half life  $t_{1/2}$  of the nucleus by the relation :  $\lambda = \ln(2)/t_{1/2}$ . If the half-life of the considered radionuclide is shorter or comparable to the irradiation time, the decay of the radionuclides will have to be taken into account in order to relate  $N_{prod}$  in the equation (22) to the number of products  $N_0$  present at the end of irradiation. In this case, and if the beam current is sufficiently stable, the cross section reaction will become :

$$\sigma_{reac} = \frac{N_0\lambda t_{irrad}}{N_{inc}N_{target}(1 - e^{-\lambda t_{irrad}})} \quad (23)$$

where  $t_{irrad}$  represents the irradiation time [s]. This is the formula we will use in our analysis.

To sum up, three parameters will be essential to obtain the cross section :  $N_0$ ,  $N_{inc}$  and  $N_{target}$ . Their obtaining will be detailed in the following sections.

## 4.4 Experimental setup

---

### 4.4.1 Germanium targets

---

#### 4.4.1.1 Production by thermal evaporation

In 2016, the collaboration acquired enriched germanium isotope powders via the supplier EURISOTOP [55]. The ordered quantities were 100 mg of  $^{70}\text{Ge}$  enriched at 95%, 100 mg of  $^{72}\text{Ge}$  enriched at 98% and 100 mg of  $^{73}\text{Ge}$  enriched at 96%. Once received, the target preparation was performed at the target laboratory of the GANIL (Grand Accélérateur National d'Ions Lourds) in Caen. To minimize background gases contamination and in order to obtain thin targets, the thermal evaporation technique was used in a high-vacuum environment. This technique, also called Physical Vapor Deposition (PVD), is a coating process in which a material is evaporated and then condensed onto a cooled solid substrate to form a thin film as shown in Fig.19 [56][57].

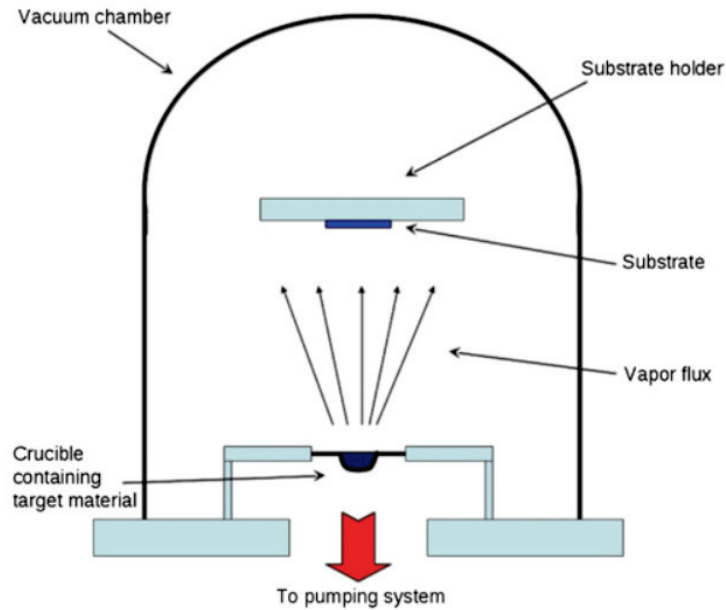


Figure 19: Illustration of the thermal evaporation deposition used for the creation of thin targets [56].

In this experiment, the germanium particles were deposited on thin aluminium foils which are commonly used as suitable backing for activation measurements. Indeed, aluminum only has one stable isotope ( $^{27}\text{Al}$ ) which produces stable nuclei under proton bombardment at low energy. As a result of this procedure,

three targets were obtained T[<sup>70</sup>Ge], T[<sup>72</sup>Ge] and T[<sup>73</sup>Ge] with 2 cm of diameter and few tenth micrometers thick.

#### 4.4.1.2 Characterization by RBS

The target characterization was performed using the Rutherford Backscattering Spectrometry technique (RBS) (see sub-section 3.3.2). Measurements were carried out at IJCLab (Irene Joliot-Curie Laboratory) in Paris-Orsay, using the ARAMIS ion accelerator of the JANNuS-SCALP facility. Germanium targets were exposed to a 1.4 MeV  $\alpha$ -beam at five different points on their surfaces. The resulting experimental spectra were analyzed using the SIMNRA7 <sup>®</sup> software [47] (see sub-section 3.4.1) allowing the extraction of the different target thicknesses whose values are displayed in Table 1.

Beam position on target	T[ <sup>70</sup> Ge] [at/cm <sup>2</sup> ]	T[ <sup>72</sup> Ge] [at/cm <sup>2</sup> ]	T[ <sup>73</sup> Ge] [at/cm <sup>2</sup> ]
Centre	2.764 x 10 <sup>18</sup>	3.076 x 10 <sup>18</sup>	2.060 x 10 <sup>18</sup>
Right	2.785 x 10 <sup>18</sup>	3.126 x 10 <sup>18</sup>	2.060 x 10 <sup>18</sup>
Top	2.785 x 10 <sup>18</sup>	3.076 x 10 <sup>18</sup>	2.030 x 10 <sup>18</sup>
Bottom	2.826 x 10 <sup>18</sup>	3.111 x 10 <sup>18</sup>	2.070 x 10 <sup>18</sup>
Left	2.851 x 10 <sup>18</sup>	3.071 x 10 <sup>18</sup>	2.070 x 10 <sup>18</sup>
Average	2.802 x 10 <sup>18</sup>	3.092 x 10 <sup>18</sup>	2.058 x 10 <sup>18</sup>

Table 1: Target thicknesses measured by RBS at various locations on each target and determined using the SIMNRA7 software.

In this table, we can see the total number of germanium nuclei present in each target and for different locations. All the stable germanium isotopes are taken into account in these thicknesses. For the determination of the parameter  $N_{target}$  necessary to obtain a reaction cross-section, we need to know the thickness of the isotope of interest in the considered target. To do that, we proceed as follows :

$$N_{target} = N_{average}f \quad (24)$$

where  $N_{average}$  represents the average target thickness shown in the Table 1 and  $f$  the fraction of isotope of interest present in the target. These percentages and their uncertainties were provided by EURISOTOP and are available in Appendix.A. Finally we estimated the  $N_{target}$  uncertainties around 10% using the formula :

$$dN_{target} = \sqrt{\left(\frac{df}{f}\right)^2 + \left(\frac{dN_{average}}{N_{average}}\right)^2} * N_{target} \quad (25)$$

#### 4.4.1.3 ICP-MS measurements

##### Context

Thanks to the isotopic percentage values communicated by EURISOTOP and to the thicknesses obtained during the RBS analyses, the  $N_{target}$  thicknesses of interest required for the cross-section calculations were obtained. However, during the analysis of the T[ $^{70}\text{Ge}$ ] target data, the first estimation of the  $^{70}\text{Ge}(p, \gamma)$  cross section that has been obtained showed significant discrepancy with the earlier result by Kiss *et al.* [1]. After a long time spent ruling out possible sources of error, the value of the isotopic enrichment was questioned. Plasma mass spectrometry (see sub-section 3.3.1) has been deemed the optimal approach for accurately assessing the composition of the T[ $^{70}\text{Ge}$ ] target. The measurement has been performed at the LANIE Laboratory (Laboratoire de développement Analytique Nucleaire, Isotopique et Elementaire) in Paris-Saclay. This technique enabled us to determine the elemental and isotopic composition of the T[ $^{70}\text{Ge}$ ] target with high precision.

In addition, the T[ $^{73}\text{Ge}$ ] target required a double check of its composition as no previous measurements have been conducted for the  $^{73}\text{Ge}(p, n)$  and  $^{73}\text{Ge}(p, \gamma)$  reactions to provide points of comparison. Therefore, the plasma mass spectrometry has also been employed in this instance to obtain accurate information regarding the elemental and isotopic composition of the target. For the T[ $^{72}\text{Ge}$ ], no further measurements have been deemed necessary as our spectroscopic analysis was in perfect agreement with the information provided by the manufacturer. Additionally, preliminary results for the reaction  $^{72}\text{Ge}(p, \gamma)$  were in reasonable agreement with previous measurement.

## Explanation of the experimental approach by ICP-MS

For the targets T[ $^{70}\text{Ge}$ ] and T[ $^{73}\text{Ge}$ ], several milligrams of germanium powder were dissolved in a mixture of analytical grade  $\text{HNO}_3$  (67–69 % purity) and  $\text{HCl}$  (32–35 %purity) from SCP Science ("PlasmaPure Plus degree"), Courtaboeuf, France, in a molar ratio of 1/3. The resulting solution was then diluted in ultrapure 2% nitric acid to achieve concentrations of several hundred nanograms per gram for the mass spectrometry analysis as shown in Fig.20. A procedural blank was prepared using the same conditions to serve as a control.

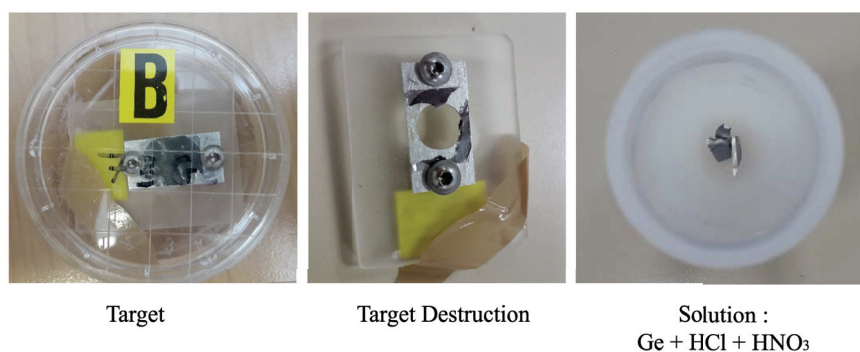


Figure 20: Pictures of sample preparation before ICP-MS measurements. Photos credit : H el ene Isnard.

The mass spectrometry analysis was conducted using a Thermo Electron "X series" quadrupole inductively coupled plasma mass spectrometer (ICP-MS) located in Winsford, UK. The samples were introduced into the plasma via a quartz cyclonic spray chamber connected to a PC3 peltier chiller from Elemental Scientific (ESI), USA, and a quartz concentric nebulizer ( $0.4 \text{ mL}\cdot\text{min}^{-1}$ ). The instrument was calibrated and tuned before each analytical session to achieve a stability of more than 2%. The rate of oxides and doubly-charged species was estimated to be less than 3%.

## Results of measurements

The Table 2 presents the relative atomic abundance of all the measured germanium isotopes for the two targets, expressed as a percentage and rounded to two decimal places. It is noteworthy that the measurements were impacted by molecular interferences on nearly all germanium isotopes, such as  $^{35}\text{Cl}^{35}\text{Cl}^+$  on  $^{70}\text{Ge}^+$ ,  $^{40}\text{Ar}^{16}\text{O}_2^+$  and  $^{36}\text{Ar}^{36}\text{Ar}^+$  on  $^{72}\text{Ge}^+$ ,  $^{58}\text{Ni}^{16}\text{O}^+$  and  $^{38}\text{Ar}^{36}\text{Ar}^+$  on  $^{74}\text{Ge}^+$ ,

Target	Germanium composition	Isotopic abundance [%]
T[ <sup>70</sup> Ge]	<sup>70</sup> Ge	20.38(0.18)
	<sup>72</sup> Ge	27.31(0.26)
	<sup>73</sup> Ge	7.76(0.08)
	<sup>74</sup> Ge	36.72(0.15)
	<sup>76</sup> Ge	7.83(0.07)
T[ <sup>73</sup> Ge]	<sup>70</sup> Ge	0.08(2)
	<sup>72</sup> Ge	1.4(0.3)
	<sup>73</sup> Ge	96.4(0.9)
	<sup>74</sup> Ge	2.1(4)
	<sup>76</sup> Ge	< 0.05

Table 2: Composition of the targets T[<sup>70</sup>Ge] and T[<sup>73</sup>Ge] in germanium extracted from the ICP-MS measurements.

and <sup>38</sup>Ar<sup>38</sup>Ar<sup>+</sup> and <sup>36</sup>Ar<sup>40</sup>Ar<sup>+</sup> on <sup>76</sup>Ge<sup>+</sup> (see Appendix.B.1). To correct for these mass interferences, a blank germanium Spex solution (SPEX CertiPrep, Metuchen, USA) was prepared under the same conditions as the samples, and the IUPAC (International Union of Pure and Applied Chemistry) reference values for germanium were used [58]. Subsequently, the relative isotopic results were determined using a sample standard bracketing approach, employing an analytical strategy comparable to those performed in the LANIE laboratory [59]. The final uncertainties on the target isotope abundances were propagated to the target thickness uncertainties.

The analysis confirmed a T[<sup>73</sup>Ge] target composition consistent with the manufacturer report while a natural isotopic abundance was revealed for the T[<sup>70</sup>Ge] target. These last results, in contradiction with those communicated by EURISOTOP (expected enrichment : 95%), allowed us to alleviate the tensions initially present between the primary calculated <sup>70</sup>Ge(*p*,  $\gamma$ ) reaction cross section estimated from our data, and the previous result by Kiss *et al.* [1]. The results of the ICP-MS measurements are detailed in Appendix.B.

#### 4.4.1.4 Final composition

Following the ICP-MS analyses, the final  $N_{target}$  values for all the investigated reactions have been derived and are shown in Table 3. The previously called T[ $^{70}\text{Ge}$ ] target is now referred as the T[ $\text{Ge}_{nat}$ ] natural germanium target.

Target	Reaction	$N_{target}$ [at/cm <sup>2</sup> ]	$dN_{target}$ [at/cm <sup>2</sup> ]
T[ $\text{Ge}_{nat}$ ]	$^{70}\text{Ge}(p, \gamma)^{71}\text{As}$	$5.71 \times 10^{17}$	$6.36 \times 10^{16}$
T[ $\text{Ge}_{nat}$ ]	$^{76}\text{Ge}(p, n)^{76}\text{As}$	$2.19 \times 10^{17}$	$2.44 \times 10^{16}$
T[ $^{72}\text{Ge}$ ]	$^{72}\text{Ge}(p, \gamma)^{73}\text{As}$	$3.04 \times 10^{18}$	$3.18 \times 10^{17}$
T[ $^{72}\text{Ge}$ ]	$^{70}\text{Ge}(p, \gamma)^{71}\text{As}$	$8.97 \times 10^{15}$	$9.39 \times 10^{14}$
T[ $^{73}\text{Ge}$ ]	$^{73}\text{Ge}(p, \gamma)^{74}\text{As}$	$1.98 \times 10^{18}$	$2.15 \times 10^{17}$
T[ $^{73}\text{Ge}$ ]	$^{73}\text{Ge}(p, n)^{73}\text{As}$	$1.98 \times 10^{18}$	$2.15 \times 10^{17}$

Table 3: Summary of the values and uncertainties for the parameter  $N_{target}$  used for the cross section calculations.

#### 4.4.2 Proton beam and fluence

The natural,  $^{72}\text{Ge}$ , and  $^{73}\text{Ge}$  targets underwent irradiation for durations of approximately 4.5, 9.5, and 7.5 hours, respectively, at beam energy of 2.5 MeV using the tandetron accelerator located at the Horia Hulubei National Institute of Physics and Nuclear Engineering (IFIN-HH) Laboratory in Romania. The Faraday cup detector was used to measure the proton beam current, which was recorded using the GENIE2000 acquisition system [60]. To prevent contributions from the beam halo, two collimators made of Ta and Al with aperture diameters of 5 mm and 1 mm, respectively, were installed at the entrance of the reaction chamber. Within the chamber, a third Ta collimator with a 3 mm diameter aperture was placed, along with a silicon detector positioned at a backward angle of  $35.8^\circ$  and 125.9 mm from the target center. The sketch of the irradiation setup is shown in Fig.21.

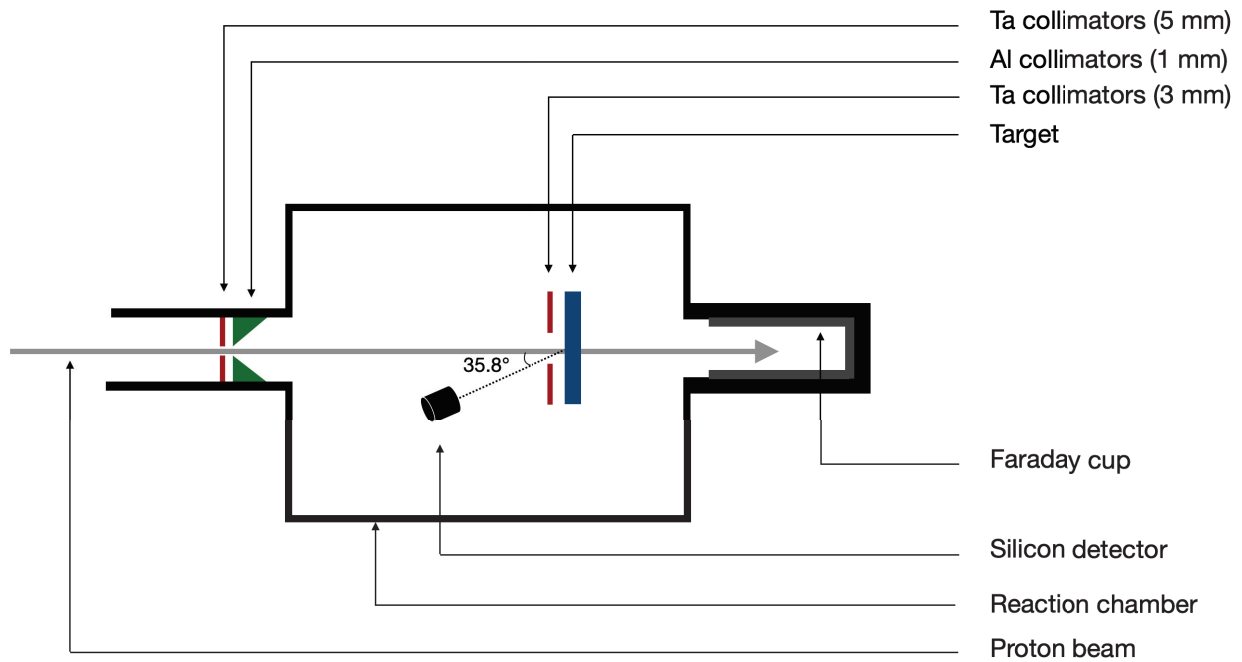


Figure 21: Sketch of the reaction chamber during the irradiation phases of the experiment (not to scale).

The data obtained from the silicon detector were used to monitor the beam current and cross-check the output signals using the RBS method. The silicon detector was calibrated using a  $^{241}\text{Am}$  source (alpha particle energies up to 5.48 MeV) and three mass-separated targets  $\text{T}[^{197}\text{Au}]$ ,  $\text{T}[^{72}\text{Ge}]$ , and  $\text{T}[^{12}\text{C}]$ . Then, the Rutherford elastic backscattering formula was used (see equation (17)) via SIMNRA to determine the number of incident particles sent on each target during each irradiation phase. The comparison of the results obtained from the RBS technique with those obtained from the Faraday cup are visible in Fig.22 where the ratio of the particle fluence from these two techniques is plotted. For almost all the runs checked, the ratio is close to one and confirmed the use of the Faraday cup data to determine  $N_{inc}$  for our cross-section calculations. At the end of the procedure, we were able to estimate the uncertainties associated with the  $N_{inc}$  parameters for each calculated cross section, which ranged from 2.5% to 6%.



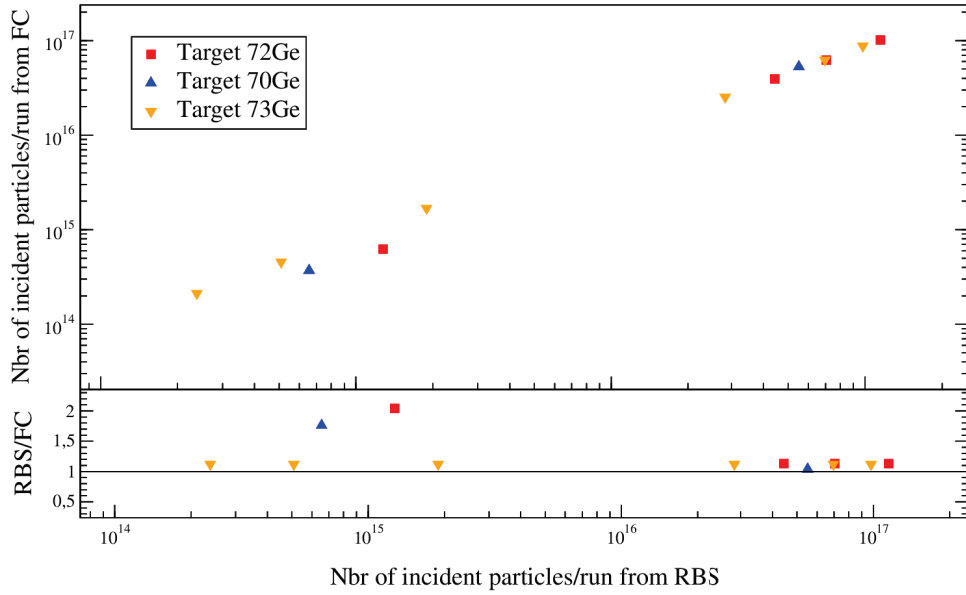


Figure 22: Comparison between the data obtained from the Faraday cup with the data obtained using the silicon detector for each target irradiation run used in this analysis.

#### 4.4.3 Detection setup

The last parameter needed to calculate the cross section,  $N_0$ , is determined by the analysis of the decay curves from the activated targets. In this section, we only describe the detection setup and more details on the analysis will be given in the following.

The induced activity measurement was performed at the underground laboratory located in the Slanic-Prahova salt mine, which is situated at a distance of 140 km from the IFIN-HH Institute. This mine, situated 200 m below ground level, exhibits lower natural radioactivity levels compared to surface environments due to reduced cosmic ray flux, making it an ideal location for low-background measurements. The  $\gamma$ -ray counting following the decay of the reaction products was performed using a MIRION (formerly CANBERRA) coaxial germanium detector from the "XtRa" series (see Appendix.C). The GX12021 model employed in this study comprises a very pure germanium crystal in the form of a cylinder, covered with a unique thin carbon window (0.6 mm) on the front surface.

For the purpose of the experiment, a cylinder made of plexiglass with a height of 12 cm was added to the setup and placed on top of the High-Purity Germanium detector (HPGe) to hold the targets. The aim was to separate the radioactive targets from the HPGe at a predetermined distance in order to minimize the

effects of the gamma summing on detection (will be later detailed). The setup is visible in Fig.24. Furthermore, the HPGe was shielded by a  $4\pi$  enclosure made of lead, copper, and tin (see Fig.23) to reduce background counts caused by external sources.

The geometry mentioned offers a large detection volume, combining high detection efficiency with excellent energy resolution. The last was measured to be of 1.35 keV at 14 keV. The counting was carried out at regular intervals of at least twice a week, with data being recorded during intervals of 0.5-4 hours, for a maximum duration of 56 days.

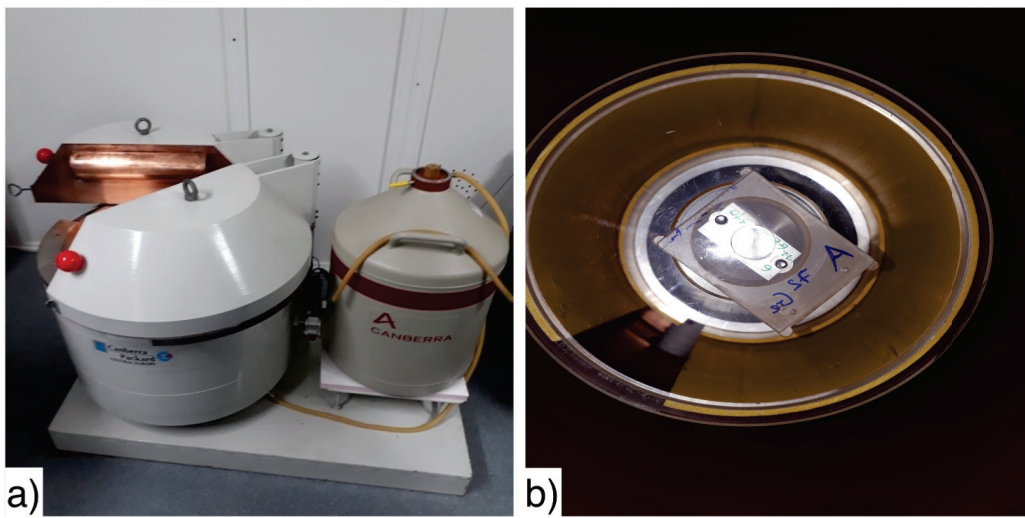


Figure 23: Pictures of the detection device. In a) is shown the lead shield inside which the HPGe is cooled by a liquid nitrogen tank from below. In b) is shown a top view of the HPGe hid by a target deposited on a plexiglass support. These pictures are extracted from the internship report of Lama Al Ayoubi who worked on this experiment during her master [61].

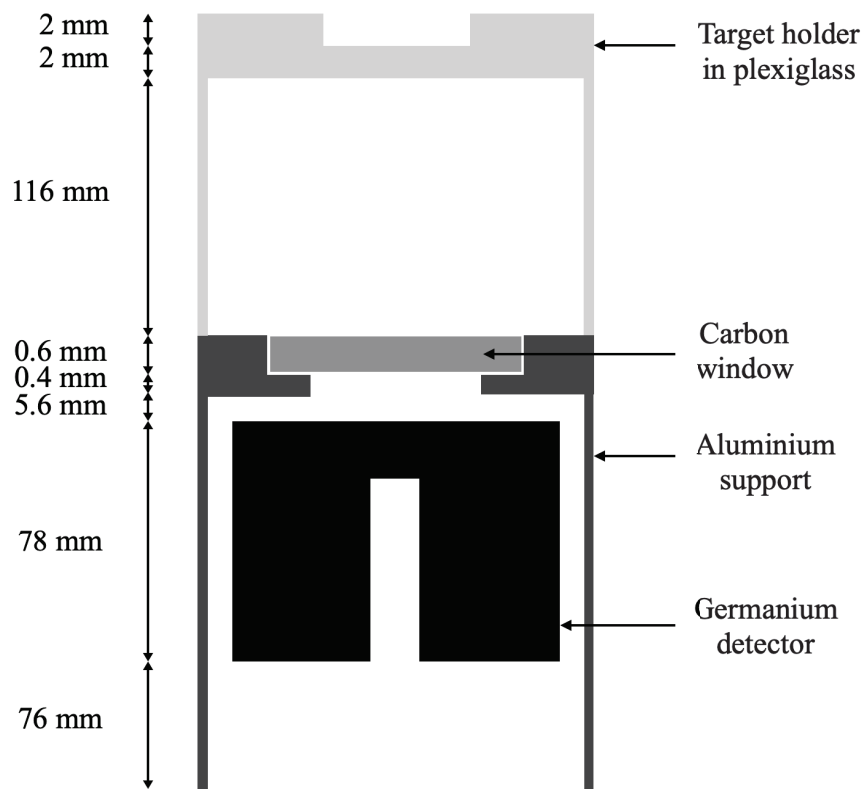


Figure 24: Diagram of the detection device present inside the lead shield (not to scale).

## 5 DATA ANALYSIS

---

### 5.1 The coaxial germanium detector

---

#### 5.1.1 Calibration

---

In order to cover a maximum range of energy, five  $\gamma$ -emitting sources were used to calibrate the HPGe :  $^{57}\text{Co}$ ,  $^{133}\text{Ba}$ ,  $^{137}\text{Cs}$ ,  $^{152}\text{Eu}$ , and  $^{241}\text{Am}$ . Two main sets of measurements were realized, one in October 2017 and another one in December of the same year to increase the duration of the acquisition runs. These durations as well as the energy of the selected gamma rays used for the calibration are shown in Table 4.

For this analysis, particular attention was focused on the low-energy calibration, as the radionuclide  $^{73}\text{As}$  produced by the reactions  $^{72}\text{Ge}(p, \gamma)^{73}\text{As}$  and  $^{73}\text{Ge}(p, n)^{73}\text{As}$  undergoes deexcitation by emitting gamma rays at 53 keV.

All gamma peaks selected in the last column of Table 4 were fitted using a code developed by Smajarit Triambak and thoroughly detailed in his doctoral thesis [62]. For the majority of spectra, the areas were obtained using a Gaussian function coupled with a linear background noise.

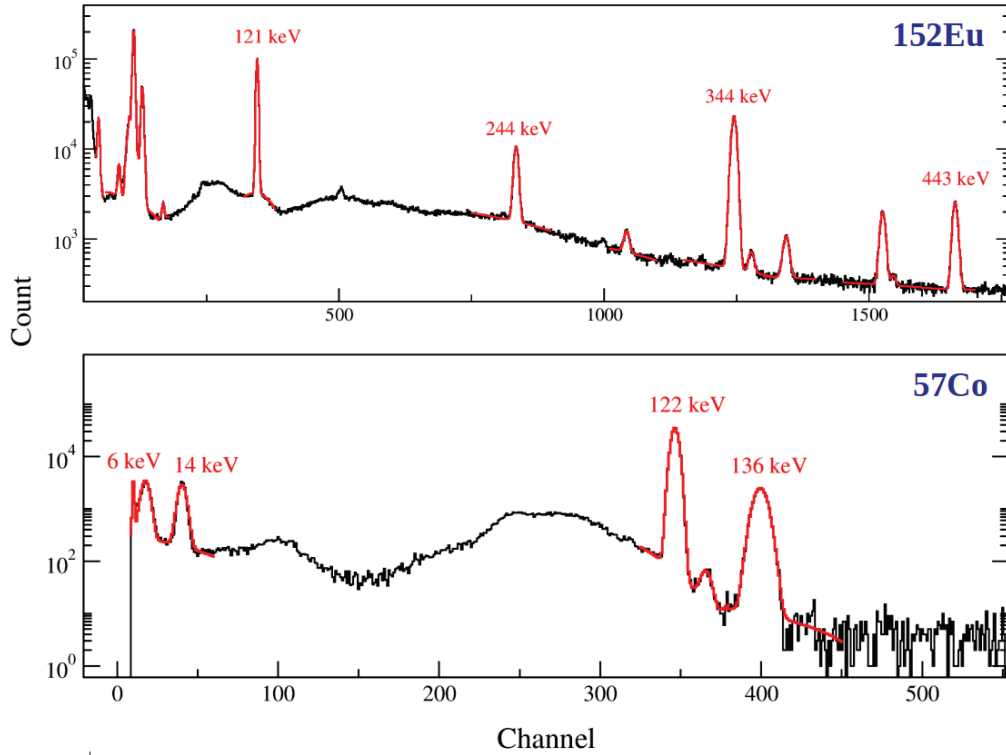


Figure 25: Example of fitting obtained on two acquisition spectra for the  $^{152}\text{Eu}$  and the  $^{57}\text{Co}$  sources. In red with labels are the fits of interest used for the analysis.

At low energies, Compton scattering coming from higher-energy photons (see sub-section 3.1.1) gives rise to a superposition of plateaus on which the peak centroids lie. These affected certain fits for which background noise had to be quadratically fitted. Similarly, the tails of the Gaussian functions were also adjusted linearly or quadratically depending on their location on the spectra. Each fit was then validated by varying the different parameters of the function in order to minimize the  $\chi^2$ . Some of the fitted photopeaks used for the analysis are visible in Fig.25. The red curves represent the final optimization of the peak shapes.

The fitting procedure provided the relative errors in the prediction of the peak areas, taking into account uncertainties from counting statistics ( $\sqrt{N_{\text{count}}}$ ) as well as systematic uncertainties related to the calibration of centroid energies. These systematic uncertainties were estimated by comparing the centroid energies with those of reference [4].

After processing the data and obtaining the centroid energies of each photopeak, we plotted a quadratic calibration curve. Only data from the December 2017

runs were used to obtain the curve, as their statistics were much better than those from October. In Fig.26 the errors between the fit and the data do not exceed 2%, this level of agreement suggests a satisfactory calibration.

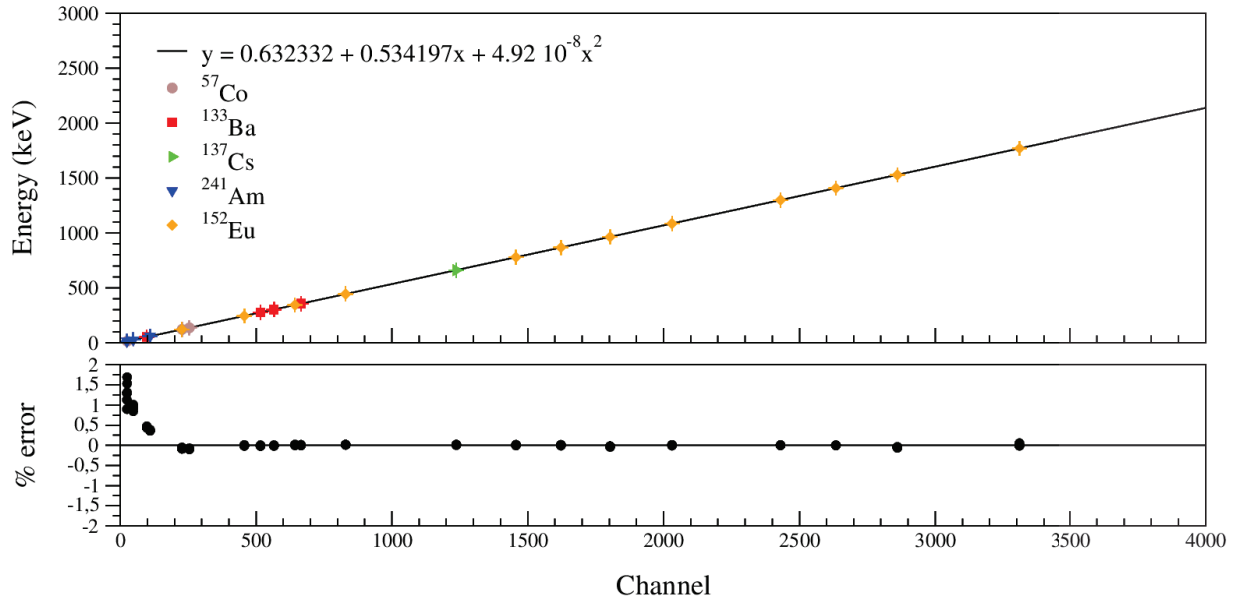


Figure 26: Energy calibration curve of the germanium detector with the associated relative error in percentage.

Source	Run time 1 Oct 2017 [min]	Run time 2 Dec 2017 [hrs]	Gamma Energy [keV]
$^{57}\text{Co}$	38.67	2.78	14.4129(6) 122.06065(12) 136.47356(29)
$^{133}\text{Ba}$	50.02	20.26	53.1622(6) 80.9979(11) 276.3989(12) 302.8508(5) 356.0129(7) 383.8485(12)
$^{137}\text{Cs}$	8.33	21.39	36.65 661.657(3)
$^{152}\text{Eu}$	50.02	96.69	121.7817(3) 244.6974(8) 344.2785(12) 443.9606(16) 778.90925(24) 867.380(3) 964.057(5) 1085.837(10) 1112.076(3) 1212.948(11) 1408.013(3) 1528.10(4) 1769.09(4)
$^{241}\text{Am}$	8.33	1.22	26.3446(2) 59.5409(1)

Table 4: List of radioactive sources used to obtain the HPGe calibration curve. The second and third columns list the duration of each data acquisition performed by the detector. The final column contains the list of gamma rays used in the analysis. Gamma energies extracted from [4].

### 5.1.2 Energy Resolution

---

From the spectra of the different radioactive sources, the energy resolution curve of the detector was also obtained from the full width at half maximum (FWHM) for the photopeaks of interest. The FWHM obtained for the December 2017 and October 2017 acquisition data are shown in Fig. 27. The choice of the December data for the analysis is here obvious when considering the large dispersion of the October data around the linear fit (usual response of detectors [38]). The December data, on the other hand, appear to be more consistent even though some points deviate from the fit around 100 keV. We compared our measurements to the resolution provided by the detector manufacturer at the time of purchase (2013). The reported resolution was 1.3 keV at 122 keV while according to our curve, the resolution at 122 keV is estimated to be 1.38 keV. This small discrepancy may be explained by multiple reasons, starting with errors in the fit performed. It could also arise from fluctuations in the number of charges carried which may result from the detector temperature, a less optimized electronic chain, a possible degradation of the germanium crystalline structure within 4 years, and many others reasons... At 1330 keV, the manufacturer predicts a resolution of 2.1 keV while we experimentally obtain 2.03 keV. The trend with the data at 122 keV is reversed, and it appears that the slope of our fit slightly differs from that of the manufacturer's. Nevertheless, these results are consistent with those of the manufacturer within the limits of error bars.

From now on, we will use a more specific definition of the energy resolution. In a Gaussian shape, the energy resolution is defined by the FWHM divided by the centroid energy  $E_c$  such as [38]:

$$R_E = \frac{FWHM}{E_c} = \frac{2\sqrt{2\ln(2)}\sigma}{E_c} \quad (26)$$

## 5.2 Spectroscopic study

---

The acquisition of the activated target spectra started shortly after irradiation and lasted from a few days to several months depending on the half-lives of the radionuclides of interest. For the shortest half-life, the acquisition time took 3 days while for the longest half-life it took almost 56 days. These spectra were



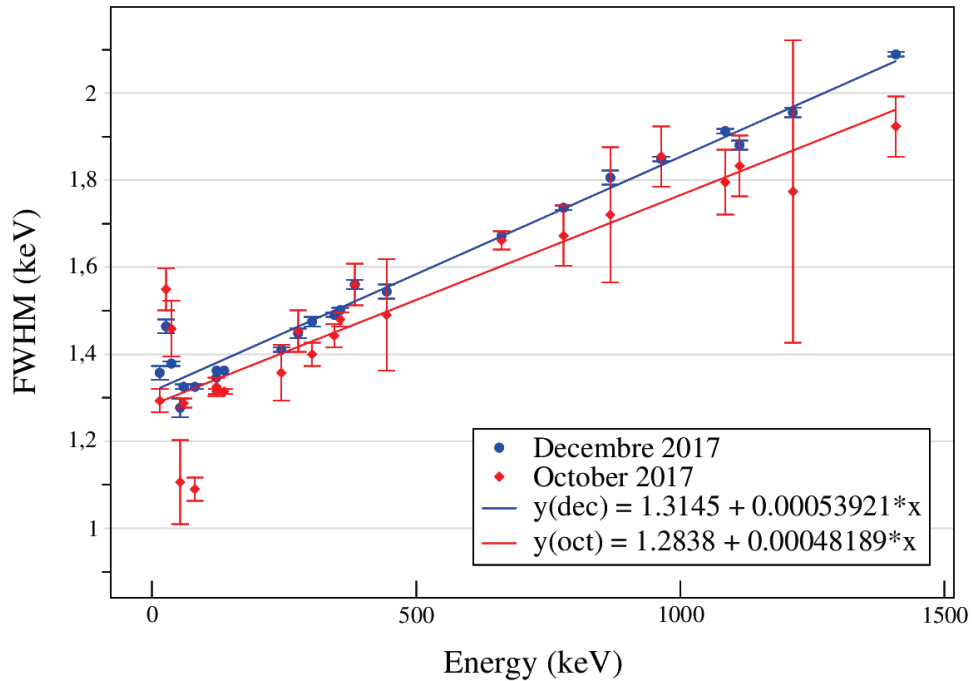


Figure 27: FWHM used for the extraction of the germanium detector resolution curve.

analyzed and compared to background spectra in order to characterize the target contaminants as well as the background contributions. A complete spectroscopic analysis allowed an accurate and reliable identification of the radionuclides of interest as we will see in the next sub-section.

### 5.2.1 Target analysis : T[Ge<sub>nat</sub>]

The experimental spectrum of Fig.28 was acquired over a 30 minutes period, 5 hours after irradiation. It is plotted with a linear Y-axis in order to better discern the most intense decay radiations. The 174 keV photopeak is due to the decay of <sup>71</sup>As nuclei, which have a half-life of the order of days. This peak was used to measure the <sup>70</sup>Ge(*p*,  $\gamma$ ) cross section.

The peaks at 559.10 and 657.05 keV are attributed to the <sup>76</sup>As nuclei, which also have a half-life of the order of days. These radionuclides were not expected to be detected so intensely in the supposedly enriched target T[<sup>70</sup>Ge]. As it turned out that it was a natural target where the isotopic fraction of <sup>76</sup>Ge is 7.76%, the short half-life of <sup>76</sup>As as well as the high cross section of the <sup>76</sup>Ge(*p*, *n*)<sup>76</sup>As reaction explain why these photopeaks are so intense. We therefore took advantage of this opportunity to measure the cross section of the <sup>76</sup>Ge(*p*, *n*) reaction at 2.5 MeV. The data from this target thus allowed us to performed

new measurements of the two reaction cross sections previously measured by Kiss *et al.* [1] in similar conditions, and cross-check results.

The decay schemes of the  $^{71}\text{As}$  and  $^{76}\text{As}$  can be seen in more details in Appendix.D.1 and D.2 respectively. All the other observable photopeaks were attributed to the background.

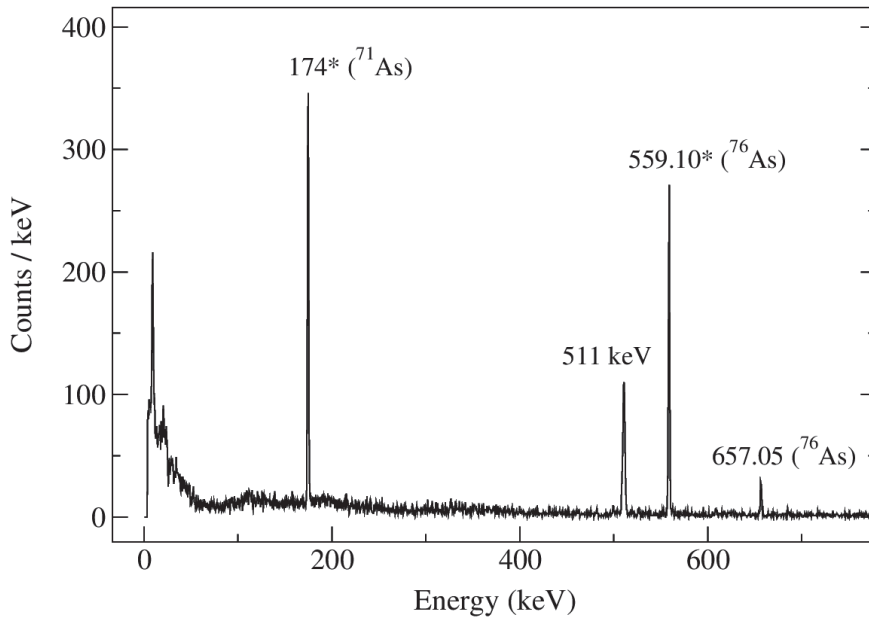


Figure 28: Calibrated energy spectrum of the target  $\text{T}[\text{Ge}_{\text{nat}}]$ . The photopeaks with a star were used for the calculation of reaction cross sections. The decay schemes of the  $^{71}\text{As}$  and the  $^{76}\text{As}$  can be seen in Appendix.D.

### 5.2.2 Target analysis : $\text{T}[^{72}\text{Ge}]$

An acquisition spectrum of the  $\text{T}[^{72}\text{Ge}]$  target is shown on Fig.29 in both logarithmic and linear scales. It was acquired over a period of 30 minutes, 4 hours post-irradiation. Two peaks are observed in the linear view of the spectrum; one corresponds to the 53.44 keV gamma emission from the decay of  $^{73}\text{As}$ , while the other one, more intense, originates from the background noise. The radionuclides  $^{73}\text{As}$  are produced both by the reaction of interest here and by the  $^{73}\text{Ge}(p,n)$  reaction on the small fraction of  $^{73}\text{Ge}$  contaminant in this target (0.29 % according to EURISOTOP). As will be detailed later, the analysis of  $\text{T}[^{73}\text{Ge}]$  will allow to disentangle the contributions from these two reactions.

After analyzing the experimental spectra and comparing them to the back-

ground spectra, it was confirmed that the 174 keV photopeak visible only in the right panel of Fig.29 results from the deexcitation of  $^{71}\text{As}$  nuclei produced during irradiation due to the presence of  $^{70}\text{Ge}$  contaminant (0.29% according to EURISOTOP). Therefore, we calculated the cross section of the  $^{70}\text{Ge}(p, \gamma)^{71}\text{As}$  reaction twice in this study, once using the T[ $\text{Ge}_{nat}$ ] target and once with the T[ $^{72}\text{Ge}$ ] target.

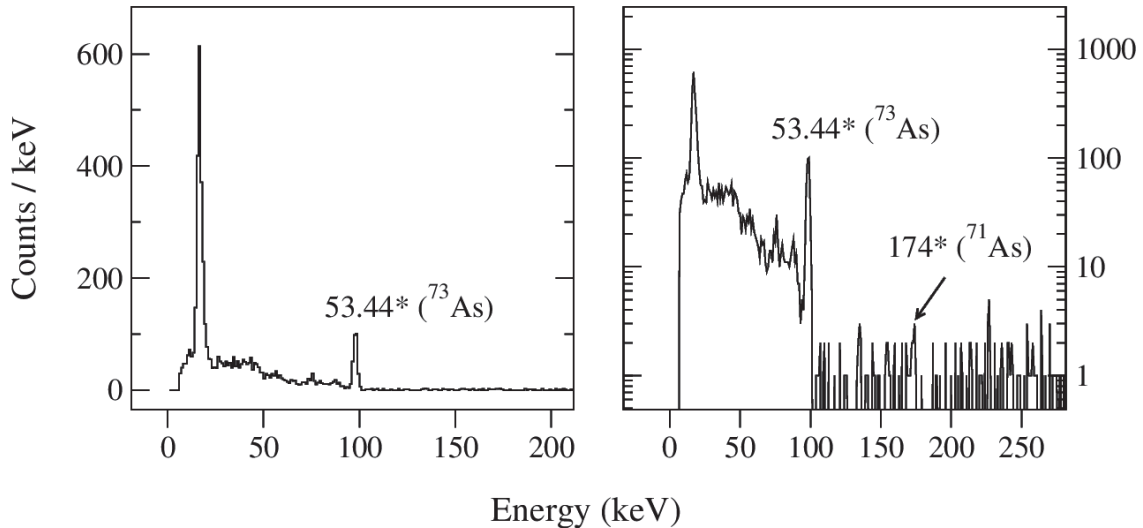


Figure 29: Calibrated energy spectrum of the target T[ $^{72}\text{Ge}$ ]. On the left the y-axis of the spectrum is in a linear form and on the right in a logarithmic form. The photopeaks with a star were used for the calculation of reaction cross sections. The decay scheme of the  $^{73}\text{As}$  nucleus can be seen in Appendix.D.3.

### 5.2.3 Target analysis : T[ $^{73}\text{Ge}$ ]

The spectrum presented in Fig.30 was obtained over a 4-hour period, 17 days after the irradiation phase. The photopeak at 53.44 keV originating from the decay of  $^{73}\text{As}$  is clearly visible. Again,  $^{73}\text{As}$  is produced both by  $^{73}\text{Ge}(p,n)$  and by  $^{72}\text{Ge}(p,\gamma)$ , since a 1.36% fraction of  $^{72}\text{Ge}$  contamination is present in this target. Of course the contribution of the  $^{72}\text{Ge}(p,\gamma)$  reaction is expected to be negligible since (p,n) reactions usually have much larger cross sections than radioactive captures, but comparison with data from T[ $^{72}\text{Ge}$ ] will allow to explicit this contribution.

The gamma rays at 595.83 and 634.78 keV, coming from the radioactive decay of  $^{74}\text{As}$  produced by  $^{73}\text{Ge}(p,\gamma)$ , are also visible in Fig.30. The linear scale has been used to facilitate the reading of the most intense peaks since the daughter nucleus of  $^{74}\text{As}$  undergoes many energy level transitions during its deexcitation

process. Part of this complex decay scheme is displayed in Appendix.D.4. All the other transitions observed in the spectrum were attributed to isotopic or background contaminants, except for the transition at 477.42 keV which could not be explained by the background contribution. After further investigation [61], it was found that this peak originates from the decay of  ${}^7\text{Be}$ , produced through the  ${}^7\text{Li}(p,n){}^7\text{Be}$  reaction, which has a half-life compatible with the measurement. Indeed, just before the production of the T[ ${}^{73}\text{Ge}$ ] target by thermal evaporation, a Li target was produced in the same chamber, explaining the presence of residues inside it.

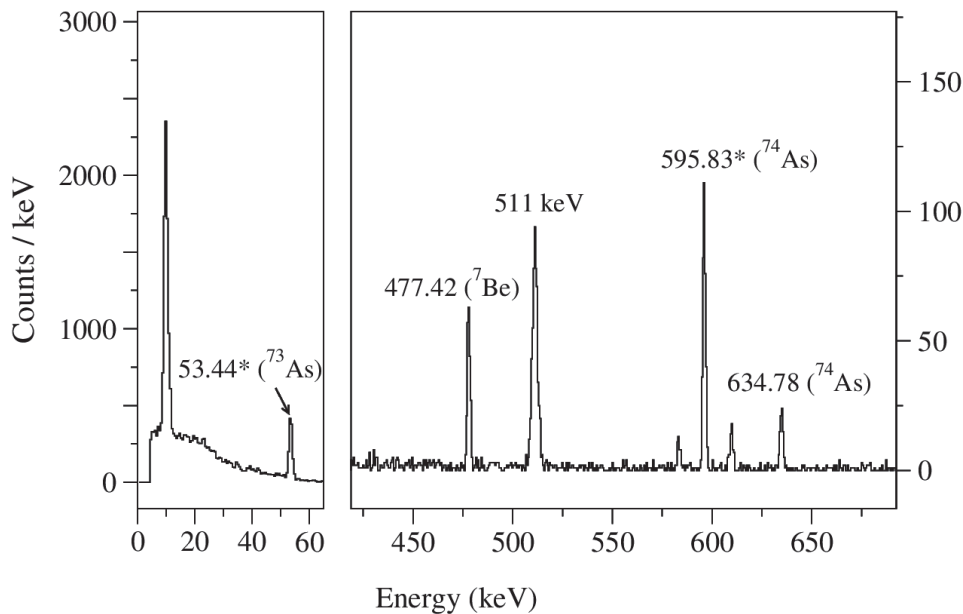


Figure 30: Calibrated energy spectrum of the target T[ ${}^{73}\text{Ge}$ ]. The photopeaks with a star were used for the calculation of reaction cross sections. Note the different scale for a same spectrum. The decay schemes of the  ${}^{73}\text{As}$  and the  ${}^{74}\text{As}$  can be seen in Appendix.D.

## 5.2.4 Conclusion

From the spectra presented above, we see that five reactions can be studied in this experiment :  ${}^{70}\text{Ge}(p, \gamma){}^{71}\text{As}$  (in two different targets),  ${}^{76}\text{Ge}(p, n){}^{76}\text{As}$ ,  ${}^{72}\text{Ge}(p, \gamma){}^{73}\text{As}$ ,  ${}^{73}\text{Ge}(p, \gamma){}^{74}\text{As}$ , and  ${}^{73}\text{Ge}(p, n){}^{73}\text{As}$ . The next step to obtain the corresponding cross sections will be to determine the decay curves from which the  $N_0$  parameter will be deduced. In order to obtain the activity curve of these four radionuclides of interest, a list of the gamma transitions previously selected for their highest possible branching ratios and well separated decay transition is summarized in Table 5.

Radionuclide	$E_\gamma$ [keV]	$I_\gamma$ [%]	$t_{1/2}$ [d]
$^{71}\text{As}$	174.954(5)	82.4(20)	2.720(11)
$^{76}\text{As}$	559.10(5)	45.0	1.094(0.7)
$^{73}\text{As}$	53.437(9)	10.6(11)	80.30(6)
$^{74}\text{As}$	595.83(8)	59.0(3)	17.77(2)

Table 5: Radionuclides and their corresponding gamma transitions selected for the reconstruction of their decay curves. ( $E_\gamma$ ) is for the detecting  $\gamma$ -ray, ( $I_\gamma$ ) for the  $\gamma$ -ray intensity and ( $t_{1/2}$ ) for their respective half-life. The information from column 2 to 4 are extracted from NNDC [4].

### 5.3 Detector efficiency

The efficiency of a detector represents its ability to detect and register the radiation emitted by a source. In an experiment, the photopeak efficiency curve is essential to estimate the ratio of fully detected particles to the actual number of incident particles at a given energy. This photopeak efficiency  $\epsilon$  can be determined using a radioactive source of known activity via the well known equation :

$$\epsilon = \frac{N_{peak}}{A \cdot I_\gamma \cdot t_{run}} \quad (27)$$

where  $N_{peak}$  corresponds to the integral of the considered photopeak,  $A$  is the activity of the source in [ $\text{s}^{-1}$ ],  $I_\gamma$  the reference or tabulated intensity of the observed gamma (also called branching ratio) and  $t_{run}$  the acquisition run time in [s]. In an activation experiment, the primary objective is to determine the activity of the radioactive source accurately. The efficiency must therefore be determined by measurements on calibrated radioactive sources whose activity is known. Consequently, measurements were performed using five  $\gamma$ -emitting radioactive sources of  $^{57}\text{Co}$ ,  $^{152}\text{Eu}$ ,  $^{241}\text{Am}$ ,  $^{137}\text{Cs}$  and  $^{133}\text{Ba}$  with well known branching ratios in the initial geometry shown on Fig.24.

An experimental efficiency curve has been obtained from these measurements but had to be carefully analyzed to account for certain corrections. Indeed, during the data acquisition process, detection can be affected by the inherent

phenomena of random and coincidence summing [63]. The random summing effect is particularly pronounced at high counting rates, where the detector experiences an elevated in-flux of particles. This leads to the phenomenon of pile-up, whereby the detector is unable to resolve the individual interactions of particles in a timely manner. As a consequence, valuable information may be lost or distorted impacting the accuracy of the measurements. But this effect does not impact our experiment, when the counting rate is moderate.

The coincidence summing instead, occurs with radionuclides emitting two or more cascading photons within the resolving time of the spectrometer. As an example, if a first photon spends its total energy in the germanium crystal and if a second photon is also detected, a sum pulse is recorded and the event is lost from the full energy peak of each of the two photons. The probability of experiencing summing effects rises as the distance between the source and detector decreases. Additionally, the presence of large active volumes can further amplify this phenomenon. These effects are particularly significant when dealing with low-activity sources [64]. In order to study the impact of coincidence summing on our efficiency curve, Monte Carlo simulations reproducing the fully decay schemes have been used. The detector geometry and the five radioactive sources were simulated using the PENELOPE(2018) code [48] as well as the SToGS-GEANT4 (Simulation toolkit fOr Gamma-ray Spectroscopy) simulation package [49].

### 5.3.1 Geometry simulation via PENELOPE(2018) and GEANT4

The geometry and decay schemes of the various radioactive sources were simulated and validated using the two widely employed tools for particle-matter interaction simulations. An example of simulated spectra by these tools is illustrated in Fig.31 for a  $^{152}\text{Eu}$  source. The obtained spectra from both GEANT4 and PENELOPE exhibit good agreement, showing accurate alignment and maintaining compliance with the expected decay and branching ratios of the photopeaks. The PENNUC subroutines, responsible for simulating the decay pathways of radioactive sources in PENELOPE, have undergone extensive testing in the past, specifically on nuclides with complex spectra, for instance in the paper of García-Toraño *et al.*[65]. These simulations have demonstrated good agreement with metrology measurements, solidifying PENELOPE as a reliable tool for simulating decay processes. Based on these verifications, we made the decision to exclusively process the data from PENELOPE in order to correct the coincidence summing effects.

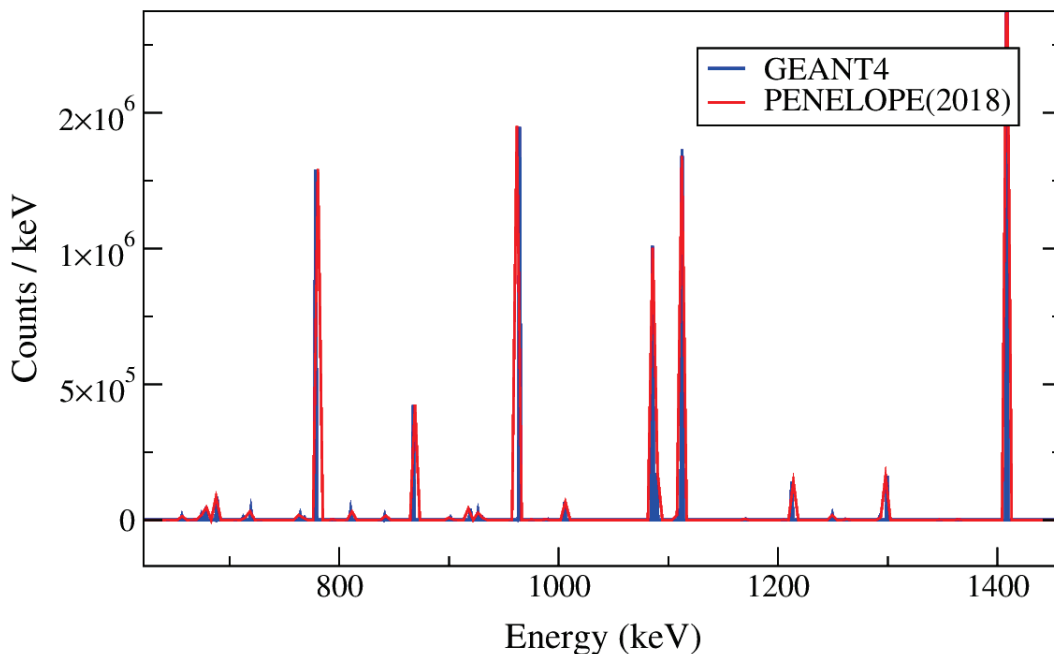


Figure 31: Comparison of two decay spectra from a  $^{152}\text{Eu}$  punctual source after 10 million decays and assuming an isotropic emission. The blue spectrum is obtained from the GEANT4 simulation, while the red spectrum is obtained from the PENELOPE simulation.

Before introducing the simulation results, it is useful to provide a detailed description of the experimental setup implemented in the code. This will help in better understanding any deviations or anomalies that may arise when compar-

ing the experimental and simulated data. The Fig.32 illustrates a schematic representation of the implemented geometry in the codes, showcasing the cylindrical configuration of the detection device as previously shown in Fig.24.

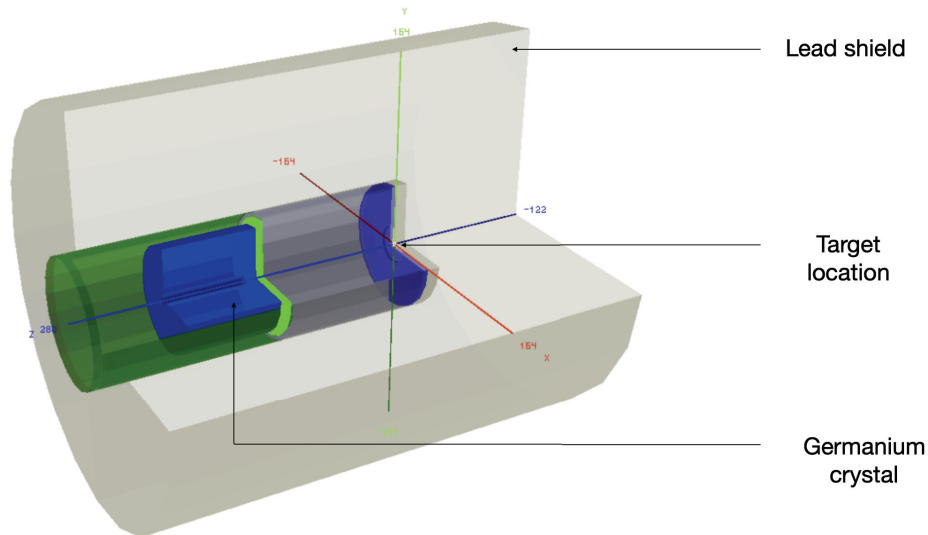


Figure 32: Schematic view of the geometry implemented in the PENELOPE and GEANT4 software tools.

The germanium detector is enclosed within a lead shield that belongs to the Packard range of the Canberra brand. The exact model was not known at the time of data analysis, however all shields of the Packard range appear to have similar characteristics. They consist of a layer of 9.5 mm steel, 100 mm lead, 1 mm tin, and 1.5 mm copper from the outside to the inside of the shield respectively. Only the lead layer is visible on Fig.32, but all these materials were incorporated into the geometry of the simulations. It is worth specifying that we did not have precise knowledge of the dimensions of the interior of the shield. Therefore, the distance between the detection device and the lead shield was set in a reasonable manner. Additionally, for the sake of simplicity, the lead shield was simulated as a fully cylindrical shape, without reproducing the visible dome shown in the picture of Fig.23.

### Missing radioactivity in primary simulations

Lead is commonly composed of stable isotopes, but it can also contain radioactive isotopes such as  $^{210}\text{Pb}$ , which may have an impact on experimental mea-



surements. For this reason, most Canberra lead shields can be purchased and guaranteed by the manufacturer to have a radioactivity level below 50 Bq/kg. Due to this particularity, we encountered two types of obstacles during the simulations. The first was the lack of knowledge about the shield's radioactivity during the measurements. The second obstacle was a restriction encountered in the PENELOPE software which does not allow the use of radioactive materials in the geometry implementation. For this reason, all simulated spectra of radioactive sources exhibited a deficiency of low-energy photons between 0 and 400 keV.

### Simulation of missing radioactivity

To address the limitations related to material definition in Penelope, a solution was implemented by replacing the use of a radioactive material with a volumetric radioactive source positioned inside the lead shield. This modification enabled us to obtain a spectrum that faithfully reproduces the contributions of decay products from lead for the particular cylinder being studied. Although the resulting radioactivity is lower compared to considering the entire lead shield, this should not impact the shape of the obtained spectrum, particularly when simulating a large number of decays (in our case 10 million). The primary influence on the spectrum arises from the counting rate rather than the volumetric characteristics. The resulting spectrum is visible in Fig.33 and is compared to an experimental background spectrum acquired during 20 hours. Note that the displayed red histogram includes all the decay chain originating from  $^{210}\text{Pb}$ .

### Incorporating missing radioactivity

By comparing the shapes of these spectra, it becomes possible to estimate the contribution of lead radioactivity to the background. It is noteworthy that the spectra exhibit a striking similarity between 70 keV and 400 keV. This suggests that a portion of the low-energy background noise could be attributed to the radioactivity of  $^{210}\text{Pb}$ . The analysis of the most intense peaks in the background predominantly attributes their origin to the most abundant radioactive elements in the Earth crust. These elements include uranium, thorium, potassium, bismuth, as well as their decay products. They were present in the walls of the room where the measurements were conducted. More specifically, we identified the 609 keV and 1120 keV gamma rays originating from  $^{214}\text{Bi}$ , the 1460 keV gamma rays from  $^{40}\text{K}$ , the 338 keV, 794 keV, 911 keV, and 698 keV gamma rays

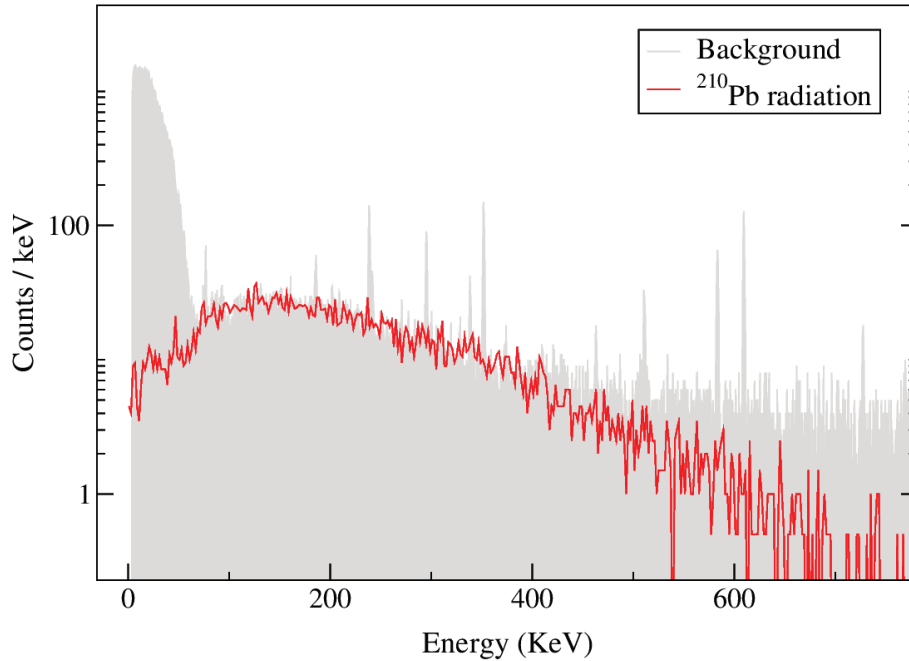


Figure 33: Simulated spectrum of a  $^{210}\text{Pb}$  source after 10 million decays (in red) compared to an experimental background acquired over a period of 20 hours (in grey). In the simulation, the radioactive lead source was placed inside the lead shield and close to a lead wall facing the germanium detector.

from  $^{228}\text{Ac}$  (a descendant of  $^{232}\text{Th}$ ), among others... However, the significance of  $^{210}\text{Pb}$  radioactivity should not be overlooked in our simulations due to its contribution at low energies. To overcome the limitation of the PENELOPE software not considering material radioactivity, we incorporated the contribution of  $^{210}\text{Pb}$  from the volumetric source simulations into the spectra obtained from PENELOPE. This was done for the sake of simplicity and in order to include the effect of radioactivity in the analysis. To achieve this, we adjusted the assumed  $^{210}\text{Pb}$  activity in order to fit the background spectrum. Then, the  $^{210}\text{Pb}$  contribution per bin was normalized by a factor dependent on the respective acquisition times of the radioactive sources. These counts were finally added to the existing PENELOPE spectra for each source. The presented results will therefore include two major simulations : one without the contribution of radioactive lead and another one which takes into account this contribution.

### 5.3.2 Results of simulations

The comparison of the simulated spectra versus the experimental spectra was performed for five radioactive sources. The spectra related to  $^{57}\text{Co}$  are shown

in Fig.34, while the four other are available in Appendix.E.1.

Overall, the simulations carried out with PENELOPE accurately reproduce the expected gamma and X-rays associated to the decay scheme of each radioactive source. In the software, this part is entirely allocated to the PenNuc subroutine, which directly uses the information from the ENSDF (Evaluated Nuclear Structure Data File) database obtained from NNDC [4]. It was crucial for us to verify the branching ratios of the different photopeaks in order to closely reconstruct the summing effects that may have occurred experimentally. By incorporating this database information into the simulation process, PenNuc ensures that the simulated spectra closely match the experimental spectra.

From the standpoint of Compton scattering, PENELOPE simulations appear to underestimate the background contribution, although this tendency is less pronounced in simulations incorporating lead radioactivity. In Fig.34, the background around 50 keV is well reproduced with the addition of lead contribution, but it is not the case around 130 keV. While these effects seem to balance out in this particular figure, it becomes evident from all other spectra in appendix that the radiation from  $^{210}\text{Pb}$  significantly contributes to reproducing the low-energy background.

However and despite these efforts, we were not able to perfectly replicate the experimental spectra, likely due to multiple reasons. We contemplated whether the use of a point source instead of a volumetric source in the PENELOPE geometry had an impact on our predictions, particularly due to the small modification of the solid angle. The studies in Appendix.E.2 and E.3 suggested that it was not the case. It finally appears that the simplifications made in the implemented geometry as well as the manually added lead radioactivity further account for the observable differences in our spectra.

Nevertheless, these differences did not impact our investigation of summing effects, as our primary objective was to obtain representative decay schemes comparable to experimental observations. Utilizing the obtained results, we determined the number of photons detected in each specific photopeak by subtracting the background contribution. To assess whether the peak areas were affected by coincidence summing effects, another set of PENELOPE simulations was conducted. In this case, the same geometry was used, but without realistic radioactive sources to exclude any complex decay cascades. Instead, mono-energetic simulations were performed, where only gamma rays at one precise energy were sent to the detector one by one. By doing so, these new simu-

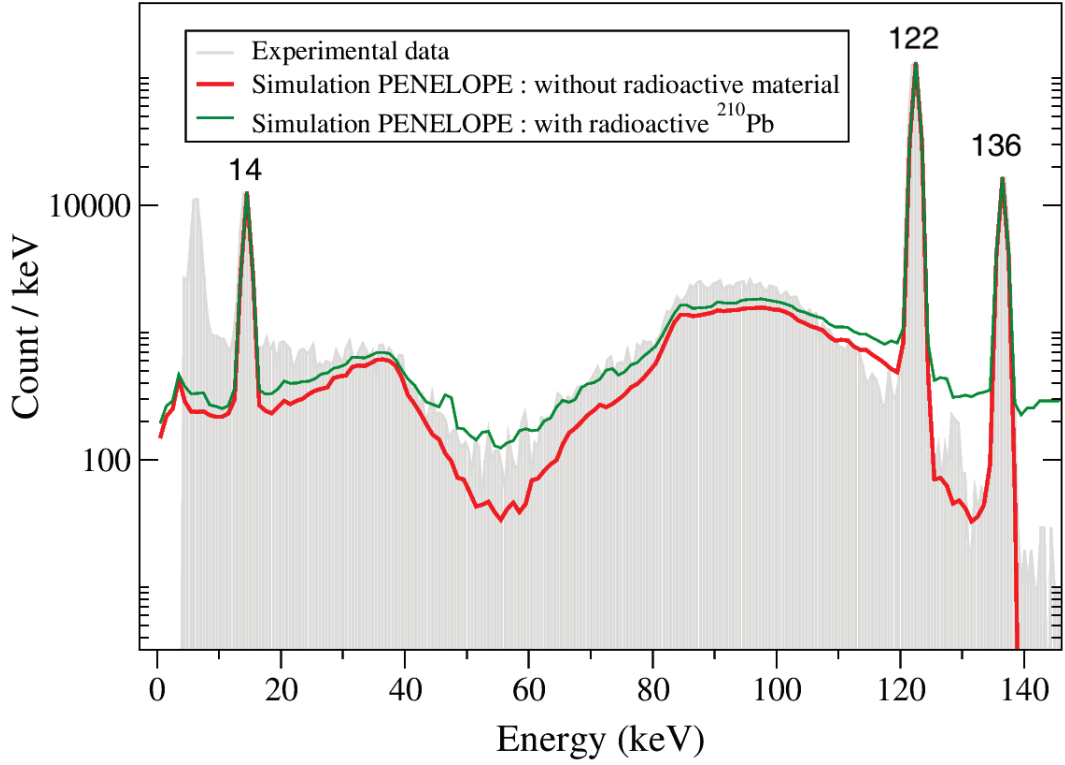


Figure 34: Comparison of the  $^{57}\text{Co}$  experimental spectrum acquired in October 2017 with two simulated spectra obtained after 10 million decays. The experimental data are rescaled on the PENELOPE data using the peaks at 122 keV.

lations eliminated any potential gamma addition effects that can occur when using a radioactive target. Once all the mono-energetic efficiencies were obtained and compared to the results from decay cascades, a correction coefficient could be derived through a simple ratio for each analyzed photopeak of interest :

$$F_{correction} = \frac{\epsilon_{mono}}{\epsilon_{cascade}} \quad (28)$$

For both cascade simulations and mono-energetic simulations, the gamma rays from lead were not considered. This detail was not a drawback as the ratio was simply calculated between consistent simulations conducted under the same conditions.

On average, the obtained correction coefficients were around 1.04 as illustrated on Fig.35, indicating a slight predominance of "out" summing (photon losses) compared to "in" summing (photon gains) in our peaks. This mean correction corresponds to approximately 4.04% in percentage, with a highest correction

observed at 17.45 % for cesium at an energy of 36 keV (point above 1.2 in Fig.35).

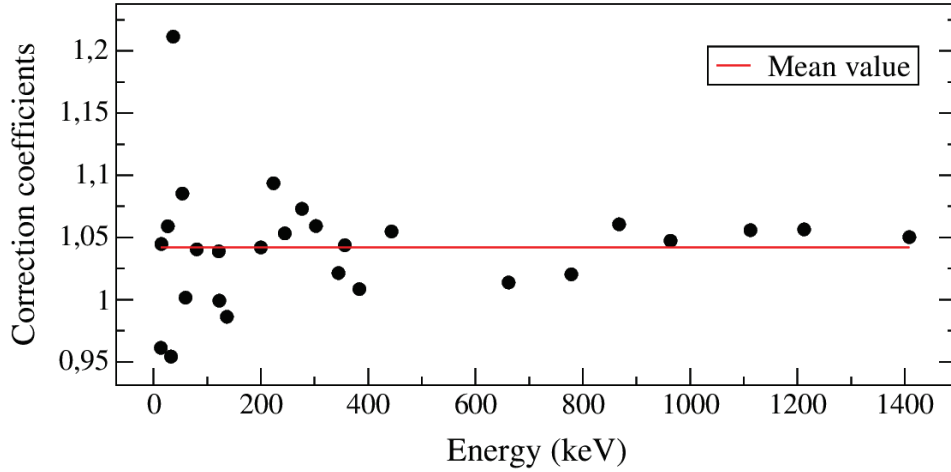


Figure 35: Results of the 27 coefficients obtained (using equation (28)) to correct the measured HPGe efficiency from the summing effect. The red line represents the average associated with these data points.

### 5.3.3 Efficiency curve

The experimental efficiencies were modified to plot a new curve of corrected efficiency. All the data points related to  $^{57}\text{Co}$ ,  $^{137}\text{Cs}$ ,  $^{152}\text{Eu}$ , and  $^{241}\text{Am}$  aligned well except for  $^{133}\text{Ba}$ . For this particular source, the seven measured data points were consistently below the trend established by the other data points. After ruling out possible timing errors in the experimental runs, a systematic error from the reference activity of the source was identified as the plausible cause for this deviation. To address this issue, the barium measurements were rescaled using the measurements performed on europium. Specifically, the  $^{152}\text{Eu}$  source has gamma emissions at 344 keV, which were used to rescale the point at 356 keV from  $^{133}\text{Ba}$ . The final efficiency curve used for this activation experiment was finally obtained and was fitted using one of the most suitable functions for germanium detectors [66]. This efficiency curve is shown in Fig.36 together with the parameters found (and their uncertainties) and the optimal  $\chi^2$  obtained.

The manufacturer-provided efficiencies are given for a source-to-detector distance of 2.5 cm. In our case, the measurements were conducted at a distance of 12 cm. Due to this difference, direct comparison becomes challenging. However, FWHM is closely related to the efficiency of a detector. Indeed, a detector

with better energy resolution can effectively distinguish between different particle energies, leading to improved detection efficiency. Based on the observed FWHM values, it could be inferred that the detector's efficiency has remained relatively stable over the past four years. But it is important to acknowledge that other factors, including detector geometry, background effects, and overall experimental conditions, might have had an impact on the experimental results.

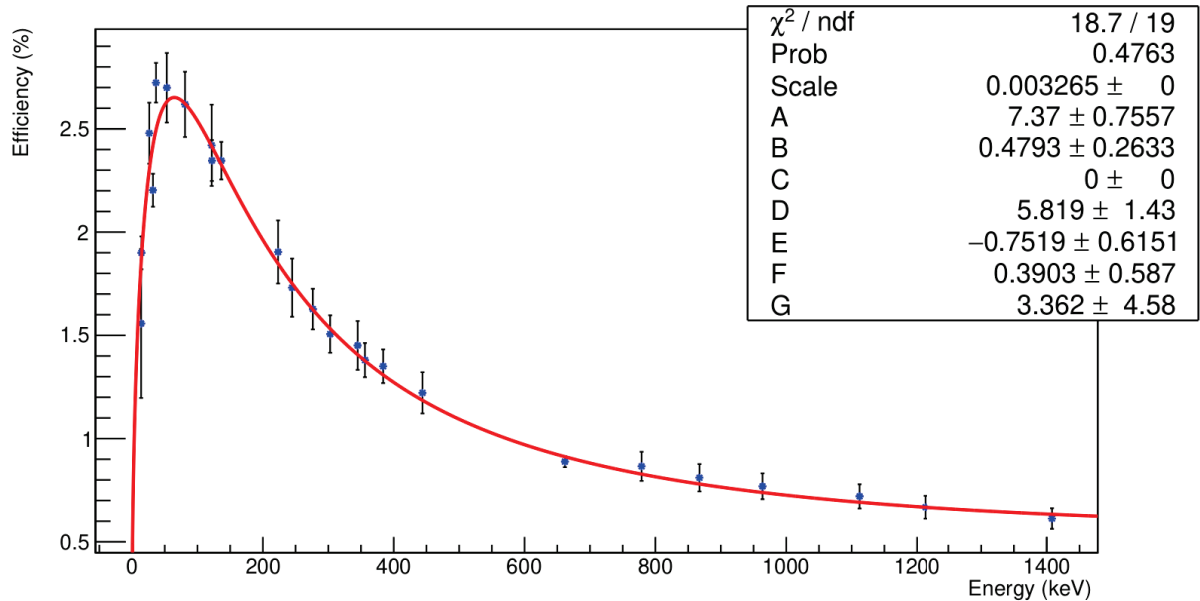


Figure 36: Absolute efficiency curve of the germanium detector employed in the measurement.

The summing correction technique used in this work has already been used in the past and have be studied in more detail in the articles of García-Toraño et al.[63] and Arnold et al.[67].

## 5.4 Activity measurements

The activities of the irradiated germanium targets were estimated using equation (27) and data from Table 6. The photopeak energy used for measurements are indicated in column five of the table, and their respective intensities are in column six. Each data acquisition run lasted either 30 minutes or 4 hours. This process involved counting the gamma rays emitted during a minimum duration of 3 days and a maximum duration of 54 days, resulting in a lengthy data acquisition time. In total, six activity curves were obtained, two of which are shown in Fig.37, and the remaining four are shown in Appendix.F.

The activities were fitted with the well-known activity equation :

$$A_r(t) = A_0 e^{-\lambda t} \quad (29)$$

where the quantity  $A_r$  represents the activity of the radioactive nuclei remaining at a given time,  $A_0$  the activity at  $t=0$ ,  $\lambda$  the decay constant (related to the half-life by :  $\lambda = \ln(2)/(t_{1/2})$ ) and  $t$  the elapsed time since the end of irradiation. To adjust the curve, the TF1 class of the ROOT software [68] has been used with the expression " $[0]*\exp(-[1]*x)$ ",  $[0]$  and  $[1]$  being the parameters to adjust. For each experimental activity plot, two fits are shown : a green one is obtained by setting both  $A_0$  and  $\lambda$  as free parameters, and a red fit is obtained by fixing the value of  $\lambda$  based on the half-life from the NUDAT database [4]. Each fitting procedure provides its own set of optimal parameters  $A_0$  and  $\lambda$ .

Target	Radionuclide	$t_{wait}$ [hrs]	$t_{count}$ [d]	$E_\gamma$ [keV]	$I_\gamma$ [%]	$t_{1/2}$ [d]
T[Ge <sub>nat</sub> ]	<sup>71</sup> As	6.694(1)	5.789(1)	174.954(5)	82.4(20)	2.720(11)
T[Ge <sub>nat</sub> ]	<sup>76</sup> As	6.694(1)	2.782(1)	559.10(5)	45.0	1.094(0.7)
T[ <sup>72</sup> Ge]	<sup>73</sup> As	3.455(1)	55.85(1)	53.437(9)	10.6(11)	80.30(6)
T[ <sup>72</sup> Ge]	<sup>71</sup> As	3.455(1)	4.22(1)	174.954(5)	82.4(20)	2.720(11)
T[ <sup>73</sup> Ge]	<sup>73</sup> As	55.65(1)	53.84(1)	53.437(9)	10.6(11)	80.30(6)
T[ <sup>73</sup> Ge]	<sup>74</sup> As	55.65(1)	53.84(1)	595.83(8)	59.0(3)	17.77(2)

Table 6: Decay parameters of the six studied radionuclides. ( $t_{wait}$ ) is for the waiting time at the end of irradiation, ( $t_{count}$ ) for the counting time, ( $E_\gamma$ ) for the detecting  $\gamma$ -ray, ( $I_\gamma$ ) for the  $\gamma$ -ray intensity and ( $t_{1/2}$ ) for the half-life. The information from column 5 to 7 are extracted from NNDC [4].

The two decay curves in Fig.37 were obtained for the same radionuclide, <sup>73</sup>As. Its half-life is estimated in NUDAT to be  $80.3 \pm 2.72$  days, corresponding to a decay constant value of  $\lambda = 9.991 \times 10^{-8} \text{ s}^{-1}$ . In this study, we estimated a decay constant of  $\lambda = 1.072 \times 10^{-7} \text{ s}^{-1}$  from target T[<sup>72</sup>Ge] and  $\lambda = 1.339 \times 10^{-7} \text{ s}^{-1}$  from target T[<sup>73</sup>Ge].

In the first case, our results are consistent with the reference data within the error bars, yielding a half-life of approximately  $74.84 \pm 4.49$  days. However, for the second case, we obtained a significantly different value of approximately  $59.91 \pm 1.99$  days. Several factors could explain this discrepancy. As can be seen



on Fig.37, for T[<sup>72</sup>Ge] (top), the statistics are lower with fewer acquired data points, and most of the run times were 30 minutes. For the T[<sup>73</sup>Ge] (bottom), the counting is higher, and the acquisition times per run were generally 4 hours. But we also noticed an unusual shift in the data around  $2500 \times 10^3$  s, indicating a possible alteration in the solid angle during the activity measurement. This observation suggests that the same effect might have also occurred for T[<sup>72</sup>Ge]. Consequently, a systematic error probably affected the obtained values.

For all our decay curves, we compared the obtained half-lives with those reported in other works. For <sup>71</sup>As, <sup>74</sup>As, and <sup>76</sup>As, more than ten references consistently agree on the measured half-lives, and our measurements are in good agreement with these referenced values.

For <sup>73</sup>As on the other hand, only two references provide clear results. One is from 1972 [69] (used in NUDAT) giving  $t_{1/2} = 80.3 \pm 0.06$  days, and another one is from 2008 [70], reporting a half-life value of  $62 \pm 23.8$  days. In view of this situation, a new and more accurate measurement of the <sup>73</sup>As lifetime is desirable. However, our data set does not allow to provide such reliable measurement due to the fluctuations in the activity curve mentioned above. For this reason, we finally decided to use consistently the half life values recommended by NUDAT for the analysis of all our decay curves.

In order to determine the reaction cross-section, it is necessary to find the number  $N_0$  of arsenic nuclei produced immediately after irradiation at time  $t=0$  (see equation 23). This number can be obtained from the activity curves using the relationship :  $N_0 = A_0/\lambda$ . The uncertainties on  $A_0$  provided by the ROOT fits as well as the uncertainties on  $\lambda$  have been propagated to  $N_0$ . Moreover, we also accounted for the discrepancy between our experimentally derived decay constant and  $\lambda$  value from NUDAT in accordance to the previous discussion. Overall, these errors impacted the quantity  $N_0$  from 0.4% to 6%.



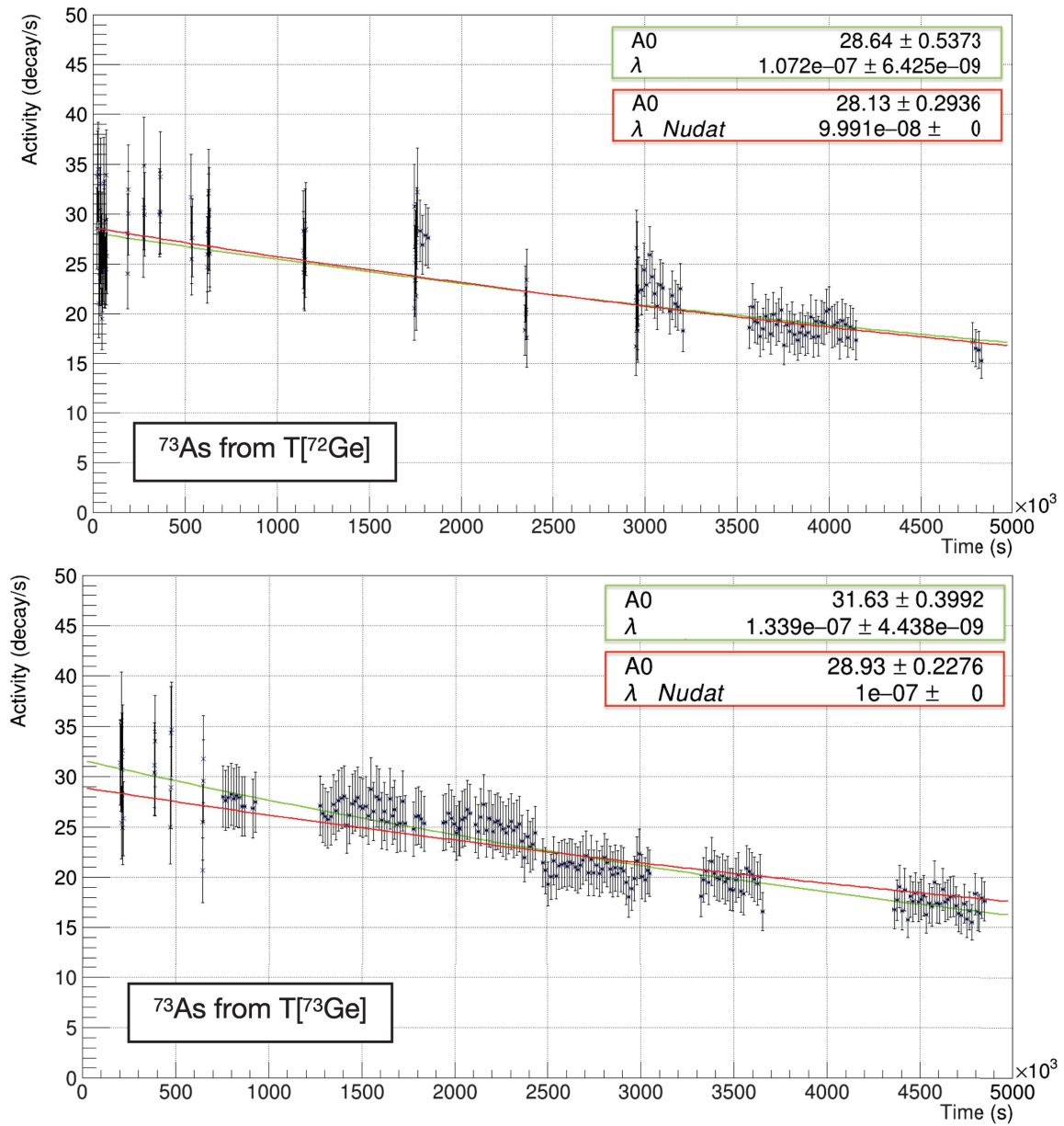


Figure 37: Experimental activity curves obtained for  $^{73}\text{As}$  and produced in two different targets. Activities with large error bars represent acquisition times of 30 minutes, while smaller error bars represent 4 hours acquisition times. The green curves correspond to fits with two free parameters  $A_0$  and  $\lambda$  while the red curves correspond to fits with one free parameter  $A_0$  and one parameter  $\lambda$  fixed to the NUDAT value.

## 6 RESULTS AND DISCUSSION

### 6.1 Determination of Cross Sections and S-Factors

The primary objective of this study was to analyze the cross sections of critical reactions involved in the production of the lightest p-nucleus, which is  $^{74}\text{Se}$ . Specifically, the aim was to measure the crucial  $^{72}\text{Ge}(p, \gamma)^{73}\text{As}$  reaction. It was also planned to make a second measurement of  $^{70}\text{Ge}(p, \gamma)^{71}\text{As}$  for comparison with previous results, and to determine the unknown  $^{73}\text{Ge}(p, n)^{73}\text{As}$  cross section in order to correct the  $^{72}\text{Ge}(p, \gamma)^{73}\text{As}$  reaction from its contribution. In addition, our data allowed a first measurement of  $^{73}\text{Ge}(p, \gamma)^{74}\text{As}$  and a new measurement of  $^{76}\text{Ge}(p, n)^{76}\text{As}$  cross sections. The Fig.38 provides an overview of all the measured reactions in this study, depicted in green. The red arrows highlight the crucial pathway reactions for the production of  $^{74}\text{Se}$  as introduced in this chapter.

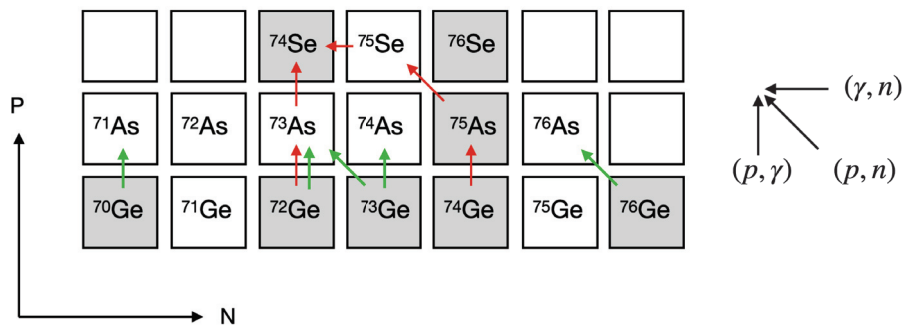


Figure 38: Resume in green of various reaction cross sections measured in this work. The red arrows indicate the major channels contributing to the formation of  $^{74}\text{Se}$ . Nuclei depicted in a light gray background are stable, while those in white are unstable.

All reaction cross sections were calculated using the equation (23). However, it should be noted that the radionuclide  $^{73}\text{As}$  was produced by both the reactions  $^{73}\text{Ge}(p, n)$  and  $^{72}\text{Ge}(p, \gamma)$  in two targets,  $\text{T}[^{72}\text{Ge}]$  and  $\text{T}[^{73}\text{Ge}]$ . In order to distinguish their mutual contribution, we employed a system of equations using an approximation of the formula (23) by neglecting the contribution associated with the decay of the radionuclide during the irradiation time, which is justified by the long half-life (80.3 days) of  $^{73}\text{As}$ .

$$\begin{aligned}
& \left. \begin{aligned} N_{\text{target}_{72 \rightarrow [72]}} \cdot \sigma_{72} \cdot N_{\text{inc}_{[72]}} &= N_{0_{72 \rightarrow [72]}} \\ N_{\text{target}_{73 \rightarrow [72]}} \cdot \sigma_{73} \cdot N_{\text{inc}_{[72]}} &= N_{0_{73 \rightarrow [72]}} \end{aligned} \right\} \text{Target: T}[^{72}\text{Ge}] \\
& \left. \begin{aligned} N_{\text{target}_{73 \rightarrow [73]}} \cdot \sigma_{73} \cdot N_{\text{inc}_{[73]}} &= N_{0_{73 \rightarrow [73]}} \\ N_{\text{target}_{72 \rightarrow [73]}} \cdot \sigma_{72} \cdot N_{\text{inc}_{[73]}} &= N_{0_{72 \rightarrow [73]}} \end{aligned} \right\} \text{Target: T}[^{73}\text{Ge}]
\end{aligned} \tag{30}$$

For each target, each row represents the contribution from either the reaction  $^{73}\text{Ge}(p, n)$  or the reaction  $^{72}\text{Ge}(p, \gamma)$ . The simplified notation " $72 \rightarrow [72]$ " indicates that the  $^{72}\text{Ge}$  nuclei are considered in the target  $\text{T}[^{72}\text{Ge}]$ , and so on. The notation  $\sigma_{72}$  represents the cross section for the  $^{72}\text{Ge}(p, \gamma)$  reaction, and  $\sigma_{73}$  for the  $^{73}\text{Ge}(p, n)$  reaction.  $N_{0_{72}}$  denotes the number of  $^{73}\text{As}$  produced by  $^{72}\text{Ge}(p, \gamma)$  and  $N_{0_{73}}$  the number of  $^{73}\text{As}$  nuclei produced by  $^{73}\text{Ge}(p, n)$ .

By combining the equations of each target, we obtained a system of two equations as follows :

$$\begin{aligned}
& (N_{\text{target}_{72 \rightarrow [72]}} \cdot \sigma_{72} \cdot N_{\text{inc}_{[72]}}) + (N_{\text{target}_{73 \rightarrow [72]}} \cdot \sigma_{73} \cdot N_{\text{inc}_{[72]}}) = (N_{0_{72 \rightarrow [72]}}) + (N_{0_{73 \rightarrow [72]}}) \\
& \underbrace{(N_{\text{target}_{73 \rightarrow [73]}} \cdot \sigma_{73} \cdot N_{\text{inc}_{[73]}})}_{\text{known}} + \underbrace{(N_{\text{target}_{72 \rightarrow [73]}} \cdot \sigma_{72} \cdot N_{\text{inc}_{[73]}})}_{\text{known}} = \underbrace{(N_{0_{73 \rightarrow [73]}}) + (N_{0_{72 \rightarrow [73]}})}_{\text{known sum}}
\end{aligned} \tag{31}$$

In this system, most of the quantities involved are available experimentally, and particularly the total  $N_0$  values. These last provide the total number of  $^{73}\text{As}$  nuclei obtained in each target for all the combined reactions. Knowing this, the cross sections become the only unknowns in these lines, so we have a system of two equations with two unknowns which can be easily solved :

$$\begin{aligned}
a \cdot \sigma_{72} + b \cdot \sigma_{73} &= c \\
d \cdot \sigma_{73} + e \cdot \sigma_{72} &= f
\end{aligned} \tag{32}$$

Through this analysis, we were able to accurately measure the cross sections of the  $^{73}\text{Ge}(p, n)$  and  $^{72}\text{Ge}(p, \gamma)$  reactions. In more details, we found that 0.61% of the created  $^{73}\text{As}$  nuclei were attributed to the  $^{73}\text{Ge}(p, n)$  reaction in the  $\text{T}[^{72}\text{Ge}]$  target. Similarly, in the  $\text{T}[^{73}\text{Ge}]$  target, we found that 0.68% of the  $^{73}\text{As}$  nuclei came from the  $^{72}\text{Ge}(p, \gamma)$  reaction.

Let us now consider the incident kinetic energy involved in the studied reactions. The proton beam energy of  $E_b = 2.5$  MeV is transformed into the effective center-of-mass energy  $E_{eff,cm}$  which has been calculated for each target at its respective center. The proton energy loss in the target was estimated to be below 12 keV for each of them via the Stopping and Range of Ions in Matter (SRIM) software.

The relative uncertainties of the derived cross sections were obtained by adding quadratically standard deviations on target densities, beam current and  $\gamma$ -counting measurements.

Finally, the astrophysical S-factors were deduced and calculated according to the equation (7). The summary of all these measurements can be seen in Table 7.

Target	Reaction	$E_{eff,cm}$ [MeV]	Cross section [mb]	S-factor [ $\times 10^6$ MeV b]
T[Ge <sub>nat</sub> ]	$^{70}\text{Ge}(p, \gamma)^{71}\text{As}$	2.454(1)	0.972(114)	1.24(15)
T[ $^{72}\text{Ge}$ ]	$^{70}\text{Ge}(p, \gamma)^{71}\text{As}$	2.453(1)	1.251(180)	1.60(23)
T[ $^{72}\text{Ge}$ ]	$^{72}\text{Ge}(p, \gamma)^{73}\text{As}$	2.454(1)	2.023(247)	2.60(32)
T[ $^{73}\text{Ge}$ ]	$^{73}\text{Ge}(p, \gamma)^{74}\text{As}$	2.458(1)	0.243(43)	0.31(5)
T[ $^{73}\text{Ge}$ ]	$^{73}\text{Ge}(p, n)^{73}\text{As}$	2.458(1)	4.197(644)	5.32(82)
T[Ge <sub>nat</sub> ]	$^{76}\text{Ge}(p, n)^{76}\text{As}$	2.457(1)	3.470(411)	4.43(53)

Table 7: Summary of the experimental cross sections and S-factors obtained for the five studied nuclear reactions of interest.

## 6.2 Discussion

### 6.2.1 Cross section sensitivity to particle widths

The results of the present study have been compared to theoretical predictions employing the Hauser-Feshbach formalism through the TALYS 1.961 code [34] (see sub-section 3.4.2). At this stage of the analysis, a common question that arises is how to obtain a good description of the data by adjusting the tunable parameters of the code, and how to quantify the uncertainties in the predictions. Addressing these questions is not a straightforward task, primarily due to the intricate nature of dealing with theoretical uncertainties. Unlike in measurements, where uncertainty quantification is typically achieved using error bars on observable values, theoretical uncertainties pose unique challenges. However,

it is possible to identify various factors that contribute to the overall theoretical uncertainty and discuss them individually. By separating the treatment of input uncertainties, it becomes feasible to gain further insight into the dependencies and their impact on the observed quantities. But it is important to note that this approach relies on the assumption of selecting an appropriate model to accurately capture the underlying physics. In this study, our primary objective is to investigate the cross section as the observed quantity. Our aim will be to provide a comprehensive overview of the essential features inherent to different models used in TALYS, enabling us to analyze their sensitivities, predictions, and uncertainties in detail.

In the Hauser-Feshback framework, when a projectile is captured by the target nucleus, it results in the formation of a compound nucleus that possesses an excitation energy at least equal to the incident kinetic energy (except specific cases). The decay probability of the composite system is represented by its total decay width, which is the sum of partial widths indicating the likelihood of decay through a specific channel. Understanding the sensitivities of the studied reaction cross sections to the various widths is therefore crucial for comprehending the predominant inputs that ultimately influence the final predictions. In 2012, Rauscher *et al.*[35] investigated the sensitivity to different particle width of nucleon,  $\alpha$  and  $\gamma$  induced reactions on nuclei ranging from the proton to neutron drip line, encompassing elements with atomic numbers  $10 \leq Z \leq 83$ . The germanium nuclei under investigation in our study fall within the scope of this research. By leveraging the findings presented in this paper, we obtained deeper insights into the variations observed in the model predictions of cross sections, which allowed us to better understand the fundamental nuclear mechanisms governing the reactions under investigation. Below, we will detail the conclusions drawn from these studies by conducting separate analyses of the (p,n) and (p, $\gamma$ ) reactions.

#### 6.2.1.1 (p,n) reactions

The sensitivity analysis of the cross section for the  $^{76}\text{Ge}(p, n)$  reaction to the neutron, proton, and  $\gamma$ -width is available from the systematic study by Rauscher *et al.*[35] and shown in Fig.39. In this figure, the sensitivity to different widths is expressed by a normalized factor, where a value of 1 and -1 represents the maximum attainable sensitivity (in a simplified manner). The sign of the sensi-

tivity provides additional information about the trend of the observed quantity. If the value is negative, it indicates that the cross section decreases with increasing width, while a positive sign implies that the cross section varies in the same manner as the width.

The observed sensitivities for the  $^{76}\text{Ge}(p, n)$  reaction reveal prominent variations at energies corresponding to the opening of the neutron reaction channel. At 2.5 MeV, the influences of the neutron and gamma widths have become negligible, while the cross section exhibits significant sensitivity primarily to the proton width. This observation is in accordance with theoretical expectations, as the sensitivity is dominated by the smaller width, and in this region the neutron width is much higher than the proton width. The primary factor contributing to the overall theoretical uncertainty is thus associated with the proton-nucleus optical potential. To a lesser extent, it also depends on the characteristics and number of excited states accessible from the compound nucleus. In the cases examined in this study, these states are relatively well-known, highlighting the optical potential as the most influential source of uncertainty.

The sensitivity of the cross section for the  $^{73}\text{Ge}(p, n)$  reaction is presented in Appendix.G. Given the early opening of the neutron channel at 1.13 MeV, the sensitivity of the cross section at the energy of interest is similar to that observed for the  $^{76}\text{Ge}(p, n)$  reaction, and mainly influenced by the proton-nucleus optical potential.

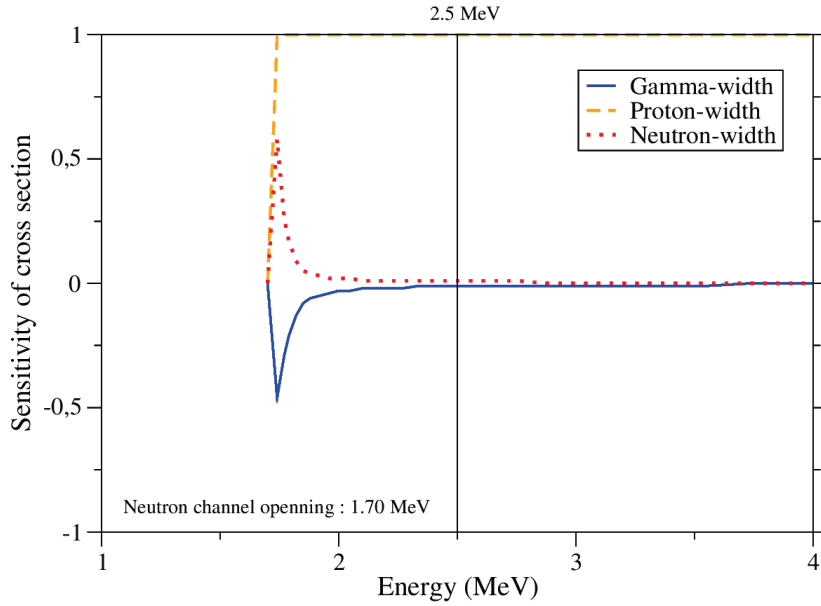


Figure 39: Laboratory cross section sensitivity to the different particle widths for the  $^{76}\text{Ge}(p, n)^{76}\text{As}$  reaction as function of energy. The vertical bar represents the energy investigated in this study. Note that the cross section sensitivity to the proton-width is maximal and equal to 1 above the neutron channel opening and overlaps with the contour of the graph. Theoretical curves extracted from [35].

### 6.2.1.2 (p, $\gamma$ ) reactions

The prevailing assumption when dealing with (p, $\gamma$ ) reaction cross sections is that they are primarily influenced by the  $\gamma$ -channel, while the nucleon-nucleus optical potential has a lesser impact. However, the significance of the optical potential in (p, $\gamma$ ) reactions relevant to the p-process has been the subject of several previous investigations, such as those conducted by [1] and more recently by Vagena *et al.*[71]. In this work, the impact of the optical model will be incorporated into the discussion. This is particularly warranted when considering the significant sensitivity of our three (p, $\gamma$ ) reaction cross sections to the proton- and neutron-widths at 2.5 MeV, as depicted in Fig.40 (but also in Fig.98 and Fig.99 from the Appendix.G). Overall, the cross sections of (p, $\gamma$ ) reactions are predominantly affected by the nucleon-nucleus optical potential, by the photon strength functions ( $\gamma$ -strength) and by the nuclear level density in the target and final nucleus, determining the available transition pathways in both the entrance and exit channels. These results emphasize the importance of experimental measurements conducted at energy values closely corresponding to astrophysical conditions, considering the presence of multiple parameters

that can affect the theoretical predictions.

It is worth noting that nuclear masses play a crucial role in the estimation of cross sections, as they determine the Q-values and separation energies, thereby influencing the relative energies of possible transitions. However, in our case where the nuclei are close to stability, the mass differences are known with exceptionally high precision, resulting in minimal uncertainty introduced into the calculations.

In the figure below, note that the sensitivity to the neutron-width shows a negative trend, exhibiting an opposite behavior compared to the cross section. The curve demonstrates a symmetric shape relative to the sensibility to the  $\gamma$ -width, indicating the competition between decay by gammas or neutrons emission which can also be observed for the (p,n) reactions. This trend is not observed in the other two (p, $\gamma$ ) reactions since the neutron channel is not open in the presented energy range.

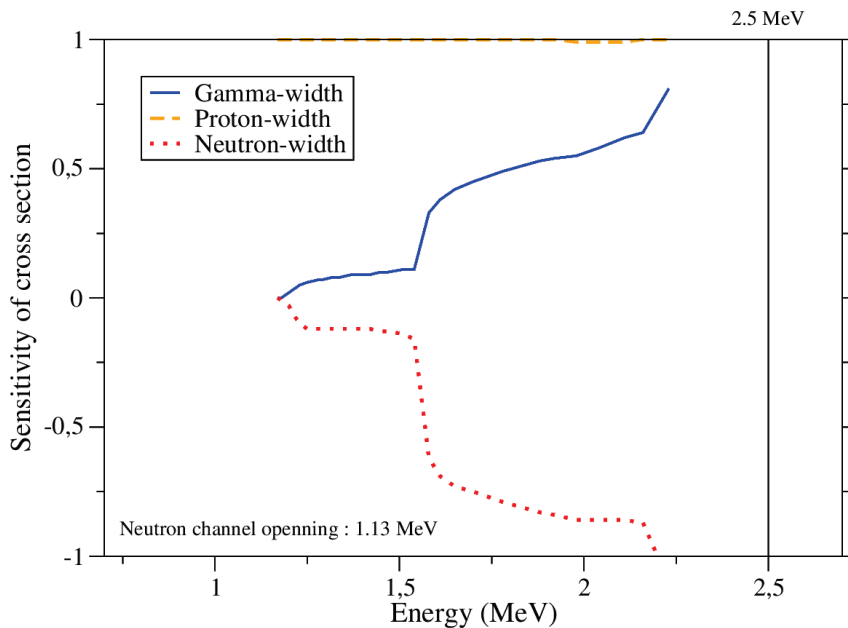


Figure 40: Laboratory cross section sensitivity to the different particle widths for the  $^{73}\text{Ge}(p, \gamma)^{74}\text{As}$  reaction as function of energy. The vertical bar represents the energy investigated in this study. Note that the cross section sensitivity to the proton-width is maximal and overlaps with the contour of the graph. Theoretical curves extracted from [35].

## 6.2.2 Theoretical models implemented in TALYS

The optimization of nuclear parameters in TALYS is a challenging endeavor, particularly when multiple reactions need to be simultaneously adjusted. The



objective of this study is not to conduct an exhaustive optimization of these parameters. Instead, we propose to explore variations in the key nuclear inputs using two different kinds of model combinations, associated with two primary methodologies for modeling nuclear properties : semi-microscopic and phenomenological approaches.

Within the framework of the TALYS code, the optical potential is treated by two main approaches : the Jeukenne-Lejeune-Mahaux (JLM) semi-microscopic approach and the Koning-Delaroche (KD) phenomenological approach. In our analysis, we employed the default parameters of the KD optical potential, while introducing a modified version of the JLM model. This modification specifically involved adjusting the real part of the JLM potential (using the corrective factor *lvadjust* in TALYS) based on recommendations outlined in the paper by Vagena *et al.*[71]. The results of this paper were highly relevant to our study, as their research focuses on improving the semi-microscopic optical potential for low-energy proton-induced reactions relevant for p-process nucleosynthesis. The adjustment (using *lvadjust*) effectively resulted in a satisfactory reproduction of the observed energy dependence in the reactions. In contrast, the imaginary part of the potential remained unaltered as it was recognized to have a smaller impact on adjustment and did not lead to a global improvement of the predictions of the data studied here.

Additionally, we made the decision to investigate an internal parameter of the JLM model, namely the radial matter densities. The radial models based on the Skyrme and Gogny approaches in TALYS employ different functional mathematical forms for the nuclear effective interaction, leading to variations in the predictions of nuclear properties. Considering the significant impact of these differences on the predictions of the optical model potential (OMP), we opted to include two different sets of semi-microscopic models using respectively the Gogny and Skyrme approaches. Consequently, three theoretical models will be used for the comparison with our experimental data. The models that respectively use the phenomenological, Skyrme and Gogny approaches will be referred in the analysis as *TALYS pheno*, *TALYS micro 1*, and *TALYS micro 2* models, see Table 8.

For the construction of the *TALYS pheno* model, the default phenomenological option for the nuclear level density (NLD) and the  $\gamma$ -strength were selected, namely respectively the Constant Temperature + Fermi gas model (CTM) and the Kopecky-Uhl generalized Lorentzian (GLO). For the *TALYS micro 1* and

*TALYS micro 2* models, the two microscopic framework Skyrme-Hartree-Fock-Bogoliubov (Skyrme-HFB) and Gogny-Hartree-Fock-Bogoliubov (Gogny-HFB) were chosen for the NLD and the  $\gamma$ -strength calculations.

Prior to summarise the construction of the different models, it is worth noting a relevant detail. During the simulation analysis, a TALYS bug related to the treatment of collective modes from the nuclear database was encountered. To address this issue, the spherical shape approximation option was utilized after confirming with a TALYS developer that the code did not support deformed nuclei at the time of the processing. For reference, the even-even germanium stable nuclei exhibit a quadrupole deformation of approximately 0.2 according to NNDC[4]. Information on odd-even nuclei are currently not available on the same reference. It should be noted that the spherical approximation made in the constructed TALYS models may introduce additional uncertainties in the predictions and seems difficult to quantify precisely.

Model	nucleon-nucleus OMP	NLD	$\gamma$ -strength	Additional option
TALYS pheno	KD	CTM	GLO	spherical
TALYS micro 1	JLM1 (Skyrme radial model) (lvadjust 0.8)	Skyrme-HFB	Skyrme-HFB	spherical
TALYS micro 2	JLM2 (Gogny radial model) (lvadjust 0.8)	Gogny-HFB	Gogny-HFB	spherical

Table 8: Overview of the three main TALYS models used for comparison purpose with the experimental reaction cross sections. The adopted options are shown from the phenomenological approach and the two microscopical approaches.

### 6.2.2.1 Theoretical uncertainty band

The estimation of theoretical uncertainties in models, as previously discussed, is a critical and challenging task. In the context of our analysis, it is important to consider the uncertainties associated with the selected models. Taking the

Nuclear Level Density (NLD) as an example, TALYS offers six different models, each employing distinct approaches and parameterizations. The variations in predictions among these models provide an initial indication of the systematic errors associated with this parameter. Notably, efforts have been made to address and improve these systematic errors, as demonstrated in the work by Goriely *et al.*[72]. This article undertakes a thorough comparison of the six available nuclear level density (NLD) models in TALYS using experimental data from 42 nuclei. The goal is to identify the model that best describes the experimental observations across the entire dataset. By selecting the most favorable model, it becomes possible to reduce uncertainties associated with NLD predictions. Rather than comparing the chosen model to existing alternatives, the focus shifts towards fine-tuning its internal parameters to achieve an optimal parametrization. This approach transforms the nature of uncertainties from structural to parametric. However, adjusting these uncertainties can be a challenging task that often requires employing Monte Carlo techniques to explore the entire parameter space. While such techniques are currently under development in our research group (see part IV of this thesis), they have not been applied in the present analysis. Therefore, in this study, theoretical uncertainty bands resulting from systematic uncertainties (namely the dependence on the chosen type of model) will be utilized.

For the construction of theoretical bands, the minimum and maximum predictions of the considered OMP, NLD, and  $\gamma$ -strength models were used. It is important to note that these bands, although tending to overestimate the theoretical uncertainties by mixing different kinds of approaches to set extreme predictions, provide a reasonable global view of the model prediction variability. In this regard, the models yielding the maximum and minimum predictions for each OMP, NLD, and  $\gamma$ -strength were selected to estimate the maximum and minimum theoretical cross sections in the energy window of interest. However, it is crucial to emphasize that no theoretical consistency is sought for the model combinations resulting in these limits. The inherent limitations and potential discrepancies in these bands neglect the intricate correlations that may exist within the nuclear properties described by the different input models.

### 6.2.3 Comparison between models and experimental data

---

The results of the present experimental analysis have been compared to theoretical calculations as well as previous experimental data where available. In addition to TALYS studies performed with the TALYS v1.961 [73], NON-SMOKER simulations were extracted from the fully web driven code available in [74] using the available standard options.

The Gamow window that will be indicated on the following plots are taken from the work of Rauscher [75] considering a temperature range of relevance for these studies which is between 2.5 and 3.5 GK.

#### $^{70}\text{Ge}(p, \gamma)^{71}\text{As}$

The two cross sections for the  $^{70}\text{Ge}(p, \gamma)^{71}\text{As}$  reaction measured in this study are depicted in red in Fig.41. They were obtained with the targets T[Ge<sub>nat</sub>] and T[ $^{72}\text{Ge}$ ]. These measurements are compared to the ones previously conducted by Kiss *et al.*[1] in 2007 using the activation technique. In their experiment, they utilized a natural germanium target, which implies that one of our two data points was obtained under the same conditions as in their experiment. The experimental data obtained from this work with the natural germanium target exhibit a very good agreement with the previous results by Kiss, with a deviation of only 3.9% estimated by fitting their data with a third-degree polynomial. The reaction measured in the enriched T[ $^{72}\text{Ge}$ ] however, shows a significant discrepancy of 25.35% compared to Kiss's data. This disparity is attributed to the extremely low isotopic percentage of  $^{70}\text{Ge}$  present in the target (0.29%) increasing the uncertainty of the measurement.

According to the sensitivity curves shown in Fig.98 in Appendix.G, the cross section of this reaction is primarily sensitive to the proton-width, accounting for approximately 62% of the total sensitivity, followed by the  $\gamma$ -width with about 38%. According to the RIPL3 database (which is used by default in TALYS), the discrete levels scheme is completely known up to an excitation energy of 3.91 MeV for  $^{70}\text{Ge}$  nuclei and 1.82 MeV for  $^{71}\text{As}$ , beyond which the discrete levels are replaced by level densities. Adding the condition of known spin and parities, these energies reduce to 2.15 MeV for the  $^{70}\text{Ge}$  nuclei and 0.00 MeV for the  $^{71}\text{As}$ . The missing levels in the  $^{71}\text{As}$ , the daughter nuclei of the reaction, appear to be the largest source of uncertainty in our data. These missing levels can have contributions to both direct and indirect reactions, and their

decay pathways are determined through theoretical modeling, introducing additional uncertainties in the calculations. However, at 2.5 MeV, we observe that all four theoretical models used for comparison are consistent with our data within the error bars. This indicates that the models have been adequately constrained within the framework of the employed approaches. Notably, the existence of giant dipole resonance (GDR) data for  $^{70}\text{Ge}$  nuclei is included in the database, which probably helped in constraining the theoretical predictions.

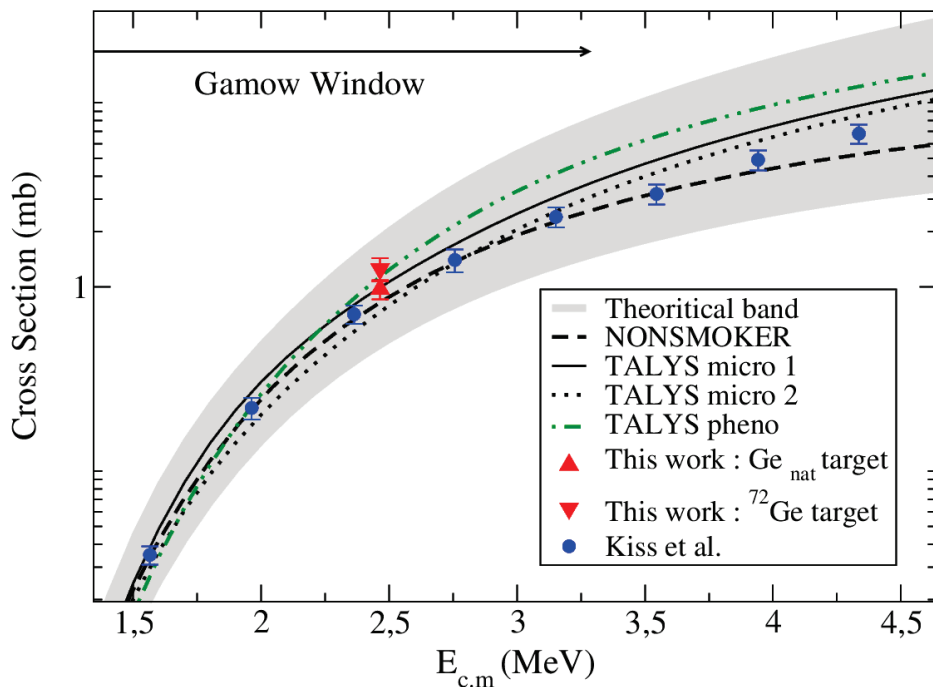


Figure 41: Experimentally measured cross section of the  $^{70}\text{Ge}(p, \gamma)$  reaction (triangles) compared with the experimental data from another work (circles) and the predictions of various theoretical models (lines) that have been adjusted according to specific nuclear parameters.

### $^{72}\text{Ge}(p, \gamma)^{73}\text{As}$

Results regarding the  $^{72}\text{Ge}(p, \gamma)^{73}\text{As}$  reaction are illustrated by Fig.42. An initial measurement was performed by Naqvi *et al.*[53] in 2015, employing the in-beam  $\gamma$ -summing technique on a natural germanium target. Naqvi's measurements can be interpolated to estimate a cross section of about 1.250 mb at 2.5 MeV, whereas our data point, obtained through the activation technique on an enriched target, yields a measurement of 2.023(247) mb. This new result is thus in tension with the previous one, with a significant difference of 38% between these two values. This has an impact for the discrimination between

theoretical models, since the two data sets select different curves. The previous data favors the NON-SMOKER results and is overestimated by all three TALYS models. On contrary, our new data point is compatible with the three TALYS models but excludes the NON-SMOKER curve. To elucidate the underlying reasons for this disparity, a detailed examination of the different experimental techniques employed and the intricacies of data treatment would be warranted. Incorporating a new activation measurement at 3 MeV would be interesting, given the increasing divergence between the theoretical curves at higher energy. Additionally, it would provide valuable insight into the slight drop observed in Naqvi's data trend, which is not reflected in the behavior of the models at this energy.

For this reaction, similar to the  $^{70}\text{Ge}(p, \gamma)$  reaction, the cross section sensitivity is predominantly influenced by the proton width (78%) and then the gamma width. In TALYS, comprehensive GDR (Giant Dipole Resonance) data are also available for the  $^{72}\text{Ge}$  nuclei. Specifically, TALYS provides information on the number of discrete levels up to an excitation energy of 3.47 MeV for the  $^{72}\text{Ge}$  nuclei and 1.40 MeV for the  $^{73}\text{As}$ . Among these levels, the number of levels with known spin and parity is determined up to an excitation energy of 2.17 MeV for the  $^{72}\text{Ge}$  and 0.07 MeV for the  $^{73}\text{As}$  nuclei. Similarly to the case of  $^{70}\text{Ge}(p, \gamma)$ , the arsenic nuclei predominantly contributes to the uncertainties associated with predicting the exit channels.

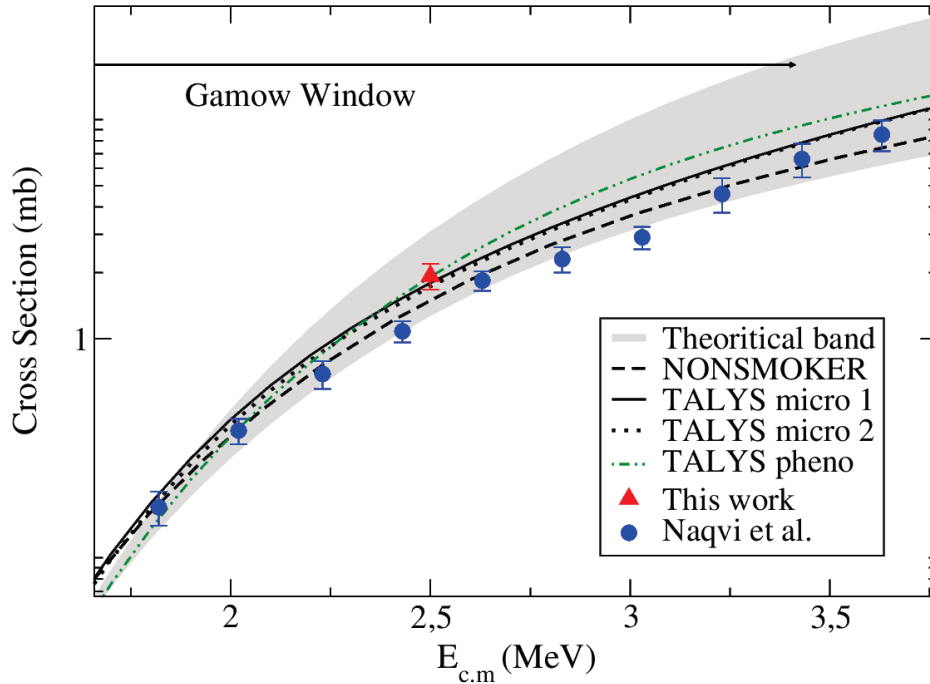


Figure 42: Experimentally measured cross section of the  $^{72}\text{Ge}(p, \gamma)$  reaction (triangle) compared with the experimental data from another work (circles) and the predictions of various theoretical models (lines) that have been adjusted according to specific nuclear parameters.

### $^{73}\text{Ge}(p, \gamma)^{74}\text{As}$

The cross section for the  $^{73}\text{Ge}(p, \gamma)^{74}\text{As}$  reaction was measured for the first time in this study and is depicted in Fig.43. At an energy of 2.5 MeV, the  $(p, \gamma)$  reaction competes with the  $(p, n)$  reaction, with the neutron channel opening at 1.13 MeV, as illustrated in Fig.40. At this energy, the cross section is notably influenced by the proton-, neutron- and  $\gamma$ -widths which all play crucial roles in determining the outcome of the reaction. TALYS offers valuable insights by supplying information regarding the number of discrete energy levels for  $^{73}\text{Ge}$  nuclei up to an excitation energy of 1.34 MeV, and for  $^{74}\text{As}$  up to 1.17 MeV. Among these levels, details such as spin and parity are available for levels up to 0.07 MeV for  $^{73}\text{Ge}$  and up to 0.0 MeV for  $^{74}\text{As}$  nuclei. It is important to note that germanium nuclei are even-proton, odd-neutron nucleus, while  $^{74}\text{As}$  is an odd-proton, odd-neutron nucleus. These nuclear properties contribute to the complexity and uncertainties associated with predicting the specific exit channels in reactions involving these isotopes. Since transition probabilities are strongly dependent on level spins and parities, the lack of information for these nuclei has a greater impact on the cross section and makes its estimation more



complex compared to even-even nuclei. Odd-odd nuclei often require more sophisticated theoretical simulations that take into account the coupling effects of nuclear levels or interference effects between different reaction pathways (direct and indirect). This is one of the reasons why the theoretical models in Fig.43 exhibit such divergent behaviors and why the theoretical band is so wide.

The phenomenological model is here the one that exhibits the best agreement with the experimental data measured at 0.243(43) mb, suggesting that certain parameters may have been adjusted using experimental data to improve the accuracy of the predictions. On the other hand, the microscopic models seem more influenced by the neutron-width. In Fig.40, sudden increases in the sensitivity to neutron- $\gamma$  competition can be observed around 1.5 MeV and 2.2 MeV. These rapid changes are reflected in Fig.43 as decreases in the  $^{73}\text{Ge}(p, \gamma)$  cross section shown by some models at these precise energies, indicating regions where neutron emission would be enhanced.

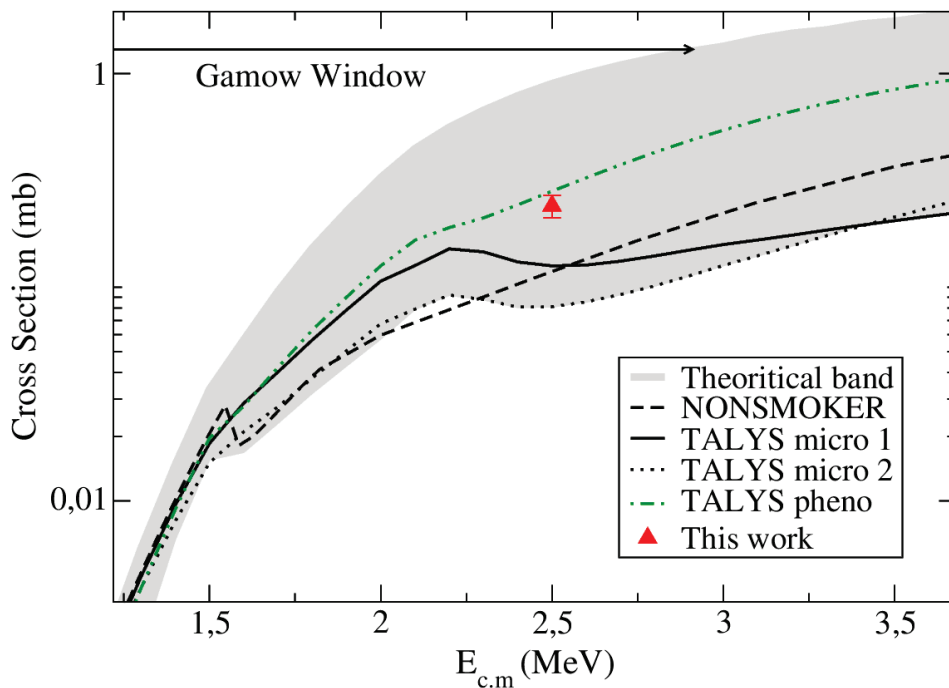


Figure 43: Experimentally measured cross section of the  $^{73}\text{Ge}(p, \gamma)$  reaction (triangle) compared with the predictions of various theoretical models (lines) that have been adjusted according to specific nuclear parameters.

### $^{73}\text{Ge}(p, n)^{73}\text{As}$

The  $^{73}\text{Ge}(p, n)^{73}\text{As}$  reaction was measured for the first time in this study and is depicted in Fig.44. At 2.5 MeV, the cross section of this reaction exhibits a 100%



sensitivity to the proton width, as illustrated in Fig.100 in Appendix.G. This distinct dependence significantly reduces the uncertainties affecting the cross section predictions, resulting in noticeably smaller theoretical band compared to previous measurements. Consequently, the reaction is entirely reliant on the optical potential employed in the theoretical models. It appears that the phenomenological model, along with NON-SMOKER, falls within acceptable bounds of agreement with this experimental measurement, while microscopic TALYS models (especially the *micro 2*) slightly underestimate its value.

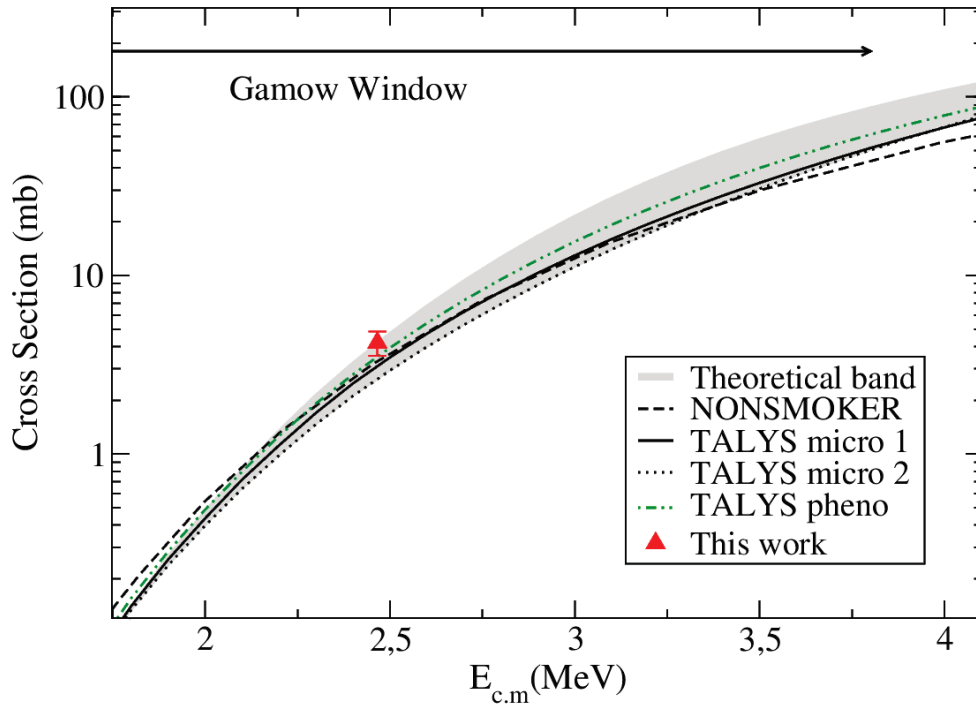


Figure 44: Experimentally measured cross section of the  $^{73}\text{Ge}(p, n)$  reaction (triangle) compared with the predictions of various theoretical models (lines) that have been adjusted according to specific nuclear parameters.

### $^{76}\text{Ge}(p, n)^{76}\text{As}$

The  $^{76}\text{Ge}(p, n)^{76}\text{As}$  reaction has undergone a second measurement subsequent to the initial study conducted by Kiss *et al.* in 2006, which coincided with the investigation of the  $^{70}\text{Ge}(p, \gamma)$  reaction. Our experimental data point demonstrates a satisfactory agreement with the previous experiment, showing an estimated deviation of 14% at 2.5 MeV. These findings, with the ones from the  $^{70}\text{Ge}(p, \gamma)$  reaction, indicate that our data aligns well with other experimental results obtained through activation technique.

The cross section of the  $^{76}\text{Ge}(p,n)$  reaction exhibits a unique sensitivity to the proton-width, as depicted in Fig.39. This characteristic, similar to the  $^{73}\text{Ge}(p,n)$  reaction, significantly reduces uncertainties in predicting the cross section, as evident from the reduced thickness of the theoretical band in Fig.45. Notably, the TALYS models show good agreement with our experimental data at the energy of interest. However, it is worth noting that certain TALYS models deviate from the bands around 3 MeV. This highlights the limitations of the prediction band and underscores the importance of considering correlations among specific nuclear parameters to improve the accuracy of the predictions.

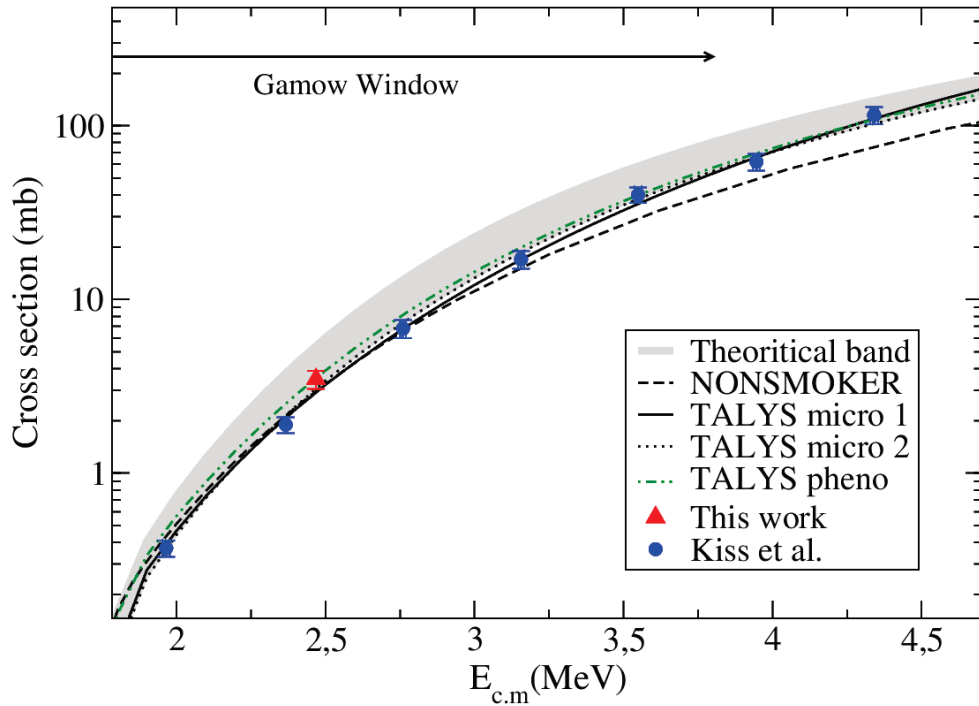


Figure 45: Experimentally measured cross section of the  $^{76}\text{Ge}(p,n)$  reaction (triangle) compared with the experimental data from another work (circles) and the predictions of various theoretical models (lines) that have been adjusted according to specific nuclear parameters.

### 6.3 Conclusion

---

In summary, this study employed the activation method to measure five  $(p, \gamma)$  and  $(p, n)$  cross sections for different germanium isotopes of interest ( $^{70,72,73,76}\text{Ge}$ ) within the Gamow window at 2.5 MeV. These isotopes are involved to varying degrees in the formation of the lightest p-nucleus, the  $^{74}\text{Se}$ . Enriched targets of T[ $^{72}\text{Ge}$ ] and T[ $^{73}\text{Ge}$ ], as well as a natural germanium target, were utilized in this experiment. The obtained cross sections for three reactions,  $^{70}\text{Ge}(p, \gamma)$ ,  $^{72}\text{Ge}(p, \gamma)$ , and  $^{76}\text{Ge}(p, n)$ , were compared with three existing data sets available in the literature. Overall, good agreement were observed with the previous data, except for a slight discrepancy in the case of the  $^{72}\text{Ge}(p, \gamma)$  reaction, which had been previously measured using an in-beam  $\gamma$ -summing technique. The two reactions  $^{73}\text{Ge}(p, n)$  and  $^{73}\text{Ge}(p, \gamma)$  were measured for the first time in this study, and confidence in these new measurements can be reinforced by the results obtained for the first three reactions.

These experimental cross sections were then compared with predictions from reaction codes using four different sets of models, each with its own parameterization. While certain models performed better than others for specific reactions, no single model consistently outperformed the others across all reactions. However, the phenomenological approach in TALYS consistently provided predictions that fell within the experimental uncertainties of the measured cross sections, demonstrating its reliability in this context.

The cross sections measured in this study were obtained using stable targets, focusing solely on the ground state component of the astrophysical cross section. In astrophysical plasma, nuclei are often thermally excited, resulting in a fraction of them existing in excited states. It will be crucial in future calculations of reaction rates to consider the reactions involving these excited nuclei. At this stage, it will be important to use the same astrophysical parameterization as used by Kiss *et al.* and Naqvi *et al.* for comparison purposes. Furthermore, it would be valuable to investigate the impact of our measured cross sections on the prediction of  $^{74}\text{Se}$  abundance by employing the astrophysical scenario used in the Rapp *et al.* article. Specifically, the differences in cross section values, particularly for the  $^{72}\text{Ge}(p, \gamma)^{73}\text{As}$  reaction, may have an influence on the  $^{74}\text{Se}$  abundance compared to the predictions of Naqvi, who demonstrated perfect agreement with the predicted values from the standard astrophysical libraries REACLIB [76]. Additionally, it will also be important to further investigate the

different statistical parameters that determine the value of the newly measured  $^{73}\text{Ge}(p, \gamma)$  cross section.

Part IV

P-PROCESS HEAVIER REGION :

Alpha elastic scattering

## 7 EXPERIMENTAL CONTEXT

---

### 7.1 Overview

---

The p-nuclei are primarily produced through a sequence of photo-disintegration reactions,  $(\gamma, n)$ ,  $(\gamma, p)$  and  $(\gamma, \alpha)$  as introduced in Parts I and II of this manuscript. The major challenge surrounding these nuclei is to improve understanding of their observed abundances. From the point of view of nuclear physics, this implies experimental measurements of cross sections, particularly at very low energies (few MeV), to enhance the accuracy of reaction rate calculations in astrophysical environments.

In Part II of this thesis, it was found that  $(\gamma, p)$  reactions and their inverse play a significant role in the production of the lighter p-nuclei. This was based on the findings of Rapp *et al.* [23], who studied the creation and destruction of p-nuclei through one of the most favored astrophysical scenarios. This section will now shift its focus to the reactions that predominantly influence the heavier nuclei of the p-process, which are characterized by their complex and intricate nuclear structures. The study by Rapp *et al.* (see also [18][77]) revealed that  $(\gamma, \alpha)$  reactions rates and their inverse have a significant impact on heavier nuclei as illustrated in Fig.46, where notable sensitivity is observed for nuclei with masses  $A > 140$ . On the figure, few exceptions appear to be unaffected by the  $(\gamma, \alpha)$  rate as the  $^{158}\text{Dy}$  or  $^{164}\text{Er}$  nuclei, although this is not the case for  $^{156}\text{Dy}$  and  $^{162}\text{Er}$  which are also p-nuclei. This emphasizes the importance of considering specific astrophysical conditions and nuclear structure details for each individual p-nucleus in order to gain a comprehensive understanding of their production.

Experimental investigations have confirmed that theoretical predictions of p-process reaction rates generally agree within a factor of 2 with measured proton and neutron capture rates, as well as photo-disintegration data. However, when it comes to  $\alpha$ -capture rates, larger discrepancies have been observed between experimental measurements and theoretical predictions, where the results from different models can often differ by one order of magnitude. While the nucleon-nucleus OMP is relatively well-established, the  $\alpha$ -nucleus OMP has been found to introduce strong variations in the predicted cross sections depending on the selected model. Fig.47 illustrates this phenomenon by comparing eight different  $\alpha$ -OMP available in Talys for a specific  $(\alpha, \gamma)$  reaction on a p-nucleus. No-

tably, the differences between these models can surpass an order of magnitude, depending on the energy range under consideration.

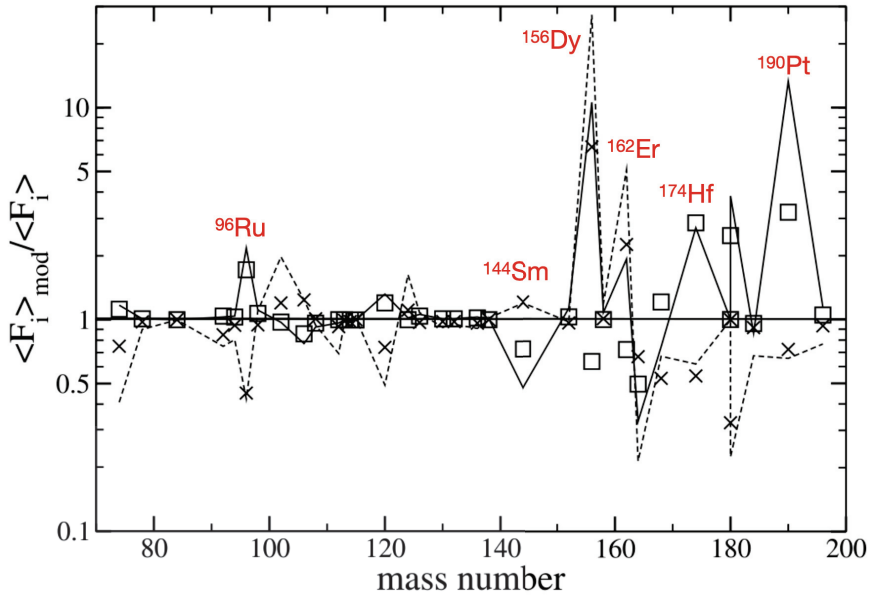


Figure 46: Ratio of simulated abundances calculated with modified  $(\gamma, \alpha)$  rates, with respect to calculations using currently accepted rates. The squares and crosses represent the ratio obtained with rates divided and multiplied by three respectively, while for the solid line and dashed line, the rates have been modified by a factor 0.1 and 10 respectively. In these calculations, all the other relevant parameters which have an impact on the p-nuclei abundances were fixed. Extracted from [23].

More precisely, the accuracy of HF calculations used in astrophysical reaction networks relies on the capacity to extrapolate nuclear statistical properties to poorly studied regions. In the past, local  $\alpha$ -OMP have been parameterized to accurately describe  $\alpha$ -elastic scattering and  $\alpha$ -induced reactions on specific nuclei. However, achieving a single global parameterization with the suitable mass and energy dependence remains a challenge. Specifically, the scarcity of low-energy elastic  $\alpha$ -scattering data, especially around the Coulomb barrier, restricts the development of a robust global  $\alpha$ -OMP suitable for astrophysical environment.

Significant research has demonstrated that an important parameter in the construction of an  $\alpha$ -OMP is the strong energy dependence observed in the real and imaginary parts, which is influenced by the number of open channels in a reaction [78][79].

Two families of modern global alpha nucleus OMP have been constructed with the explicit goal to be applicable to reactions at low energies of relevance for

astrophysics. These models are described by Demetriou in 2002 *et al.* [80] based on a double folding description of the real part. Secondly, a series of papers by Avrigeanu *et al.* develop phenomenological potentials whose real parts are based on Wood Saxon shapes with energy dependent parameters. The parameterization given in Avrigeanu *et al.* 2014 [81] is used as the default model in Talys. Although both families of potential give an overall satisfactory reproduction of existing data, it is underlined that the scarcity of existing constraints of low energy in the mass range  $A \sim 100$  to 200 makes their predictions still uncertain over the wide range of nuclei involved in nucleosynthesis networks.

Despite extensive efforts, it is important to acknowledge the limited availability of low-energy  $\alpha$ -scattering data especially in the mass range of  $152 < A < 190$ . While elastic  $\alpha$ -scattering measurements exist for some p-nuclei, most of them are conducted at relatively high beam energies. As a result, the uncertainties in the calculated cross sections mainly arise from the selection of global  $\alpha$ -nucleus potentials used in the calculations.

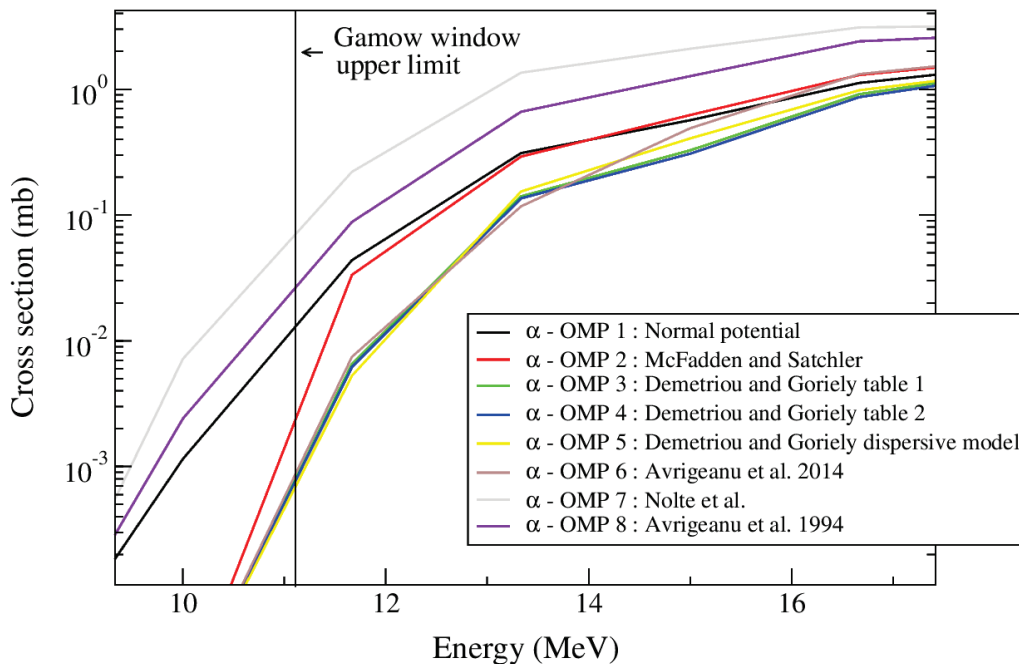


Figure 47: Estimation of the  $^{144}\text{Sm}(\alpha, \gamma)^{148}\text{Gd}$  cross section using eight distinct  $\alpha$ -OMP models available in Talys. All the other parameters were kept at their default values.

The objective of this part of the thesis is to prepare experiments that will provide new elastic scattering in the region of heavy p-nuclei, specifically targeting the vicinity of the Coulomb barrier. The purpose will be to enhance the precision in determining the energy dependence of the  $\alpha$ -OMP within this specific



region, and ultimately to help in the development of a global optical potential that faithfully reproduces the measured scattering cross sections.

In pursuit of this objective, a collaboration based on IP2I-Lyon and GANIL decided to propose measurements of elastic scattering cross sections on  $^{144}\text{Sm}$ ,  $^{162}\text{Er}$ , and  $^{177}\text{Hf}$  using the Splitpole magnetic spectrometer at the ALTO facility of the IJCLab Orsay. Bernadette Rebeiro at that time a post doctoral fellow at IP2I, was the spokesperson of the proposal, which has been submitted and accepted in 2020. The experiment is currently in the waiting phase for scheduling. This particular section of the thesis addresses the initial stage in the preparation of the experimental campaign. Hence, we will thoroughly explore and discuss the observables of interest in the subsequent pages, but also provide a description of the experimental apparatus that is foreseen in the forthcoming experiment.

## 7.2 Principle of the angular distribution

---

In elastic scattering experiments, the angular distribution plays a crucial role in providing valuable insights into the interaction between incident particles and target nuclei. This distribution characterizes how the scattered particles are spatially distributed as a function of their scattering angles, thereby revealing important information about the underlying nuclear properties. Central to describing the angular distribution is the differential cross section, denoted as  $d\sigma/d\Omega$ , which is expressed as a function of the rate at which particles are scattered into a solid angle  $d\Omega$ . In the context of a given scattering angle  $\theta_{cm}$ , which corresponds to the center-of-mass angle, and a certain number of produced particles  $N_{prod}$ , the differential cross section is expressed by :

$$\frac{d\sigma}{d\Omega} = J(\theta_{cm}) \frac{N_{prod}}{N_{inc} N_{target} \Delta\Omega} \quad (33)$$

with  $N_{inc}$  the beam intensity integrated over the duration of the experimental run,  $N_{target}$  the number of target nuclei per unit area and  $\Delta\Omega$  the detector acceptance.  $J(\theta_{cm})$  is the Jacobian  $J(\theta_{cm})$ , which represents the dilatation between the center-of-mass frame and the laboratory frame ( $d\Omega/d\Omega_{cm}$ ) [82]. In this work, where direct kinematics will be applied, the Jacobian is approximately equal to one, simplifying the normalization process. However, in more complex scenarios, such as inverse kinematics, the Jacobian can have a significant im-

pect on the angular distribution and must be carefully taken into consideration during the normalization procedure.

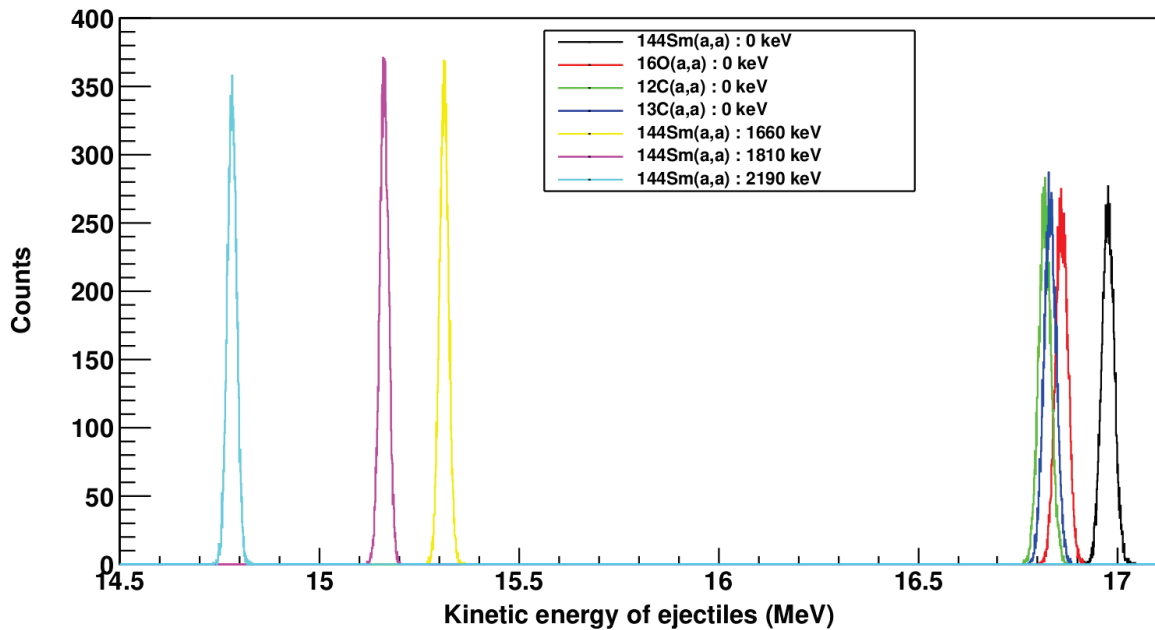


Figure 48: Simulated spectrum encompassing the elastic peak along with the first three inelastic peaks of the  $^{144}\text{Sm}(\alpha, \alpha)$  reaction. This simulation involves incident alphas at an energy of 17 MeV, interacting with a target of thickness  $40 \mu\text{g}/\text{cm}^2$ , and detected at an angle of  $10^\circ$ . In addition to the  $^{144}\text{Sm}$  spectrum, the plot also includes the elastic peaks resulting from  $(\alpha, \alpha)$  reactions conducted at the same angle on the nuclei  $^{16}\text{O}$ ,  $^{12}\text{C}$ , and  $^{13}\text{C}$ .

In order to discriminate between the shapes of different angular distributions associated with the differential cross sections, experimentalists need to collect a significant number of scattering events at various scattering angles during an experiment. Indeed, a large amount of data is necessary to obtain statistically significant data points in the angular distribution. The more data points collected, the more precise the differential cross section measurement and the more accurate the characterization of the nuclear properties possibly allowing to discriminate between candidate models. But obtaining such data is not as simple and involves carefully designing the experimental setup, optimizing the beam intensity and target thickness, and collecting data during sufficient time over a full angle range.

The simulated spectrum shown in Fig.48 serves as an illustrative example of what we can expect for alpha scattering on  $^{144}\text{Sm}$  with a specific target thickness at a detection angle of  $10^\circ$  taking into account the contribution of inelastic scattering as well as elastic scattering on carbon and oxygen target contaminants. In this simplified spectrum, we can clearly observe that the elastic peak

of the  $^{16}\text{O}$  nucleus is well-separated, with a difference of 100 keV, from the elastic peak of the  $^{144}\text{Sm}(\alpha, \alpha)$  reaction under this particular experimental configuration. This emphasizes the importance of having a detection setup with a resolution much better than 100 keV if we aim to accurately detect the elastic peak of this reaction. Once we successfully obtain high-resolution spectra, the subsequent crucial step will involve normalizing the differential cross-section to Rutherford scattering as shown in Fig.49. This normalization process will enable us to reduce uncertainties associated to the number of target nuclei and the beam intensity. It also emphasizes the part of the cross section that is affected by nuclear effects.

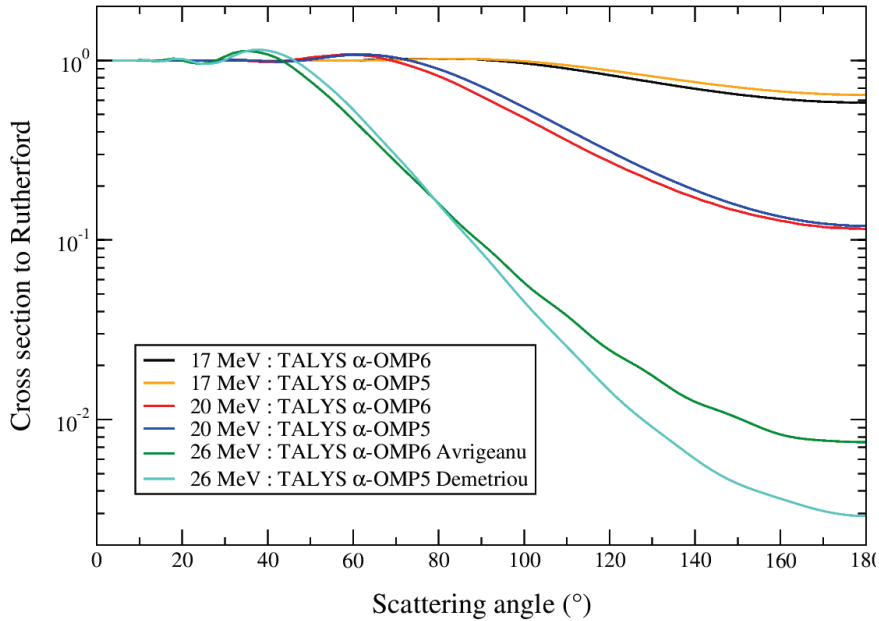


Figure 49: Comparison between the predictions of two modern global models of  $\alpha$ -OMP for the  $^{144}\text{Sm}(\alpha, \alpha)$  scattering cross section, for different  $\alpha$  particle energies.

Fig.49 shows a comparison between the predictions of Demetriou and Avrigneanu models of global  $\alpha$ -OMP. It should be noticed that both models take into account low energy data for  $\alpha$ -induced reactions on  $^{144}\text{Sm}$  :  $\alpha$  elastic scattering at 20 MeV [83] and  $\alpha$  radiative capture down to 13 MeV [84]. Consequently, their predictions are very close for  $^{144}\text{Sm}(\alpha, \alpha)$  up to 20 MeV, but show significant differences at higher energy, demonstrating different energy dependence around coulomb barrier.

## 7.3 Target

### 7.3.1 List of targets to characterize

The acquisition of dedicated targets for the envisaged experiments is a difficult process, due to the cost of enriched material, the theoretical constraints and delay of target making. A first approach was then to use targets already available in laboratories. After some investigations, the collaboration has obtained in this way a set of targets, among which eleven targets corresponding to different isotopes of samarium, erbium and hafnium have been selected as most serious candidates for the experiment. These selected targets, along with their thicknesses and, where available, the thicknesses of their substrates, are listed in Table 9.

Target	Origin	Element thickness [ $\mu\text{g}/\text{cm}^2$ ]	Carbon thickness [ $\mu\text{g}/\text{cm}^2$ ]
$^{144}\text{Sm} - 1$	ANL	56	40
$^{144}\text{Sm} - 2$	ANL	56	40
$^{144}\text{Sm} - 3$	ANL	81	20
$^{144}\text{Sm} - 4$	ANL	81	20
$^{177}\text{Hf} - 1$	Munich	120	?
$^{177}\text{Hf} - 2$	Munich	120	?
$^{179}\text{Hf}$	Munich	?	?
$^{180}\text{Hf}$	Munich	100	50
$^{166}\text{Er}_2\text{O}_3$	Munich	60	60
$^{170}\text{Er}_2\text{O}_3$	Munich	50	?
$^{154}\text{Sm}$	Munich	60	?

Table 9: Summary of the pre-selected targets characterized using the Rutherford Backscattering Spectrometry technique for the upcoming elastic scattering experiment.

All these targets have probably been used in the past, making their condition uncertain. The targets of  $^{144}\text{Sm}$  were obtained from the Argonne National Laboratory (ANL) in the USA. They were sent to Lyon in hermetically sealed boxes with valves that suggest they have been regularly placed in a vacuum environment. These targets date back to the year 1995.

All the others target samples have been sourced from the Technological Laboratory at LMU Munich in Germany. A notable observation is that there is incomplete data regarding the thicknesses and ages of these targets. The ac-

companying Fig.50 indicates that the "Munich" targets have consistently been stored in plastic boxes raising a concern as such storage conditions might have led to oxidation over the years.

The primary goal of this work will therefore be to characterize the 11 pre-selected target samples using the RBS technique. This characterization will involve measuring their thicknesses, evaluating their homogeneity, and identifying potential contaminants. These essential measurements will enable us to conduct precise scattering simulations between alpha particles and the target nuclei, aiming to optimize our experimental measurements. Specifically, we will assess whether the elastic scattering peak for the nucleus of interest can be effectively differentiated in the experimental spectra from other elastic scattering peaks caused by contaminants, as well as its first inelastic peaks from the target nuclei (see Fig.48). In addition, the target thickness information will be a primordial information to evaluate the expected count rate.



Figure 50: Pictures showcasing the two different storage methods of our targets. On the left, a vacuum reservoir contains two samarium targets from the Argonne National Laboratory, and on the right, a plastic box contains multiple hafnium targets sourced from the Technological Laboratory at the University of Munich.

### 7.3.2 RBS Characterization

---

The Rutherford scattering measurement for the characterization of the targets was conducted at the Laboratoire de Physique des 2 Infinis Irène Joliot Curie (IJCLab) of Orsay, using the 2MV tandem accelerator ARAMIS (Accelerator for Research in Astrophysics, Microanalysis, and Implantation in Solids). Two sets of measurements were required to collect the data. The first set was performed in October 2020 for a portion of our targets, while the second set was performed

in January 2021. During both experiments, a focused and accelerated beam of alpha ions was directed onto our samples at an energy of 1.4 MeV. The characterization setup and device details are visible in Fig.51. Throughout the beam time, the incident particles were quantified using a beam chopper that recorded the accumulated charge for each run. The backscattered alpha particles were detected at  $165^\circ$  using a PIPS detector with an energy resolution of 15 keV. Following a calibration procedure, the data were processed using the SIMNRA software (see subsection 3.4.1). In the following lines, we will present (as an example of the procedure realized for each of the studied targets) a detailed analysis that enabled to extract the properties of the  $^{177}\text{Hf} - 2$  target.

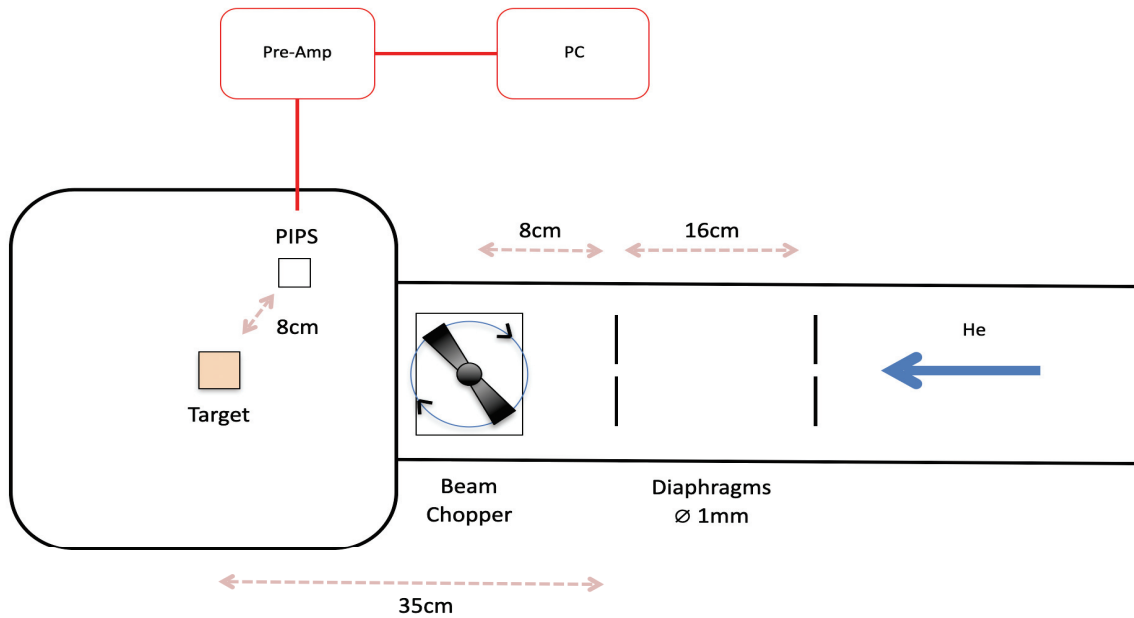


Figure 51: Setup of the two RBS characterization measurements conducted at IJCLab [85].

### 7.3.2.1 Study of the target $^{177}\text{Hf} - 2$

The  $^{177}\text{Hf} - 2$  target was analyzed at seven distinct points on its surface, and the associated backscattering spectra, along with the x and y coordinates indicating the location of the beam on the target, are shown in Fig.52. In these histograms, the seven peaks centered around channel 1000 correspond to the elastic backscattering of alpha particles on hafnium. At low energies, between channels 0-400, some of the backscattering spectra show much higher counting rates than the other measurements. This increasing trend resembles that of an infinite thickness, suggesting an interaction of the alphas with a material

of thickness on the order of  $\text{nm}/\text{cm}^2$ . We assume that this front is due to the backscattering of alphas on the aluminum frame used at IJCLab to hold the target during data acquisition. This is likely due to a misalignment of the beam with the target in this specific case.

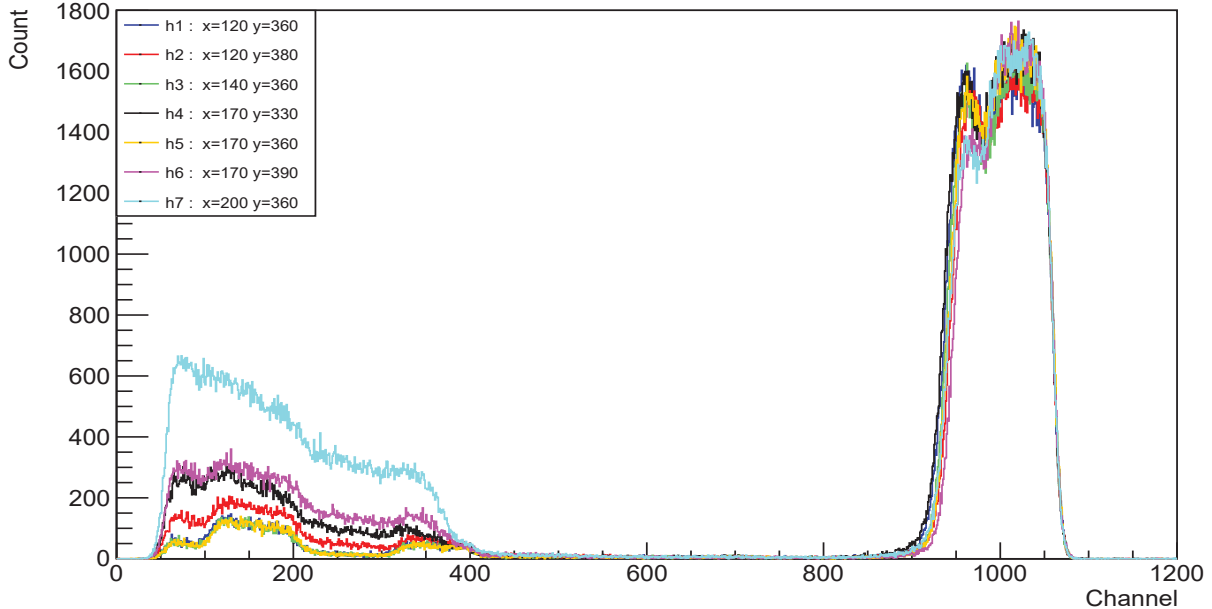


Figure 52: Superposition of the seven experimental measurements conducted on the  $^{177}\text{Hf} - 2$  target. The x and y coordinates are displayed in the legend.

The seven RBS spectra were individually and thoroughly studied using SIMNRA software to characterize the target. Fig.53 shows two histograms displaying a linear and logarithmic view of the "x=170,y=360" measurement which has been taken at the center of the target (yellow spectrum in Fig.51). Three peaks can be identified based on their energy fronts : hafnium, oxygen, and carbon. The term "energy front" refers to the energy of an alpha particle backscattered by an atom on the surface of the target. In the linear view of Fig.53, a small explanatory diagram aids in understanding this concept, with the blue point "1" representing the starting point of this energy front. By employing kinematic equations (20) and (21), we can then determine the mass of the target nucleus of interest. However, it should be noted that the mass sensitivity is too low to allow distinction between various isotopes.

SIMNRA simulations have been carried out to characterize all the targets listed in Table 9. However, the results of the additional measurements closely resemble those presented in this report, and thus are not presented in detail here.



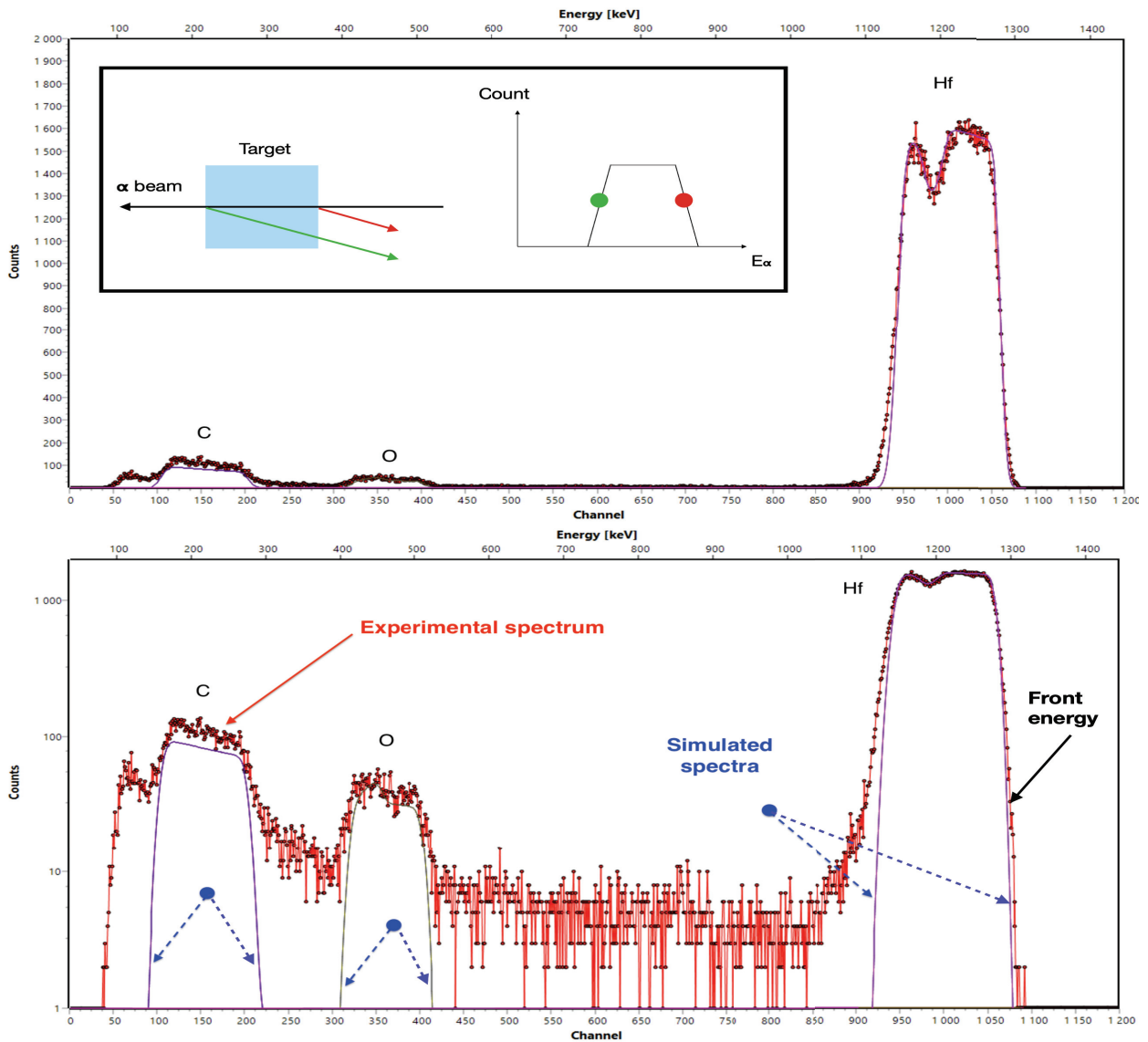


Figure 53: RBS spectrum from a measurement conducted on the  $^{177}\text{Hf} - 2$  target at the position "x=170, y=360" and loaded into the SIMNRA software. The top spectrum represents a linear view, while the bottom spectrum presents a logarithmic view of the same data. The fits used for the thickness extraction are clearly visible in logarithmic view.

The width of the peaks in the RBS spectra is mainly due to energy loss in material and is related to the target thickness and composition, determined through fits conducted by the software user. In Fig.53, the three peaks related to hafnium, oxygen, and carbon are simulated spectra. For accurate analysis, it is essential that the simulated spectra closely match the experimental spectra, enabling the software to precisely estimate their surface thicknesses. In this particular example, the spectra were modeled by estimating four distinct layers in the target : three Hf+O layers in which the concentrations vary with depth,



and a carbon layer corresponding to the target backing. The different relative concentrations of these layers are shown in the depth profile in Fig.54. It is noticeable that hafnium appears to be strongly oxidized throughout its thickness, with maximum oxidation surprisingly found in the middle of the Hf layer. Note that hafnium oxide is  $\text{HfO}_2$ , so for fully oxidized hafnium the oxygen number is twice the hafnium number. Again referring to Fig.53 in linear view, a reduction in the number of backscattered alpha particles is observed around 1200 keV (channel 1000) in the hafnium peak, forming a distinct "hole" in the spectrum. The detector recorded an average of 1300 backscattered alphas for this observed deficit, while 1600 and 1550 alphas were counted for the surrounding channels. Consequently, we observe a maximum deficit of 18.7% of hafnium atoms in a deep layer of the target, which appears to be compensated by the abundant presence of oxygen nuclei.

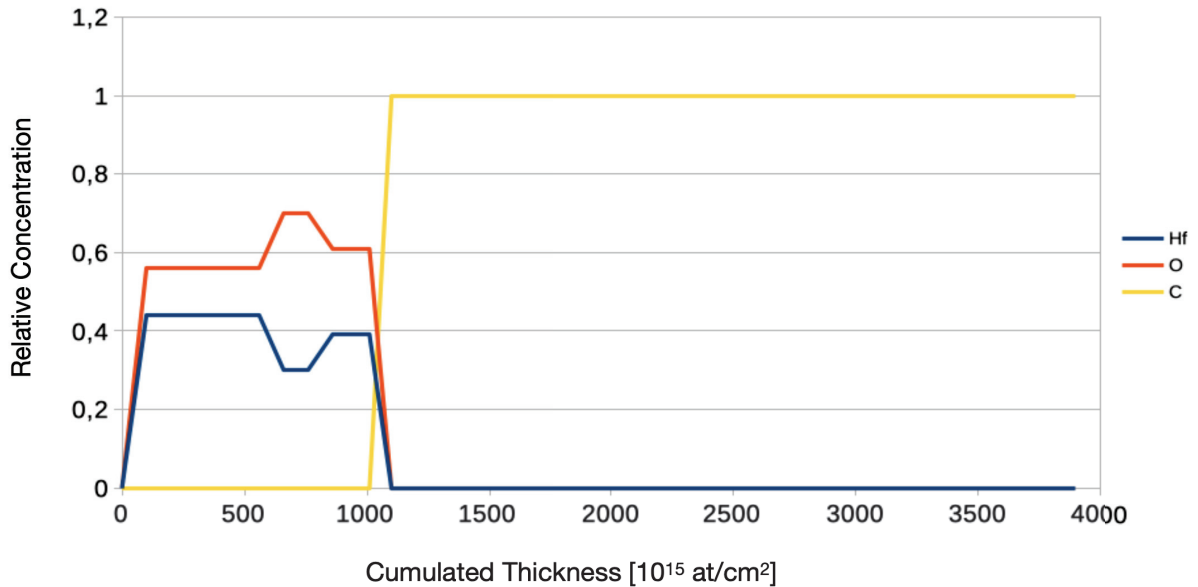


Figure 54:  $^{177}\text{Hf} - 2$  Target depth profile. The target is decomposed into four distinct layers with varying concentrations.

Thus, based on the SIMNRA results, the total thickness of the target is estimated at  $194.79 \mu\text{g}/\text{cm}^2$ , comprising  $119.84 \mu\text{g}/\text{cm}^2$  of hafnium and  $17.13 \mu\text{g}/\text{cm}^2$  of oxygen on a carbon substrate with a thickness of  $57.82 \mu\text{g}/\text{cm}^2$  (see Table 10). The reported uncertainties associated with these values arise from various factors, such as stopping power measurements, mathematical methods used, counting statistics, stability of the accelerator beam energy during the experiment, among others. However, these uncertainties are considered relatively minor compared to the energy resolution of the detector. After applying

calibrations, for this particular analysis, each channel of the histogram corresponds to 1.17 keV, while the detector resolution is 15 keV (according to the manufacturer), which spread over around 12.8 channels.

Considering the seven measurements conducted at various locations on the hafnium target (see Fig.55), we observe that these different spectra yield distinct thickness estimates. By comparing the largest thickness difference between the  $h_4$  and  $h_6$  spectra in the legend, we find a variation of approximately 12.5 channels for the width of the hafnium peak. We can note that this corresponds approximately to the channel extent of the energy resolution of the detector. The average full width at half maximum peaks for the seven measurement is of 120 channels, so the variation in the hafnium peak width is of around 10%.

Another way to compare the hafnium content obtained in the seven measurements is to determine the integrals of the seven peaks in Fig.55 to obtain a comparative ratio. For this target, a maximum difference of 11% between the peak integrals corresponding to the different locations is observed. This difference is of the order of magnitude of the precision of the RBS technique, where a 10% difference between thickness measured at different locations is generally accepted for a homogeneous target.

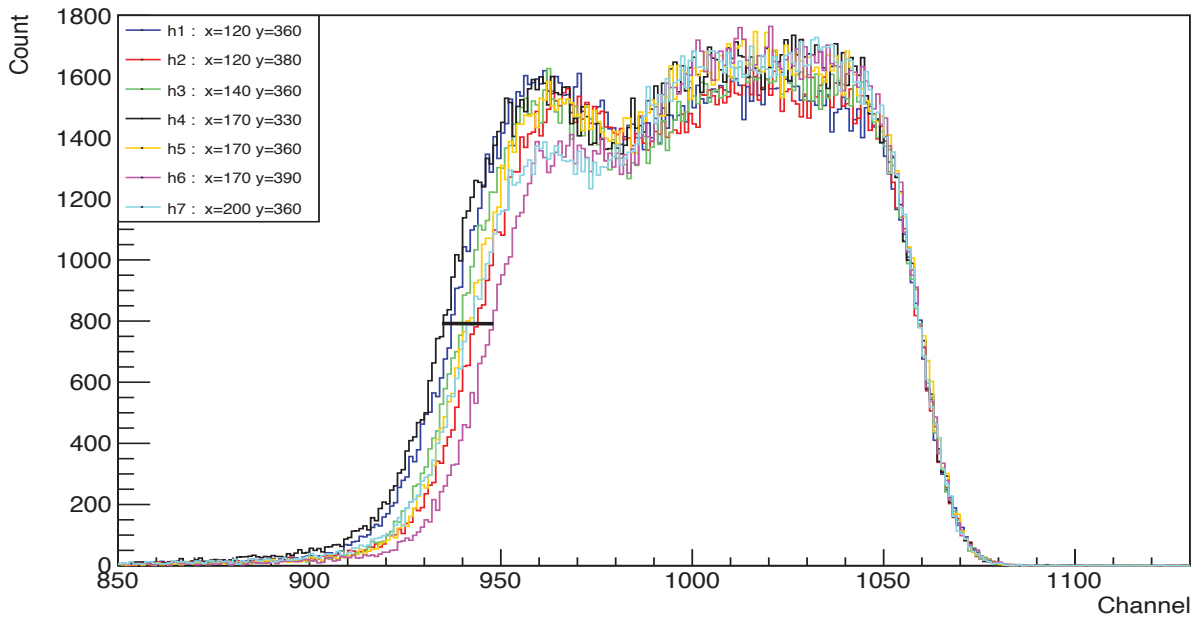


Figure 55: Superposition of the seven hafnium peaks measured at seven different locations on the target. The x and y coordinates are displayed in the legend.

In conclusion, the  $^{177}\text{Hf} - 2$  target is strongly oxidized throughout the hafnium layer. Its thickness is estimated to be  $194.79 \mu\text{g}/\text{cm}^2$ , with hafnium accounting

for  $119.84 \pm 12.77 \mu\text{g}/\text{cm}^2$ . The target is considered homogeneous in terms of surface composition, where an equal number of atoms are found in different regions of the target. However, it is not considered homogeneous in terms of atomic arrangement, as it appears that more oxidized hafnium layer is sandwiched between two less oxidized hafnium regions.

### 7.3.3 Global conclusions on target characterization

This comprehensive investigation was carried out for each of the 11 targets, involving 5-7 measurements for each target, leading to specific conclusions. Due to limited space, only one analysis was presented in this manuscript. However, Table 10 provides the measured thicknesses obtained during these investigations for the other 10 targets, along with the recommended guidelines for their utilization in the view of the experiment to come.

Target	Thickness				Feedback
	Element announced [ $\mu\text{g}/\text{cm}^2$ ]	Element measured [ $\mu\text{g}/\text{cm}^2$ ]	Carbon announced [ $\mu\text{g}/\text{cm}^2$ ]	Carbon measured [ $\mu\text{g}/\text{cm}^2$ ]	
$^{144}\text{Sm} - 1$	56	$34.33 \pm 6.22$	40	44.98	x
$^{144}\text{Sm} - 2$	56	$29.84 \pm 6.15$	40	46.70	x
$^{144}\text{Sm} - 3$	81	broken	20	broken	
$^{144}\text{Sm} - 4$	81	broken	20	broken	
$^{177}\text{Hf} - 1$	120	$104.40 \pm 15.35$	?	52.73	++
$^{177}\text{Hf} - 2$	120	$119.84 \pm 12.77$	?	57.82	-
$^{179}\text{Hf}$	?	$159.90 \pm 17.63$	?	53.83	-
$^{180}\text{Hf}$	100	$110.78 \pm 7.46$	50	39.88	++
$^{166}\text{Er}_2\text{O}_3$	60	broken	60	broken	
$^{170}\text{Er}_2\text{O}_3$	50	$66.43 \pm 12.09$	?	57.82	-
$^{154}\text{Sm}$	60	$73.89 \pm 8.67$	?	28.71	+

Table 10: Summary of the measured target thicknesses through the RBS method. Three targets broke during data collection and can no longer be used. The last column provides recommendations related to the condition of the targets, primarily concerning their atomic and surface homogeneity, as well as the presence or absence of contamination. A "++" sign indicates a highly favorable recommendation, a "+" sign denotes a good recommendation, a "-" sign indicates a low recommendation, and an "x" sign signifies that using the target is not recommended.

## 7.4 Detection set-up

---

In order to accurately determine the  $\alpha$ -OMP, it is necessary to perform elastic  $\alpha$ -scattering measurements over a range of  $5^\circ$ - $180^\circ$ , as the OMP is sensitive to the shape of the elastic scattering angular distribution. To achieve this, the split-pole (SP) magnetic spectrometer available at the ALTO facility of the IJCLab can be used in combination with PIPS detectors. While the spectrometer is currently capable of measuring up to angle of  $100^\circ$ , additional detectors are required to obtain data points in the remaining angular region from  $100^\circ$  to  $180^\circ$ . The detection systems used for this experiment will be detailed in the following subsections.

### 7.4.1 Alpha beam

---

SP is located at the Orsay tandem facility, as shown in Fig.56, which allows for the use of the Van de Graaf type accelerator to perform the desired reaction in direct kinematics. The Tandem accelerator produces a continuous beam by accelerating the desired ions in two steps. Firstly, the atoms to be accelerated are transformed into negative ions and injected at one end of the tandem, where they experience the electrostatic field. Then, these ions are stripped through a thin layer of carbon, becoming positive ions in the center of the machine, and are accelerated once more. The beam is then transported toward the target in the SP area.

For our experiment, we need alpha beams of energies between 16 and 26 MeV. ALTO can deliver such beams with typical intensity between 100 and 300 nA, and negligible energy spreading ( $\Delta E/E \simeq 10^{-4}$ ). The alpha particles of the beam are in the charge state  $2^+$ .

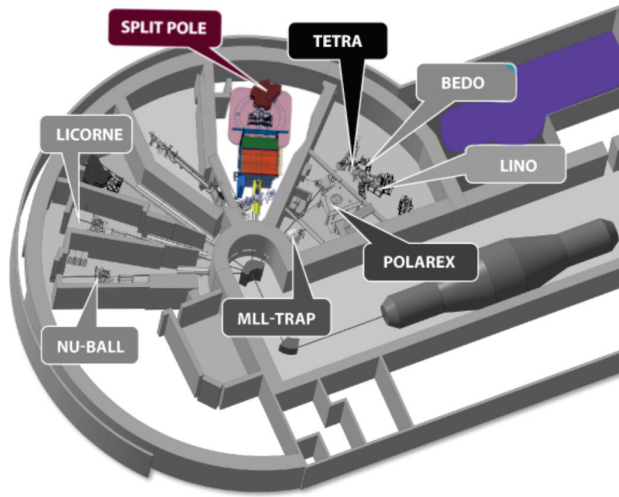


Figure 56: Diagram of the ALTO facility where is shown in color the Splitpole area as well as the control room in purple [86].

#### 7.4.2 SPLITPOLE spectrometer

The Splitpole magnetic spectrometer [87] comprises two magnetic field regions through which charged particles travel from the target to the detection setup situated at the focal plane. The term "Splitpole" arises from the fact that it features two separate pole pieces encased within a single coil, as illustrated in Figure 57. The primary objective of this design is to provide double focusing capabilities across a wide range of particle energies.

From a general point of view, the degree of curvature in the particle trajectory depends on its momentum and the strength of the magnetic field. To elaborate, when a charged particle with charge  $q$  enters a magnetic field  $\vec{B}$ , it encounters a Lorentz force  $\vec{F}$  perpendicular to both the magnetic field and its velocity vector  $\vec{v}$  :

$$\vec{F} = q\vec{v} \wedge \vec{B} \quad (34)$$

If  $\vec{v}$  is perpendicular to  $\vec{B}$ , the trajectory of the particle can be described, non-relativistically, by the expression [82] :

$$B\rho = \frac{mv}{q} = \frac{\sqrt{2mE}}{q} \quad (35)$$

with  $m$  the mass of the particle,  $E$  the kinetic energy of the particle, and  $\rho$  the

radius of the particle's circular orbit through the spectrograph. The product  $B\rho$ , known as the magnetic rigidity, plays a crucial role by characterizing the particle charge and momentum. Consequently, each energy value corresponds to a unique particle position in the focal plane of a spectrograph.

The geometric parameters of the SplitPole spectrometer are carefully adjusted through ion optics simulations in order to satisfy two important requirements for nuclear experiments : high energy resolution, which means precise focusing of particles of same momentum, and large angular acceptance to allow sufficient statistics [87]. The nominal acceptance of the spectrometer is around 2 milliradians, but can be fine-tuned by adjusting the aperture of vertical and horizontal slits during the experiment. The energy resolution is determined by the dispersion  $D = \Delta y / \Delta \rho$  (variation of the detection position with  $\rho$ ) and is typically  $D \approx 1.8$  for the SplitPole.

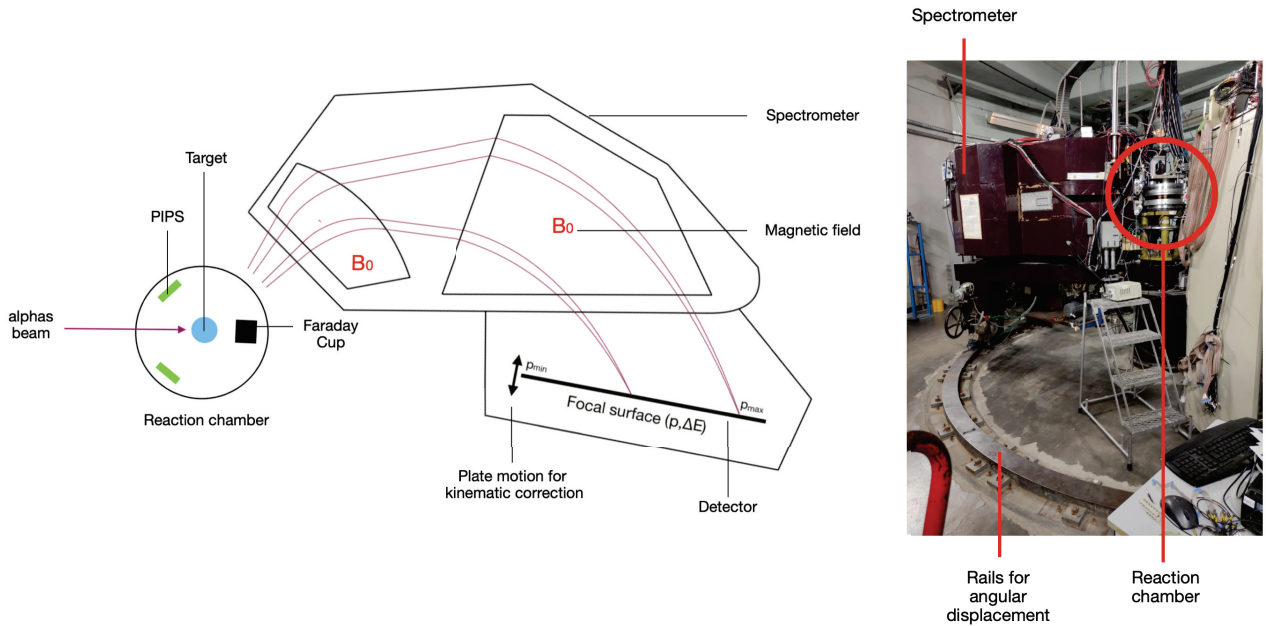


Figure 57: Schematic view and photograph of the Splitpole spectrometer and the reaction chamber.

### 7.4.3 Particle identification

The focal plane detection system of SP is composed of three detectors [82][88][87]. The first detector is a high-resolution position-sensitive proportional counter, operating as a gas-filled detector. It enables the reconstruction of the particle's trajectory by analyzing the timing properties of the signal, as illustrated in Fig.58. The second detector is a proportional counter, responsible for providing

a  $\Delta E$  signal. The last corresponds to the energy loss experienced by the particle as it interacts with the gas, typically iso-butane. By combining the signals of the two detectors, different particles can be discriminated in mass and charge by a  $B\rho$  versus  $E$  spectrum, as demonstrated on the left side of Fig.59, which is extracted from a previous SP experiment. Finally, positioned behind the first two detectors, the third detector is a plastic scintillator. Its purpose is to stop the particle and measure the residual energy deposited. This detector generates an  $E$  signal and allows to use a second particle identification method through a  $\Delta E$ - $E$  configuration. The kind of plot obtained in this configuration is depicted on the right side of Fig.59. The two plots in this figure are extremely useful during the experiment for recognizing and selecting the events of interest. By discriminating the alpha particles from other particles, we will be able to plot them according to their energies, resulting in a spectrum that will provide detailed information about the elastic and inelastic reactions undergone. This spectroscopic analysis realized at different angles will allow us to extract the angular distributions of interest for the determination of differential cross sections.

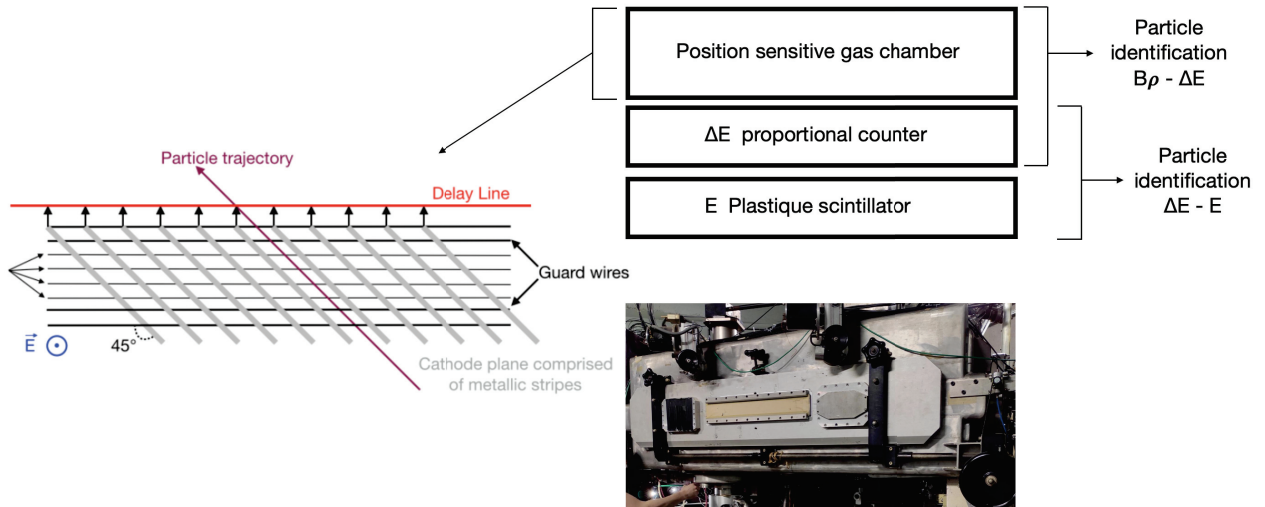


Figure 58: Schematic view of the three detectors forming the focal plane detection system. The position-sensitive counter scheme is extracted from [82].

As mentioned above, the SP spectrometer offers the capability of providing two distinct types of spectra, that can be used for identifying the detected particles. One of these spectra is a  $\Delta E$ - $E$  plot, where the energy loss of the particles in a first detector ( $\Delta E$ ) is plotted against the residual energy deposited in a second detector ( $E$ ). The calculation of energy loss in a material follows the Bethe-



Bloch formula. The energy loss can be expressed as a function of energy  $E$ , the mass  $A$  and the charge of the particle  $Z$  (in the 1-100 MeV energy range) such as :

$$\Delta E \propto AZ^2 \frac{\ln(E)}{E} \quad (36)$$

By using the equation (35) as well as the expression of the detected particle kinetic energy  $E = \frac{1}{2}Av^2$ , the energy loss can be expressed as a function of the magnetic rigidity instead of the energy (more details available in [82]) :

$$\Delta E \propto \frac{2A^2}{(B\rho)^2} (2\ln(Z) + 2\ln(B\rho) - \ln(2A)) \quad (37)$$

In equation (36), the  $Z$  dependence is stronger ( $Z^2$  instead of  $\ln(Z)$  in equation (37)), showing that  $\Delta E$ - $E$  plot present a better separation in  $Z$ . However, the  $A$  dependence is stronger in equation (37) ( $A^2$  instead of  $A$  in equation (36)), so that  $\Delta E$ - $B\rho$  plot are more efficient for mass separation.

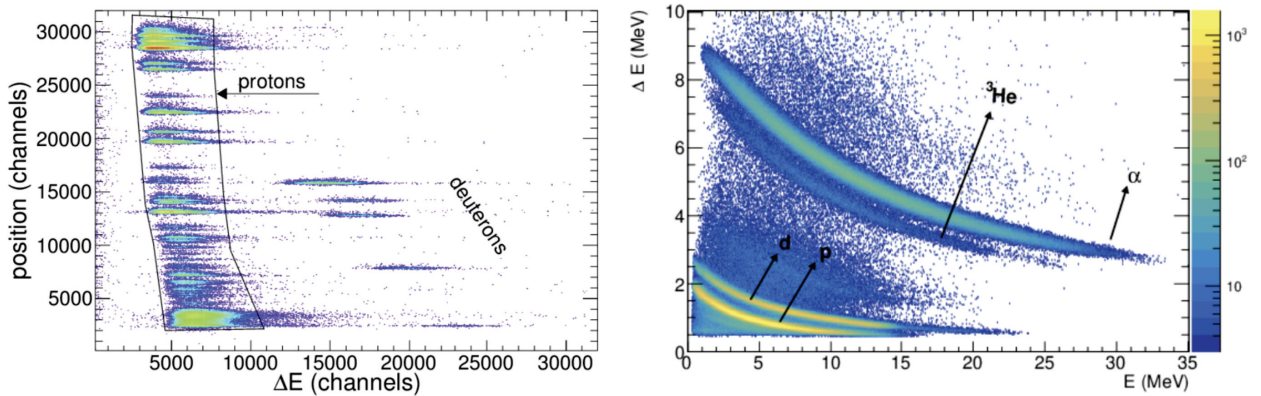


Figure 59: Particle identification plot on the left side representing a  $B\rho$ - $E$  spectrum obtained from a previous experiment using the SP detector [88]. This spectrum enables particle identification as well as the one on the right side, depicting a  $\Delta E$ - $E$  spectrum extracted from [89], and allowing visualization of the particles detected during a study of a  ${}^7\text{Be}(d, p){}^8\text{Be}^*$  transfer reaction at 5 MeV.

## 7.5 Silicon detector

In the experiment we would like to perform, silicon detectors will be used at the backward angles between  $100^\circ$  and  $180^\circ$  to access the angular region currently inaccessible by the SP spectrometer. To achieve this, it was planned to



used PIPS detectors placed in a  $\Delta E$ - $E$  telescope configuration in the reaction chamber to allow for optimal particle identification.

Silicon detectors, with their high sensitivity to charged particles, are ideal for elastic scattering experiments. Both the PIPS and DSSD (double-sided silicon strip detectors) have been considered suitable for the experiment based on the available space in the reaction chamber. However, ultimately, the decision to choose PIPS over DSSD was primarily driven by electronic limitations. Given the pile-up effect and the high particle count rates resulting from their large angular resolution, DSSD detectors were deemed unsuitable for this experiment. Consequently, PIPS detectors were preferred with collimators to compensate for the absence of strips (as it is the case for DSSD detectors) in order to enhance angular resolution.

Due to space constraints in the reaction chamber and the limitation of only 6 available channels on the COMET data acquisition card for the upcoming experiment, three telescopes in a  $\Delta E$ - $E$  configuration will be placed every 30 degrees, as illustrated in Fig.60. This arrangement ensures a minimum of three measurements at backward angles. If time and favorable experimental conditions permit, these detectors will be repositioned using the rotation of their support (detailed in section 7.6.1) to access additional measurements at backward angles.

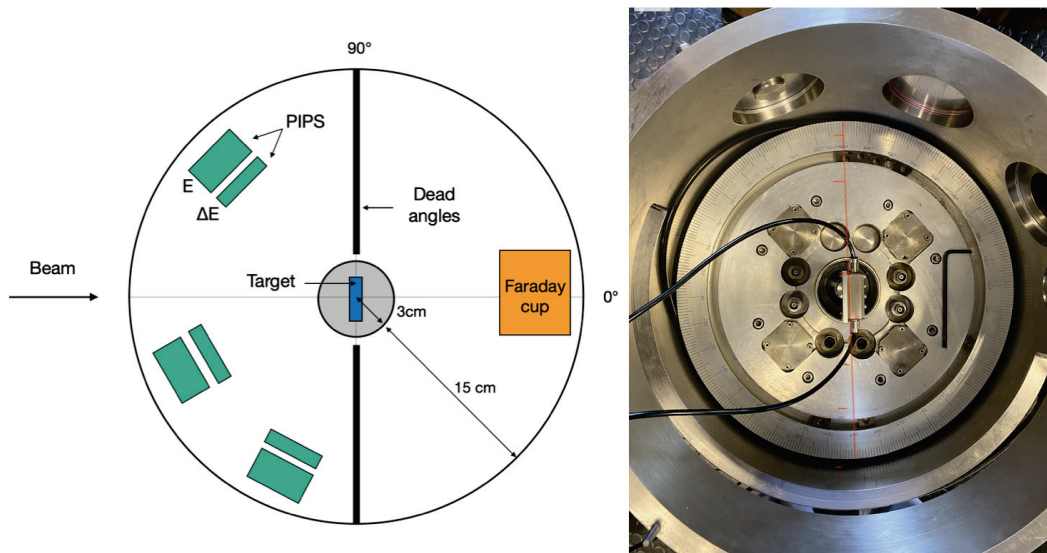


Figure 60: Diagram and picture of the inside of the SP reaction chamber. The left drawing illustrates the positioning of the three telescopes at the backward angles.

### 7.5.1 Energy loss

---

Since the silicon detectors have to be used in a  $\Delta E$ - $E$  configuration, it imposes two requirements. Firstly, the particle energy must be sufficiently high to traverse the target and the  $\Delta E$  detector, and sufficiently low to be fully absorbed in the  $E$  detector. In other words, the  $\Delta E$  detector must be thin, especially for low energy alpha particles, and the  $E$  detector needs to have sufficient thickness, especially when dealing with higher incident energies of alpha particles. To procure these detectors and prepare the experiment to come, energy loss in the materials were determined using the Bethe-Bloch formula and simulated using the SRIM software. These simulations were conducted at three specific energies, namely 17, 20, and 26 MeV, which correspond to the alpha beam energies at which the scattering measurements are to be performed. Fig.101, found in Appendix.H, displays the average path length of an alpha particle in silicon as a function of its incident energy. It reveals that at 17 MeV, the average path length is 165.44  $\mu\text{m}$  in silicon, while at 20 MeV, it increases to 217.15  $\mu\text{m}$ , and at 26 MeV, it further rises to 338.43  $\mu\text{m}$ . Armed with this valuable information, a preliminary simulated  $\Delta E$ - $E$  diagram was constructed and is depicted in Fig.102 of the same appendix.

However, the energy of the alpha particles that will reach these detectors are obviously lower than the beam energy, due to the kinematics of elastic scattering at backward angles and to energy loss in the target material. In our case, the targets have thicknesses on the order of tens of  $\mu\text{g}/\text{cm}^2$ , making them relatively thin. However, at backward angles, when the incident particle is backscattered, it traverses a greater amount of material, interacting with more atoms, leading to an increased energy loss compared to a particle incident perpendicular to the material. To estimate the possible impact of this energy loss, simulations were performed for each target and at each energy of interest, taking into account different target thicknesses. This approach accounts for uncertainties in the thickness estimates obtained via the Rutherford Backscattering Spectrometry technique and the use of targets that have not been characterized yet. An illustrative example of energy loss in a  $^{177}\text{Hf}$  target is depicted in Fig.61 where the black curve corresponds to elastic scattering without energy loss in the target material (the energy variation is then only due to kinematics). At angles close to  $0^\circ$ , the energy loss is minimal, as expected. It is more important at backward angles where both incident and scattered particle have to cross the target. The maximal loss occurs around  $90^\circ$  due to geometric effect since the path of

scattered particle inside the target is maximal at this angle. Through extensive simulations, a comprehensive list of detectors to be acquired was established, based on the range of thicknesses required to cover the full experimental scope.

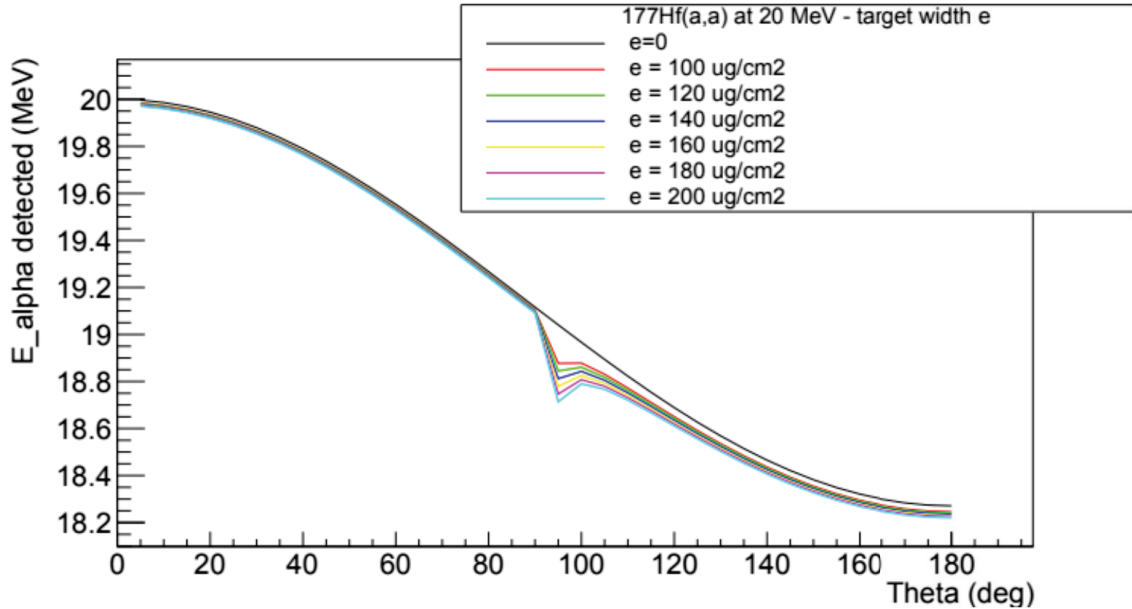


Figure 61: Energy of the detected alpha particles as a function of detection angle for an alpha beam of 20 MeV incident on a  $^{177}\text{Hf}$  target. The different curves correspond to different target thickness and consider that the scattering occurred after full crossing of the target.

## 7.5.2 PIPS characterisation

Three telescopes will be utilized for detecting the backscattered alphas during the upcoming experiment at rear angles. This configuration necessitates the possession of three  $E$ -type detectors and three  $\Delta E$ -type detectors. As we lacked such equipment at the time, we made concerted efforts to equip ourselves adequately for the forthcoming research. In pursuit of this, we reached out to the collaboration of this experiment. Colleagues from LPC Caen and GANIL then provided several PIPS detectors, the list of which is displayed in Table 11. Their invaluable support has significantly contributed to ensuring the success of our pre-experimental endeavors.

Upon receiving the detectors, we immediately initiated an evaluation of their condition through comprehensive detection tests, ensuring their functionality and suitability for the planned experiment. To recreate an experimental context and verify their performance, 10 SMA/BNC cables were purchased, guaranteeing optimal connections with the relevant devices. Moreover, using these new

cables during the experiment aimed to minimize potential background noise that could arise from older cables.

N°	Detector type	Company	Serial n°	State	Thickness [ $\mu\text{m}$ ]	Silicon surface [ $\text{mm}^2$ ]	Silicon diameter [mm]	Come from
1	E	Ortec	50-002F	?	1011	300	19.5	LPC
2	E	Ortec	50-002E	?	1018	300	19.5	LPC
3	E	Ortec	49-174D	HS	1014	300	19.5	LPC
4	E	Ortec	49-174E	NVGS	1014	300	19.5	LPC
5	$\Delta\text{E}$	Ortec	51-028A	?	164	300	19.5	LPC
6	$\Delta\text{E}$	Ortec	50-003A	?	152	300	19.5	LPC
7	$\Delta\text{E}$	Ortec	50-003D	?	161	300	19.5	LPC
8	$\Delta\text{E}$	Ortec	48-129D	NVGS	159	300	19.5	LPC
9	$\Delta\text{E}$	Ortec	51-028D	?	156	300	19.5	LPC
10	$\Delta\text{E}$	Ortec	48-129J	HS	159	300	19.5	LPC
11	$\Delta\text{E}$	Ortec	17-721D	NVGS	28.7	300	19.5	GANIL
12	$\Delta\text{E}$	Ortec	24-0202D	NVGS	52.8	300	19.5	GANIL
13	$\Delta\text{E}$	Ortec	5505412	NVGS	100	600	27.6	GANIL

Table 11: List of available PIPS detectors for the experiment. The information regarding the condition of the detectors was taken into account based on what was indicated on their respective boxes. The "HS" inscription signifies that the detector is out of order, "NVGS" indicates not in very good state, while the question mark indicates that no information is available regarding the condition. The first column represents only the allocation of a number to a detector in order to facilitate their description.

Once the setup was complete, we proceeded with the initial detector tests using a tri-alpha source consisting of  $^{239}\text{Pu}$ ,  $^{241}\text{Pu}$ , and  $^{244}\text{Cm}$ , all conducted within a vacuum chamber located at IJCLab Orsay. A picture depicting the reaction chamber used in the experiment, along with the implemented electronics, can be found in Fig.62. The reaction chamber was evacuated to a pressure of  $10^{-3}$  bar to create a vacuum environment. For conducting detector tests, a pre-amplifier (PA) was borrowed from IJCLab, specifically selected for its suitability in such testing scenarios. This PA was connected to a signal generator, an oscilloscope, and ultimately to a computer for data acquisition and analysis. It is worth mentioning that, during all the tests, the PA was firmly secured to the reaction chamber using adhesive tape and aluminium to ensure optimized electromagnetic compatibility : this allows to better associate the electric grounds and significantly reduce the electric noise.

Once the signals obtained, the spectra were acquired using the software MAE-

STRO, a Multichannel Analyzer Emulation Software package. This software, designed to work with gamma and alpha spectroscopy systems, is sold by the ORTEC industry and specifically tailored to interpret data from the detectors we used.

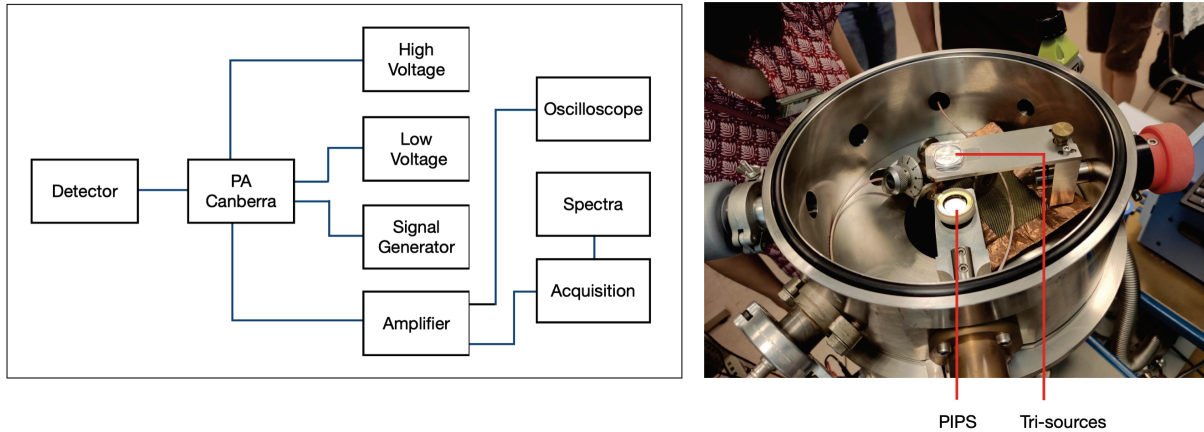


Figure 62: Diagram showing the setup used for testing the 13 potentially usable PIPS detectors for the experiment. The photo on the right displays the interior of the reaction chamber before the vacuum is applied, with the detector positioned approximately 13 cm away from the source in a vertical plane.

During the data acquisition process, a series of steps were undertaken, beginning with the verification of the leakage current in each detector. In electronics, specifically in the context of PIPS detectors, a leakage current refers to the unintended flow of electric current through the semiconductor material when it is reverse-biased. In a PIPS detector, a reverse bias voltage is applied across the silicon material, creating a depletion region, also known as the space charge region. This depletion region is crucial for the proper functioning of the detector, as it allows for the efficient collection of charge carriers (electrons and holes) generated by incident particles. Ideally, under a reverse-biased condition, the leakage current should be minimal or ideally zero, indicating that no significant current flows through the detector [37].

However, in practical scenarios, small imperfections or defects in the semiconductor material can contribute to unwanted noise, reduce the detector sensitivity and precision, and even generate excess heat within it. It is therefore of importance to measure and assess the leakage in order to ensure it within acceptable parameters set by the manufacturer. In our situation, specific data regarding the exact leakage current for each detector was not indicated. However, the recommended voltage values for each detector were provided on their protective cases. In the absence of direct information, we took a step-wise approach, grad-

ually increasing the bias voltage for each detector, while closely monitoring its stability during several minutes. This method allowed us to detect any potential leakage current and confirm that it remained within acceptable limits. This verification was applied to each detector before starting the data acquisition. The whole process lasted several days. Each run of interest was set to a duration of 12 minutes using the Maestro software, enabling us to extract the spectra afterward. These spectra were then calibrated using the well-established alpha energies from the tri-source used in the experiment.

Among the 13 characterized detectors listed in Table 11, one detector (n°13) was excluded due to its dimensions not meeting the required specifications (silicon diameter = 19.5 mm) imposed by the mechanical support. Among the remaining detectors, only 6 provided acceptable and well-separated alpha peaks. The list of detectors, their acquisition spectra as well as their intrinsic resolution are displayed in Fig.63. According to this figure, four  $\Delta E$  detectors appear to be in working condition, although one of them exhibits a relatively poor resolution exceeding 100 keV. As for the  $E$ -type detectors, two of them seem to be functioning properly (n°1 and n°2). However, detector n°1 shows a resolution higher than 100 keV, and both failed to meet the required validation for leakage current during the tests. The last were conducted at temperatures around 20°C, with a maximum duration of 20 minutes for each detector. Unfortunately, neither of the two detectors leakage currents stabilized during the test. The case of detector n°2 could be further investigated during a new series of tests of PIPS detectors, in order to see if it can be used for the experiment.



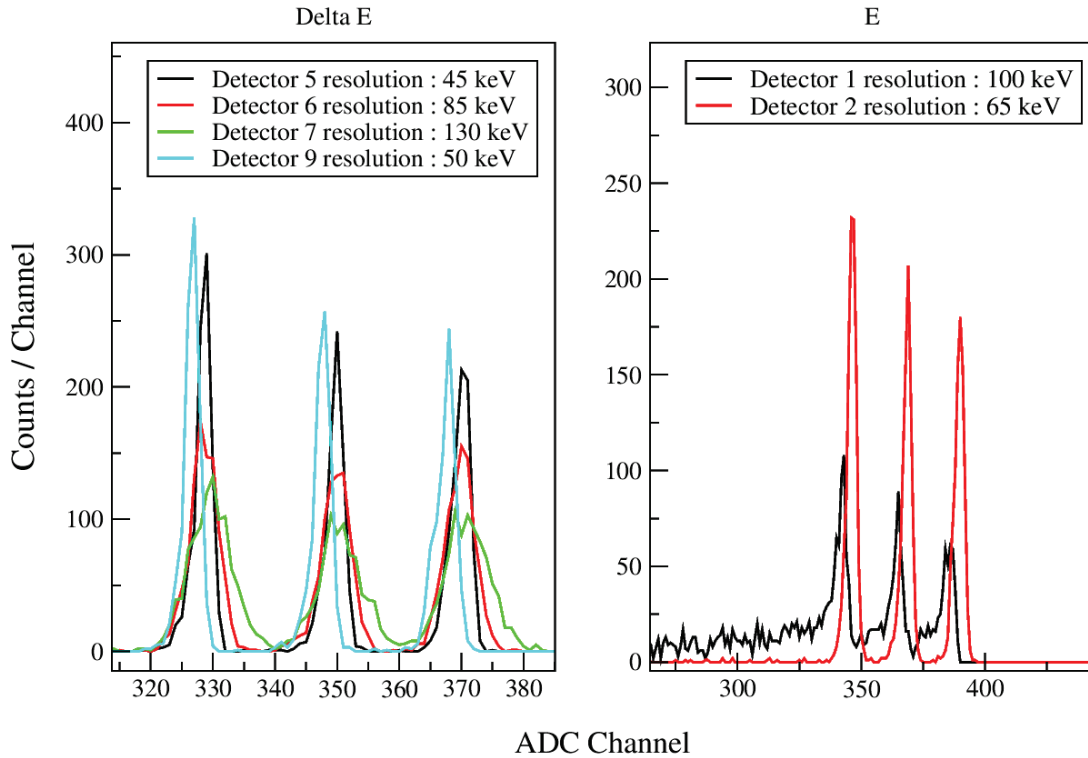


Figure 63: Acquisition spectra obtained after 12 minutes for each tested detector. The  $\Delta E$  and  $E$ -type detectors are displayed separately for better clarity and readability.

### 7.5.3 Current list of available detectors

In conclusion, three of the provided  $\Delta E$  detectors are in acceptable conditions for the experiment (although the availability of thinner  $\Delta E$  would be preferred for the lower energy part of the proposed measurements). However, for the  $E$ -type detectors, only one presents a correct energy resolution, but its leakage current shows instability, raising concerns about its long-term reliability. In response to these results, the IP2I group has decided to purchase three additional partially depleted  $E$ -type detectors from two approved suppliers, namely MIRION [90] and ORTEC AMETEK [91]. The manufacturers estimate the resolution of these detectors to be between 14-18 keV. The next crucial step in the experiment will involve conducting tests with these newly acquired detectors and the associated electronics and mechanical supports to ensure their optimal performance.

N°	Type detector	Company	Serial n°	Resolution [keV]	Thickness [ $\mu\text{m}$ ]	Silicon surface [ $\text{mm}^2$ ]	Come from
1	E	Ortec	50-002F	100	1011	300	LPC
2	E	Ortec	50-002E	65	1018	300	LPC
5	$\Delta\text{E}$	Ortec	51-028A	45	164	300	LPC
6	$\Delta\text{E}$	Ortec	50-003A	85	152	300	LPC
7	$\Delta\text{E}$	Ortec	50-003D	130	161	300	LPC
9	$\Delta\text{E}$	Ortec	51-028D	50	156	300	LPC
14	E	Ortec	23055255	18	1000	300	IP2I
15	E	Mirion	149789	14	500	300	IP2I
16	E	Mirion	149790	14	500	300	IP2I

Table 12: Final list of available PIPS detectors for the experiment at the date of the writing. The numbering of the first column remains consistent with that of the Table 11.

#### 7.5.4 Electronic test

During the silicon detector testing, we employed a single Canberra pre-amplifier that was used for each detector. In our experimental setup with three telescopes, which means six PIPS detectors, each detector will be individually connected to its dedicated PA. Upon receiving the PIPS detectors from the LPC laboratory, several associated PA were also provided, along with low-voltage power supply cables operating at  $\pm 6\text{V}$ . Photos of these components can be seen in Fig.64.

As part of the verification process for the silicon detectors, it was also planned to conduct tests on the PA to ensure their proper functionality and determine their gain. To achieve this, controlled currents are injected into each PA using a generator and the amplitude of the output signal is measured. The PA properties are mainly based on the well-known capacitor property :

$$V = \frac{Q}{C} \quad (38)$$

with  $V$  the voltage across the capacitor in volts,  $Q$  the deposited charge and  $C$  the capacitance in farads. The gain between the energy deposited by a particle resulting in charge  $Q$  in the capacitor, and the obtained electric signal amplitude  $V$  is then controlled by the PA capacitance  $C$ . The goal of the test is to determine  $C$ . For this, a voltage  $V_{in}$  is applied to a test capacitor of known capacitance  $C_t$  linked to the entrance of the PA. This induces the charge



$Q_{in}=C_t*V_{in}$  in both the test and the PA capacitors. As a result, the voltage created in output of the PA is  $V_{out}=\frac{Q_{in}}{C}=\frac{C_t*V_{in}}{C}$ , and we deduce C from  $C = C_t \frac{V_{in}}{V_{out}}$ .

As we were already aware of our PA capacitances (2.5 or 5 pF depending on the PA), our main goal was to ensure their proper functionality during the verification process. However, the results did not turn out as expected, as none of the PA could be successfully tested. After investigating the possible reasons for this issue, it was discovered that these PA cannot be powered by a standard 6V power supply due to a specific wiring configuration designed for the unique power supplies of the LPC. This means that the pins of the cables shown in the right photo of Fig.64, have specific and proprietary placements. Due to this unique configuration, none of them can hence be directly used in their current state for the experiment. Several solutions are now being considered : obtaining the specific low-voltage power supplies from LPC, purchasing new PA, having six PA custom-built by the engineering laboratory at IJCLab, or borrowing them from another source.



Figure 64: Photos of the 8 pre-amplifiers (left) and the low-voltage cables (right) supplied with the PIPS from the LPC.

### 7.5.5 Counting rate

---

The number of angles that can be measured, both forward and backward, during the experiment, depends on various factors, including the allocated measurement time and the counting rates at each angle. These rates are influenced

by several parameters such as target thickness, beam intensity, energy, reaction cross-section, scattering angle, solid angle etc... To estimate the counting rates for our hafnium, samarium, and erbium targets, we conducted simulations using two modern theoretical models for the  $\alpha$ -OMP which can be considered as providing the reasonable interval of expectation for the count rate. Results for a typical configuration are shown in Fig.65.

Another parameter that received considerable scrutiny was the detector-target distance and the collimator aperture. This was motivated by their profound influence on the solid angle coverage and the resulting counting rates, as depicted in Fig.66 for the  $^{177}\text{Hf}(\alpha, \alpha)$  reaction at 20 MeV beam with an intensity of 100 nA, over a one-second run. The simulations considered the presence of oxygen and carbon, taking into account the counting rate limits set by the experimental apparatus, approximately 1000 counts/s. As observed, the counting rates between different configurations on the figure exhibited significant variations, prompting us to carefully control and optimize this parameter.

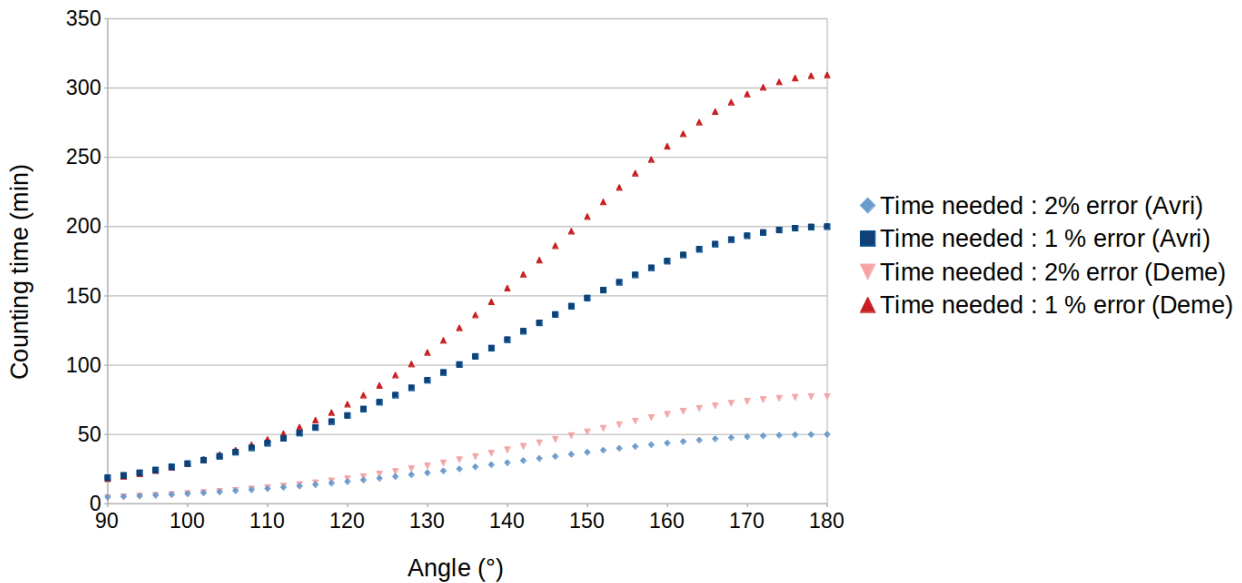


Figure 65: Estimation of the counting rate for the  $^{177}\text{Hf}(\alpha, \alpha)$  reaction over the angular range considered for PIPS detectors. Theoretical cross sections based on the models of Avri (Avri) and Demetriou (Deme) were used for the calculations, with a required measurement error of less than 1-2%. We considered a target thickness of  $104 \mu\text{g}/\text{cm}^2$ , a 20 MeV  $\alpha$ -beam with an intensity of 100 nA, a 1 mm collimator, and a target-to-detector distance of 10 cm, among other conditions.

Through a systematic exploration of various configurations, we sought to identify the most optimal setup that ensures precise and reliable measurements while adhering to the constraints of our experimental conditions. The insights gained

from these simulations significantly informed our decision-making process, leading to a well-designed and efficient experimental arrangement but one that still requires fine-tuning. Practical tests are still needed, especially concerning the mechanical integration. The stability of the solid angle will have to be ensured through the installation of the target support, target holder, and appropriate cabling during commissioning. Once established, our attention will shift to the resolution of the PIPS detectors as well as SP which underwent a two-year shutdown due to the COVID-19 period. We must ensure that the elastic peaks that we want to detect are sufficiently isolated from any potential interference, such as elastic and inelastic peaks arising from contaminants of isotopes with higher cross sections inside our targets. Ultimately, the observed cross sections will play a crucial role in adjusting the counting rates for each angle and determining the reasonable level of measurement precision. This interplay between theoretical factors and observed data will shape our priorities for an optimal use of the beam time.

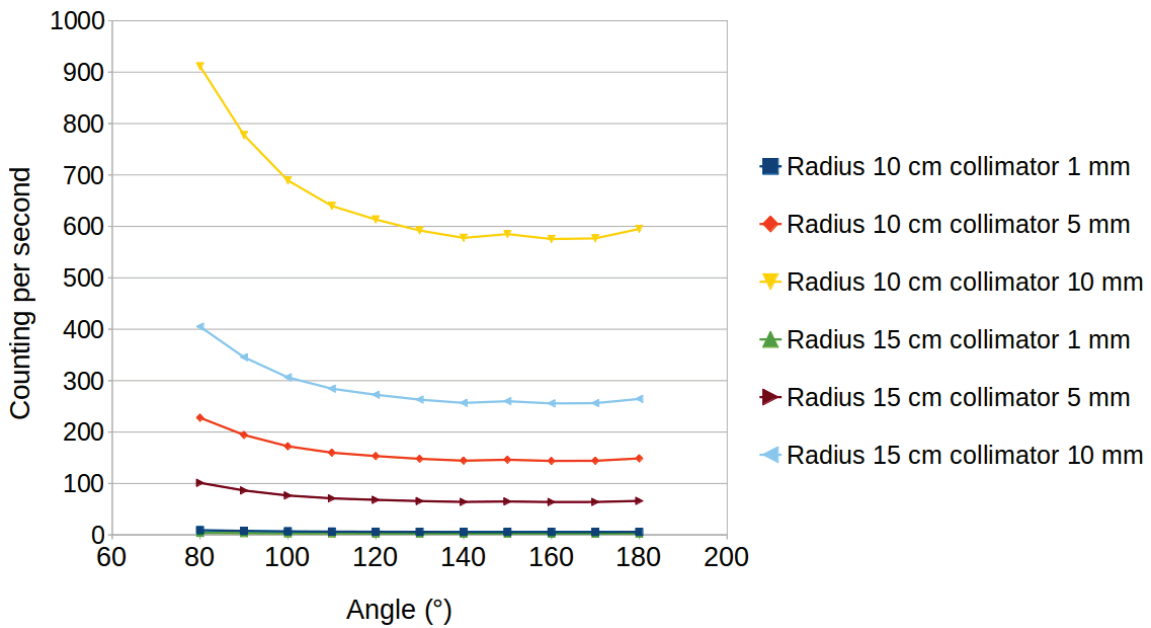


Figure 66: Different counting rate configurations as a function of the change in solid angle. Radius represents the target-detector distance. These simulations are based on the same experimental conditions as in Fig.65.

## 7.6 Piece manufacturing

---

### 7.6.1 PIPS support

---

Inside the SP reaction chamber at the ALTO facility, a  $\Delta E$ -E telescope is consistently positioned at  $25^\circ$  to serve as a continuous control monitor for all experiments (not shown schematically in Fig.60). The support structure holding this telescope can be seen in Fig.67 within the chamber. Here, the  $E$ -type detector is connected axially, while the  $\Delta E$ -type detector is connected transversely, following the constraints of the support design. In order to carry out our experimental setup, it is crucial to have three telescopes, as emphasized in various sections. To fulfill this requirement, the collaboration faced the challenge of obtaining three more support structures identical to the one depicted in the photo because only one prototype of this support is available at the SP facility. To address this issue, the collaboration sought assistance from the IP2I engineering team to recreate the support and produce three identical copies.

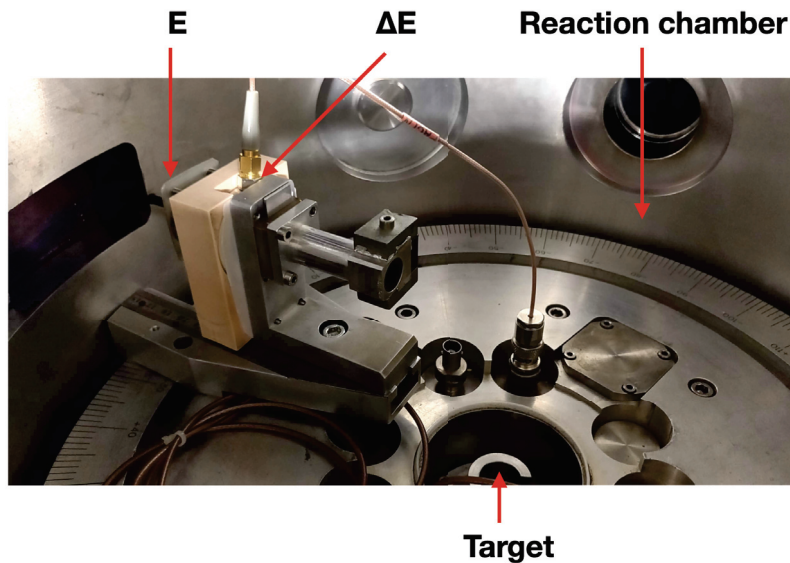


Figure 67: Inside of the reaction chamber in which the PIPS support is visible. The last is mounted on rails that allow it to move  $360^\circ$  inside the chamber. The target is not shown on the photo.

The engineering team took a proactive approach and initiated the process by disassembling the existing support piece. They then meticulously scanned the components to obtain precise digital data using the powerful computer-aided design software CATIA [92], and transformed them into a comprehensive digital

model of the support structure. With this digital representation, the team could make any necessary adjustments or modifications to ensure the support structures aligned perfectly with our experimental objectives. Indeed, by considering the age of the original support, the absence of existing blueprints, and the specific requirements for our program, the engineering team skillfully adapted the digital model.

The support structure is depicted in Fig.68, presented in the form of a CATIA plan, accompanied by several photos highlighting the major modifications made to it. The following is a list of the adaptations made, with each point number corresponding to the respective number listed on the figure :

1. Due to the LPC detectors external diameter requirement of 31.6 mm, the position for the  $E$ -type detector had to be enlarged. The internal diagonal distance between the two screws, as seen in the photo, was increased from 29.53 mm to 32.33 mm.
2. You can see a brass tube inserted inside the pipe, allowing access of particles to reach the detector. This tube was replicated using duralumin material (a strong, hard, lightweight alloy of aluminum), but without the notches that are visible on the picture, as their utility could not be demonstrated.
3. An annular piece of internal diameter 32.24 mm was added to reduce the cylindrical hole in order to accommodate a  $\Delta E$  detector of external diameter 31.6 mm.
4. The end of the tube had a recess that did not have any function in the device, where it seems that some disparate pieces were assembled. We removed this recess.
5. The front of the tube was equipped with a magnet, likely intended to prevent the entry of electrons in the channel. Unfortunately, we didn't have any magnets available at the Lyon study engineering office, so the new prototypes were designed without them. Nonetheless, a designated space for their potential placement was kept in case we manage to acquire suitable magnets later on.

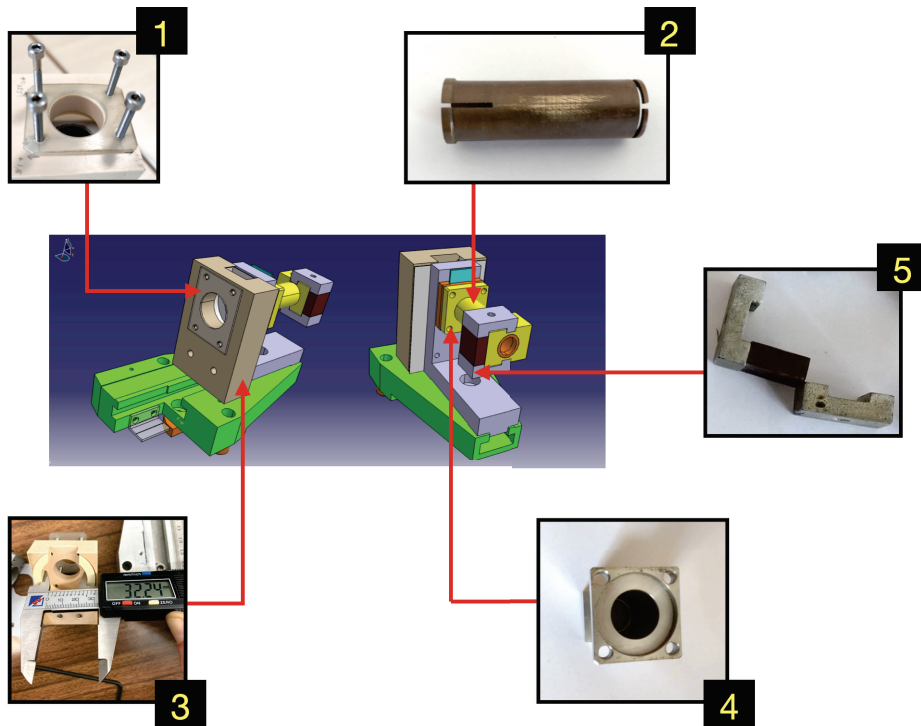


Figure 68: Diagram explaining the major adaptations made to the PIPS support. The CATIA drawings represent the support before the improvements. The different points displayed are explained in the text.

The mentioned modifications were carefully incorporated, and three new prototypes were successfully recreated using duralumin. Thorough testing was conducted to ensure their proper fit within the dimensions of the reaction chamber. Additionally, during the project, we took the opportunity to manufacture fifteen collimators that can be inserted into these new supports. These collimators come in different sizes, 1, 2, 3, and 5 mm apertures, offering a versatile selection for adaptation during the experiment (in accordance with simulated count rates).

### 7.6.2 Target support

The frames of the targets from Munich are larger than standard target frames used at ALTO, and do not fit properly into the Splitpole target ladder, as depicted in Fig.69. It was then necessary to seek assistance from the IP2I engineering team once again in order to find a suitable solution to this issue. Since then, two target support structures have been designed and created in two copies whose plans are also visible in Fig.69. However, during testing at SP, we encountered some challenges. Attaching the support structures to the



target ladder proved to be slightly difficult due to the slight discrepancy between the hole spacings and the screws. Although the operation is still achievable, it requires more careful handling. It appears that the age and extensive use of the target ladder may have caused some deformation in the material over time, leading to the small alteration in the hole spacings.

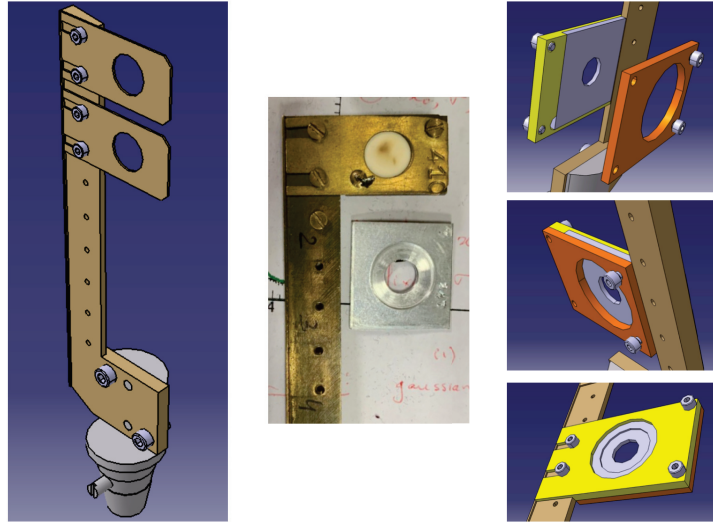


Figure 69: Picture of an aluminum frame from one of the Munich targets placed next to the head of the target ladder and showing the difference in geometry between these two objects (center). On the left, the entire target ladder is shown, with its base used for fixation in the center of the reaction chamber. On the right, CATIA diagrams of the target support structures created by the IP2I engineering team are displayed.

## 7.7 Summary and Outlook

---

A substantial portion of my doctoral research involved the preparation of an experiment initially scheduled for late 2020. Unfortunately, this project faced delays due to the constraints imposed by the COVID-19 pandemic and other setbacks related to the programming of the SP facility. However, the postponement has also presented us with some valuable opportunities as it afforded us additional time to address outstanding issues and further refine our experimental setup. One of the aspects that had to be treated was the adaptation of the target support to Munich target frames. Furthermore, one notable enhancement was the considerable extension of our angular coverage from the previously attainable  $100^\circ$  to encompass wider angular range thanks to the addition of PIPS detectors. This also involved mechanical studies and manufacturing to accommodate them in the SP chamber, as well as calculations, simulations, propection and tests to acquire PIPS detectors with required properties. These detectors will allow the precise collection of data at backward scattering angles, which is of paramount importance, and will enable us to better investigate discrepancies in the  $\alpha$ -nucleus optical models, which tend to amplify as the scattering angle approaches  $180^\circ$ .

From an experimental standpoint, one of the main points still to be settled is the availability of 6 pre-amplifiers. As mentioned previously, we need to figure out a way to power the existing PA or procure new ones. Once this challenge is overcome, it will be essential to thoroughly test the new  $E$ -type PIPS detectors purchased by IP2I, together with the three  $\Delta E$ -type detectors selected from LPC, to ensure their optimal performance and reliability during the experiment.

During the commissioning phase, several critical aspects will be thoroughly examined. First and foremost, the detectors resolution and performance in their specific experimental configurations will be carefully assessed. Ambient noise levels will be estimated and minimized. Additionally, the durability and stability of our targets under the anticipated beam intensities, considering their age, will have to be checked. Adjustments to the priority physical case will be made at this stage. Once the experiment has been performed, a meticulous analysis of the data will be undertaken to identify the peaks of interest and the presence of isotopes in the target material. It is important to note that while the targets have been characterized, the RBS method cannot distinguish between isotopes



of the same element. It should be also noted that the first excited level is very low for many nuclei of interest, and a theoretical treatment to disentangle inelastic from elastic contribution will probably have to be applied in some cases.

If we encounter any issues with the existing targets, such as breakage or overly complicated scenarios, alternative targets may be available at the time of the experiment. Although not discussed in this part of the thesis, orders are currently being placed for the production of several isotopes of interest for hafnium and samarium targets from a target laboratory using the SIDONIE isotope separator at the JANnuS-SCALP platform of the IJCLab Orsay. These new targets are expected to comprise a diverse range of isotopes, each with distinct characteristics. Having multiple replicas of these targets, in a non-oxidized state and with very high isotopic purity, would significantly enhance the accuracy and reliability of our experimental results. The increased variety of isotopes will allow us to explore  $\alpha$ -OMP sensitivity to different nuclear properties (deformation, magic numbers, odd-even effect...) and gain deeper insights into the underlying physics. Moreover, having several target replicas will enable us to validate and cross-verify our findings, reducing potential uncertainties and improving the overall quality of the data. This approach ensures a robust and comprehensive analysis, bolstering the scientific significance of our research outcomes.

Part V

# MACHINE LEARNING TECHNIQUES FOR P-PROCESS ADVANCEMENT

# 8 TOOL EXPLORATION

---

## 8.1 Introduction

---

The complexity of nuclear matter is heightened by the fundamental principle of Pauli exclusion, which forbids identical nucleons from occupying the same quantum state. Nucleons interact in a quantum-mechanical manner, leading to intricate quantum configurations, non-trivial bound states, and a nuanced description of the atomic nucleus. The strong nuclear forces, which govern nucleon behavior, are not fully understood within the framework of Quantum Chromodynamics, the theory describing quark and gluon dynamics in nuclei. Consequently, these forces present considerable computational challenges and require the application of approximations and advanced theoretical models, which require fine-tuning to reproduce experimental data [93].

Due to the complexity of the systems involved, certain observables, such as nuclear reaction cross-sections, remain challenging to predict, especially when dealing with exotic nuclei as encountered in the p-process. While the factors influencing these cross-sections, such as reaction energy or scattering angle, have been somewhat well-established, it remains difficult to catch the true correlation between many different input variables even by using sophisticated and recent models. To address this, statistical modeling and machine learning (ML) techniques have emerged as powerful tools for exploring these relationships and identifying the key factors that influence for instance cross-sections. In recent years, these ML approaches have been widely utilized in nuclear physics research, contributing significantly to our understanding of nuclear reactions [94, 95, 96, 97, 98].

In the IP2I group, ML techniques have been explored for many years in particular for signal processing [99]. In the context of astrophysics studies, new challenges arise, requiring the implementation of additional aspects that have not been previously explored. Several questions are currently under consideration :

1. How machine learning can help in predicting direct standard observables such as cross sections? This would indeed be a valuable tool to conduct experiments.
2. Given that various theoretical models (OMP, NLD,  $\gamma$ -strength) are exten-

sively used in reaction codes such as Talys, could we estimate their intrinsic uncertainties? This would facilitate a more comprehensive comparison between these models.

3. Could we establish a connection between a specific model predictions and experimental data? This avenue has already been explored by Shelley *et al.*[97] concerning mass predictions.
4. How can ML techniques assist in extracting correlations and patterns hardly accessible for humans, directly from the various data set already available ?

This segment of the thesis marks the inception of a dedicated campaign aimed at enhancing our tools to more accurately predict astrophysical cross-sections of interest, and make an effort to address, at least in part, the posed questions. The theoretical background of the various techniques used will not be described in details. However, an introduction together with some illustrative results, will be provided for two different approaches currently under scrutiny in the group, referred as "direct" and "indirect".

## 8.2 Cross section determination : Direct approach

---

In this section, we explore two techniques which allow for the direct estimation of cross-sections by leveraging a substantial amount of experimental cross-section data : the Bayesian and the frequentist methods.

### 8.2.1 Bayesian Inference : The Gaussian process

---

Bayesian inference is a powerful statistical approach used to estimate model parameters based on observed data. It leverages the principles of Bayesian probability theory to update and refine our beliefs about these parameters as new data is collected. By incorporating prior knowledge and combining it with the likelihood of the data, Bayesian inference provides probabilistic estimates of the parameters, allowing us to better understand the uncertainty associated with the predictions. It treats the relationship between the measured data  $B$  and model parameters  $A$  as a logical interplay of conditional probabilities such as :

$$P(A/B) = \frac{P(B/A).P(A)}{P(B)} \quad (39)$$

Or commonly mentioned as :

$$\text{Posterior} = \frac{\text{likelihood.prior}}{\text{evidence}}. \quad (40)$$

Prior probabilities in Bayesian inference represent our initial knowledge about the parameters of the model before considering any data. These probabilities need to be assigned for each parameter that we want to estimate. On the other hand, the likelihood function describes how the model parameters are related to the observed data, expressed in probabilistic terms. This function is also present in frequentist approaches, with a common example being the  $\chi^2$  function. The evidence, also known as the marginal likelihood, ensures that the product of the likelihood and the priors is normalized, allowing us to obtain valid probabilistic estimates for the model parameters [96, 100].

The Gaussian Process (GP) [101] is a versatile statistical learning method used for probabilistic modeling and prediction of functions. Unlike deterministic models that provide a single fixed prediction for each input, the GP offers a more flexible approach by providing a distribution of predictions. It considers functions to be drawn from an infinite family of Gaussian distributions, each characterized by a mean function and a covariance function (kernel). These Gaussian distributions allow to capture various potential realizations of the target function, accounting for uncertainties associated with each prediction [102, 97].

In this thesis, the first machine learning code developed was based on the GP in order to predict differential cross sections from elastic scattering data. We employed the open-source machine learning library Scikit-learn, which supports both supervised and unsupervised learning [103]. This extensively used and thoroughly documented tool provided us with a solid foundation for our introduction to the GP whose code operates as follows :

1. The kernel, chosen by the user based on the data behavior (e.g., exponential, constant), acts as a probabilistic model capturing the similarity between any pair of data points by specifying their covariance : it plays a role akin to the prior in Bayesian approaches. By tuning the kernel hyper parameters, we can adjust its flexibility and influence on the function distribution, leading to more precise and generalizable predictions. In this sense, the kernel acts as a regularization mechanism in the Gaussian

Process, allowing us to control the model complexity based on our prior knowledge and assumptions about the data. The likelihood and evidence are then derived from the observed data and the probabilistic Gaussian Process model itself.

2. In the regression task, the model is trained using the available dataset, where  $X$  represents the input features, and  $Y$  corresponds to the target values to be predicted. The model learns from this data to make accurate predictions on new, unseen data.
3. Once the model is trained, it can make predictions for new inputs  $X$ , providing a corresponding output  $Y_{pred}$ . Additionally, the model predictions come with an associated standard deviation, which serves as an indicator of the prediction reliability and uncertainty. This standard deviation allows us to assess the accuracy of the model fit and understand the level of confidence in its predictions.

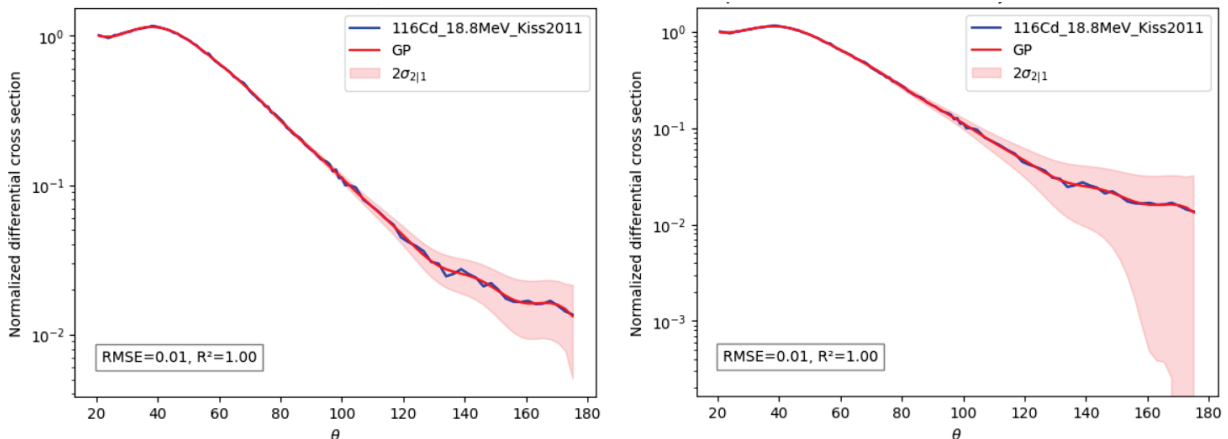


Figure 70: Plots illustrating the angular cross section of the  $^{116}\text{Cd}(\alpha, \alpha)$  reaction at 18.8 MeV. The blue points represent the experimental data, while the red curve corresponds to the GP fits. In both studies, the same kernel has been used, which include white noise. On the right plot however, the allowed range of the white noise parameter has been set to a lower limit. The pale red shading around the fit represents the deviation from the mean, captured by the standard deviation. This subtle variation in the plots arises from minor adjustment in the kernel parameterization.

In Fig.70, we illustrate an example of using the Gaussian Process in a simple case where the model is trained and tested on the same data set. The last consists of elastic angular scattering data coming from the reaction  $^{116}\text{Cd}(\alpha, \alpha)$

at 18.8 MeV. In the figures, we can clearly see the variation in the standard deviation of the different predictions, resulting from the modification of a specific hyperparameter within the kernel. The last is a combination of an exponential function multiplied by a sine function (see Duvenaud for a comprehensive survey about the main kernels), and its hyperparameter was deliberately adjusted to assess its influence on the model predictions. In this particular example, when the Gaussian Process was trained on the available data, it significantly improved predictions for those data points. However, without proper parameterization and when the code lacked access to the data, the accuracy of the predictions and the estimation of the standard deviation were notably compromised. In order to ensure accurate and reliable predictions, customizing the hyperparameters and functions available in the Gaussian Process library to fit the data becomes essential.

During the course of this research, certain promising aspects emerged, but due to time constraints imposed, we couldn't fully explore all avenues. One notable observation was that the GP exhibited slower performances when handling a large volume of training data, indicating potential limitations in scalability for such cases. Moreover, we found that the predictions were more effective when the training data focused on the same element at different energies, rather than multiple nuclei at the same energy. Despite its scalability and kernel challenges, the GP remains a powerful tool for smaller data sets and holds potential for further investigation in the future.

### 8.2.2 Boosted Decision Tree

---

A Boosted Decision Tree (BDT) is an advanced machine learning algorithm used for classification and regression tasks. It falls under the category of ensemble methods, which combine the predictions of multiple individual models to achieve better overall performances. BDT operates by building a sequence of decision trees using a training data set. Each decision tree partitions the data into subsets based on specific features to predict the target classification or output value (regression). The final prediction of the BDT is obtained by aggregating the predictions of all the individual decision trees, where each tree is assigned a weight based on its performance. During the learning process, the BDT focuses on improving its predictions by assigning more weight to examples that were misclassified and giving less importance to well-classified examples when

constructing subsequent trees [103]. As a result, the BDT can effectively model intricate relationships between data features and the target output [103].

Among the various machine learning library available in Scikit-learn, we chose to utilize the XGBoost (Extreme Gradient Boosting) model for regression tasks. XGBoost is adept at combining weak decision tree models to create a powerful ensemble model. Its regularization feature helps prevent over fitting, and it excels in handling large data sets efficiently [103]. Given the substantial amount of experimental data required for predicting reaction cross sections, XGBoost capabilities make it a suitable choice for our studies.

Due to the challenging nature of predicting the oscillations in the differential cross sections with respect to energy for each nucleus under study, we decided to focus on reactions with more predictable cross section shapes. As a result, the  $(p,\gamma)$  reactions were selected after ensuring that a large quantity of data was available. The choice of  $(p,\gamma)$  reactions was motivated by the desire to establish a connection between our experimental measurements and theoretical predictions, particularly considering the three  $(p,\gamma)$  cross section reactions measured on germanium in Part II.

A total of 173 sets of measurements were compiled from the experimental database EXFOR-NNDC [4] and the resulting cross section evolution as a function of energy are presented in Fig.71, using both linear and logarithmic scales. While no clear trend can be easily discerned from the logarithmic view, inspecting the experimental data on a linear scale reveals that the majority of curves exhibits an exponential-like behavior, with few exceptions. Interestingly, around energies of 3.4 MeV and 6 MeV, denoted by dotted lines, a distinct pattern emerges. At these energy regions, certain nuclei exhibit reaction cross sections significantly higher than their neighboring mass regions. These peculiar reactions occur around mass numbers  $A = 74$  and  $A = 120$ , within a range of  $\pm 5$  mass units. The shape of the reaction cross sections as a function of energy does not follow a simple exponential curve; instead, it takes the form of a pseudo-Lorentzian distribution, with a peak resulting from the opening of neutron channels. The competition between the open channels then leads to a rapid decline in the  $(p,\gamma)$  reaction cross sections as the energy increase.



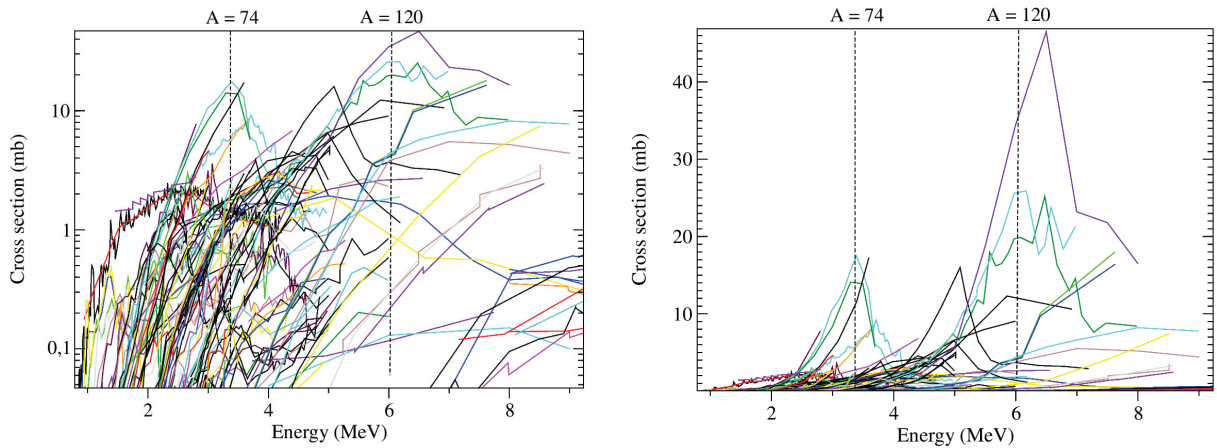


Figure 71: Two graphs of 173  $(p,\gamma)$  cross section reactions used for the BDT analysis and plotted as a function of energy. They are displayed in both logarithmic (left) and linear (right) scales.

In this section, we employed the same library, `scikit-learn`, as in the Bayesian inference, making the Python code and its functioning quite similar. However, for regression purposes, we utilized the XGBoost model, which comes with its own set of hyperparameters. In order to find the optimal hyperparameters for our data set, we used the Grid-Search approach (`GridSearch` tool in `scikit-learn`) which involve specifying a list of potential values for each hyperparameter we aimed to optimize. The model was then trained and evaluated for every combination of these values. Finally, the model with the hyperparameters that exhibited the best performance on the evaluation with experimental data was selected as the optimal one. By employing a dedicated tool name `GridSearchCV`, cross-validation was applied to assess the model performance.

In order to test the built model, six reactions removed from the training data sets were selected to be predicted using the BDT, covering a broad range of nuclear masses. To assist the code in capturing trends and comprehending the underlying physics within the data, 10 dimensions of information were included in the input variable  $X$  concerning reactions or nuclei. Each cross section ( $Y$ ) to be predicted requires then a 10-dimensional input vector  $X$ , containing essential features such as energy, mass, spin, and more. It is worth mentioning that thanks to the selected training data sets, the model was built with reactions falling within the Gamow window of most of reactions (up to 4 MeV).

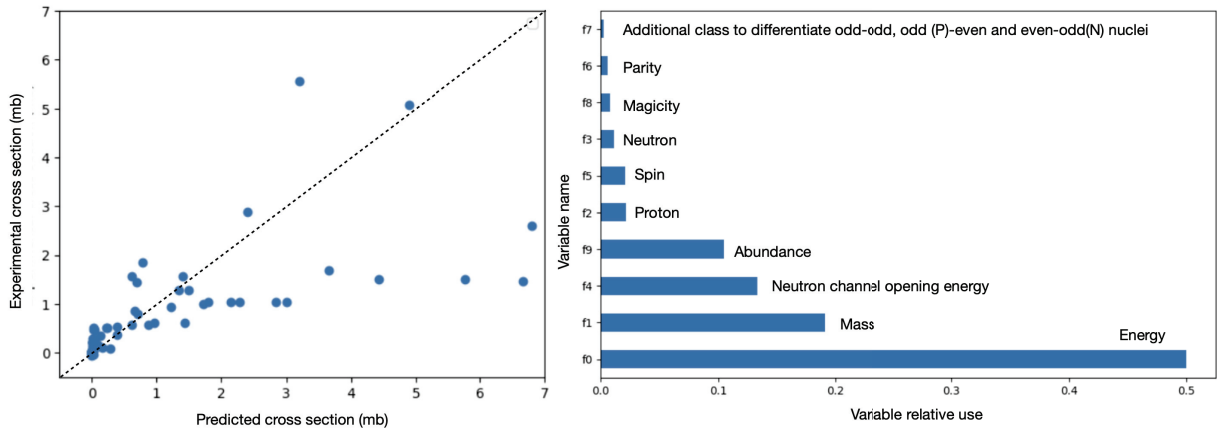


Figure 72: Left : Plot of the experimental cross section as a function of the predicted cross section. Right : Histogram showing the percentage utilization of different components of the vector  $X$  by the BDT.

Six of the BDT predictions can be found in Fig.103 of Appendix I. The overall predictions seems quite inconclusive, as it can also be quessed from the left plot of Fig.72. On this plot, for the six test reactions, we have displayed for all the energies at which cross sections have been measured, a point which coordinates correspond to the prediction by the BDT and the experimental data. While the first diagonal is well populated for low cross sections, a significant dispersion appears for highest cross sections.

Constructing a BDT involves handling numerous parameters, and it is not surprising that achieving accurate predictions can be challenging. In particle physics, BDT are commonly employed for classification tasks and can incorporate hundreds of dimensions to describe the underlying physics of reactions. Consequently, obtaining reliable predictions using this approach requires extensive methods and time. Moreover, the predictions and weights assigned to the data depend directly on the specific data set and its uncertainties. Therefore, a BDT with limited data may propagate errors in predictions more easily.

Finally, the right plot of Fig.72 presents valuable insights into the dependencies of the studied reactions by displaying the most utilized variables by the code. Notably, the abundance of elements is ranked as the fourth most influential parameter affecting the reaction cross section according to the code. This observation aligns with the understanding that cross sections are partially responsible for elemental abundances : taking a results-driven approach and tracing back to essential predictions can be sometimes meaningful strategy.

## 8.3 Cross section determination : Indirect approach

---

### 8.3.1 Bayesian Optimization : The MCMC method

---

Bayesian Optimization (BO) is an optimization technique that leverages probabilistic models to make informed decisions about which points to evaluate next in the search for the optimal solution. It is particularly useful when dealing with expensive or time-consuming objective functions. Instead of exhaustively exploring the entire parameter space, BO intelligently selects points to evaluate based on the information gained from previous evaluations. The process starts with an initial set of points sampled randomly from the parameter space. These points are used to build a surrogate probabilistic model, which estimates the objective function behavior. The model provides predictions and uncertainty estimates for unexplored regions. After each evaluation, the model is updated with the new data, refining its predictions. The optimization process continues iteratively, with the model guiding the search towards regions likely to contain the global optimum. This iterative and adaptive approach allows BO to efficiently find good solutions while minimizing the number of expensive function evaluations.

In Part II of this thesis, we observed that the key parameters affecting  $(p,\gamma)$  reactions are mostly the nuclear level density (NLD), the  $\gamma$ -strength, and the proton-nucleus optical potential. In this section, we will focus on applications of BO specifically to the NLD, a major influential parameter for cross sections. By leveraging available experimental data on nuclear level schemes, the BO enables us to use this information as a prior in the optimization process. Therefore, in this study, BO was utilized to estimate 98% confidence intervals for the Back-shifted Fermi Gas (BSFG) model implemented in Talys [104][105], using OSLO data [106]. The BSFG model parameters were optimized across the energy range, taking advantage of its applicability to proton capture excitation energies relevant to the p-process. Specifically, the model allows adjustments for four free parameters,  $\alpha$ ,  $\beta$ ,  $\gamma$ , and  $\delta$ , while a fifth parameter  $\tilde{a}$  captures the combined effects of  $\alpha$  and  $\beta$ . The ultimate objective was to improve these parameters accuracy and reduce prediction uncertainties related to the BSFG model.

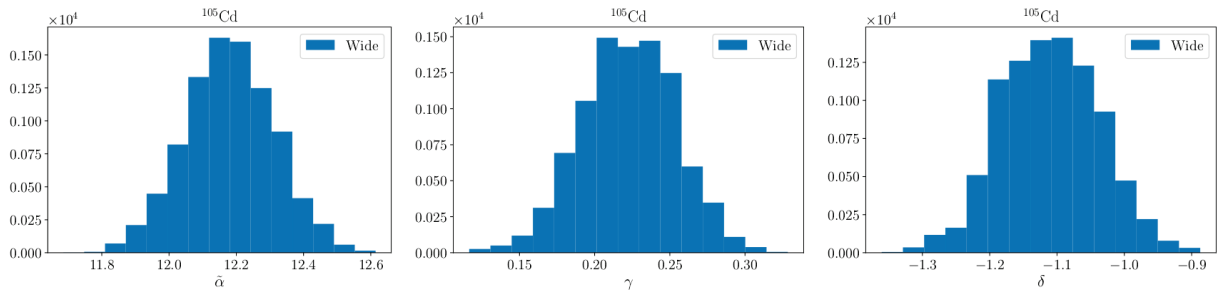


Figure 73: Histogram of three posterior distributions used to extract the three parameters of interest for adjusting the BSFG model.

Let's recall the Bayes equation (39), where the model evidence represents the sum of probabilities of all possible hypotheses, encompassing all potential parameter configurations. Generally, this sum cannot be calculated and one get ride of it because it is mainly a normalization factor in the right side of the Bayes equation (39). Indeed, Markov Chain Monte Carlo (MCMC) methods enable us to sample the likelihood times prior distribution to obtain the posterior distribution. In Fig.73, we demonstrate an example of the evaluation procedure, showing the obtained posteriors for the BSFG model parameters regarding the nuclear level density of  $^{105}\text{Cd}$ . The posteriors are plotted with a wide Gaussian prior having a standard deviation of 100%. By determining the characteristics of these posterior distributions, we can extract the optimal parameter together with 95% confidence limits.

In Fig.74, the left plot illustrates the predictions of the BSFG model after Bayesian inference and adjustments of the fitting parameters, alongside the experimental data. It is evident that the data points, used in the BO process, lie well within the predicted zone. Using the predicted confidence intervals, we endeavored to estimate the uncertainty in the cross-section of the reaction  $^{105}\text{Ag}(p, \gamma)^{105}\text{Cd}$ , where no experimental data were available. The prediction is depicted in the right plot of Fig.74. We observed a relatively narrow band of cross-section predictions when considering only the uncertainty associated to NLD in the reaction. The narrow band (1.5-3.3 MeV) within the Gamow window (in grey in the figure) suggests a minor influence of the nuclear level density in this energy range. However, the wider band predicted between 3.3-4.7 MeV shows a larger variation, with differences of up to approximately 1.5 mb between the upper and lower limits. Nonetheless, this variation is much lower when compared to the overall discrepancies arising from the utilization of different NLD models used in Talys for cross-section predictions, showing the

interest of Bayesian approach.

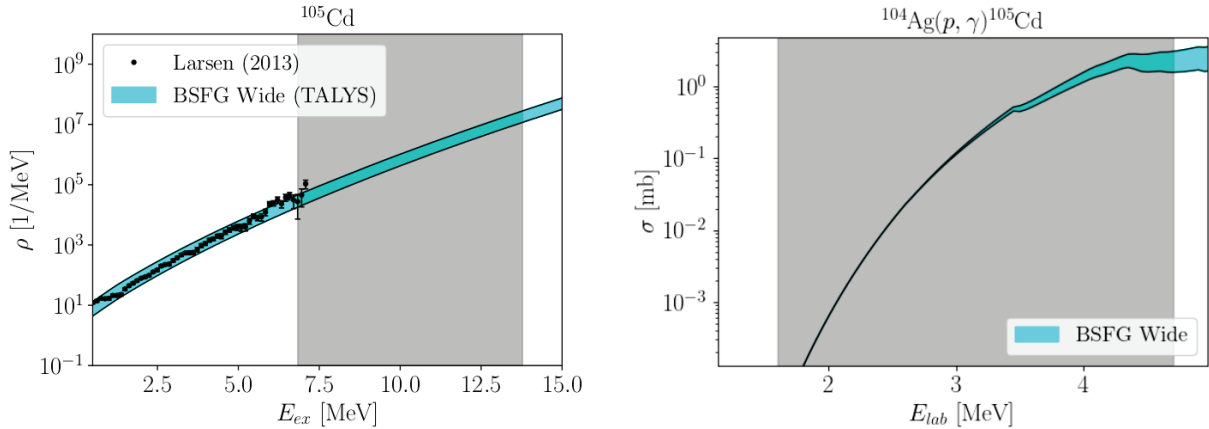


Figure 74: Left : Comparison between Bayesian optimization predictions and nuclear level density data. Right: Estimation of the cross section uncertainties associated with NLD in a 95% confidence range. The grey part represents the Gamow window of the reaction.

This ongoing research is giving promising results and offering valuable insights for improving astrophysical model calculations and cross-section predictions. However, its application is limited by the availability of data, which can be not accessible for all reactions of interest. Furthermore, the technique requires experimental data to efficiently adjust predictions, making it unsuitable for cases like the OMP parameters. In this context, Achmet Chalil, a postdoctoral researcher from our research group, has been at the forefront of developing and refining the Monte Carlo code for this application within our research group, contributing significantly to the progress of this work.

## 8.4 Discussion

---

In this section, we have delved into three specific machine learning techniques that can greatly assist in predictions and mitigate theoretical uncertainties. These techniques, among numerous others available, showcase the vast possibilities for exploration, while also underscoring the challenges associated with each approach explored.

The Gaussian Process stands out as a relatively easy-to-use technique, especially when dealing with limited data sets, offering valuable confidence intervals for its predictions. However, its main challenge lies in the need to define appropriate equations for data description and implementation.

The Boosted Decision Tree is relatively user-friendly and proves valuable when dealing with large data sets, providing insights into the major variables involved and their influence on a prediction as long as the variables and data quality meet acceptable standards. However, the manual parameter tuning can make the process time-consuming and tedious for potentially limited improvements.

The Bayesian Optimization technique, while delivering immediate impact, can be more time-consuming to master compared to other methods. It adopts a comprehensive approach, utilizing both theoretical models and existing experimental data. However, its applicability is limited to regions near the available experimental data and may not be well-suited for handling complex dependencies beyond those regions.

Each of these techniques comes with its own set of advantages and disadvantages, which may not be immediately apparent when one starts working with them. This can make the choice between them quite challenging in the beginning. Therefore, to facilitate decision-making, a comparative summary of the advantages and disadvantages of each technique is proposed in the Table 13.

ML technique	Amount of data required	Maximal amount of data	Learning time	Results interpretation	Equation requirement
GP	few	few	rapid	clear	yes
BDT	few	a lot	rapid	not clear	no
BO	few	few	long	clear	yes

Table 13: Advantages and disadvantages of the explored ML techniques.

The findings from the table highlight the distinct nature of these techniques, each with its unique strengths and limitations. Rather than competing, they offer complementary approaches depending on the specific context of the study. Short and simple techniques may reach their limitations quickly, while more evolved methods can provide deeper insights over time, albeit with a slower and steady development process. Ultimately, the choice of technique depends on the specific requirements and objectives of the analysis.

Part VI

# THESIS GLOBAL CONCLUSION AND PERSPECTIVES



Although the  $\gamma$ -process involves a reaction network with numerous individual reactions, not all reactions within the network need to be precisely known. Rather, it is crucial to accurately understand the dominant reaction sequences, and particularly, to identify the slowest reaction within such a sequence that governs the extent of processing. Following this line of reasoning, it was shown that several proton-induced reactions on germanium isotopes play a crucial role in the production of  $^{74}\text{Se}$ , the lightest p-nucleus. Current anomalies are observed concerning its abundance, highlighting the importance to know accurately the reactions leading to its production and destruction. A previous study was conducted by Naqvi *et al.*[53], to measure the  $^{72}\text{Ge}(p, \gamma)$  cross section by in-beam  $\gamma$ -summing. This result did not solve the  $^{74}\text{Se}$  issue. Our measurement is higher by a significant margin of 38%. This discrepancy might be attributed to the different measurement techniques employed. However, it is crucial to thoroughly investigate the impact of this new measurement on the reaction rates affecting the abundance of  $^{74}\text{Se}$  nuclei. Although this aspect was not originally included in this thesis, ongoing efforts are being made in this direction.

New measurements of the  $^{70}\text{Ge}(p, \gamma)$  and  $^{76}\text{Ge}(p, n)$  reaction cross sections have also been performed, and fall within the range of acceptance of the data obtained by Kiss *et al.*[1].

Finally, two previously unmeasured cross sections involving the odd-odd nucleus  $^{73}\text{Ge}$  were investigated. It is interesting that a phenomenological TALYS model could successfully predict these specific measurements, even in the presence of a significant number of uncertainties associated with the nuclear parameters. However it remains difficult to identify a model that performs better than the others for the all set of data available in this region.

While the  $(p, \gamma)$  reaction was recognized as crucial for studying light p-nuclei, it is the  $(\gamma, \alpha)$  reactions that have been emphasized for their influence on heavy p-nuclei. Despite ongoing discussions about new activation experiments to measure  $(\alpha, \gamma)$  capture reaction cross sections within our group, we have chosen to focus first on studying the  $\alpha$ -elastic scattering which is a fundamental tool for the improvement of the  $\alpha$ -OMP. For this study, an experiment is currently awaiting scheduling. A significant portion of this thesis involved mechanical studies and manufacturing pieces for the setup, especially to include the use of PIPS detectors at backward angles. This involved conducting simulations, practical tests and prospection. The thesis therefore marks the initiation of a comprehensive experimental program which will ultimately help the develop-



ment of a global  $\alpha$ -nucleus optical potential and the incorporation of a vast amount of experimental data for reaction rate calculations.

While the number of studied reactions remains extremely small compared to the vast number of reactions involved in a  $\gamma$ -process network, we decided, at IP2I, to start developing techniques that can effectively address the complex task of relating existing nuclear data to model predictions over the whole range of involved nuclei. To tackle this challenge, one proposed solution was the adoption of machine learning techniques, as explored in part IV of this thesis. In particular, Bayesian inference that relies on probabilistic modeling, leveraging experimental data to make predictions. The larger and more comprehensive the data set, the more robust the links and predictions derived from it. This underscores the importance of understanding and harnessing the insights of these tools, as they hold great potential for advancing our understanding of complex astrophysical processes.

The development of experimental techniques holds great promise as well. Activation measurements of cross sections is only feasible for reactions leading to radioactive products. However, advancements in in-beam techniques offer the possibility of analyzing a broader range of reactions, provided we can distinguish the emitted radiations accurately. Furthermore, enhancing the Accelerator Mass Spectrometry (AMS) technique would enable rapid measurements of multiple reaction cross sections, significantly accelerating data collection for p-nuclei studies. We can also mention on-going development of high-intensity proton and alpha beams, such as NFS-SPIRAL2, that could be used to access very low cross sections. On the other hand, facilities for the study of  $\gamma$ -induced reactions are also developing, such as ELI-NP (Extreme Light Infrastructure) in Romania.

Overall, a wealth of new nuclear data are expected to enlighten the nucleosynthesis issues that have been discussed in this thesis, in the coming years. A great challenge will be to relate these data in an efficient way to the improvement of nuclear models and the selection of relevant astrophysical scenarios.

Part VII  
ANNEXES

# A EURISOTOP : Targets isotopic percentages

## A.1 Analysis certificate of the target T[<sup>70</sup>Ge]

PRODUCT	<b>GERMANIUM 70</b>		
REFERENCE	<b>MGE70M</b>		
ANALYSIS N°	<b>014</b>		
LOT	<b>P2091</b>		

1 ISOTOPE	:	<b>70Ge</b>	isotope / mg	<b>113,6</b>	element / mg	<b>118,5</b>
2 CHEMICAL FORM	:	<b>Metal</b>	Compound / mg	<b>118,5</b>		
3 ISOTOPIC CONTENT	:	<b>95,85</b>	%			

ISOTOPE	70	72	73	74				
Content %	<b>95,85</b>	<b>4,09</b>	<b>0,04</b>	<b>0,02</b>				

4 CHEMICAL IMPURITIES

ELEMENT	<b>Ag</b>	<b>Al</b>	<b>Au</b>	<b>B</b>	<b>Ba</b>	<b>Be</b>	<b>Bi</b>	<b>Ca</b>	<b>Cd</b>	<b>Cl</b>	<b>Co</b>
Ppm	-	<b>500</b>	-	-	-	-	-	<b>&lt;50</b>	<b>30</b>	-	<b>50</b>
ELEMENT	<b>Cr</b>	<b>Cs</b>	<b>Cu</b>	<b>Dy</b>	<b>Er</b>	<b>Eu</b>	<b>Fe</b>	<b>Ga</b>	<b>Gd</b>	<b>Ge</b>	<b>Hf</b>
Ppm	<b>10</b>	-	<b>30</b>	-	-	-	<b>50</b>	-	-	-	-
ELEMENT	<b>Ho</b>	<b>In</b>	<b>Ir</b>	<b>K</b>	<b>La</b>	<b>Li</b>	<b>Lu</b>	<b>Mg</b>	<b>Mn</b>	<b>Mo</b>	<b>Na</b>
Ppm	-	-	-	-	-	-	-	-	<b>50</b>	-	-
ELEMENT	<b>Nd</b>	<b>Ni</b>	<b>Pb</b>	<b>Pr</b>	<b>Rb</b>	<b>Rh</b>	<b>Ru</b>	<b>Sb</b>	<b>Si</b>	<b>Sm</b>	<b>Sn</b>
Ppm	-	-	-	-	-	-	-	-	-	-	-
ELEMENT	<b>Sr</b>	<b>Ta</b>	<b>Tb</b>	<b>Tl</b>	<b>Tm</b>	<b>V</b>	<b>W</b>	<b>Y</b>	<b>Yb</b>	<b>Zn</b>	<b>Zr</b>
Ppm	<b>&lt;50</b>	-	-	-	-	-	-	-	-	<b>10</b>	-

5 ANALYTICAL METHOD : **ICP - MS**

RESPONSABLE QUALITE	DATE	VISA
<b>F. ROBERT</b>	<b>27/07/2016</b>	

Figure 75: Detailed composition of the T[<sup>70</sup>Ge] target provided by EURISOTOP.

## A.2 Analysis certificate of the target T<sup>[72Ge]</sup>

PRODUCT	<b>GERMANIUM 72</b>										
REFERENCE	<b>MGE72M</b>										
ANALYSIS N°	<b>162</b>										
LOT	<b>P0611</b>										

1 ISOTOPE	:	<b>72Ge</b>	isotope / mg	<b>98,2</b>	element / mg	<b>100,0</b>
2 CHEMICAL FORM	:	<b>Metal</b>	Compound / mg	<b>100,0</b>		
3 ISOTOPIC CONTENT	:	<b>98,20</b>	%			

ISOTOPE	70	72	73	74	76			
Content %	<b>0,29</b>	<b>98,20</b>	<b>0,29</b>	<b>1,04</b>	<b>0,18</b>			

4 CHEMICAL IMPURITIES

ELEMENT	Ag	Al	Au	B	Ba	Be	Bi	Ca	Cd	Cl	Co
Ppm	-	<b>10</b>	-	-	-	-	-	<b>20</b>	-	-	-
ELEMENT	Cr	Cs	Cu	Dy	Er	Eu	Fe	Ga	Gd	Ge	Hf
Ppm	<b>&lt;30</b>	-	<b>&lt;5</b>	-	-	-	<b>&lt;8</b>	<b>10</b>	-	-	-
ELEMENT	Ho	In	Ir	K	La	Li	Lu	Mg	Mn	Mo	Na
Ppm	-	<b>30</b>	-	<b>30</b>	-	-	-	<b>&lt;5</b>	<b>&lt;5</b>	-	<b>10</b>
ELEMENT	Nd	Ni	Pb	Pr	Rb	Rh	Ru	Sb	Si	Sm	Sn
Ppm	-	<b>&lt;10</b>	<b>20</b>	-	-	-	-	-	<b>20</b>	-	<b>20</b>
ELEMENT	Sr	Ta	Tb	Ti	Tm	V	W	Y	Yb	Zn	Zr
Ppm	-	-	-	-	-	-	-	-	-	-	-

5 ANALYTICAL METHOD : **ICP - MS**

RESPONSABLE QUALITE	DATE	VISA
<b>F. ROBERT</b>	<b>01/03/2016</b>	

Figure 76: Detailed composition of the T<sup>[72Ge]</sup> target provided by EURISOTOP.

### A.3 Analysis certificate of the target T<sup>[73Ge]</sup>

PRODUCT	<b>GERMANIUM 73</b>										
REFERENCE	<b>MGE73M</b>										
ANALYSIS N°	<b>059</b>										
LOT	<b>Q2501</b>										

1 ISOTOPE	:	<b>73Ge</b>	isotope / mg	<b>48,2</b>	element / mg	<b>50,0</b>
2 CHEMICAL FORM	:	<b>Metal</b>	Compound / mg	<b>50,0</b>		
3 ISOTOPIIC CONTENT	:	<b>96,34</b>	%			

ISOTOPE	<b>70</b>	<b>72</b>	<b>73</b>	<b>74</b>	<b>76</b>			
Content %	<b>0,005</b>	<b>1,36</b>	<b>96,34</b>	<b>2,29</b>	<b>0,005</b>			

4 CHEMICAL IMPURITIES

ELEMENT	<b>Ag</b>	<b>Al</b>	<b>Au</b>	<b>B</b>	<b>Ba</b>	<b>Be</b>	<b>Bi</b>	<b>Ca</b>	<b>Cd</b>	<b>Cl</b>	<b>Co</b>
ppm	-	<b>65</b>	-	-	-	-	-	<b>65</b>	<b>65</b>	-	<b>65</b>
ELEMENT	<b>Cr</b>	<b>Cs</b>	<b>Cu</b>	<b>Dy</b>	<b>Er</b>	<b>Eu</b>	<b>Fe</b>	<b>Ga</b>	<b>Gd</b>	<b>Ge</b>	<b>Hf</b>
ppm	<b>65</b>	-	<b>65</b>	-	-	-	<b>65</b>	-	-	-	-
ELEMENT	<b>Ho</b>	<b>In</b>	<b>Ir</b>	<b>K</b>	<b>La</b>	<b>Li</b>	<b>Lu</b>	<b>Mg</b>	<b>Mn</b>	<b>Mo</b>	<b>Na</b>
ppm	-	-	-	-	-	-	-	-	<b>65</b>	-	-
ELEMENT	<b>Nd</b>	<b>Ni</b>	<b>Pb</b>	<b>Pr</b>	<b>Rb</b>	<b>Rh</b>	<b>Ru</b>	<b>Sb</b>	<b>Si</b>	<b>Sm</b>	<b>Sn</b>
ppm	-	-	-	-	-	-	-	-	-	-	-
ELEMENT	<b>Sr</b>	<b>Ta</b>	<b>Tb</b>	<b>Ti</b>	<b>Tm</b>	<b>V</b>	<b>W</b>	<b>Y</b>	<b>Yb</b>	<b>Zn</b>	<b>Zr</b>
ppm	-	-	-	-	-	-	-	-	-	<b>65</b>	-

5 ANALYTICAL METHOD : **ICP - MS**

RESPONSABLE QUALITE	DATE	VISA
<b>F. ROBERT</b>	<b>08/09/2017</b>	

Figure 77: Detailed composition of the T<sup>[73Ge]</sup> target provided by EURISOTOP.

## B Results of ICP-MS analysis

---

### B.1 Preliminary step to isotopic measurements

---

Before being analyzed, the two T<sup>[70,73Ge]</sup> targets were dissolved using a mixture of nitric acid (HNO<sub>3</sub>) and hydrochloric acid (HCl) solutions to be inserted into the analysis chamber. This step introduces elements that can contaminate the final mass spectrum and requires a separate measurement. The Fig.78 shows the obtained spectrum for the acid solution without the presence of germanium inside. Interferences at mass 76 are highlighted and will be subtracted for the measurements in presence of germanium.

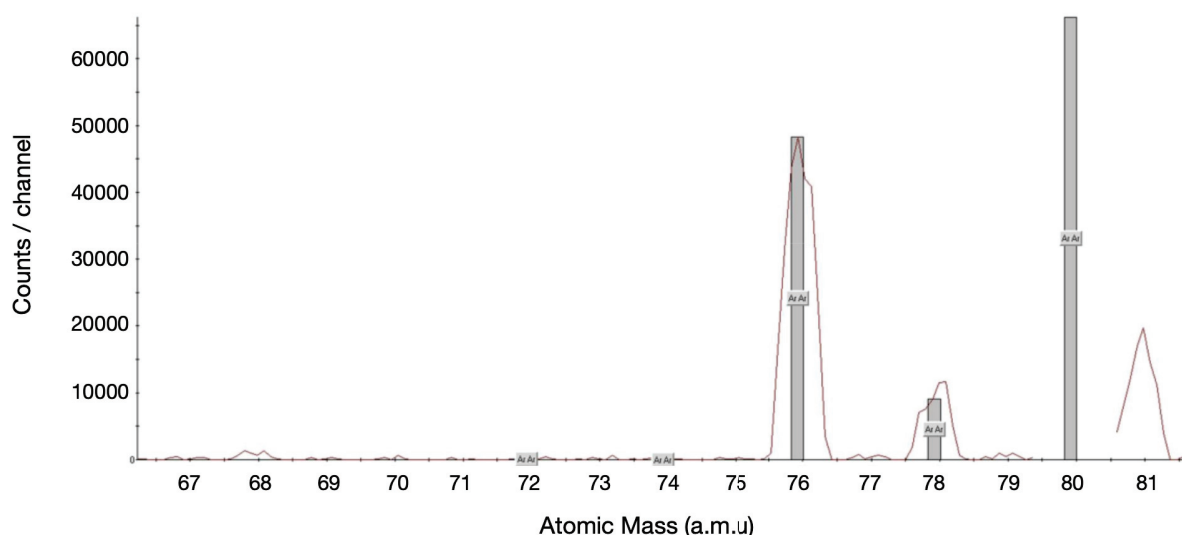


Figure 78: The experimental interference spectrum obtained from the mixture of nitric acid and hydrochloric acid solutions is shown in red. The bars represent the expected components in the plasma, with argon being the carrier gas in the ICP-MS technique.

## B.2 ICP-MS measurements : target T<sup>[70Ge]</sup>

---

The spectrum obtained from the T<sup>[70Ge]</sup> target and the spectrum from a naturally occurring germanium target according to IUPAC standards are shown in pink and violet on Fig.79, respectively. The solid lines represent the data collected using pulse counting mode of the detector, while the dashed lines represent the data collected using an analog mode triggered automatically at a certain detection threshold (to protect the detector's electron multiplier). The mass spectrum obtained for the T<sup>[70Ge]</sup> target overlaps with the reference spectrum known as the "IUPAC standard<sup>1</sup>" (International Union of Pure and Applied Chemistry) [58]. Since the "T<sup>[70Ge]</sup> enriched target" is finally a natural germanium target, the IUPAC isotopic percentages and their associated uncertainties will be used for calculating reaction cross sections.

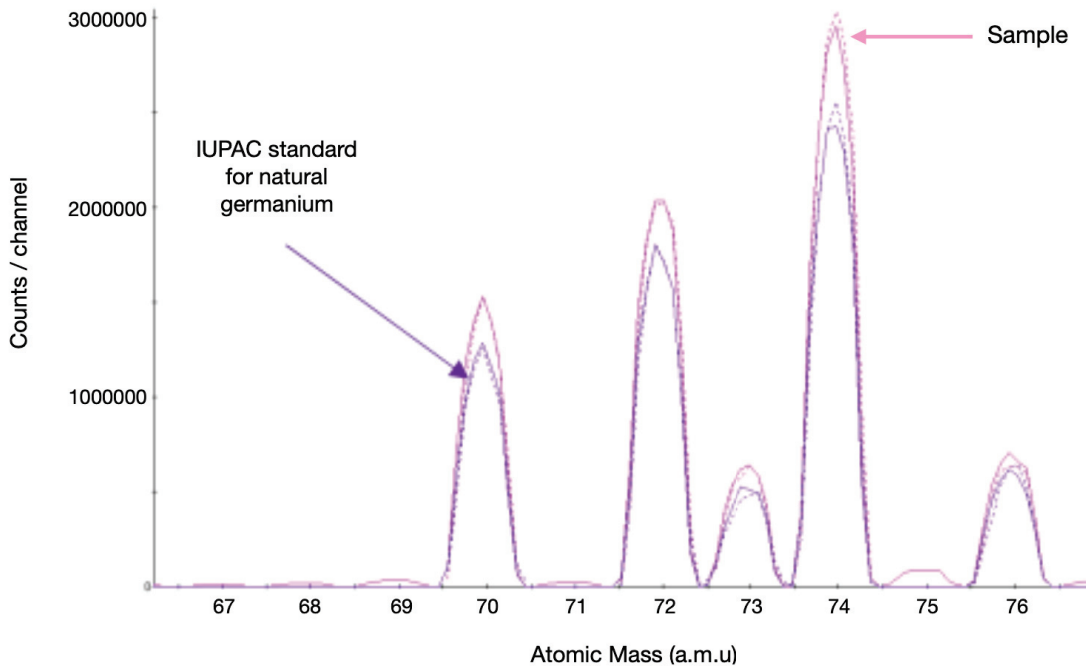


Figure 79: Abundance spectrum of the stable germanium isotopes detected in the T<sup>[70Ge]</sup> target.

---

<sup>1</sup>The IUPAC standards represent a worldwide database of references to fix all information related to chemical elements such as nomenclature, terminology, symbols, abundances etc...

### B.3 ICP-MS measurements : target T[<sup>73</sup>Ge]

---

The experimental spectrum of the T[<sup>73</sup>Ge] target is shown in Fig. 80. It indicates the presence of <sup>73</sup>Ge at a level of 96% which is consistent with the initial announcement by EURISOTOP. The figure shows the presence of the <sup>72</sup>Ge and <sup>74</sup>Ge isotopes also initially reported by the supplier analysis certificate of the powder (see Appendix.A.3).

The solid line in the figure is (as the T[<sup>70</sup>Ge] measurement) obtained using the pulse counting mode, while the dashed line is obtained using the analog mode. The peak at mass 72.5 observed in the solid line is an artifact representing the growth of the mass 73 peak prior to automatic switching to the analog mode.

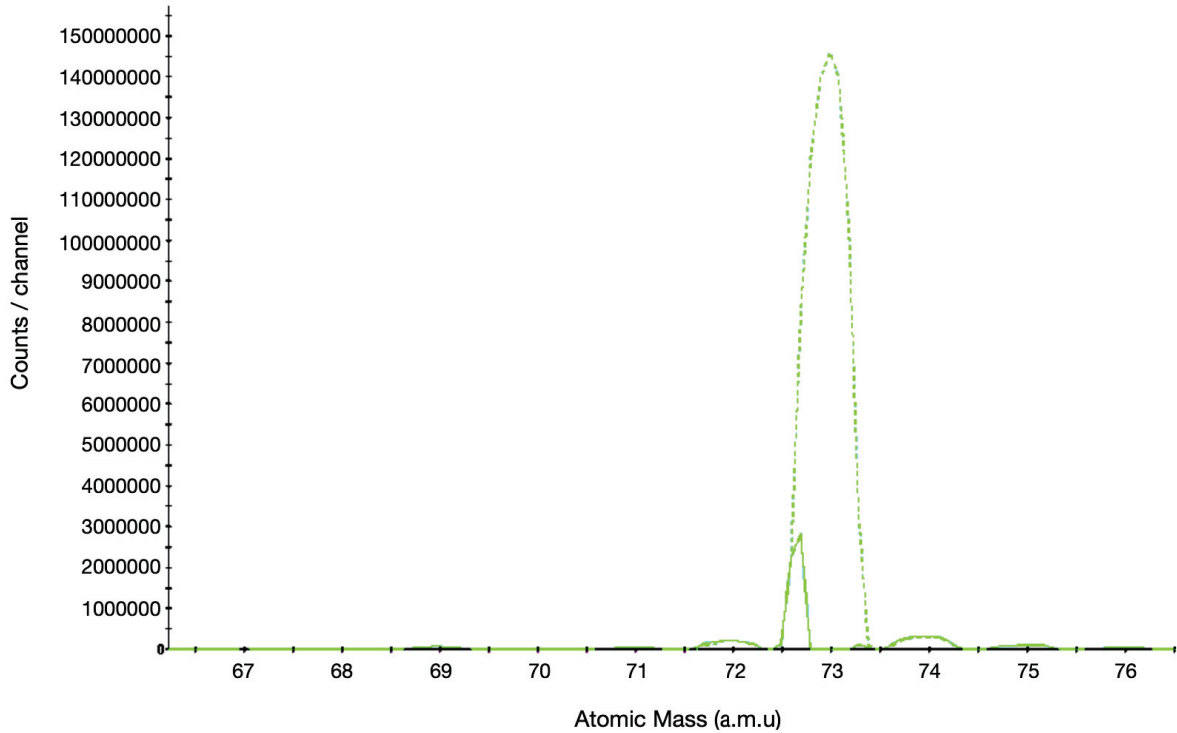



Figure 80: Abundance spectrum of the stable germanium isotopes detected in the T[<sup>73</sup>Ge] target.



# C Instrumentation : Germanium detector



**Features**

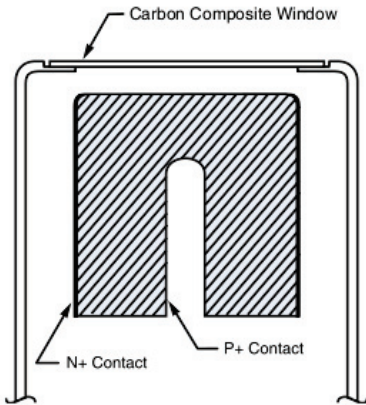
- Spectroscopy from 3 keV to >10 MeV
- Wide range of efficiencies
- High resolution – good peak shape
- Excellent timing resolution
- High energy rate capability
- Diode FET protection
- Warm-up/HV shutdown
- High rate indicator

## Extended Range Coaxial Ge Detectors (XtRa)

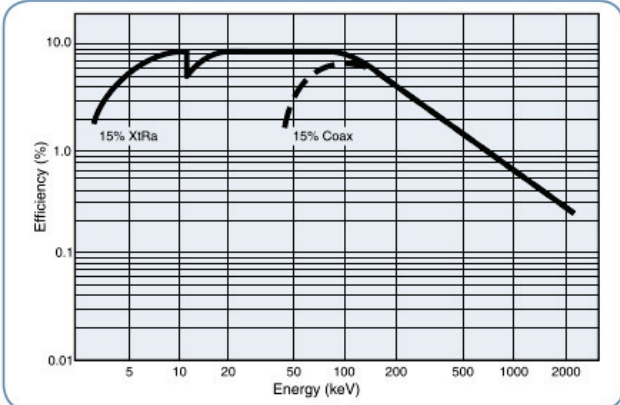
**Description**

The CANBERRA XtRa is a coaxial germanium detector having a unique thin-window contact on the front surface which extends the useful energy range down to 3 keV. Conventional coaxial detectors have a lithium-diffused contact typically between 0.5 and 1.5 mm thick. This dead layer stops most photons below 40 keV or so rendering the detector virtually worthless at low energies. The XtRa detector, with its exclusive thin entrance window and with a Carbon Composite cryostat window, offers all the advantages of conventional standard coaxial detectors such as high efficiency, good resolution, and moderate cost along with the energy response of the more expensive Reverse Electrode Ge (REGe) detector.

The response curves (below) illustrate the efficiency of the XtRa detector compared to a conventional Ge detector. The effective window thickness can be determined experimentally by comparing the intensities of the 22 keV and 88 keV peaks from <sup>109</sup>Cd. With the standard 0.6 mm Carbon Composite window, the XtRa detector is guaranteed to give a 22 to 88 keV intensity ratio of greater than 20:1. Beryllium and aluminum windows are also available.



**XtRa Coaxial Ge Detector**



**Typical Efficiency curves comparing XtRa with Be window and Coax Detectors with detector-source spacing of 2.5 cm**

CANBERRA IS THE NUCLEAR MEASUREMENTS BUSINESS UNIT OF AREVA.

[www.canberra.com](http://www.canberra.com)

We are **“Measurement solutions for nuclear safety and security.”**

C37440 4/10 Printed in U.S.A.

Figure 81: Front page of the data sheet for the germanium "XtRa" MIRION detector (formerly Canberra) used in the activation experiment [41].

## Extended Range Coaxial Ge Detectors (XtRa)

### XtRa GERMANIUM DETECTOR

#### General Specifications and Information

Standard configuration includes:

- Vertical Slimline dipstick cryostat with Carbon Composite window and 30 liter Dewar.
- Model 2002C preamplifier with 3 meter bias, high voltage inhibit, signal and power cables.

Specify cryostat option from options price list.

Resolutions at 22 keV and 88 keV are **typical values**, not specification limits.

The XtRa detector is guaranteed to give a 22 to 88 keV intensity ratio of greater than 20:1.

Model Number	Relative Efficiency (%) ≥	Full Width Half Max (FWHM) Resolution (keV)			Peak to Compton Ratio (P/C)	Endcap diameter mm (in.)
		At 22 keV energy	At 88 keV energy	At 1.3 MeV energy		
GX1018	10	0.7	0.8	1.8	40:1	76 (3.0)
GX1020	10	0.8	0.9	2.0	38:1	76 (3.0)
GX1518	15	0.7	0.8	1.8	46:1	76 (3.0)
GX1520	15	0.8	0.9	2.0	42:1	76 (3.0)
GX2018	20	0.7	0.8	1.8	50:1	76 (3.0)
GX2020	20	0.9	0.9	2.0	46:1	76 (3.0)
GX2518	25	0.7	0.8	1.8	54:1	76 (3.0)
GX2520	25	0.9	0.9	2.0	50:1	76 (3.0)
GX3018	30	0.7	0.8	1.8	58:1	76 (3.0)
GX3020	30	0.9	1.0	2.0	54:1	76 (3.0)
GX3518	35	0.8	0.9	1.8	60:1	76 (3.0)
GX3520	35	0.9	1.0	2.0	54:1	76 (3.0)
GX4018	40	0.8	0.9	1.8	62:1	76 (3.0)*
GX4020	40	1.0	1.1	2.0	56:1	76 (3.0)*
GX4518	45	0.9	1.0	1.8	63:1	83 (3.25)
GX4520	45	1.0	1.1	2.0	58:1	83 (3.25)
GX5019	50	0.9	1.0	1.9	64:1	83 (3.25)*
GX5021	50	1.1	1.2	2.1	58:1	83 (3.25)*
GX5519	55	1.0	1.1	1.9	64:1	89 (3.5)
GX5521	55	1.1	1.2	2.1	60:1	89 (3.5)
GX6020	60	1.0	1.1	2.0	66:1	89 (3.5)
GX6022	60	1.1	1.2	2.2	60:1	89 (3.5)
GX6520	65	1.0	1.1	2.0	68:1	89 (3.5)
GX6522	65	1.1	1.2	2.2	62:1	89 (3.5)
GX7020	70	1.0	1.1	2.0	70:1	89 (3.5)*
GX7022	70	1.1	1.2	2.2	64:1	89 (3.5)*
GX8021	80	1.0	1.1	2.1	72:1	95 (3.75)
GX8023	80	1.1	1.2	2.3	66:1	95 (3.75)
GX9021	90	1.2	1.3	2.1	78:1	95 (3.75)
GX9023	90	1.3	1.4	2.3	70:1	95 (3.75)
GX10021	100	1.2	1.3	2.1	78:1	95 (3.75)*
GX10023	100	1.3	1.4	2.3	70:1	95 (3.75)*

For availability of detectors above 100% relative efficiency consult factory.

Model Number	Relative Efficiency (%) ≥	Full Width Half Max (FWHM) Resolution (keV)			Peak to Compton Ratio (P/C)	Endcap diameter mm (in.)
		At 22 keV energy	At 88 keV energy	At 1.3 MeV energy		
GX11021	110	1.2	1.3	2.1	78:1	102 (4.0)
GX11023	110	1.3	1.4	2.3	70:1	102 (4.0)
GX12021	120	1.2	1.3	2.1	78:1	102 (4.0)
GX12023	120	1.3	1.5	2.3	70:1	102 (4.0)

\*Note: Due to variations in crystal size endcap diameter may be larger. For guaranteed endcap diameter or custom specifications and hardware customization consult factory.

Above specifications are in accordance with IEEE Std 325-1996. Resolution performance is tested with Lynx<sup>®</sup> digital MCA. For resolution performance guarantee using other CANBERRA digital MCAs consult factory.



Lynx is a registered trademark of Canberra Industries, Inc.

© 2010 Canberra Industries, Inc. All rights reserved.

Figure 82: Back page of the data sheet for the MIRION 'XtRa' germanium detector (formerly Canberra) used in the activation experiment [41].

# D Arsenic decay schemes

## D.1 Decay schemes of the $^{71}\text{As}$

Below the decay schemes of one of the radionuclides detected in the natural germanium target in Fig.83.

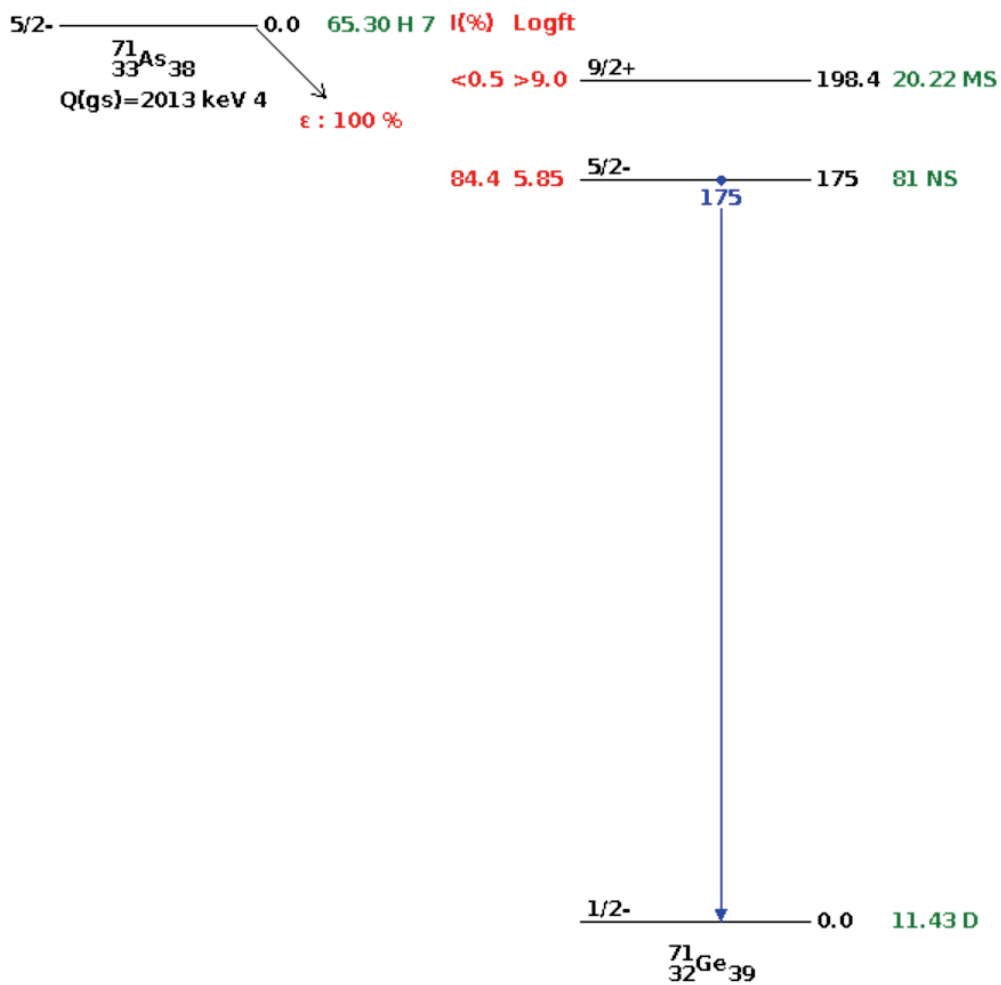


Figure 83: Decay radiation scheme of the  $^{71}\text{As}$  between the energy level [0-200 keV] [4].

## D.2 Decay schemes of the $^{76}\text{As}$

Below the decay schemes of one of the radionuclides detected in the natural germanium target 84.

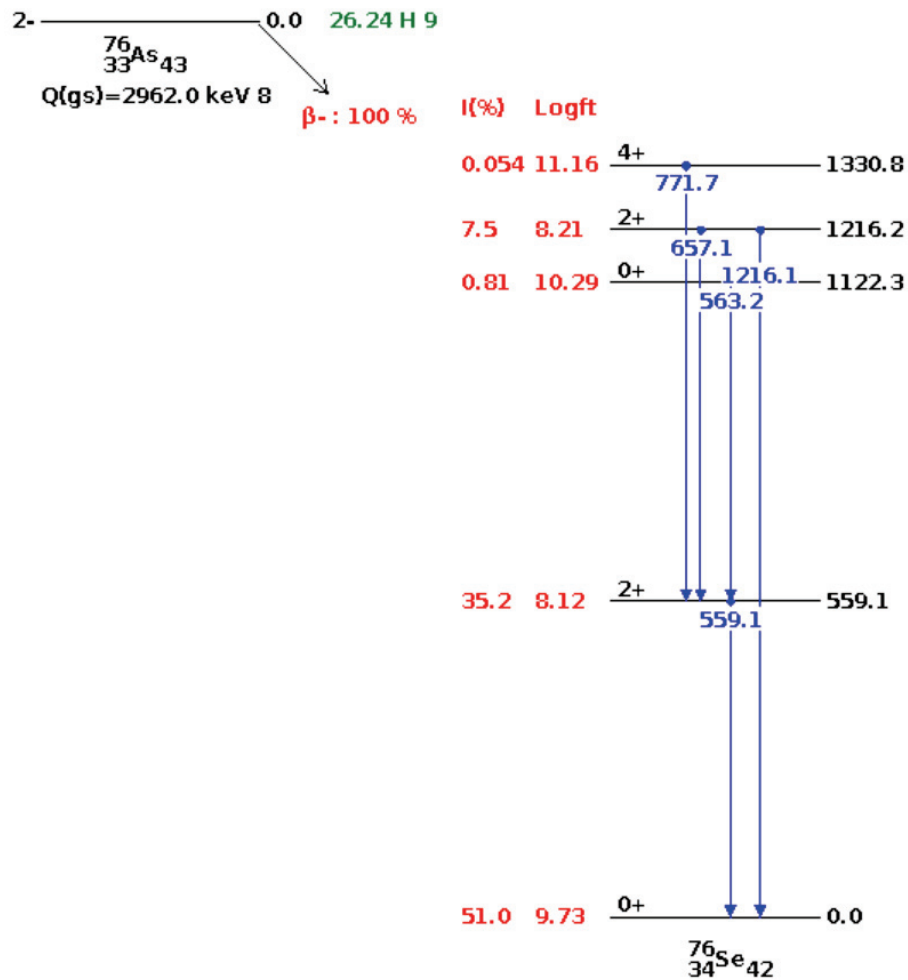


Figure 84: Decay radiation scheme of the  $^{76}\text{As}$  between the energy level [0-1500 keV] [4].

### D.3 Decay schemes of the $^{73}\text{As}$

Below the decay schemes of the radionuclides detected in the T[ $^{72}\text{Ge}$ ] and T[ $^{73}\text{Ge}$ ] targets 85.

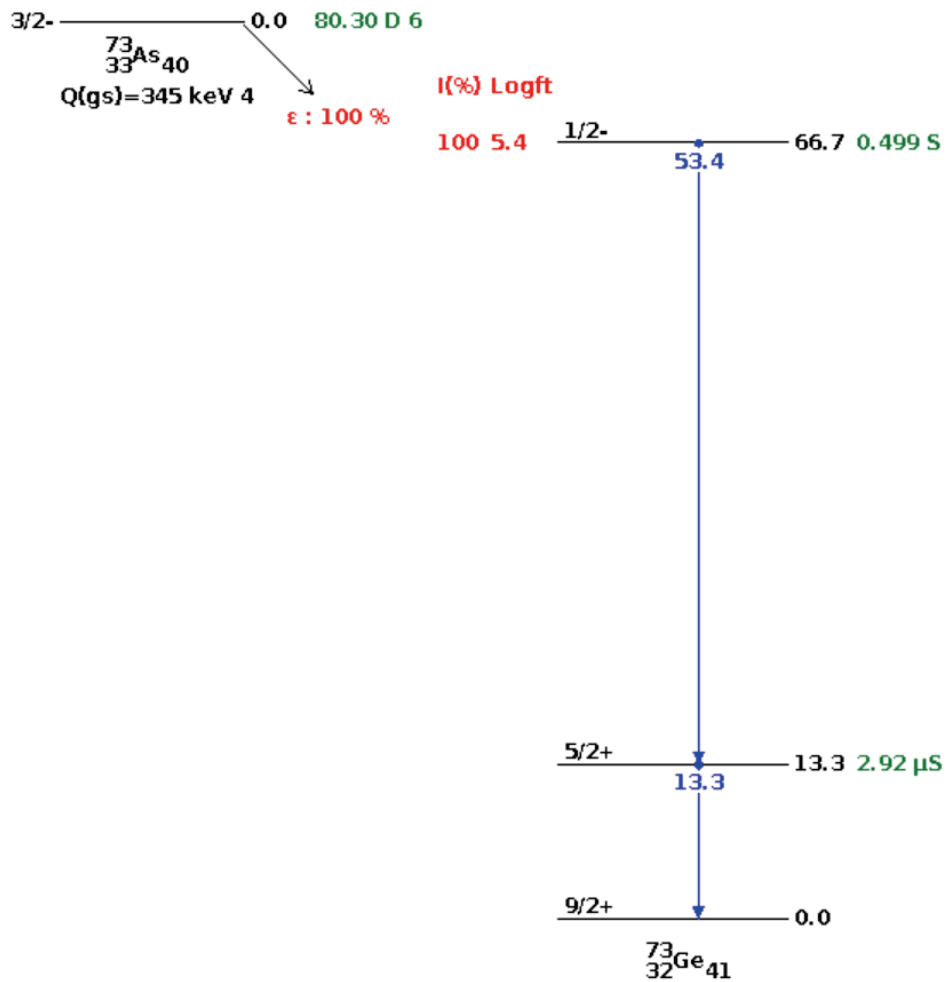


Figure 85: Decay radiation scheme of the  $^{73}\text{As}$  between the energy level [0-73 keV] [4].

## D.4 Decay schemes of the $^{74}\text{As}$

Below the decay schemes of one of the radionuclides detected in the T[ $^{73}\text{Ge}$ ] target 86.

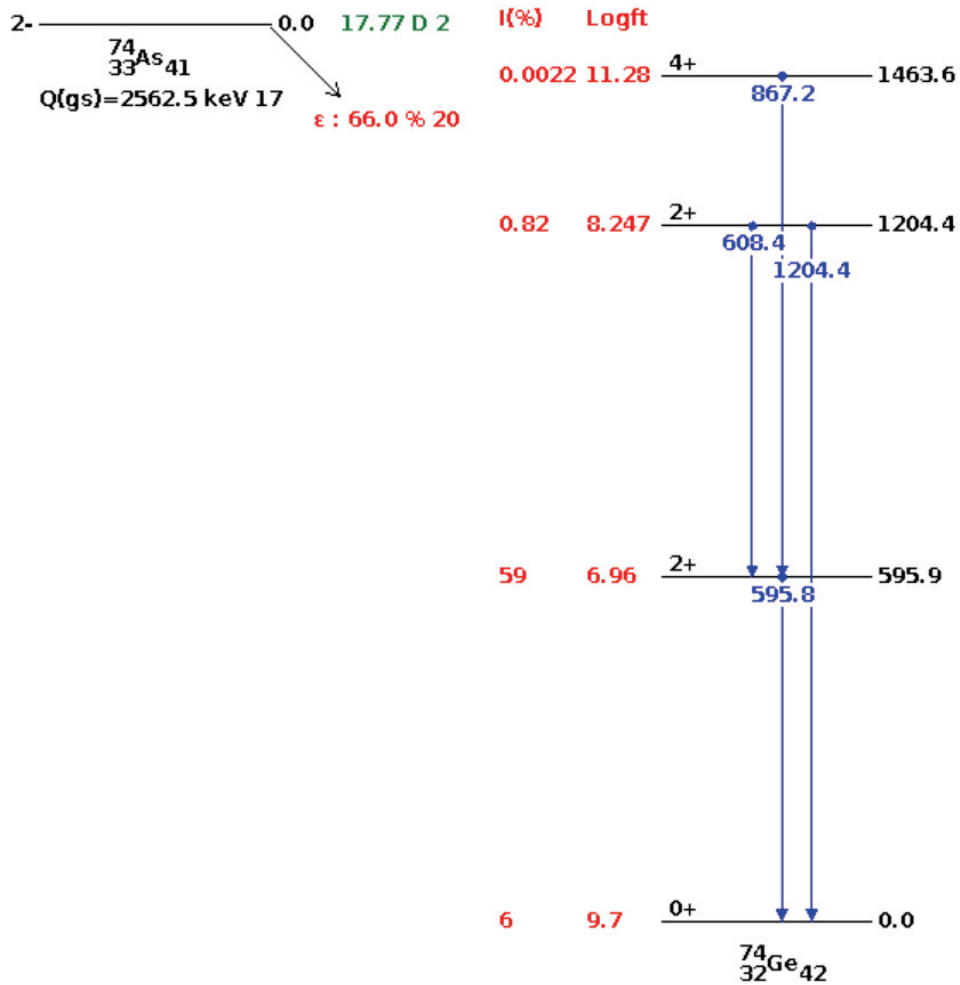


Figure 86: Decay radiation scheme of the  $^{74}\text{As}$  between the energy level [0-1470 keV] and originating from an electron capture [4].

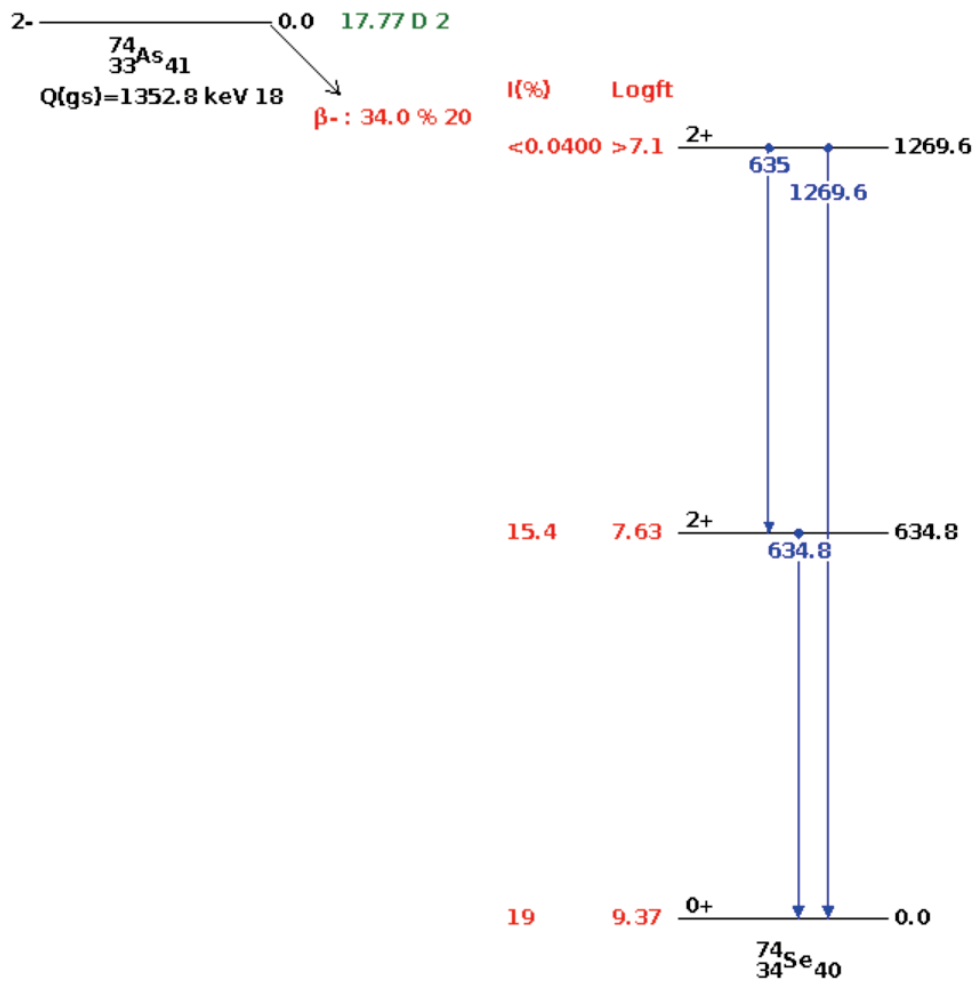


Figure 87: Decay radiation scheme of the  $^{74}\text{As}$  between the energy level [0-1270 keV] and originating from a beta decay [4].

# E Monte Carlo simulations for Ge efficiency determination

---

## E.1 Comparison of experimental vs. simulated data

---

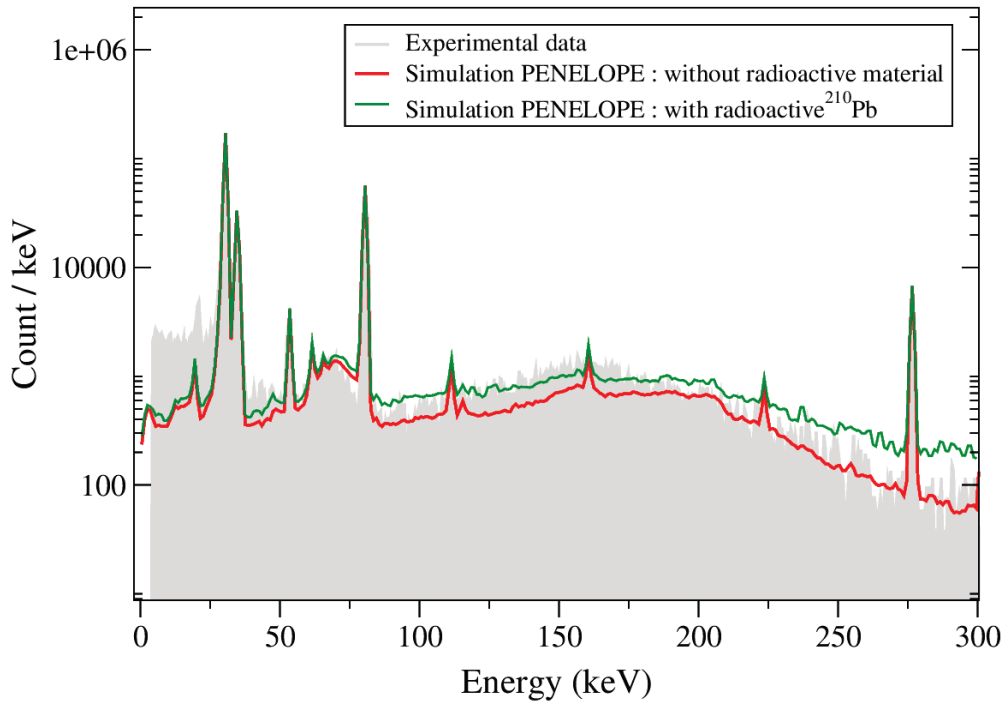


Figure 88: Comparison of the  $^{133}\text{Ba}$  experimental spectrum acquired in October 2017 with two simulated spectra obtained after 10 million decays. The experimental data are rescaled on the PENELOPE data using the peak at 356 keV.



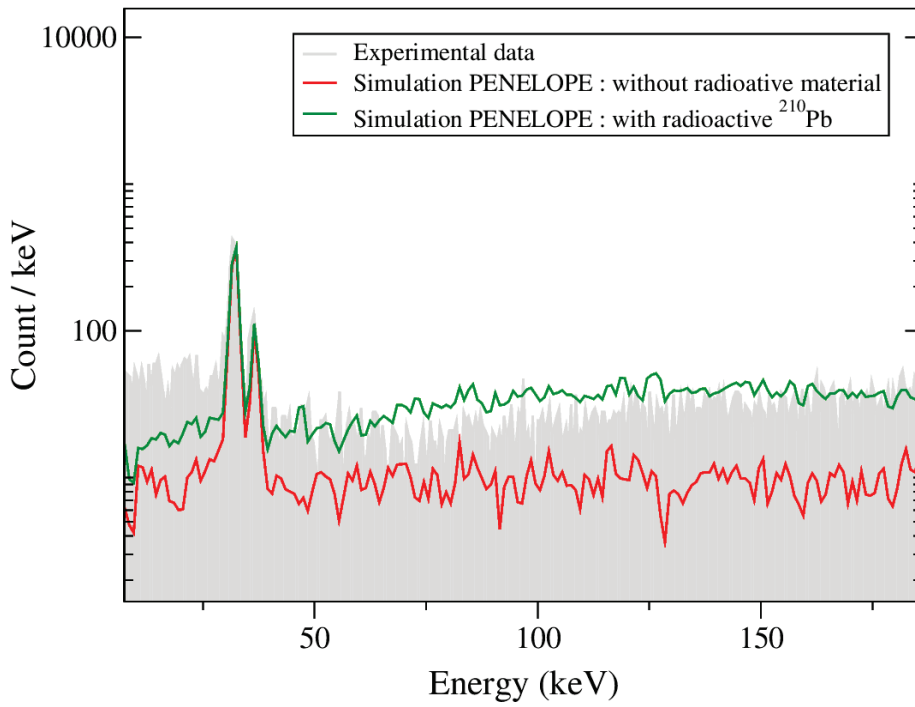


Figure 89: Comparison of the  $^{137}\text{Cs}$  experimental spectrum acquired in October 2017 with two simulated spectra obtained after 500 000 decays. The experimental data are rescaled on the PENELOPE data using the peak at 661 keV.

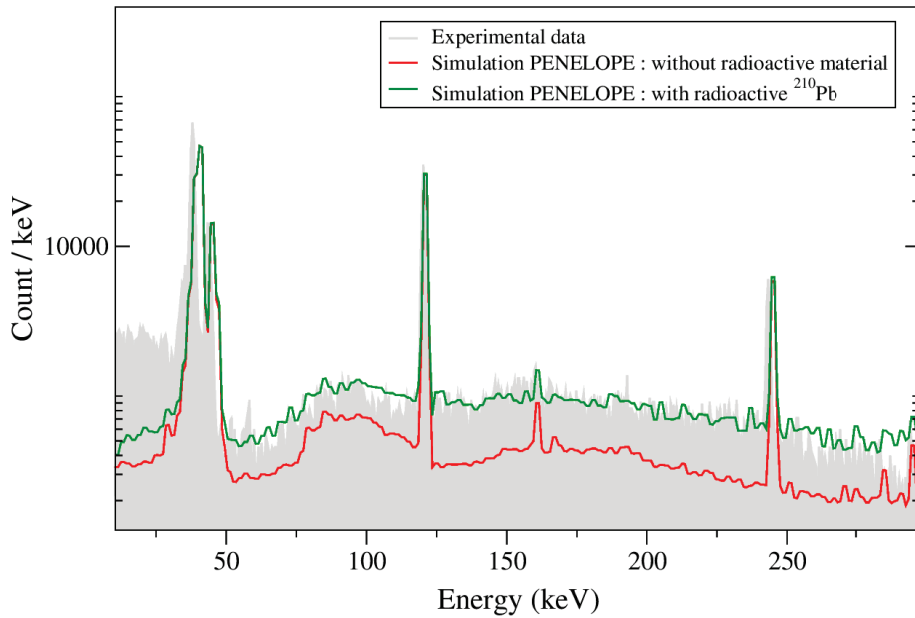


Figure 90: Comparison of the  $^{152}\text{Eu}$  experimental spectrum acquired in October 2017 with two simulated spectra obtained after 10 million decays. The experimental data are rescaled on the PENELOPE data using the peak at 344 keV.

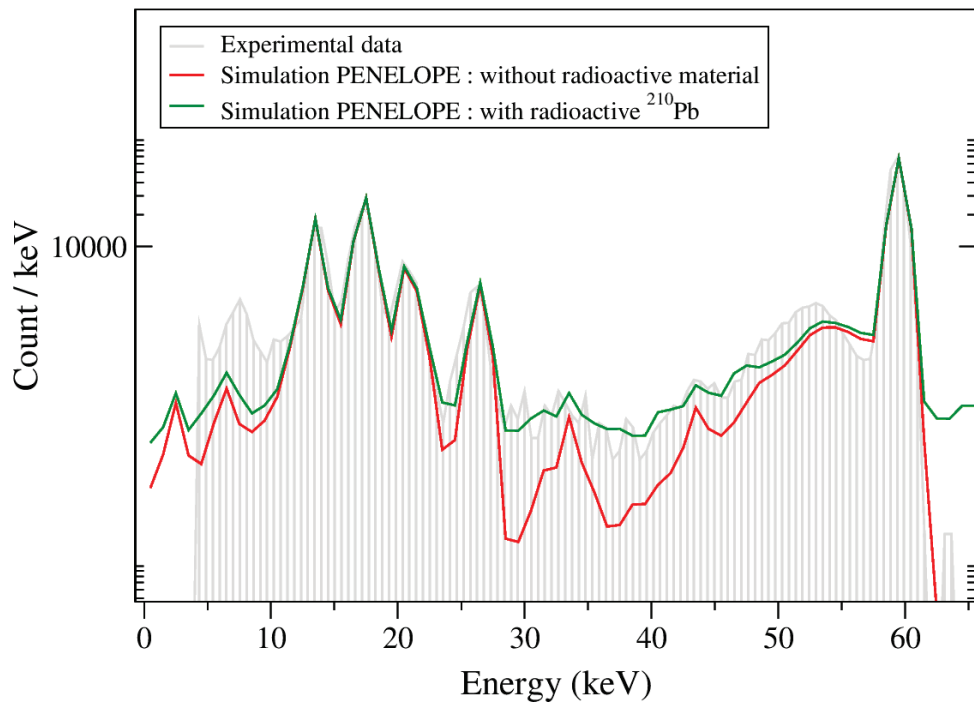


Figure 91: Comparison of the  $^{241}\text{Am}$  experimental spectrum acquired in October 2017 with two simulated spectra obtained after 10 million decays. The experimental data are rescaled on the PENELOPE data using the peak at 59 keV.

## E.2 Effect of source shape modification

---

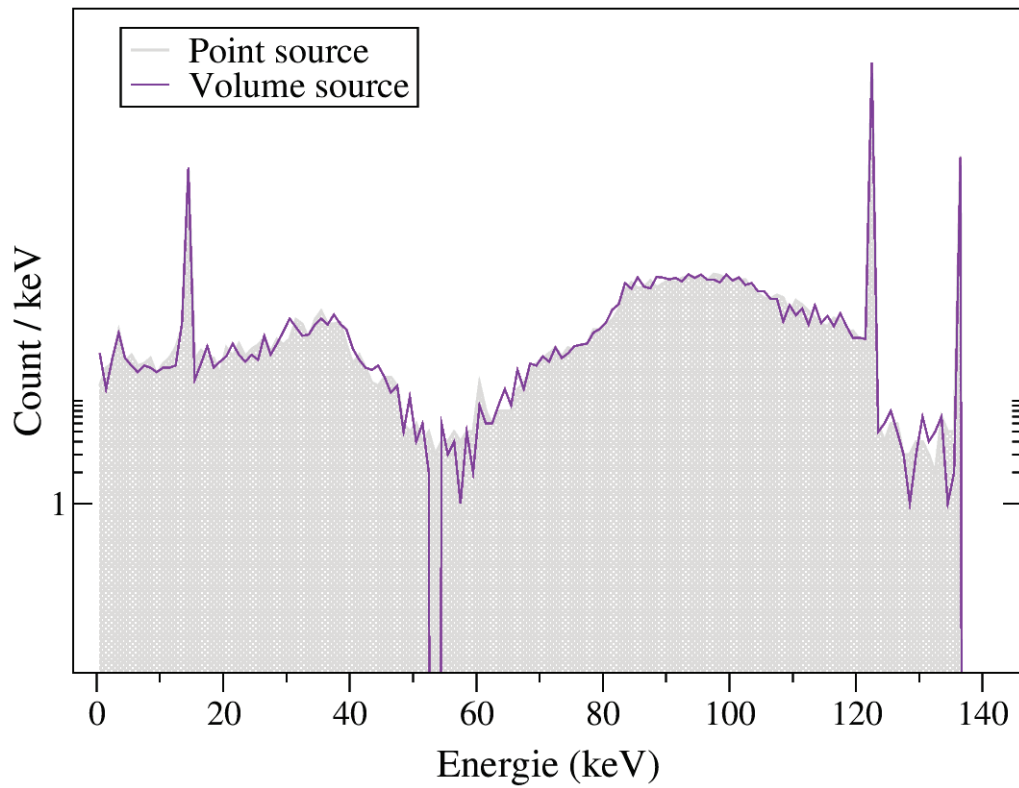


Figure 92: Comparison of two simulated spectra of  $^{57}\text{Co}$  for 10 million decays, one is for a volumetric source and one is for a point source located on the target holder at 12 cm from the germanium detector. The volumetric source had a diameter of 2 cm and a height of 2 mm.

### E.3 Impact of source displacement in x and y directions

---

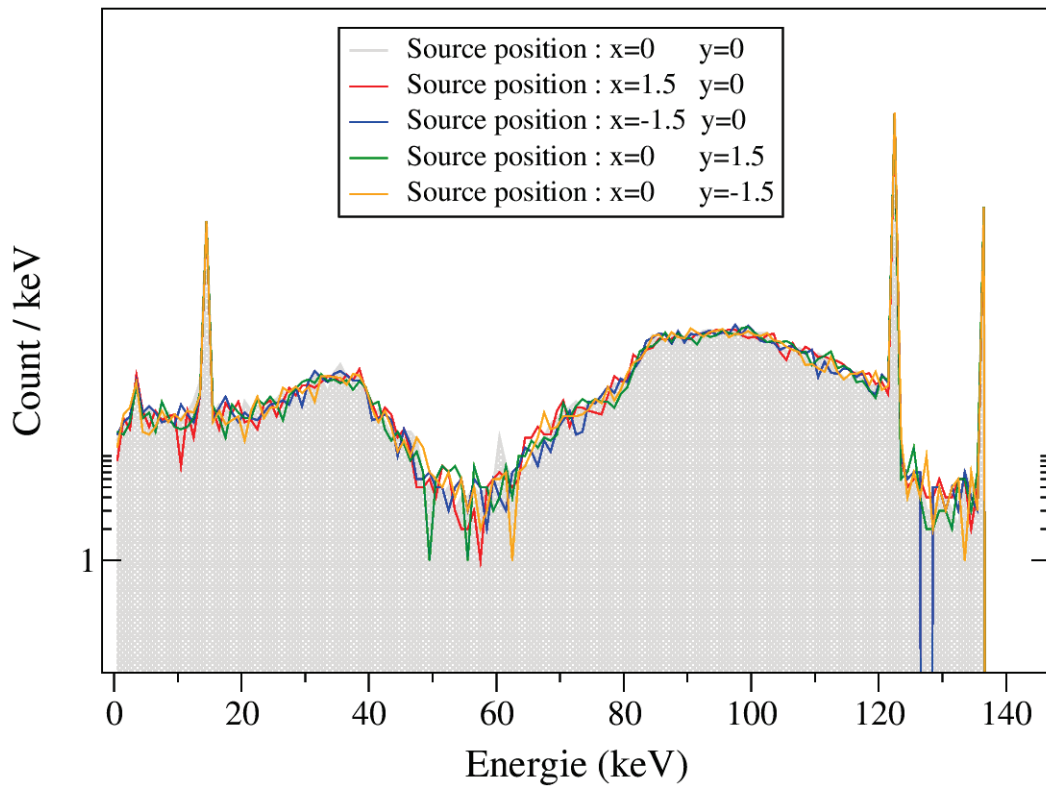


Figure 93: Comparison of five simulated spectra of  $^{57}\text{Co}$  for 10 million decays with five different positions in the x-y plan. The source positions are in centimeter and the position in  $x=0$  and  $y=0$  is located at 12 cm from the germanium detector.

## F Activity curves

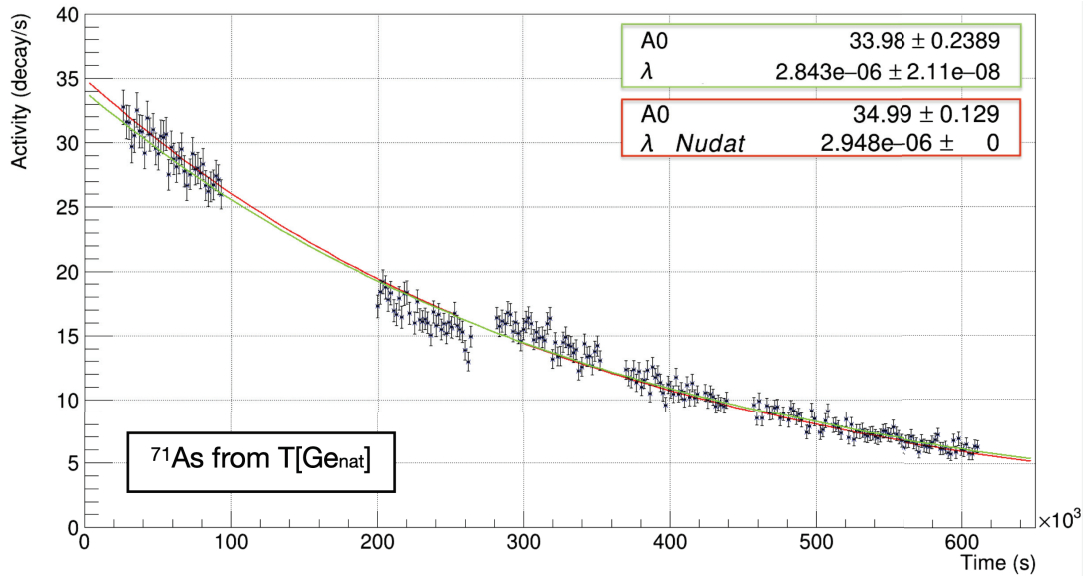


Figure 94: Experimental activity curve obtained for  $^{71}\text{As}$  from measurements in the  $\text{T}[\text{Ge}_{\text{nat}}]$ . The green curves correspond to fits with two free parameters  $A_0$  and  $\lambda$  while the red curves correspond to fits with one free parameter  $A_0$  and one parameter  $\lambda$  fixed to the NUDAT value.

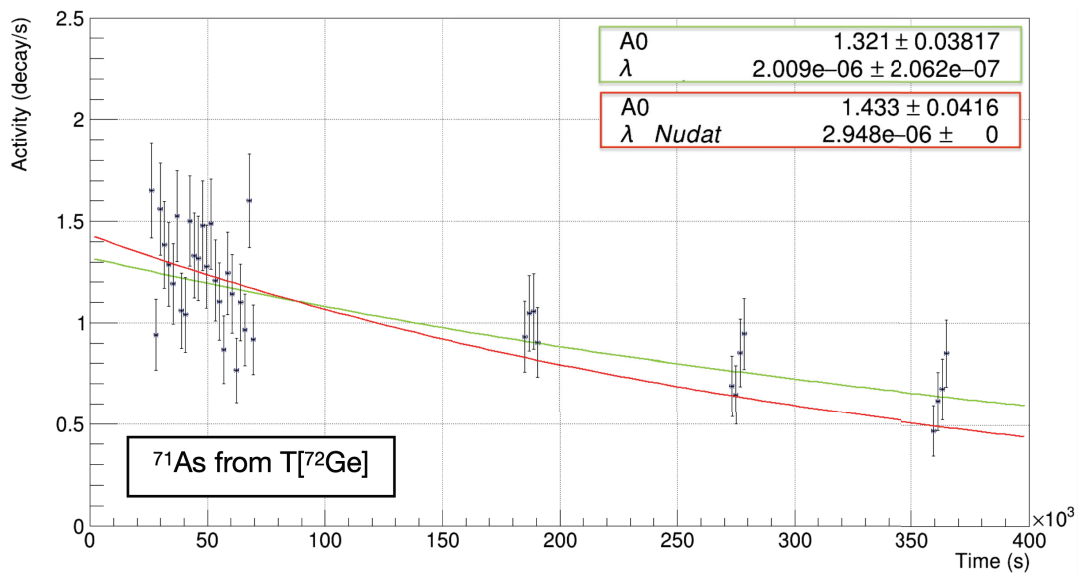


Figure 95: Experimental activity curve obtained for  $^{71}\text{As}$  from measurements in the  $\text{T}[^{72}\text{Ge}]$ . The green curves correspond to fits with two free parameters  $A_0$  and  $\lambda$  while the red curves correspond to fits with one free parameter  $A_0$  and one parameter  $\lambda$  fixed to the NUDAT value.

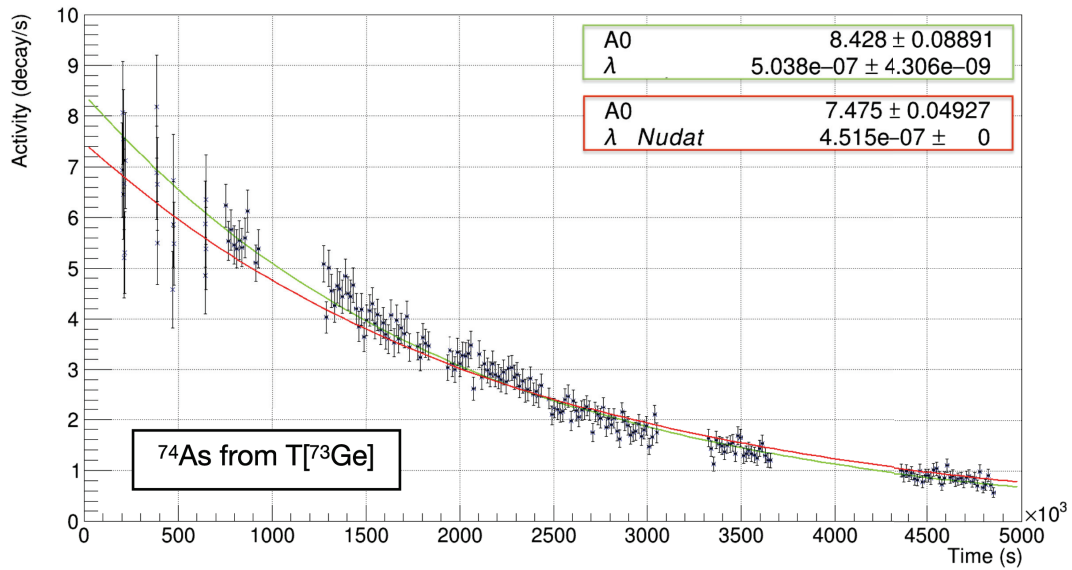


Figure 96: Experimental activity curve obtained for  $^{74}\text{As}$  from measurements in the T[ $^{73}\text{Ge}$ ]. Activities with large error bars represent acquisition times of 30 minutes, while runs with smaller error bars represent 4 hours acquisition times. The green curves correspond to fits with two free parameters  $A_0$  and  $\lambda$  while the red curves correspond to fits with one free parameter  $A_0$  and one parameter  $\lambda$  fixed to the NUDAT value.

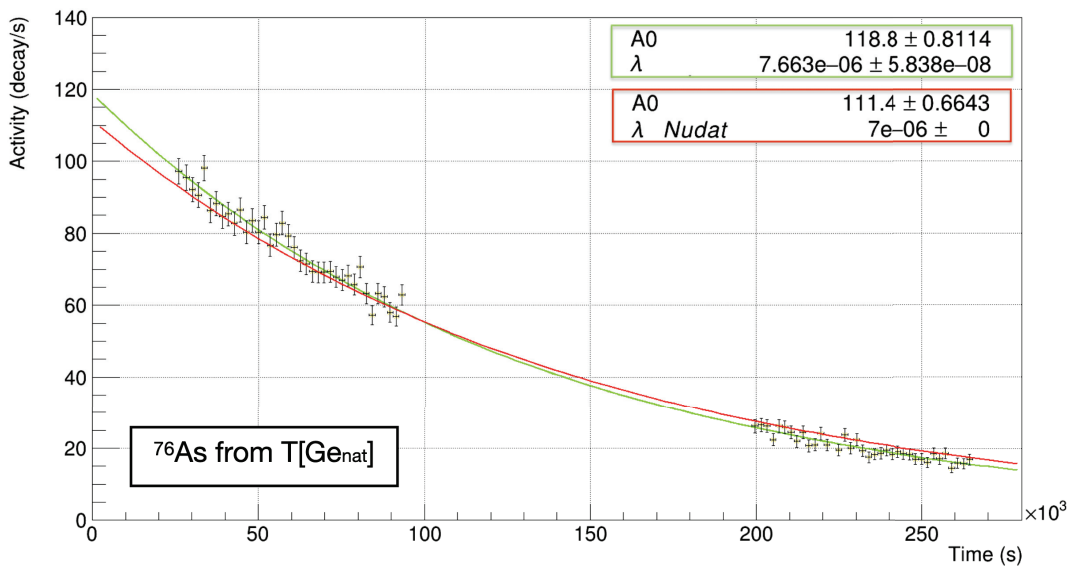


Figure 97: Experimental activity curve obtained for  $^{76}\text{As}$  from measurements in the T[ $\text{Ge}_{nat}$ ]. The green curves correspond to fits with two free parameters  $A_0$  and  $\lambda$  while the red curves correspond to fits with one free parameter  $A_0$  and one parameter  $\lambda$  fixed to the NUDAT value.

## G Cross Section Sensitivity

---

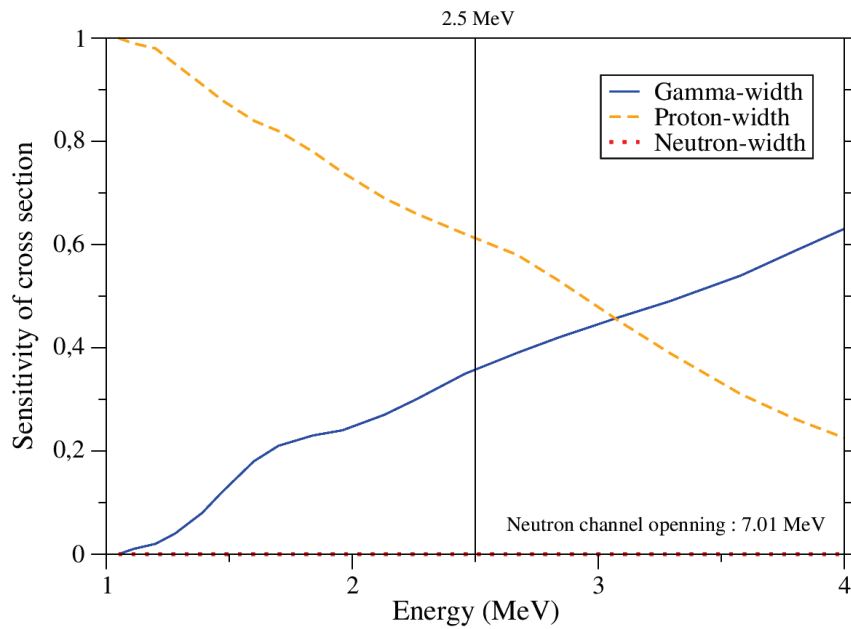


Figure 98: Laboratory cross section sensitivity to the different particle widths for the  $^{70}\text{Ge}(p, \gamma)^{71}\text{As}$  reaction as function of energy. The vertical bar represents the energy investigated in this study. Note that the cross section sensitivity to the neutron-width is equal to 0 and overlaps with the contour of the graph. Theoretical curves extracted from [35].

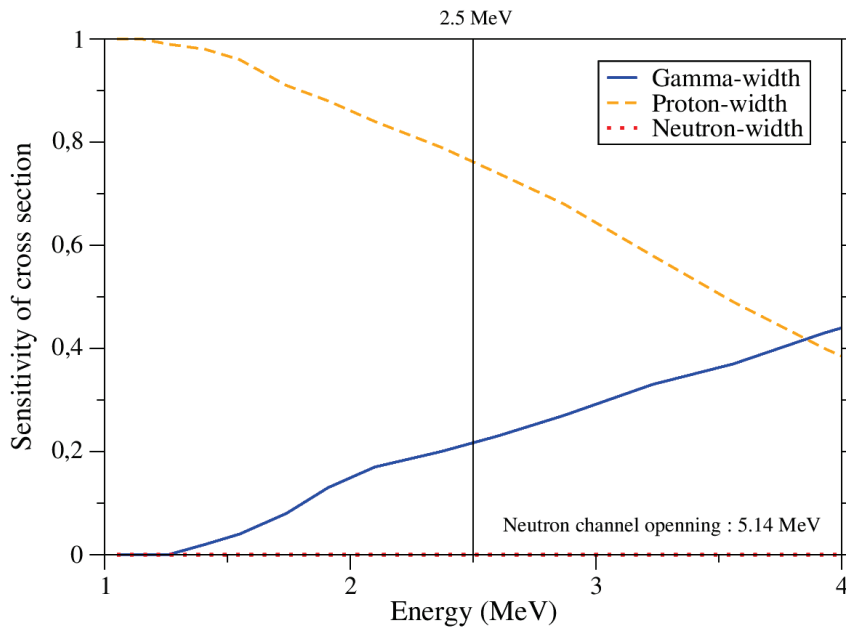


Figure 99: Laboratory cross section sensitivity to the different particle widths for the  $^{72}\text{Ge}(p, \gamma)^{73}\text{As}$  reaction as function of energy. The vertical bar represents the energy investigated in this study. Theoretical curves extracted from [35].

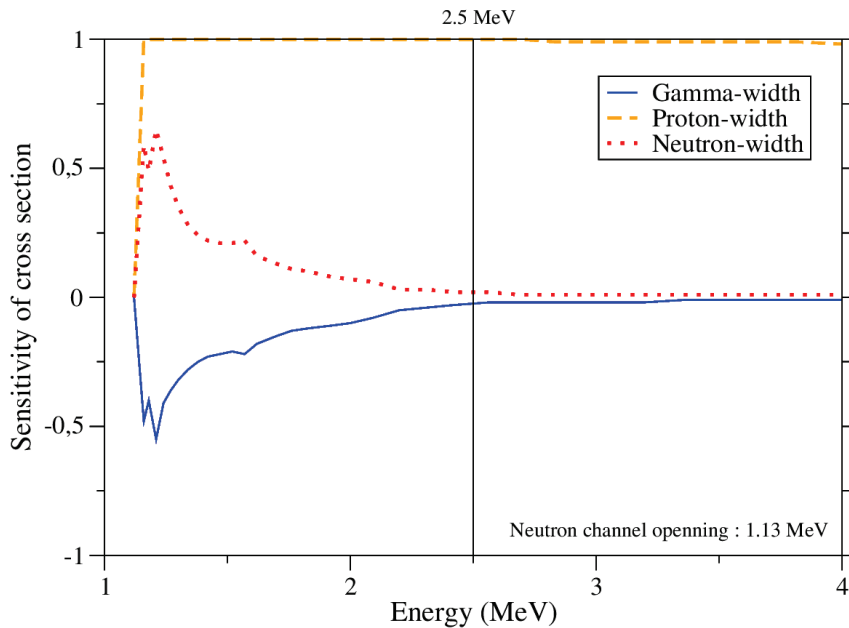


Figure 100: Laboratory cross section sensitivity to the different particle widths for the  $^{73}\text{Ge}(p, n)^{73}\text{As}$  reaction as function of energy. The vertical bar represents the energy investigated in this study. Note that the cross section sensitivity to the proton-width is maximal and equal to 1 above the neutron channel opening and overlaps with the contour of the graph. Theoretical curves extracted from [35].



# H Alphas energy loss in silicon

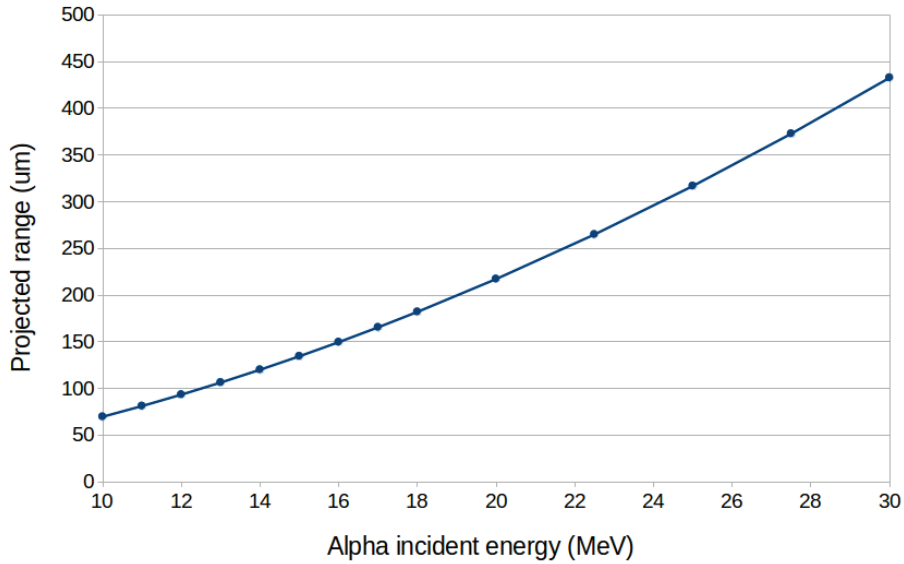


Figure 101: Maximum projected range of alphas in silicon as a function of the incident energy of the particles.

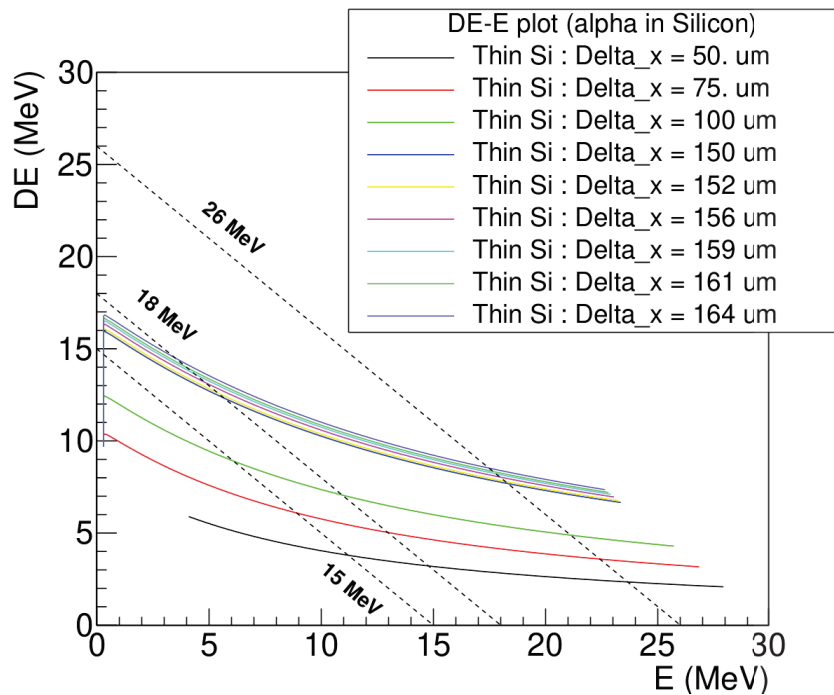


Figure 102: Estimation of the experimental  $\Delta E$ -E diagram for various  $\Delta E$  thicknesses. The plot has been generated using information on alpha particle energy loss in silicon obtained from Fig101.

# I Boosted decision tree prediction on $(p,\gamma)$ reaction

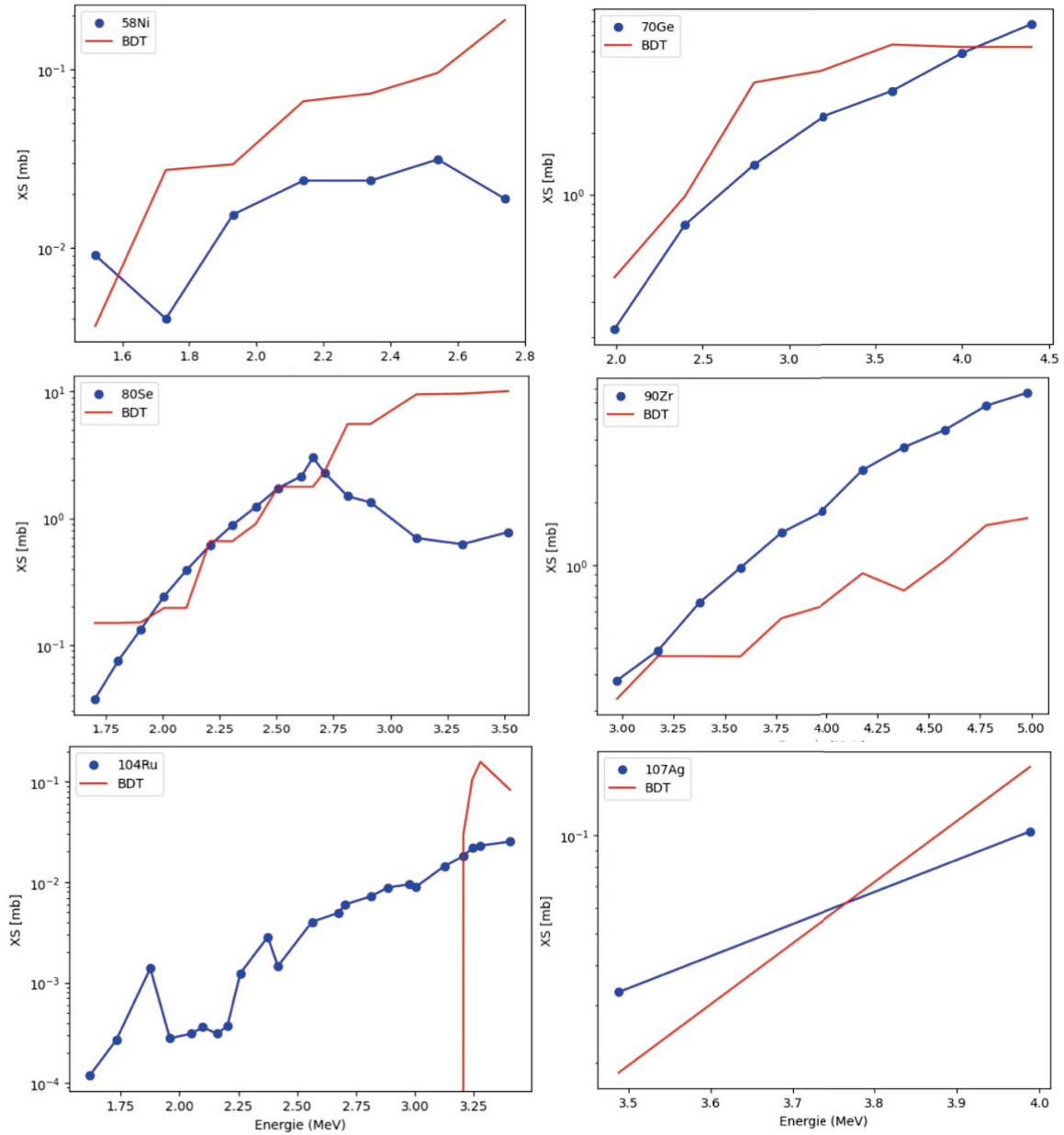


Figure 103: Panels displaying the prediction fits obtained by the BDT (in red) for six  $(p,\gamma)$  reactions realized on nuclei indicated in blue on the plots.

## References

---

- [1] G. G. Kiss et al. “ $^{70}\text{Ge}(p, \gamma)^{71}\text{As}$  and  $^{76}\text{Ge}(p, n)^{76}\text{As}$  cross sections for the astrophysical  $p$  process: Sensitivity of the optical proton potential at low energies”. In: *Phys. Rev. C* 76 (5 2007), p. 055807. DOI: 10.1103/PhysRevC.76.055807. URL: <https://link.aps.org/doi/10.1103/PhysRevC.76.055807>.
- [2] Hans E. Suess and Harold C. Urey. “Abundances of the Elements”. In: *Rev. Mod. Phys.* 28 (1 1956), pp. 53–74. DOI: 10.1103/RevModPhys.28.53. URL: <https://link.aps.org/doi/10.1103/RevModPhys.28.53>.
- [3] E. Anders and N. Grevesse. “Abundances of the elements: Meteoritic and solar”. In: 53.1 (Jan. 1989), pp. 197–214. DOI: 10.1016/0016-7037(89)90286-X.
- [4] *National Nuclear Data Center, Brookhaven National Laboratory*. URL: <https://www.nndc.bnl.gov/>.
- [5] E. Margaret Burbidge et al. “Synthesis of the Elements in Stars”. In: *Rev. Mod. Phys.* 29 (4 1957), pp. 547–650. DOI: 10.1103/RevModPhys.29.547. URL: <https://link.aps.org/doi/10.1103/RevModPhys.29.547>.
- [6] A. G. W. Cameron. “NUCLEAR REACTIONS IN STARS AND NUCLEOGENESIS”. In: *Publications of the Astronomical Society of the Pacific* 69.408 (1957), p. 201. DOI: 10.1086/127051. URL: <https://dx.doi.org/10.1086/127051>.
- [7] Ralph A. Alpher and Robert C. Herman. “Remarks on the Evolution of the Expanding Universe”. In: *Phys. Rev.* 75 (7 1949), pp. 1089–1095. DOI: 10.1103/PhysRev.75.1089. URL: <https://link.aps.org/doi/10.1103/PhysRev.75.1089>.
- [8] R. A. Alpher, H. Bethe, and G. Gamow. “The Origin of Chemical Elements”. In: *Phys. Rev.* 73 (7 1948), pp. 803–804. DOI: 10.1103/PhysRev.73.803. URL: <https://link.aps.org/doi/10.1103/PhysRev.73.803>.
- [9] Christian Iliadis. “Nuclear Physics of Stars, Second, Revised and Enlarged Edition”. In: WILEY-VCH, 2015. ISBN: 978-3-527-33648-7.
- [10] Richard H Cyburt, Brian D Fields, and Keith A Olive. “Primordial nucleosynthesis in light of WMAP”. In: *Physics Letters B* 567.3 (2003), pp. 227–234. ISSN: 0370-2693. DOI: <https://doi.org/10.1016/j.physletb.2003.06.026>. URL: <https://www.sciencedirect.com/science/article/pii/S037026930300916X>.
- [11] Socratic Q&A. *What is the Hertzsprung-Russell diagram and why is it so important to astronomy research?* 2016. URL: <https://socratic.org/>.
- [12] Claus E. Rolfs and William S. Rodney. “Cauldrons in the Cosmos, Nuclear Astrophysics”. In: The University of Chicago Press, 1988. ISBN: 0-226-72457-3.
- [13] Debades Bandyopadhyay and Kamales Kar. “Supernovae, Neutron Star Physics and Nucleosynthesis”. In: Springer, 2022. ISBN: 978-3-030-95170-2.
- [14] Francesco Pogliano et al. *Experimentally constrained  $^{165,166}\text{Ho}(n, \gamma)$  rates and implications for the  $s$  process*. 2023. arXiv: 2304.14517 [nucl-ex].

- [15] F. Käppeler et al. “The  $s$  process: Nuclear physics, stellar models, and observations”. In: *Rev. Mod. Phys.* 83 (1 2011), pp. 157–193. DOI: 10.1103/RevModPhys.83.157. URL: <https://link.aps.org/doi/10.1103/RevModPhys.83.157>.
- [16] Evan Patrick O’Connor. “Topics in Core-Collapse Supernova Theory: The Formation of Black Holes and the Transport of Neutrinos”. PhD thesis. California Institute of Technology, 2012.
- [17] Anna Frebel and Alexander P. Ji. “Observations of R-process Stars in the Milky Way and Dwarf Galaxies, Handbook of Nuclear Physics – Part III, Section 15 “Supernovae and Neutron Star Mergers””. In: Springer Nature, 2022.
- [18] S. E. WOOSLEY and W. M. Howard. “THE P-PROCESS IN SUPERNOVAE”. In: *Astrophysical Journal Supplement Series* 36 (1978), pp. 285–304. DOI: 10.1086/190501. URL: <https://ui.adsabs.harvard.edu/abs/1978ApJS...36..285W/abstract>.
- [19] G. R. Burbidge et al. “Californium-254 and Supernovae”. In: *Phys. Rev.* 103 (5 1956), pp. 1145–1149. DOI: 10.1103/PhysRev.103.1145. URL: <https://link.aps.org/doi/10.1103/PhysRev.103.1145>.
- [20] M. Arnould, S. Goriely, and K. Takahashi. “The r-process of stellar nucleosynthesis: Astrophysics and nuclear physics achievements and mysteries”. In: *Physics Reports* 450.4-6 (2007), pp. 97–213. DOI: 10.1016/j.physrep.2007.06.002. URL: <https://doi.org/10.1016%2Fj.physrep.2007.06.002>.
- [21] T Rauscher et al. “Constraining the astrophysical origin of the p-nuclei through nuclear physics and meteoritic data”. In: *Reports on Progress in Physics* 76.6 (2013), p. 066201. DOI: 10.1088/0034-4885/76/6/066201. URL: <https://dx.doi.org/10.1088/0034-4885/76/6/066201>.
- [22] N. Prantzos M. Rayet and M. Arnould. “The p-process revisited”. In: *Astronomy and Astrophysics* 227 (1990), pp. 271–281. ISSN: 0004-6361.
- [23] W. Rapp et al. “Sensitivity of p-Process Nucleosynthesis to Nuclear Reaction Rates in a 25 M Supernova Model”. In: *The Astrophysical Journal* 653.1 (2006), p. 474. DOI: 10.1086/508402. URL: <https://dx.doi.org/10.1086/508402>.
- [24] M. Rayet et al. “The p-process in Type II supernovae.” In: 298 (June 1995), p. 517. URL: <https://ui.adsabs.harvard.edu/abs/1995A&A...298..517R>.
- [25] M. Arnould and S. Goriely. “The p-process of stellar nucleosynthesis: astrophysics and nuclear physics status”. In: *Physics Reports* 384.1 (2003), pp. 1–84. ISSN: 0370-1573. DOI: [https://doi.org/10.1016/S0370-1573\(03\)00242-4](https://doi.org/10.1016/S0370-1573(03)00242-4). URL: <https://www.sciencedirect.com/science/article/pii/S0370157303002424>.
- [26] C. Fröhlich et al. “Neutrino-Induced Nucleosynthesis of  $A_{gt} \leq 64$  Nuclei: The  $\nu p$  Process”. In: *Phys. Rev. Lett.* 96 (14 2006), p. 142502. DOI: 10.1103/PhysRevLett.96.142502. URL: <https://link.aps.org/doi/10.1103/PhysRevLett.96.142502>.
- [27] J. Pruet et al. “Nucleosynthesis in Early Supernova Winds. II. The Role of Neutrinos”. In: *The Astrophysical Journal* 644.2 (2006), p. 1028. DOI: 10.1086/503891. URL: <https://dx.doi.org/10.1086/503891>.

- [28] Stephen J. Quinn. “Doctoral thesis : CAPTURE CROSS SECTIONS FOR THE ASTROPHYSICAL P PROCESS”. In: (2015). URL: [https://groups.nsc1.msu.edu/nsc1\\_library/Thesis/Quinn,%20Stephen.pdf](https://groups.nsc1.msu.edu/nsc1_library/Thesis/Quinn,%20Stephen.pdf).
- [29] Nevin N. Weinberg, Lars Bildsten, and Hendrik Schatz. “Exposing the Nuclear Burning Ashes of Radius Expansion Type I X-Ray Bursts”. In: *The Astrophysical Journal* 639 (2005), 1018–1032. ISSN: 0004-637X. DOI: 10.1086/499426.
- [30] H. Schatz et al. “rp-Process Nucleosynthesis at Extreme Temperature and Density Conditions”. In: 294 (Feb. 1998), pp. 167–264. DOI: 10.1016/S0370-1573(97)00048-3.
- [31] Carlos Alberto Calvachi Salas. “Astrophysical S-factor calculation for selected reactions”. In: (2023). URL: <https://repositorio.uniandes.edu.co/bitstream/handle/1992/64404/monograph-project.pdf?sequence=2&isAllowed=y>.
- [32] Thomas Rauscher and Friedrich-Karl Thielemann. “Astrophysical Reaction Rates From Statistical Model Calculations”. In: *Atomic Data and Nuclear Data Tables* 75.1 (2000), pp. 1–351. ISSN: 0092-640X. DOI: <https://doi.org/10.1006/adnd.2000.0834>. URL: <https://www.sciencedirect.com/science/article/pii/S0092640X00908349>.
- [33] VINAY SINGH. “ASTROPHYSICAL S-FACTORS FOR FUSION REACTIONS AND NUCLEOSYNTHESIS”. In: (2019). URL: <http://www.hbni.ac.in/phdthesis/phys/PHYS04201504002.pdf>.
- [34] A. Koning, S. Hilaire, and S. Goriely. “TALYS version 1.96 free software”. In: (2021). URL: [https://www.nds.iaea.org/talys/tutorials/talys\\_v1.96.pdf](https://www.nds.iaea.org/talys/tutorials/talys_v1.96.pdf).
- [35] T. Rauscher. “SENSITIVITY OF ASTROPHYSICAL REACTION RATES TO NUCLEAR UNCERTAINTIES”. In: *The Astrophysical Journal Supplement Series* 201.2 (2012), p. 26. DOI: 10.1088/0067-0049/201/2/26. URL: <https://dx.doi.org/10.1088/0067-0049/201/2/26>.
- [36] CEA. *Les réactions nucléaires : Le modèle optique*. 2023. URL: <https://www-phynu.cea.fr/>.
- [37] In: *Particle Physics Reference Library*. Ed. by Christian W. Fabjan and Herwig Schopper. Springer, 2020, p. 7. ISBN: 978-3-030-35318-6.
- [38] In: *Radiation Detection and Measurement, Fourth Edition*. Ed. by Glenn F. Knoll. John Wiley Sons, Inc., 2020, pp. 29–53. ISBN: 978-0-470-13148-0.
- [39] In: *Backscattering Spectrometry*. Ed. by Wei-Kan Chu. Elsevier Science, December 2, 2012 (originally published in 1978). ISBN: 9780323152051.
- [40] Selim Kaya, Necati Çelik, and Tuncay Bayram. “Effect of front, lateral and back dead layer thicknesses of a HPGe detector on full energy peak efficiency”. In: *Nuclear Instruments and Methods in Physics Research Section A: Accelerators, Spectrometers, Detectors and Associated Equipment* 1029 (2022), p. 166401. ISSN: 0168-9002. DOI: <https://doi.org/10.1016/j.nima.2022.166401>. URL: <https://www.sciencedirect.com/science/article/pii/S0168900222000626>.
- [41] MIRION Compagny. URL: <https://www.mirion.com/>.

- [42] MIRION Technologies. *An Introduction to the Fundamentals of Inductively Coupled Plasma – Mass Spectrometry (ICP-MS)*. 2023. URL: <https://www.agilent.com/>.
- [43] John R. de Laeter et al. “Atomic weights of the elements. Review 2000 (IUPAC Technical Report)”. In: *Pure and Applied Chemistry* 75.6 (2003), pp. 683–800. DOI: doi: 10.1351/pac200375060683. URL: <https://doi.org/10.1351/pac200375060683>.
- [44] Elemental Analysis Core. *ICP-MS as a Technique*. 2023. URL: <https://www.ohsu.edu/>.
- [45] CEA. *Analyse par spectrométrie de masse couplée à un plasma inductif (ICP-MS)*. 2023. URL: <https://iramis.cea.fr/>.
- [46] M. Bourgeois et al. “Sm isotope composition and Sm/Eu ratio determination in an irradiated  $^{153}\text{Eu}$  sample by ion exchange chromatography-quadrupole inductively coupled plasma mass spectrometry combined with double spike isotope dilution technique”. In: *J. Anal. At. Spectrom.* 26 (8 2011), pp. 1660–1666. DOI: 10.1039/C1JA10070J. URL: <http://dx.doi.org/10.1039/C1JA10070J>.
- [47] M. Mayer. “Improved physics in SIMNRA7”. In: *Nuclear Instruments and Methods in Physics Research Section B: Beam Interactions with Materials and Atoms* 332 (2014). 21st International Conference on Ion Beam Analysis, pp. 176–180. ISSN: 0168-583X. DOI: <https://doi.org/10.1016/j.nimb.2014.02.056>. URL: <https://www.sciencedirect.com/science/article/pii/S0168583X14003139>.
- [48] PENELOPE 2018. *Code System for Monte-Carlo Simulation of Electron and Photon Transport, Nuclear Energy Agency*. 2018. URL: <https://www.oecd-nea.org/tools/abstract/detail/NEA-1525>.
- [49] STOGS-GEANT4 package. *Simulation Toolkit fOr Gamma-ray Spectroscopy, IP2I Laboratory*. 2016. URL: <https://github.com/stezow/stogs>.
- [50] A. Sauerwein et al. “Investigation of the reaction  $^{74}\text{Ge}(p,\gamma)^{75}\text{As}$  using the in-beam method to improve reaction network predictions for  $p$  nuclei”. In: *Phys. Rev. C* 86 (3 2012), p. 035802. DOI: 10.1103/PhysRevC.86.035802. URL: <https://link.aps.org/doi/10.1103/PhysRevC.86.035802>.
- [51] S. J. Quinn et al. “Probing the production mechanism of the light  $p$ -process nuclei”. In: *Phys. Rev. C* 88 (1 2013), p. 011603. DOI: 10.1103/PhysRevC.88.011603. URL: <https://link.aps.org/doi/10.1103/PhysRevC.88.011603>.
- [52] D. Wu et al. “New measurement of the  $^{74}\text{Ge}(p,\gamma)^{75}\text{As}$  reaction cross sections in the  $p$ -process nucleosynthesis”. In: *Physics Letters B* 805 (2020), p. 135431. ISSN: 0370-2693. DOI: <https://doi.org/10.1016/j.physletb.2020.135431>. URL: <https://www.sciencedirect.com/science/article/pii/S0370269320302355>.
- [53] F. Naqvi et al. “Proton capture cross section of  $^{72}\text{Ge}$  and astrophysical implications”. In: *Phys. Rev. C* 92 (2 2015), p. 025804. DOI: 10.1103/PhysRevC.92.025804. URL: <https://link.aps.org/doi/10.1103/PhysRevC.92.025804>.
- [54] György Gyürky et al. “The activation method for cross section measurements in nuclear astrophysics”. In: *The European Physical Journal A* 55 (Mar. 2019). DOI: 10.1140/epja/i2019-12708-4.
- [55] EURISOTOP Company. URL: <https://www.eurisotop.com/>.



- [56] Almas Bashir et al. “Chapter 3 - Interfaces and surfaces”. In: *Chemistry of Nanomaterials*. Ed. by Tahir Iqbal Awan, Almas Bashir, and Aqsa Tehseen. Elsevier, 2020, pp. 51–87. ISBN: 978-0-12-818908-5. DOI: <https://doi.org/10.1016/B978-0-12-818908-5.00003-2>. URL: <https://www.sciencedirect.com/science/article/pii/B9780128189085000032>.
- [57] SEMICORE Company. URL: <https://www.semicore.com/>.
- [58] John R. de Laeter et al. “Atomic weights of the elements. Review 2000 (IUPAC Technical Report)”. In: *Pure and Applied Chemistry* 75.6 (2003), pp. 683–800. DOI: [doi: 10.1351/pac200375060683](https://doi.org/10.1351/pac200375060683). URL: <https://doi.org/10.1351/pac200375060683>.
- [59] Silvia Diez-Fernández et al. “A new method for determining  $^{236}\text{U}/^{238}\text{U}$  isotope ratios in environmental samples by means OF ICP-MS/MS”. In: *Talanta* 206 (2020), p. 120221. ISSN: 0039-9140. DOI: <https://doi.org/10.1016/j.talanta.2019.120221>. URL: <https://www.sciencedirect.com/science/article/pii/S0039914019308549>.
- [60] GENIE2000, Basic Spectroscopy Software, MIRION Compagny. URL: <https://www.mirion.com/products/genie-2000-basic-spectroscopy-software/>.
- [61] Lama Al Ayoubi. “Master Report : Study of the  $^{72}\text{Ge}(p, \gamma)^{73}\text{As}$  reaction involved in the nucleosynthesis of p-nuclei”. In: (2018).
- [62] Smarajit Triambak. “THE ISOBARIC MULTIPLET MASS EQUATION AND ft VALUE OF THE  $0 + \rightarrow 0 +$  FERMI TRANSITION IN  $^{32}\text{Ar}$ : TWO TESTS OF ISOSPIN SYMMETRY BREAKING”. In: *Dissertation submitted to the Graduate School of the University of Notre Dame* (2007). URL: <https://www.npl.washington.edu/sites/default/files/phd-theses/TriambakS042007.pdf>.
- [63] Eduardo García-Toraño, Milagros Pozuelo, and Francesc Salvat. “Monte Carlo calculations of coincidence-summing corrections for volume sources in gamma-ray spectrometry with Ge detectors”. In: *Nuclear Instruments and Methods in Physics Research Section A: Accelerators, Spectrometers, Detectors and Associated Equipment* 544.3 (2005), pp. 577–583. ISSN: 0168-9002. DOI: <https://doi.org/10.1016/j.nima.2005.01.299>. URL: <https://www.sciencedirect.com/science/article/pii/S0168900205004821>.
- [64] Klaus Debertin and Ulrich Schötzig. “Coincidence summing corrections in Ge(Li)-spectrometry at low source-to-detector distances”. In: *Nuclear Instruments and Methods* 158 (1979), pp. 471–477. ISSN: 0029-554X. DOI: [https://doi.org/10.1016/S0029-554X\(79\)94845-6](https://doi.org/10.1016/S0029-554X(79)94845-6). URL: <https://www.sciencedirect.com/science/article/pii/S0029554X79948456>.
- [65] E. García-Toraño et al. “Simulation of decay processes and radiation transport times in radioactivity measurements”. In: *Nuclear Instruments and Methods in Physics Research Section B: Beam Interactions with Materials and Atoms* 396 (2017), pp. 43–49. ISSN: 0168-583X. DOI: <https://doi.org/10.1016/j.nimb.2017.02.002>. URL: <https://www.sciencedirect.com/science/article/pii/S0168583X17301131>.
- [66] D-C. Radford. *The RadWare package, Oak Ridge National Laboratory*. URL: <https://radware.phy.ornl.gov/gf3/#5.3..>

- [67] Dirk Arnold and Octavian Sima. “Extension of the efficiency calibration of germanium detectors using the GESPECOR software”. In: *Applied Radiation and Isotopes* 61.2 (2004). Low Level Radionuclide Measurement Techniques - ICRM, pp. 117–121. ISSN: 0969-8043. DOI: <https://doi.org/10.1016/j.apradiso.2004.03.031>. URL: <https://www.sciencedirect.com/science/article/pii/S0969804304000922>.
- [68] ROOT Collaboration. *ROOT - An Object-Oriented Data Analysis Framework, Software package, version 6.22/02*. URL: <https://root.cern.ch>.
- [69] E.I.Wyatt G.I.Gleason J.F.Emery S.A.Reynolds. “Half-Lives of Radionuclides—IV”. In: *Chemistry of Nuclear Science and Engineering IV*. Vol. 48. 1972, pp. 319–323. DOI: 10.13182/NSE72-A22489.
- [70] H Y Liao et al. “Production and decay of the  $^{73}\text{Ge}^*(1/2)$  metastable state in a low-background germanium detector”. In: *Journal of Physics G: Nuclear and Particle Physics* 35.7 (2008), p. 077001. DOI: 10.1088/0954-3899/35/7/077001. URL: <https://dx.doi.org/10.1088/0954-3899/35/7/077001>.
- [71] E. Vagena, M. Axiotis, and P. Dimitriou. “Systematics of the semimicroscopic proton-nucleus optical potential at low energies relevant for nuclear astrophysics”. In: *Phys. Rev. C* 103 (4 2021), p. 045806. DOI: 10.1103/PhysRevC.103.045806. URL: <https://link.aps.org/doi/10.1103/PhysRevC.103.045806>.
- [72] Stephane Goriely, Ann-Cecilie Larsen, and Dennis Mucher. “Comprehensive test of nuclear level density models”. In: *Phys. Rev. C* 106 (4 2022), p. 044315. DOI: 10.1103/PhysRevC.106.044315. URL: <https://link.aps.org/doi/10.1103/PhysRevC.106.044315>.
- [73] A. Koning, S. Hilaire, and S. Goriely. “TALYS version 1.961, private communication”. In: (2023).
- [74] T. Raushcher. “NON-SMOKER Database”. In: *Atomic Data Nuclear Data Tables* 79 (2001). URL: <https://nucastro.org/nonsmoker.html>.
- [75] Thomas Rauscher. “Relevant energy ranges for astrophysical reaction rates”. In: *Phys. Rev. C* 81 (4 2010), p. 045807. DOI: 10.1103/PhysRevC.81.045807. URL: <https://link.aps.org/doi/10.1103/PhysRevC.81.045807>.
- [76] Richard H. Cyburt et al. “THE JINA REACLIB DATABASE: ITS RECENT UPDATES AND IMPACT ON TYPE-I X-RAY BURSTS”. In: *The Astrophysical Journal Supplement Series* 189.1 (2010), p. 240. DOI: 10.1088/0067-0049/189/1/240. URL: <https://dx.doi.org/10.1088/0067-0049/189/1/240>.
- [77] Thomas Rauscher. “Branchings in the  $\gamma$  process path revisited”. In: *Phys. Rev. C* 73 (1 2006), p. 015804. DOI: 10.1103/PhysRevC.73.015804. URL: <https://link.aps.org/doi/10.1103/PhysRevC.73.015804>.
- [78] U. Atzrott et al. “Uniform  $\alpha$ -nucleus potential in a wide range of masses and energies”. In: *Phys. Rev. C* 53 (3 1996), pp. 1336–1347. DOI: 10.1103/PhysRevC.53.1336. URL: <https://link.aps.org/doi/10.1103/PhysRevC.53.1336>.



- [79] V. Avrigeanu, P. E. Hodgson, and M. Avrigeanu. “Global optical potentials for emitted alpha particles”. In: *Phys. Rev. C* 49 (4 1994), pp. 2136–2141. DOI: 10.1103/PhysRevC.49.2136. URL: <https://link.aps.org/doi/10.1103/PhysRevC.49.2136>.
- [80] P. Demetriou, C. Grama, and S. Goriely. “Improved global -optical model potentials at low energies”. In: *Nuclear Physics A* 707.1 (2002), pp. 253–276. ISSN: 0375-9474. DOI: [https://doi.org/10.1016/S0375-9474\(02\)00756-X](https://doi.org/10.1016/S0375-9474(02)00756-X). URL: <https://www.sciencedirect.com/science/article/pii/S037594740200756X>.
- [81] V. Avrigeanu, M. Avrigeanuilescu, familyi=u., given=C., giveni=C., ,, and. “Further explorations of the  $\alpha$ -particle optical model potential at low energies for the mass range  $A \approx 45$ –209”. In: *Phys. Rev. C* 90 (4 2014), p. 044612. DOI: 10.1103/PhysRevC.90.044612. URL: <https://link.aps.org/doi/10.1103/PhysRevC.90.044612>.
- [82] MORFOUACE Pierre. “Doctoral thesis : Single-particle states in neutron-rich 69,71 Cu by means of the (d, 3 He) transfer reaction”. In: (2014). URL: [https://theses.hal.science/tel-01133389/preview/VA2\\_MORFOUACE\\_PIERRE\\_26092014.pdf](https://theses.hal.science/tel-01133389/preview/VA2_MORFOUACE_PIERRE_26092014.pdf).
- [83] P. Mohr et al. “ $^{144}\text{Sm}$ - $\alpha$  optical potential at astrophysically relevant energies derived from  $^{144}\text{Sm}(\alpha, \alpha)^{144}\text{Sm}$  elastic scattering”. In: *Phys. Rev. C* 55 (3 1997), pp. 1523–1531. DOI: 10.1103/PhysRevC.55.1523. URL: <https://link.aps.org/doi/10.1103/PhysRevC.55.1523>.
- [84] E. Somorjai et al. “Experimental cross section of  $^{144}\text{Sm}(\alpha, \alpha)^{148}\text{Gd}$ ”. In: *Nuclear Physics A* 621.1 (1997). Nuclei in the Cosmos, pp. 293–296. ISSN: 0375-9474. DOI: [https://doi.org/10.1016/S0375-9474\(97\)00258-3](https://doi.org/10.1016/S0375-9474(97)00258-3). URL: <https://www.sciencedirect.com/science/article/pii/S0375947497002583>.
- [85] Cyril Bachelet. “Ligne de caractérisation des expériences RBS, IJCLab Orsay”. In: (2021).
- [86] IJCLAB Orsay. *Instrumentation at ALTO*. 2023. URL: <https://alto.ijclab.in2p3.fr/en/instrumentation-en/>.
- [87] J.E. Spencer and H.A. Enge. “Split-pole magnetic spectrograph for precision nuclear spectroscopy”. In: *Nuclear Instruments and Methods* 49.2 (1967), pp. 181–193. ISSN: 0029-554X. DOI: [https://doi.org/10.1016/0029-554X\(67\)90684-2](https://doi.org/10.1016/0029-554X(67)90684-2). URL: <https://www.sciencedirect.com/science/article/pii/0029554X67906842>.
- [88] Nicolas de Sereville. “The Enge Split-Pole at ALTO: recent nucleosynthesis studies”. In: *Institut de Physique Nucléaire d’Orsay* (2018). URL: [https://indico.in2p3.fr/event/17616/contributions/63243/attachments/48731/61677/lia\\_bresil\\_deSereville.pdf](https://indico.in2p3.fr/event/17616/contributions/63243/attachments/48731/61677/lia_bresil_deSereville.pdf).
- [89] Sk M. Ali et al. “Resonance Excitations in  $^7\text{Be}(d, p)^8\text{Be}^*$  to Address the Cosmological Lithium Problem”. In: *Phys. Rev. Lett.* 128 (25 2022), p. 252701. DOI: 10.1103/PhysRevLett.128.252701. URL: <https://link.aps.org/doi/10.1103/PhysRevLett.128.252701>.
- [90] Mirion Technologies. *MIRION*. 2023. URL: <https://www.mirion.com/>.
- [91] ORTEK Company. *ORTEK AMETEK*. 2023. URL: <https://www.ortec-online.com/>.

- [92] Dassault Systemes. *CATIA*. 2023. URL: <https://discover.3ds.com/>.
- [93] Gordon Kane. *Modern Elementary Particle Physics: Explaining and Extending the Standard Model*. 2nd ed. Cambridge University Press, 2017. DOI: 10.1017/9781316691434.
- [94] M. Catacora-Rios et al. “Exploring experimental conditions to reduce uncertainties in the optical potential”. In: *Physical Review C* 100.6 (2019). DOI: 10.1103/physrevc.100.064615. URL: <https://doi.org/10.1103/physrevc.100.064615>.
- [95] A. E. Lovell and F. M. Nunes. “Constraining transfer cross sections using Bayes’ theorem”. In: *Physical Review C* 97.6 (2018). DOI: 10.1103/physrevc.97.064612. URL: <https://doi.org/10.1103/physrevc.97.064612>.
- [96] C. Marshall et al. “Bayesian analysis of the  $^{70}\text{Zn}(d, ^3\text{He})^{69}\text{Cu}$  transfer reaction”. In: *Phys. Rev. C* 102 (2 2020), p. 024609. DOI: 10.1103/PhysRevC.102.024609. URL: <https://link.aps.org/doi/10.1103/PhysRevC.102.024609>.
- [97] M. Shelley and A. Pastore. *A new mass model for nuclear astrophysics: crossing 200 keV accuracy*. 2021. arXiv: 2102.07497 [nucl-th].
- [98] S. Goriely et al. *Progress in Nuclear Astrophysics: a multi-disciplinary field with still many open questions*. 2022. arXiv: 2212.02156 [nucl-th].
- [99] X. Fabian et al. “Artificial neural networks for neutron/ discrimination in the neutron detectors of NEDA”. In: *Nuclear Instruments and Methods in Physics Research Section A: Accelerators, Spectrometers, Detectors and Associated Equipment* 986 (2021), p. 164750. ISSN: 0168-9002. DOI: <https://doi.org/10.1016/j.nima.2020.164750>. URL: <https://www.sciencedirect.com/science/article/pii/S0168900220311475>.
- [100] U. v. Toussaint and V. Dose. “Bayesian inference in surface physics”. In: *Applied Physics A: Materials Science & Processing* 82.3 (Feb. 2006), pp. 403–413. DOI: 10.1007/s00339-005-3360-8.
- [101] Carl Edward Rasmussen and Christopher K. I. Williams. *Gaussian processes for machine learning*. Adaptive computation and machine learning. MIT Press, 2006, pp. I–XVIII, 1–248. ISBN: 026218253X.
- [102] Evan Baker, Peter Challenor, and Matt Eames. *Diagnostics for Stochastic Gaussian Process Emulators*. 2021. arXiv: 1902.01289 [stat.ME].
- [103] Machine Learning in Python. *scikit-learn*. 2023. URL: <https://scikit-learn.org/stable/>.
- [104] “Level density parameters for the back-shifted fermi gas model in the mass range  $40 < A < 250$ ”. In: *Nuclear Physics A* 217.2 (1973), pp. 269–298. ISSN: 0375-9474. DOI: [https://doi.org/10.1016/0375-9474\(73\)90196-6](https://doi.org/10.1016/0375-9474(73)90196-6).
- [105] M.K. Grossjean and H. Feldmeier. “Level density of a Fermi gas with pairing interactions”. In: *Nuclear Physics A* 444.1 (1985), pp. 113–132. ISSN: 0375-9474. DOI: [https://doi.org/10.1016/0375-9474\(85\)90294-5](https://doi.org/10.1016/0375-9474(85)90294-5). URL: <https://www.sciencedirect.com/science/article/pii/0375947485902945>.
- [106] University of Oslo. *Level densities and gamma-ray strength functions*. 2023. URL: <https://www.mn.uio.no/fysikk/english/research/about/infrastructure/ocl/nuclear-physics-research/compilation/>.